# Studies of a fixed bed chemical looping reactor for $H_2$ production by *in-situ* and *operando* x-ray and neutron diffraction

**Christopher de Leeuwe**

A thesis submitted for the degree of Doctor of Philosophy (PhD) in Chemical Engineering at Newcastle University

School of Engineering

# Abstract

The purpose of this thesis focused on the investigation of the use of non-stoichiometric oxides as oxygen carrier materials for chemical looping $H_2$ production. It concentrated on the use of strontium doped lanthanum ferrite ($La_{0.6}Sr_{0.4}FeO_{3-\delta}$, LSF641) for the chemical looping water-gas shift reactor.

Chemical looping consists of the cyclic oxidation and then reduction of a solid oxygen carrier material. This process is used to split a redox reaction into its two half reactions using the solid as an intermediate. In a water-gas shift reactor this consist of the oxidation of CO to $CO_2$ and the reduction of $H_2O$ to $H_2$.

It was shown that theoretically such a system would achieve higher conversions than a conventional reactor; 50% when operated at 1093 K for the conventional reactor and complete conversion when operated using a suitable non-stoichiometric oxide in a chemical looping system. When studied experimentally it was found that such a system could achieve conversions of 88% for both the reduction and oxidation half cycles. The system was also shown to continue to achieve these high conversions for over 1000 cycles without noticeable degradation in product quality or oxygen carrier material.

By using the thermal and chemical expansivities of LSF641 it was possible to determine its oxidation state of the LSF641 *in operando*. This was carried out through the use of synchrotron x-ray diffraction, this showed that how the gradient in chemical potential changed along the bed as a function of time.

This was compared with the results of an equilibrium limited thermodynamic model of the system. Both the outlet gas composition and the internal chemical potential of the system were compared to experimental results and showed good agreement. This indicates that the system operates close to its thermodynamic limitations making it a worthy system for further study.

# Acknowledgements

I would like to start by thanking Professor Ian Metcalfe, Dr Wenting Hu and Dr Mortiz Von Stosch for their guidance and supervision throughout this research. For the opportunities they gave to travel and present my work at conferences around the world. Also Professor John Evans for his guidance and support with the analysis of diffraction patterns and for sharing his knowledge of best practise for beamline experiments.

Synchrotron *in-situ* and *operando* XRD experiments were conducted and prepared at ID22 of ESRF and required the help and assistance from many members of "The Application of Ion Transport Group". Professor Ian Metcalfe for the beamline proposals. Dr Brain Ray, Dr Catherine Dejoie, Dr Carlotta Giacobbe, Dr Francisco García-García and Dr Wenting Hu for carrying out the pre-experimental assessments. Dr Evangelos Papioannou for driving the equipment down from Newcastle to Grenoble three times. Dr Danny Mak, Dr Dragos Neagu, Dr Stevin Pramana, Dionysios Vroulias, Dr Kelly Kousi, Leonida Bekris, Selim Ungut and everyone else already mentioned for their help running these round the clock experiments. Thanks are also owed to Trevor Ingham from IGI systems for the design and construction of the water delivery system and reactor furnaces here used.

*In-situ* neutron powder diffraction collected using the High Resolution Powder Diffractometer (HRPD) at the ISIS facilitates at the Rutherford Appleton laboratories required the help and assistance of Professor Martin-Owen Jones and Professor Paul Henry of ISIS. Also thanks are needed to Professor John Evans, Professor Ian Metcalfe, Dr Wenting Hu, Dr Brain Ray and Dr Stevin Pramana for their help in collecting and analysing the data.

I also need to thank the rest "The Application of Ion Transport Group" for their company in the lab and making me feel so welcome. Also for not complaining too much when I transported (stole) half the equipment in the lab to Grenoble once a year. In particular Liam, Maria and Stephen for keeping me on the straight and narrow. Also Danny for teaching me everything he knew about the equipment in the lab and how to make it work.

Thanks to the staff and technicians in Merz court for always being ready to help when equipment broke or something had gone wrong with an order and to Maggie for always having time to squeeze in some *ex-situ* XRD work when it was needed.

Thanks to EPSRC for making this all possible with the funding via a doctoral training award.

Also thanks to The Brown, Pies (especially the DP lot), everyone at HT Jesmond, Tom and my loving family for reminding me there was life outside my PhD and that the world wouldn't end if I relaxed and looked after myself.

Finally, Lord thank you for saving even a wretch like me, without You none of this would have been possible.

I declare that this thesis is my own work and that I have correctly acknowledged the work of others. This submission is in accordance with University and School guidance on good academic conduct. I certify that no part of the material offered has been previously submitted by me for a degree or other qualification in this or any other University. The work carried out here has been published and presented in the following locations:

# CV and list of publications

## Education

**2015-Present** Studying for a PhD in Chemical Engineering (Studies of a fixed bed chemical looping reactor for $H_2$ production by in-situ and operando x-ray and neutron diffraction) at Newcastle University in Professor Ian Metcalfe's group. I have completed my viva with minor corrections.

This consisted of:

Synthesis of perovskite materials via the pechini sol gel method.

Computational modelling of gas solid reactors, this required independent work to make the model and ensure its validity.

Designing and carrying out Lab based experiments on packed beds up to 4 g in weight.

The design and construction of an experimental rig for *operando* XRD studies.

*In-situ* neutron diffraction (5 day campaign at HRPD on the ISIS Neutron and Muon source).

*Operando* X-ray diffraction (3 campaigns on ID22 of ESRF) Working with beamline technology required a great deal of flexibility due to heat up times and times when the beam line went down.

Analysis of neutron and x-ray powder diffraction patterns, requiring collaboration with chemists and material scientists to ensure the data analysis was carried out using best practises.

**2011-2015**: Studied for M.A. (Cantab Hons) and M.Eng in Chemical Engineering via Engineering at Jesus College, Cambridge.

This required a research project to develop a flexible heat pipe. This consisted of redesigning the geometry and materials of the heat pipe and creating a novel manufacturing technique.

## Publications

Metcalfe IS, Ray B, Dejoie C, Hu W, **de Leeuwe C,** Dueso C, Garcia-Garcia F, Mak C M, Papaioannou E, Thompson C Evans JSO (2019) "Overcoming chemical equilibrium limitations

using a thermodynamically-reversible chemical reactor" Nature Chemistry published 27/05/2019

**de Leeuwe C**, Hu W, Neagu D, Pramana S, Ray B, Evans JSO & Metcalfe IS "Revisiting the thermochemical expansion and stability of $La_{0.6}Sr_{0.4}FeO_{3-\delta}$" in preparation

**de Leeuwe C**, Hu W, Neagu D, Pramana S, Ray B, Evans JSO & Metcalfe IS "An equilibrium model of a packed bed chemical looping reactor for hydrogen production" in preparation

## Awards and Honours

2018 Newcastle School of Engineering Best Oral Research Presentation

2014 EPSRC studentship - 1659082

2013 Jesus College Cambridge Scholarship

2012 Jesus College Cambridge Exhibitioner

## Conferences

2018 5th International Conference on Chemical Looping in the US (Park City Utah) Oral

CEAM 2018 PGR conference in the UK (Newcastle) Oral

2017 7th High Temperature Solid Looping Cycles Network in Sweden (Lulea) Oral

H2FC SUPERGEN Researcher Conference in the UK (St Andrews) Oral

CEAM 2017 PGR conference in UK (Newcastle) Oral

2016 CEAM 2016 PGR conference in the UK (Newcastle) Poster

## Relevant Teaching Experience

2017-2019

Supervision of three MEng students in chemical looping in the Applications of Ion Transport Group PI: Prof Ian Metcalfe

Development of an adiabatic simulation of a chemical looping reactor of WGS reaction. This made use of my skills in communication and included the orchestration of weekly meetings to ensure that the student was continuing to progresses and helping them overcome issues with the governing equations and their coding

Testing of $La_{0.8}Sr_{0.2}MnO_3$ for use as a chemical looping oxygen carrier material

Testing of $La_{0.6}Sr_{0.4}MnO_3$ for use as a chemical looping oxygen carrier material, both the experimental masters needed careful planning and distributing of resources so that they had access to the correct equipment when they needed it without hindering my research or that of the rest of the group.

## Work Experience

*2014 July – August ExxonMobile, Internship*

I spent 8 weeks working at the Fawley Oil refinery as part of their internship program.

Determined if waste 3 bar steam could be used to replace 9 bar stripping steam being used in a sour water stripping column and the best system for transporting the steam to the column. Developing my industrial experience of chemical engineering techniques.

I created mass balances for the steam system to determine the quantity of 3 bar steam being vented and to use existing models to determine the effect of dropping the pressure of the inlet steam. Showing experience simulating industrial scaled equipment and plant management.

I also enhanced my networking in order to gain information about the state of the plant as a whole, to determine the cheapest route for connecting the column to the 3 bar system, from seasoned employees.

*2013 August – October Hotel Chocolat, Industrial Researcher*

I spent over two months working in the Huntington Manufacturing site.

Carrying out research into partial coco butter extraction from pure coco liquor. Planning and carrying out these experiments alone

Ran experiments using 100-300g of coco liquor

Design and built a medium scale rig capable of processing 3 to 5kg.

This design would be up-scaled to develop a system capable of processing 500 kg in 24 hours.

I developed the concept, planned and orchestrated the experiments independently, while, improving my critical thinking and time management skills.

Demonstrated my findings to senior management requiring skills in presentation and report writing for non-specialists.

*2012 July – August Meridian, Civil Engineering Team*

I spent 2 months working in New Zealand as part of a Civil Engineering team responsible for maintaining and operating hydroelectric projects on the South Island.

Working as part of an Engineering team developed my collaboration skills as well as providing me a better understanding of how successful teams of engineers work together.

Completed reports documenting concrete cracking and 'Flood Inspection Checklists' giving me knowledge of completing reports and manging my time to hit internal company deadlines for these documents and the ability to contribute to the management of the dams and structures.

I completed a selection of smaller projects which developed my time management skills.

## Additional Skills

I have experience working with and using:

- C, C++and C#
- Computational fluid dynamics
- Linux computers
- Maple
- Mass Spectrometers
- Matlab
- Mathematica
- Microsoft office
- Neutron scattering equipment
- Topas (using Jedit)

- UniSim
- X-ray diffraction equipment

## Professional Memberships

Institute of Chemical Engineers – Associate Member

UK Carbon Capture and Research Centre – Early Career Research Member

# Contents

# List of figures

## List of tables

# Nomenclature

| *Symbol* | *Description* | *Units* |
|---|---|---|
| *A* | Site in perovskite crystal structure, defined in Figure 1.8 | - |
| *B* | Site in perovskite crystal structure, defined in Figure 1.8 | - |
| $D_{axCO}$ | The axial diffusivity of CO in Ar for the packed bed | $m^2\ s^{-1}$ |
| $D_{axCO_2}$ | The axial diffusivity of $CO_2$ in Ar for the packed bed | $m^2\ s^{-1}$ |
| $D_{axH_2}$ | The axial diffusivity of $H_2$ in Ar for the packed bed | $m^2\ s^{-1}$ |
| $D_{axH_2O}$ | The axial diffusivity of $H_2O$ in Ar for the packed bed | $m^2\ s^{-1}$ |
| *F* | total volumetric flow rate | ml $min^{-1}$ (STP) |
| $I$ | Current | mA |
| $K^*$ | Equilibrium constant defined in Equation 2a.11 | - |
| $K_c$ | Equilibrium constant for 6a.11 | - |
| $K_{Fe}$ | Equilibrium constant for 1b.7 | - |
| $K_H$ | Equilibrium constant for 6a.15 | - |
| $K_{ox}$ | Equilibrium constant for 1b.6 | - |
| $K_{WGS}$ | Equilibrium constant for the water-gas shift, defined in Equation 3a.2 | - |
| *LSF* | Strontium doped lanthanum ferrite | - |
| *LSM* | Strontium doped lanthanum manganite | - |
| $M_s$ | Molar mass of sample | g $mol^{-1}$ |
| $M_o$ | Molar mass of oxygen | g $mol^{-1}$ |
| $[M]$ | Thermodynamic activities of the metal = | bar |
| $[MO]$ | Thermodynamic activities of the metal oxide | bar |
| *NTP* | Normal temperature and pressure | |
| *OCM* | Oxygen carrier material | - |
| $PT_x$ | Pressure measured by transducer x | bar |
| *SEM* | Secondary electronic multiplier | - |
| *STP* | standard temperature and pressure | - |
| *T* | Temperature | K |
| *WGS* | water-gas shift | - |
| *XRD* | X-ray diffraction | - |

| | | |
|---|---|---|
| $a$ | unit cell parameter | Å |
| $a_0$ | unit cell parameter at 0 K and $\delta$=0 | Å |
| $a_{cub}$ | unit cell parameter of a cubic or pseudo cubic crystal structure | Å |
| $a_{hex}$ | unit cell parameter of a hexagonal crystal structure | Å |
| $c_{cub}$ | unit cell parameter of a pseudo cubic crystal structure that is perpendicular to the direction of $a_{cub}$ | Å |
| $c_{hex}$ | unit cell parameter of a hexagonal crystal structure, the height of the hexagon | Å |
| $k$ | rate constant | mol $m^{-3}$ $s^{-1}$ |
| $m$ | Sample mass | g |
| $n$ | Molar flow rate | mol $s^{-1}$ |
| $pCO$ | Partial pressure of CO | bar |
| $pCO_2$ | Partial pressure of $CO_2$ | bar |
| $pH_2$ | Partial pressure of $H_2$ | bar |
| $pH_2O$ | Partial pressure of $H_2O$ | bar |
| $pO_2$ | partial pressure of $O_2$ | bar |
| $r$ | radius | m |
| $r_{CO}$ | rate of consumption of CO | mol $m^{-3}$ $s^{-1}$ |
| $r_{H_2O}$ | rate of consumption of $H_2O$ | mol $m^{-3}$ $s^{-1}$ |
| $t$ | time | s |
| $u$ | molar flux during the reduction half cycle | mol $m^{-2}$ $s^{-1}$ |
| $v$ | molar flux during the oxidation half cycle | mol $m^{-2}$ $s^{-1}$ |
| $x$ | Extent of substitution of La by Sr | mol mol $^{-1}$ |
| $y$ | mole fraction | mol mol $^{-1}$ |
| | | |
| $\Delta$ | Denotes change in | - |
| $\Delta$H | Change in enthalpy | KJ $mol^{-1}$ |
| $\Delta G$ | Change in Gibbs energy | KJ mol $^{-1}$ |
| $\Delta$S | Change in entropy | KJ $mol^{-1}$ $K^{-1}$ |

| | | |
|---|---|---|
| $\alpha_{chemical}$ | Chemical expansivity | $K^{-1}$ |
| $\alpha_{thermal}$ | thermal expansivity | Å $K^{-1}$ |
| $\delta$ | Oxygen non-stoichiometry of perovskites | mol mol $^{-1}$ |
| $\theta$ | Internal angle of rhombohedral unit cell | - |
| $\sigma$ | standard error | - |
| $\varepsilon$ | voidage of the bed | - |
| $\hat{\rho}_g$ | molar density of the gas phase | mol $m^{-3}$ |
| $\hat{\rho}_s$ | molar density of the solid phase | mol $m^{-3}$ |

# Chapter 1: Introduction

## 1a Background

$H_2$ is a common and important raw material in many industrial processes, where it is used either as a major feed stock as in the Haber Bosch Process or in hydrogenation reactions.

The Haber Bosch process is the main synthesis method for ammonia, a feed stock for fertilisers and other nitrogenous compounds like nitric acid. The process consists of the exothermic reaction of elemental nitrogen and $H_2$ over an iron catalyst (Czuppon et al 2000). With over 450 million tonnes of nitrogen fertilizer are produced each year (Vaclav S 2004) ensuring the Haber Bosch process is as environmentally friendly as possible is of vital importance.

While, hydrogenation is a process that saturates unsaturated hydrocarbons with $H_2$, it is often carried out over a nickel, palladium, or platinum based catalyst. It is commonly carried out in the food industry, converting oils into fats, to produce margarine (Rylander 2005). Ensuring the source of this $H_2$ has as little impact on the environment as possible is a key concern.

$H_2$ has also been used as a lifting agent for lighter than air flight almost since its discovery in 1766, with the first manned $H_2$ balloon flight taking place in 1783 (Gough, J.B. 1974). However, this practise was stopped after the Hindenburg disaster in 1937 which resulted in 36 fatalities (Archbold 1994).

Additionally, $H_2$ is used as a rocket fuel for the space programs (Mayer and Tamura 1996) as in liquid form it is able to release massive amounts of energy when oxidised. $H_2$ has the most intensive and efficient oxidation reaction per unit mass of rocket fuel.

In terms of ground based locomotion, where rockets would be unsafe and impractical, there are two main routes to obtain the energy stored in the $H_2$, an internal combustion engine or a fuel cell. An advantage of the internal combustion engine is that existing engines can be retrofitted to run on $H_2$ allowing for a quick change over once storage and production methods are optimised (Dieges 1974). As internal combustion engines are heat engines, the inevitable heat losses of the system lowers the efficiency. On the other hand, a fuel cell generates electricity via an electrochemical reaction which can be used directly by the vehicle, a more efficient system. Solid oxide fuel cells suffer from either high operating

temperatures (circa 800-1000$^{o}$C) (Boudghene 2002) and other varities are more susceptible to poisoning. This means that the $H_2$ used in fuel cell systems must be of a very high purity (Hoogers 2003). Industry standards are for less than 1 ppm of impurities. (Dincer 2015, Vaidya and Rodrigues 2006).

Currently there are three challenges that need to be overcome before $H_2$ can be used as a fuel for automobiles. The first of these is its storage, both for point of use and large scale transport. $H_2$ gas only has an energy density of 5.6 MJ/L while petrol has one almost six times larger (33MJ/L) meaning the fuel tank on a $H_2$ fuelled vehicle would have to be six times larger than that of a petrol powered one. There are other methods being researched including liquefaction of the $H_2$ (requires cryogenic systems), metal hydrides or liquid organic $H_2$ carriers which could work to improve the energy density (US department of Energy, 2004). The second challenge is the lack of a distribution network, currently there is no way to get $H_2$ from large scale plants to the consumers. This would necessitate the production of a network of pipes or tankers to move the $H_2$ from the production locations to fuel stations. Another option is the use of existing natural gas pipework, where the addition of $H_2$ would not affect the natural gas uses, with downstream separation processes (Pivovar et al 2018). The final hurdle is a low carbon method for $H_2$ production (Chu and Majumdar 2012). The work detailed in this thesis aims to address the requirement for a low carbon production method, this hurdle was selected as improvements to $H_2$ production methods would limit the environmental impact of $H_2$ produced for industrial purposes therefore having an impact on climate change whether or not the other two hurdles are solved. Ideally this production method would also have the potential to be scaled to be part of a distributed $H_2$ production system reducing the need for a large scale distribution networks.

The main production method for $H_2$ is steam methane reforming which involves the partial oxidation of hydrocarbons by steam to form a mix of $H_2$, $H_2O$, CO and $CO_2$, which must then undergo expensive separation processes to obtain the product $H_2$ with further separations being required to obtain $CO_2$ of storage or utilisation. The details of both this method and other existing $H_2$ production systems are laid out in Section 1b.

### 1b $H_2$ production methods

$H_2$ when combusted produces only $H_2O$ meaning that if it is produced via a renewable energy or “green” process it can be thought of as environmentally friendly. However, currently most production methods require the use of fossil fuels either as an energy source

or as a feed material. Any method of production using fossil fuels will release $CO_2$ into the atmosphere unless some form of carbon capture system is employed (Simbeck 2004). While several of the methods outlined in the following sections do allow for $H_2$ production that would not require carbon capture and storage, either through using nuclear energy or some other renewable energy source, in-depth study of them are still in early stages excluding them from wide industrial use but do show promise.

*1b.i Steam methane reforming*

Steam Hydrocarbon reforming is the dominant technology in the market for $H_2$ production, it accounts for 48% of global $H_2$ production (Raissi and Block 2004). Methane is the most common reducing gas and is reacted with steam, in Equation 1b.1 at 700-850°C and pressures ranging from 3 to 25 bar over a nickel oxide catalyst (Ding and Alpay 2000).

$$CH_4 + H_2O \rightleftharpoons CO + 3H_2 \qquad 1b.1$$

Steam Methane Reforming is carried out in two stages, in the first the methane is reacted with the steam to form a mix of CO, $CO_2$ and $H_2$. This stage is carried out at high temperatures due to its highly endothermic nature. The second stage is exothermic and is used to increase the yield of $H_2$ by reacting CO formed by the first stage with the remaining steam, this is referred to as the $H_2O$-gas shift (WGS).

$$CO + H_2O \rightleftharpoons CO_2 + H_2 \qquad 1b.2$$

The WGS reaction occurs in two reactors, the first at 350°C and the second at a lower temperature of 250°C, this is done to minimise the CO content of the product stream as it is a reversible exothermic reaction (Barelli et al 2000).

The mixture of CO, $CO_2$, $H_2$ and $H_2O$ must then be separated such that high purity $H_2$ can be produced. If necessary the low concentrations of $H_2O$ cab be removed by cooling the mixture such that the $H_2O$ condenses out, this method would not work to remove the CO and $CO_2$. To separate the remaining components pressure swing adsorption is required. This is expensive both in capital and operation costs (Sircar and Golden 2000).

*1b.ii Partial oxidation of hydrocarbons*

$H_2$ can also be produced through the partial oxidation of hydrocarbons, where the ratio of oxygen to hydrocarbon is below the stoichiometric ideal (Roman J. et al 2008). This means the hydrocarbon is only oxidised to a mix of CO and $H_2$ rather than completely to $CO_2$ and

$H_2O$. This can occur non-catalytically at temperatures above 1000°C but this is lowered to 725°C using a nickel catalyst (Dissanayake et al 1991). The process, as with steam methane reforming, requires further separation steps such as pressure swing adsorption to achieve the high purity $H_2$ required by most industrial applications.

*1b.iii Hydrocarbon decomposition*

Hydrocarbon decomposition occurs in a complete lack of oxygen, producing elemental $H_2$ and carbon. This can occur over a temperature range of 500-1300˚C depending on the catalyst used. This system offers a method for $H_2$ production from hydrocarbon sources without $CO_2$ release or the need for carbon capture and storage. The disadvantage of this is that either high temperatures or expensive catalysts that are easily poisoned by the carbon deposition are required (Ahmed et al 2009). This system would allow for $H_2$ production without pressure swing adsorption but does require the catalyst to have the solid carbon, which has been deposited during reaction, removed.

*1b.iv Electrolysis*

$H_2$ can also be produced through the dissociation of $H_2O$ by an electrical current. This produces gaseous $H_2$ and oxygen. The most common method used is alkaline electrolysis but solid oxide and proton exchange membrane cells are being developed (Holladay et al 2009 and Grigoriev et al 2006). This system has the potential to be carbon neutral if the electricity to force the separation is also carbon neutral and green practises are used during manufacturing. However when the electricity is from non-renewable sources the process can emit more $CO_2$ than steam methane reforming, due to inefficiencies in the production and transportation of the electricity required. Additionally, studies by Koroneos et al (2004) found that even $H_2$ production via photovoltaic or biomass resulted in more $CO_2$ in the atmosphere than steam methane reforming due to CO produced during the manufacture of equipment.

*1b.v Thermolysis*

This is the thermal decomposition of $H_2O$ in gaseous $H_2$ and oxygen. $H_2O$ dissociates at 2770 K (Holladay et al 2009) when not in the presence of a catalyst. This high temperature is a major disadvantage to the use of this method for $H_2$ production. While it can be lowered through the use of an appropriate catalyst, the system produces a stream of $H_2$ and oxygen which can easily recombine to reform the $H_2O$ if not separated before the system is allowed to cool. This results in the system requiring an inherent separation process to be feasible.

*1b.vi Bio $H_2$ routes*

Some bacteria produce $H_2$ if put in a stressed environment through a photosynthesis like system. These biological systems have the potential to be carbon neutral but biological systems are sensitive to environmental factors and mutations that lower efficiency. Additionally the rate of production achieved by these bio $H_2$ routes are slow, with only nanomoles per hour being produced using current technology, with improved scale up technology this could be improved but it is still in its infancy (Hemschemeier et al 2009).

## 1c Chemical looping

Fan (2011) defines chemical looping as dividing a single reaction into multiple sub-reactions each typically carried out in a different reactor through the use of "chemical intermediates that are reacted and regenerated" for the purpose of linking the separated sub reactions. Through using solid intermediaries, such as metal oxides, it is possible for redox reactions to be performed linking sub reactions into one reaction. This separation of the oxidation and reduction half equations of a redox reaction means that separation processes are not required to produce pure product streams.

Techniques similar to chemical looping has been used for $H_2$ production since 1903 by Howard Lane (Hurt 1939). The process for $H_2$ production was later refined and named the steam iron process by Messerschmitt (1910) but has gained recent recognition as a method for $H_2$ production with inherent carbon capture and storage.

Using a chemical looping reactor results in the system having inherent carbon capture and not requiring the pressure swing adsorption used by the other hydrocarbon-based $H_2$ production methods detailed here. The lack of separation stages decreases both operating and capital costs for $H_2$ production as well as decreasing plant footprint making a distributed $H_2$ production system easier to design.

Additionally, because the reactant feeds are never mixed, chemical looping systems have the potential to achieve conversions in excess of those of a conventional reactor. This is because without the entropic loses associated with mixing the reactants overall thermodynamic limitations of the system are moved so that higher conversions are achievable (Metcalfe et al 2019). The thermodynamics of such a chemical looping system are detailed in Chapter 3.

Chemical looping can produce $H_2$ in two different ways, through the oxidation of the carrier by $H_2O$ producing $H_2$ or through the reduction stage by the partial oxidation of hydrocarbons to syngas, a mixture of CO and $H_2$. It allows for the production of high purity $H_2$ without expensive separation steps that would be required to remove carbon-containing compounds present in the outlet of a conventional reactor.

*1c.i Reactor configuration*

Chemical looping reactors have three configurations: packed bed, fluidised bed and circulating reactors. Packed and fluidised beds reactors separate the half reactions temporally with different gasses being flowed through the reactor at different times with both the reduction and oxidation occurs in the same vessel. This contrasts with the circulating reactors or fluidised beds where separation is achieved spatially. That is the OCM moves between different reactors, where it is either reduced or oxidised. This allows for continuous production without multiple reactor setups but has increased attrition and operation costs do the movement of the solids both inside and between the reactors.

The advantages and disadvantages of packed bed and circulating fluidised set ups are detailed below. Fluidised beds are rarely used outside of laboratory conditions as they neither allow for the high conversion and OCM life time that a packed bed achieves nor the continuous production afforded by circulating fluidised beds.

*1c.i.a Packed bed reactors*

Early work on the Steam-Iron process originally used a packed bed system, which allowed only for periodic reduction and oxidation of the OCM. This resulted in an inability to sustain continuous production while utilising only one reactor. Packed bed reactors also suffer from cold spots or temperature gradients in the bed due to poor heat transfer inside the reactor and the exothermic or endothermic nature of the reactions occurring. The reactor can also have issues due to the pressure drop across the system either causing fluidisation or bed displacement leading to channelling, where the gas bypasses the OCM and leaves the vessel unreacted. Unreacted reactants lowers the yield and increases separation costs down stream decreases the viability of the system. (Noorman 2009)

There are many systems consisting of multiple reactors for chemical looping $H_2$ production in literature, but they all are fundamentally reliant on the same principle. That is multiple fixed bed reactors with gas supplies connected via alternating valves (Hamers et al 2013, Noorman et al 2010). A system meeting these requirements can be seen in Figure 1.1. It is possible, using this configuration, to switch the reactors between reduction and oxidation simultaneously whenever product production rate drop below an acceptable level.

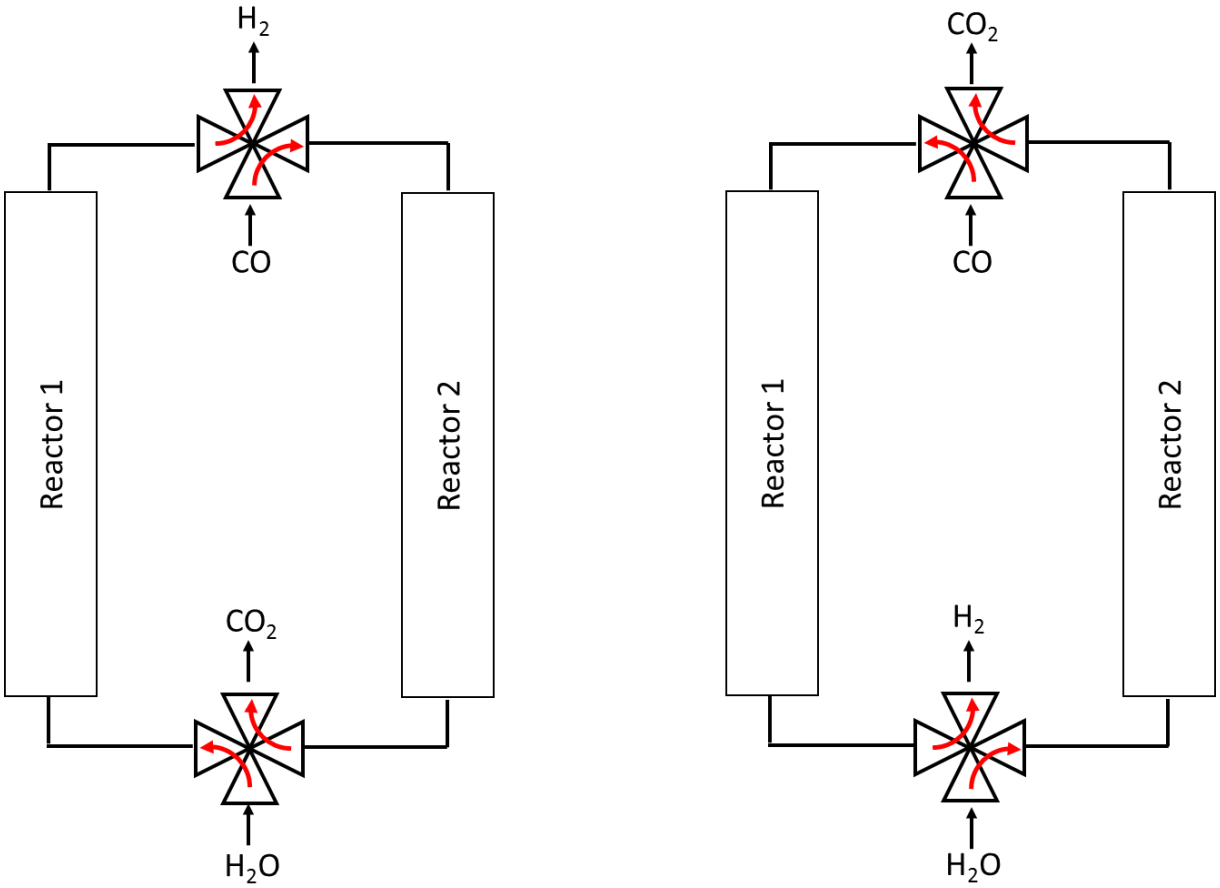


Figure 1.1: A two reactor system for continuous $H_2$ production via a chemical looping method.

The reactor system shown in Figure 1.1 shows a counter current system, where the oxidising and reducing gasses flow in opposite directions through the packed bed. Literature studies of the effectiveness of counter current and co-current flow packed bed reactors have shown that counter-current systems are less prone to OCM deactivation and utilise the reducing and oxidising gasses more effectively (Heidebrecht et al 2008). This reactor set up was more efficient and the study suggested the use of short cycle duration to improve the performance further.

Heidebrecht and Sundmacher (2009) also studied the thermodynamics of counter current packed beds and found that the highest possible purity of the products from the reactor was dependent on the oxidation state of the solid at the outlet of the reactor and not limited by the equilibrium point of the mixed reactant streams. By using a counter current flow system this allows for high conversions to be obtained, with the outlet gasses from each half cycle being in equilibrium with the optimal phase change.

It was also found that as the gas phase is of significantly lower density than the OCM there is a discrepancy between the gas and reaction front velocities when phase changes are occurring. If the reaction kinetics are fast enough this would cause each phase change that the OCM goes through to have an independent reaction front, each of which can move through the bed individually. Knowing how these fronts move through the bed can allow for optimal switching between reducing and oxidising gasses increases yields. In order to fully understand this system an understanding of how the internals of the bed change during reaction would be required. (Heidebrecht and Sundmacher 2009)

*1c.i.b Circulating Fluidised Beds*

In a circulating fluidised bed reactor, the solid OCM travels between two or more distinct reactors. A simplified reactor system is shown in Figure 1.2. Typically, the reduction reactor, a riser, has a smaller diameter and uses a higher flowrate of the reactive gas to fluidise the OCM. Once the OCM reaches the top of the reactor it is removed and sent to the oxidation reactor. The OCM would then fall through the oxidation reactors, where the lower gas flowrate means that the solids can exit the reactor towards its base. To ensure that only the OCM moves between the reactors, so that there is no gas cross over occurring, cyclone separators and loop-seals are used. (Basu and Butler 2009, Kolbitsch et al 2010)

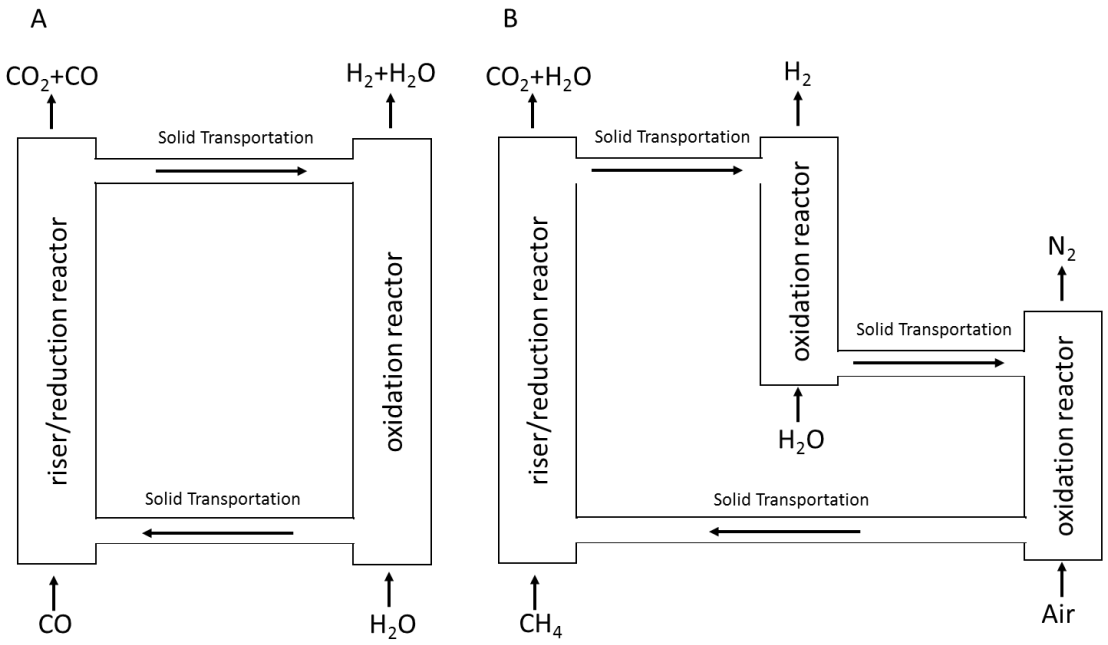


Figure 1.2: Circulating fluidised bed reactor system with (A) two or (B) three stages

Fluidised bed reactors require high flowrates to ensure that the OCM is fluidised and that the material is capable of leaving the reactor at the top when compared to a fixed bed reactor. These increased flowrates complicated reactor design if optimal conversions are to be achieved. Additionally, the movement of the solids both inside the reactors and between them increases the attrition and formation of fine powders. Attrition can decrease the surface area of specialist OCM structures lowering the reaction rates and decreasing yields. Fine powders produced by attrition can escape solids traps and cyclones so would pass downstream into the separation equipment or to the final products. These fines would damage the separation equipment, potentially causing system failures and requiring expensive refits or becoming a safety risk. If the fines were present in the $H_2$ feed leaving the plant, they could cause physical damage to fuels cells or cause side reactions in other chemical processes decreasing yields and conversions.

In a fluidised bed the OCM are much more uniform in their oxidation state due to the effective mixing that occurs during fluidisation. This mixing and uniformity means that the material leaving the reactor, which under ideal conditions would still be in equilibrium with the OCM at the gas outlet, is limited to the equivalent conditions of a conventional reactors mixed gas equilibrium. This results in a lower purity gas phase and lower conversions when compared to fixed bed reactors.

*1c.ii Reducing agents*

During chemical looping $H_2$ production in order for the oxidation of the OCM to produce $H_2$ the OCM must first be reduced. Different gasses can be used as this reducing agent with differing kinetics, potential oxygen content, thermodynamics and cost. The choice of the reducing gas has a large impact on the operation of the chemical looping systems. One potential reducing agent is methane, found in natural gas, this is commonly used in many industrial processes and in chemical looping power generation reactors (Thursfield et al 2012). Methane oxidation, however, has poor selectivity and can form carbon on the surface of the OCM decreasing the reactivity of the material. Other options for the reducing gas like biogas or natural gas have similar problems with selectivity and carbon deposition. The use of syngas or CO diminish the chance of carbon deposition, but these agents have a higher cost as they need to be processed or produced from other sources before they can be used.

*1c.ii.a Methane and natural gas*

Methane is the primary component of natural gas with the remaining mole fraction consisting of higher order hydrocarbons such as ethane or butane and impurities like $CO_2$ and $H_2$ sulphide. The use of methane as a reducing agent in a reforming process was first proposed in 2002 and demonstrated experimentally in 2006 (Ryden and Lyngfelt 2006). Methane can undergo partial or complete oxidation depending on the availability of oxygen in the carrier material. In higher equivalent partial pressures of oxygen the production of $CO_2$ and $H_2O$ will dominate but in less oxygen rich environments the methane is only partially oxidised to $H_2$ and CO (Diego 2009).

Full oxidation of methane:

$$CH_4 + 2O_2 \rightarrow CO_2 + 2H_2O \qquad 1.c.1$$

Partial oxidation of methane:

$$CH_4 + \frac{1}{2}O_2 \rightarrow CO \quad + 2H_2 \qquad 1.c.2$$

Partial oxidation of methane is the preferred reaction route due to the higher economic value of $H_2$ and CO (Enger 2008). However this partial oxidation limits the amount of reduction that the OCM would undergo which would have a knock on effect on the oxidation

half cycle. The total $H_2$ production from the reduction half cycle can be further increased by using the water-gas shift reaction to convert the CO into $CO_2$ while reducing the $H_2O$ to $H_2$.

However, carbon deposition is a significant problem when using hydrocarbons as reducing agents, due to the catalytic effect of iron containing OCMs (Ermakova 2001 and Go *et* al 2009). This deposition of carbon onto the OCM both decreases reactivity and causes the $H_2$ produced during the oxidation stage to be contaminated with CO formed by the reaction of $H_2O$ with the deposited carbon.

Carbon can be formed via a variety of different paths; through thermal cracking of the hydrocarbons present (Go et al 2009), the Boudouard reaction or via the reduction of CO and $CO_2$ by $H_2$.

At higher temperatures the Boudouard reaction and CO and $CO_2$ reduction become less thermodynamically favourable but thermal cracking becomes more pronounced. Olsson et al (1974) conducted a study that showed that CO and $CO_2$ reduction was lowered significantly by increasing the temperature above 1073 K. It is also possible to reduce the rate of carbon deposition from the Boudouard reaction through the addition of $H_2$ to the feed gas. However the addition of $H_2$ does promote the reduction of CO and $CO_2$.

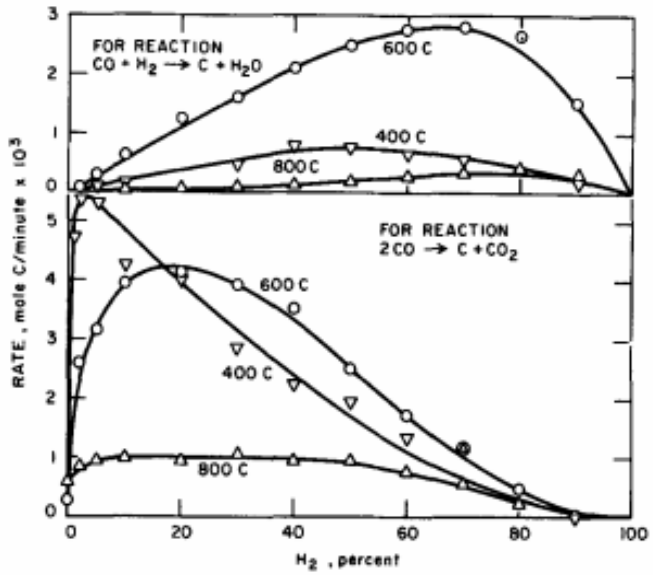


Figure 1.3: Rate of carbon deposition at different temperatures and $H_2$ contents in the system of 660 mg of iron taken from Olsson et al (1974).

If iron based OCMs were used (further details about the properties of oxygen carrier are found in Section 1c.iii), an additional complication arises when using with methane or natural gas as the reducing agent. This is the potential to form iron hydroxides and iron carbides. The formation of either of these compounds leads to the deactivation of the OCM. However, the formation of iron hydroxides is highly unlikely when the system is operated above 683 K. The formation of iron carbide in the system is thermodynamically more likely than the formation of iron hydride. Zhou et al (2017) carried out a density functional theory study that showed in the temperature range of interest to chemical looping $H_2$ production the most likely reaction route would be:

$$3Fe + 2CH_4 \leftrightarrow Fe_3C + 4H_2 + C \qquad \Delta G_{1023\,K} = -80\ KJ/mol \qquad \text{1.c.3}$$

Iron carbide can also be formed through the reaction of the CO, formed by the partial oxidation of methane, with the OCM. Svoboda et al (2008) studied these reactions between 400 and 900 K and found that it was thermodynamically possible to form $Fe_3C$ at 900 K through the reaction of magnetite with CO but that other routes were less favourable.

Akiyama et al (2004) has shown that the iron carbide formed can be removed through reaction with steam at temperatures ranging from 550 to 1400 K. When the iron carbide was reacted, CO, $CO_2$, $H_2$ and hydrocarbons were formed. In chemical looping $H_2$ production this would occur during the oxidation half cycle, regenerating the OCM but contaminating the exit gasses with difficult to separate by-products.

*1c.ii.b CO*

CO is often used by researches as a reducing agent in chemical looping due to the simplicity of the reduction reaction. CO also decreases the tendency towards carbon formation, and therefore the OCM deactivation that is seen when using hydrocarbons like methane as the reducing agent. This is because solid carbon can only form via the Boudouard reaction and not through the reduction of CO or $CO_2$ by $H_2$ or by the thermal cracking that can occur when using hydrocarbons.

Solid carbon formation can be mitigated by performing the reduction at higher temperatures where the Boudouard reaction is less favourable. A study carried out by Mondal et al (2004) showed that carrying out the reduction in the presence of metallic iron leads to the

formation of solid carbon species. Adding 15 vol% $CO_2$ to the reducing gas has been found to avoid the formation of metallic iron as the feed is less reducing so does not drive the reaction. It was also found that increasing the temperature increased the rate of reduction

Industrially the use of CO is limited as in order to produce a pure CO stream expensive separation steps would be required increasing costs when compared to hydrocarbons or syngas.

*1c.ii.c Syngas*

Syngas is produced from coal or biomass using gasification (Iv et al 2007 and Li et al 2010) or by reforming natural gas or oil. Multiple studies have been carried out showing its utility as a reducing agent in chemical looping $H_2$ production (Cleeton et al 2009, Müller et al 2011 and Gupta et al 2007))

Syngas typically contains 30 to 60 vol% CO and 25 to 30% $H_2$. The remainder consist of a mixture of methane, $CO_2$, $H_2O$, $H_2$ sulphide and carbonyl sulphide, with the exact composition depending on the feedstock and process used in its acquisition. The presence of sulphur containing compounds can require the feed to be purified before entering the chemical looping reactor due to its ability to deactivate and damage the system. However, Huebler et al (1969) carried out a study that found that the presence of small amounts of sulphide contaminates can benefit the process by inhibiting the deposition of carbon, increasing the OCM's stability.

Previous work by Hacker et al (1998) showed that, when using iron containing OCMs, the presence of amine and sulphur containing impurities and hydrochloric acid in simulated syngas did not affect the kinetics of the reaction. They found that even with these impurities the system had high $H_2$ production stability at 1173 K. It was also found that the quantities of impurities harmful to downstream processes in the $H_2$ stream were low enough for fuel cell technology to operate without interference (<4ppm of HCl and <1 ppm of $H_2S$). Müller et al (2011) had similar findings, showing that the contaminants in the syngas did not adversely affect the cyclic stability of the OCM.

*1c.ii.d Biomass and coal*

Biomass can undergo gasification to produce syngas which is then used in chemical looping $H_2$ production. Biomass covers a wide range of materials with different sources having different ratios of cellulose, hemicellulose, lignin and other organic compounds. This results in different materials needing different processing procedures. In general, the first stage of processing biomass is the conversion to pyrolysis oil, which consists of heating the solid biomass in an absence of oxygen. This produces a liquid combination of 65-75 wt% pyrolysis oil with the majority of the remainder being $H_2O$. Pyrolysis oil, as a liquid, is easier to process and contains lower concentrations of metals and minerals than soild biomass or coal. This means that it would be a better option for use directly as a reducing agent than direct injection of solids. It can also be further processed into syngas. (Bleeker et al 2007, Bleeker et al 2010, Omae 2006)

Pyrolysis oil gives advantages with a lack of upstream processing for producing $H_2$ via chemical looping from a renewable source and can be used in similar manner to CO and syngas. Yet the impurities present, such as methane and other organic compounds, cause solid carbon to be deposited on the iron oxide causing deactivation. The presence of carbon containing compounds in the $H_2$ product stream requires additional separation steps. In addition to this, pyrolysis oil has been found to form tar and soot during the reduction step that causes the loss of reactivity in the process. This effect is partially mitigated by the present of $H_2O$ in the oil which prevents the formation of metallic iron but this effect was not enough to stop high losses of surface area (Bleeker et al 2010).

Coal can also undergo gasification to obtain syngas. As with biomass there are many impurities that are present in this fuel. These impurities vary with quality and source of the coal used.

Coal has also been used for direct reduction though solid-solid reaction in fluidised bed systems (Yang et al 2008) and it was found that impregnating potassium in to the coal aided fuel conversions. Additional Aspen Plus studies have been carried out (Gnanapragasam et al 2009) comparing the efficiency of using coal directly verses using gasification to convert to syngas first. It was found that direct injection of the solid material lowered capital costs

associated with the gasification processes and increased $H_2$ production for the same raw materials. This comes at the cost of increased solids handling for circulating bed reactors.

*1c.ii.e Alternative fuels*

Steinfeld et al (1999) carried out a design study exploiting solar energy as the reducing agent. This two stage process involved the heating of the OCM to high temperatures such that decomposition occurred (2100 to 2500 K) then cooling the material and oxidising the material using $H_2O$ to produce $H_2$. The main limitation found in the study was producing a solar reactor capable of concentrating enough solar energy to efficiently reach these temperatures. Additionally this study fails to specify the materials used to construct a reactor capable of withstanding these high temperatures.

*1c.iii Properties of good oxygen carrier materials*

The OCMs used for chemical looping systems must be able to survive harsh operating conditions not limited to highly reducing atmospheres, high temperatures and oscillating conditions. As the performance and efficiency of the overall system is highly dependent on the properties of the OCM (Bohn et al 2008, Mattisson et al 2001, Ada'nex et al 2004 and Fan 2011). As such literature suggests several general requirements for ideal OCMs (Rydén et al 2008, Fan et al) namely:

- The material must have a large capacity for oxygen take up and release.
- The material must exhibit high reactivity and fast kinetics with both the reducing and the oxidising agent.
- The material must have favourable thermodynamics for the chemistry involved.
- The material must demonstrate a low tendency to attrition, agglomeration, fragmentation and other thermal or mechanical degradation. Thus resulting in a long life time for the material.
- The material should not promote the deposition of solid carbon during reduction and must be resistant to other contaminants, such as sulphur or nitrogen containing compounds, present in the feeds.
- The material should have a low production cost.
- The material's production should have minimal impact on the environment.

There are also additional specific requirements and specifications for different chemical looping processes or reactor types. In a fluidised bed there is a greater dependence on the materials resistance to attrition as the material is required to be recirculated multiple times and should the particle size break down too quickly the makeup rate of material would need to be higher, increasing costs. In comparison, for a packed bed reactor it is much more important that the material can be manufactured in such a form that the pressure drop across the bed is small without compromising on the kinetics of the system or the diffusion time from the solid bulk to the reaction sites. (Noorman 2009) As this work concentrates on packed bed systems this criteria shall be weighed more heavily when judging the suitability of the OCMs here studied.

*1c.iii.a. Iron oxide*

Iron oxide has been, and continues to be, used as the oxygen carrier for chemical looping since its advent in the Steam-Iron process in 1903 (Thursfield et al 2012, Hacker et al 2000 and Bohn et al 2008). Iron oxide is a good candidate due its low manufacturing costs even when compared to simple OCMs like nickel and copper oxides (Solunke et al 2010). Iron ore is a cheap source of iron oxide but contains impurities such as silica, alumina and traces of other metals. The exact make up of iron ore changes depending on the particular source of iron oxide. Sponge iron, made from the direct reduction of metallic iron, is an alternative that for a higher cost has much lower concentrations of impurities. (Selan et al 1996 Bandopadhyay et al 1996)

Iron oxide naturally occurs in three possible oxidation states. The most oxidised of these is haematite ($Fe_2O_3$) where the iron ions have an oxidation state of +3. The next most oxidised of these is Magnetite ($Fe_3O_4$) where the iron ions have a mixed oxidation state of +2 and +3. The final iron oxide phase is wüstite (FeO) in which the iron ions exhibit a +2 oxidation state. Wüstite can exist in an iron-deficient state, with an iron/oxygen ratio as low as 0.9 but for the purposes of this work this is ignored and the ideal case of a ratio of one is used (Svoboda et al 2007 Hacker et al 1998). Further reduction of wüstite gives metallic iron.

When used to produce $H_2$ via the steam iron process the iron oxide is reduced using CO to form $CO_2$, as stated in the section on reducing agents syngas is an almost equivalent reducing agent. The reduced OCM is then re-oxidised using steam to produce $H_2$. As the chemical looping is carried out the iron oxide exists in two or three different states at different points in the cycle.

As steam is used as the oxidising agent the thermodynamics of the system means that haematite cannot be formed and wüstite is only stable above 838 K (Svoboda et al 2007, Pineau et al 2006, Lin et al 2003, Graham et al 1975). When the material changes phase oxygen is released or taken up. Iron oxide cannot supply or take oxygen from the gas phase without undergoing a phase change. A Baur-Glaessner phase diagram in Figure 1.4 shows the interaction between different gas environments and the phase of iron oxide present.

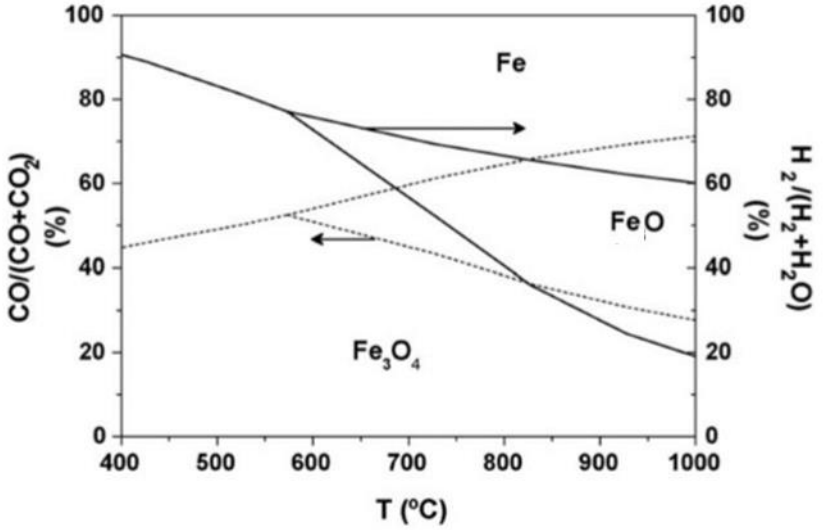


Figure 1.4: Baur-Glaessner phase diagram for different partial pressure of oxygen for both reducing condition and oxidising condition at different temperatures. Note that wüstite only occurs above 838 K and haematite is unable to be formed due to thermodynamic limitations when $H_2O$ is used to oxidise iron. (Bleeker et al 2007)

As steam is not capable of oxidising the material beyond magnetite (Bleeker et al 2007) the only way to increase the oxygen capacity of the material would be to ensure that the reduction feed gas is capable of producing metallic iron in the reactor. However, metallic iron promotes carbon deposition on the material, which as discussed previously decreases the activity of the material and can cause contamination of the $H_2$ product stream. (Go et al 2009 Svoboda et al 2007).

A method for limiting carbon deposition is the use of a three stage reactor where the iron oxide is reduced, then partially oxidised using steam before being fully oxidised using air or oxygen. The air or oxygen feed burns off any deposited carbon on the OCM ensuring that there is no loss of surface area of in the OCM due to carbon deposition. However, the exothermic nature of both the oxidation of the OCM and the oxidation of the deposited carbon could cause thermal sintering of the OCM which would further reduce its activity as

well as limiting the $H_2$ production possible as some of the reducing potential of the reduction feed goes to reaction with the $O_2$ rather than the $H_2O$.

As the life time of the material is of vital importance to the economic viability of a chemical process Bohn (2010) studied the effect of repeated cycling between steam and CO on the quality and quantity of $H_2$ production. This was carried out at three different temperatures and can be seen in Figure 1.5. For all three temperatures studied the quantity of $H_2$ produced dropped rapidly with cycle number, with the 10th cycle only producing approximately 17% of the $H_2$ that was produced during the 1st. Of the temperatures studied 1173 K, the highest studied, initially produced the largest quantity of $H_2$ but also saw the quickest decrease in production. It was suspected that this was caused by thermal sintering, precipitated by the higher temperature, which led to a decrease in the reactivity and therefore the $H_2$ production.

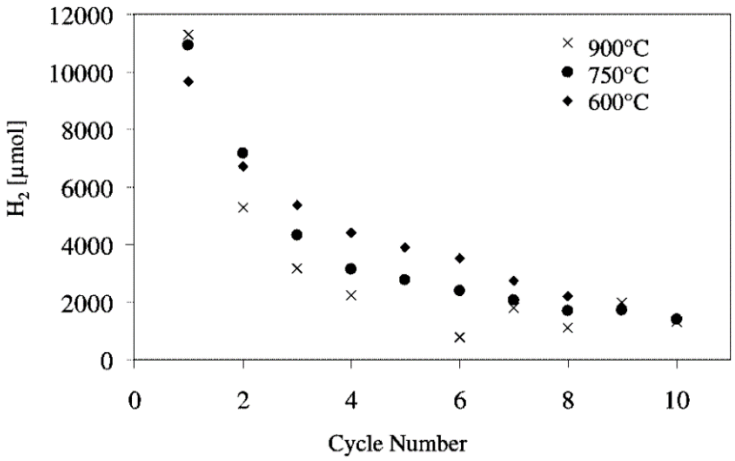


Figure 1.5: $H_2$ production versus cycle number at three different temperatures using 1 g of iron oxide reduced with CO and then oxidised with steam at 900 °C. Theoretical maximum yield of $H_2$ can be produced from 1 g of $Fe_2O_3$ is 16700 µmol. (Bohn 2010)

The study also used mixtures of CO and $CO_2$ as the reducing gas such that the iron oxide would be unable to be reduced past the wüstite phase. This was carried out to increase the materials life time and limit the decrease in $H_2$ yield. It was found that the total $H_2$ production was lower but that the decrease in $H_2$ production was much less pronounced with the 10th cycling only dropping to 80% of the 1st, a much larger fraction than was found when using pure CO as the reducing agent.

For chemical looping $H_2$ production the majority of reactions studied are gas-solid reactions. Direct feed coal or the use of pyrolysis oil would require solid-solid or liquid-solid kinetics but

these were not considered outside of the literature review. The kinetics governing the reaction of direct solid and liquid feeds are complicated and this paired with the additional intricacies for the design of such a system make the operation, for chemical looping $H_2$ production, less appealing than the use of gas feeds. Consequently, the discussion of studies and models for packed bed reactors has been limited to gas-solid systems only.

For gas-solid interactions, in packed beds of iron oxide, a variety of mechanisms have been proposed in the literature, these include, but are not limited to, the shrinking core and cracking core model. The most basic of those conventionally used is the simplified gas-solid reaction mechanism, which was detailed by Szekely et al (1976). This consists of separating the reaction into a series of steps. These are:

1. Reactant gasses moving from the bulk phase to the surface of the OCM
2. Gas molecules diffusion through pores in the OCM to the surface of an unreacted core
3. Gas molecules adsorb on to the surface
4. The reaction between adsorbed molecules and the solid phase occurs
5. The products desorb and return to the bulk phase back along the path detailed in step 1 and 2.

The kinetics limiting the reduction of iron oxide were explored by Alamsari et al (2011) based on the assumption that when the OCM is reduced layers consisting of the different iron oxide phases would form, as detailed in Figure 1.6. The study describes the reduction as initially starting by the gaseous molecules and the (non-reactive) ash on the outside of the OCM particles. These molecules reduce the outer haematite layer to metallic iron while a core of wüstite remains unreacted, as the reaction progresses the gas penetrates deeper into the particle forming layers of different iron oxide phases. This model indicates that the rate of reduction depends highly on the rate of the diffusion into the particle.

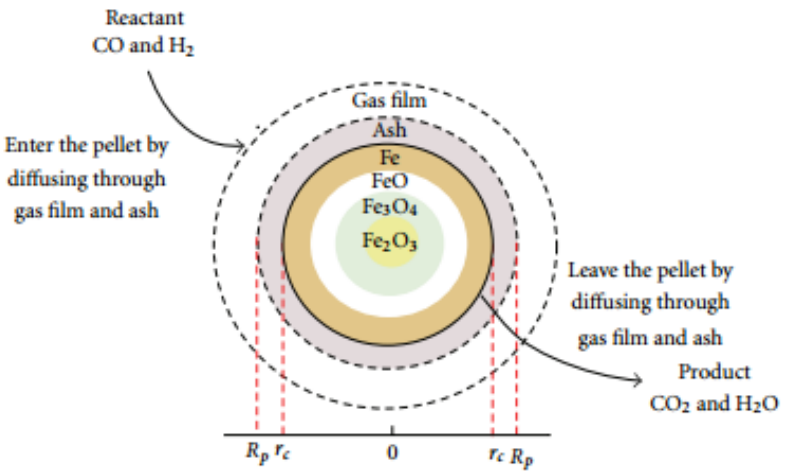


Figure 1.6: Shrinking core model of an iron oxide particle taken from Alamsari et al (2011), showing the iron oxide phases present in the particle during reduction.

The shrinking core model assumes that the kinetic equation is not dependent on the concentration of wüstite and magnetite, which becomes invalid in some situations during fixed bed chemical looping such as when under strong reduction, where the proportion of the metal oxide, in comparison to the metallic iron, is higher. (Alamsari et al 2011).

Park and Levenspiel (1977) developed a cracking core model to simulate both oxidation and reduction during chemical looping $H_2$ production. The cracking core model assume that the pores present in the particle increases, with the iron oxide particle therefore becoming more porous, during reduction due to fragmentation. This increased pore size and fragmentation creates new routes for the gas-solid interaction, increasing the surface area and allows for higher rates per unit mass. The increased pore size also increases the gas diffusion rate.

Hossain and de Lasa (2010) proposed a more complex kinetic model where nuclei are formed during the initial portion of the reaction, allowing the reaction to progress. As the reaction spreads these nuclei grow and proliferate through the particle, increasing the rate of reaction. Over time these growing nuclei overlap and combine. This formation of these nuclei requires a larger activation energy when compared to the shrinking or cracking core models. Lorente et al (2008) modelled this behaviour using the Johnson-Mehl-Acrami-Kolmogorov equations, which is based on the nucleation model. The results of this simulation were compared to those collected using a thermogravimetric differential reactor and showed good agreement. This was carried out at 600 K to 720 K a much lower temperature that conventionally used for chemical looping $H_2$ production and as the

temperature of the reactor is increased it is expected that the nuclei growth rate would increase, speeding up the reaction rate.

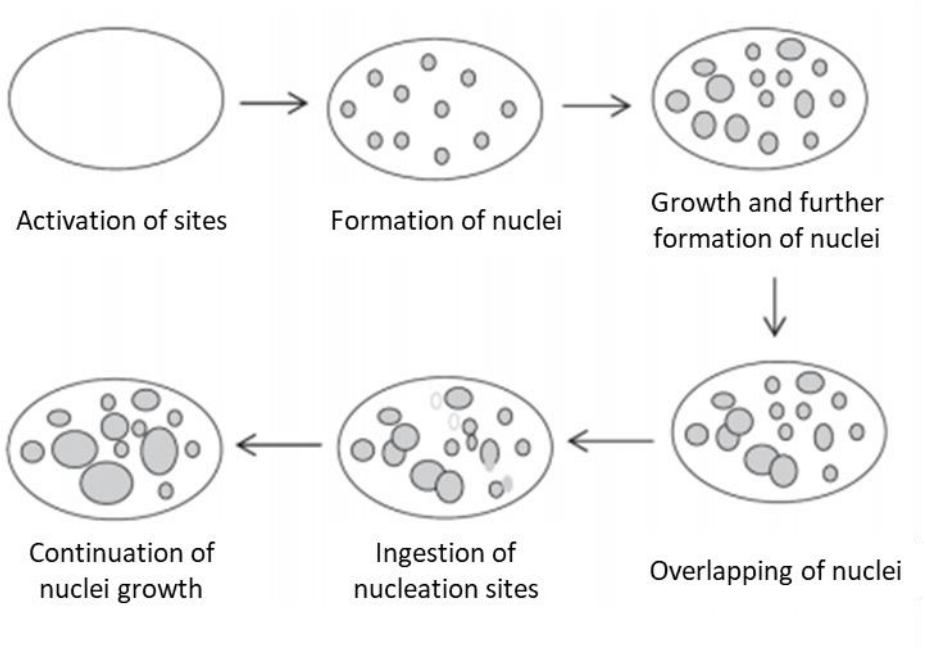


Figure 1.7: Diagram of nucleation and mechanism of nuclei growth on the surface of an OCM during reduction reaction (Hoosain and de Lasa 2010)

Peña et al (2006) suggests a combination approach, using the shrinking core model for the initial stage of the reaction before transitioning to the cracking core and nucleation models in later reduction stages. It was found that this methodology successfully predicted the behaviour under reducing conditions.

The utilisation of support materials has been shown to increase the lifetime of iron oxide. Kierzkowska et al (2010) used three different loading of alumina on iron oxide and compared the performance to pure iron oxide. It was found that a 40 wt% loading of alumina consistently outperformed the other loadings (0, 10 and 20 wt%) regardless as to whether the material was reduced past the wüstite phase or the reaction was stopped once this was reached. The higher stability of this mixture was attributed to the formation of $FeO.Al_2O_3$ spinels.

Murugan et al (2011) also used 40 wt% alumina on iron oxide in a 150 cycle campaign, using CO and steam as the reducing and oxidising agents respectively. It was found that the reactivity of both stages was stable for the first 40 cycles at which point the material began to degrade causing the reactivity to drop until the $80^{th}$ cycle from which point the material remain steady and a new lower reactivity.

Numerous studies have been carried out exploring the use of additives to the iron oxide systems with the aim of reducing the temperature of reaction and improving material life time. Otsuka et al carried out two experiments looking at the addition of 5 mol% of various metals (Otsuka et al 2003a and Otsuka et al 2003b), it was found that the addition of Al, Cr, surface area of these materials was studied using the Brunauer-Emmett-Teller(BET) method before and after cycling, it was found that the surface area dropped over cycling regardless of the additives present. However of those studied Al and Cr had the least loss of surface area.

Takenaka et al (2004) studied the effect of adding Rh and Mo both independently and co-operatively. It was found that both reduced the apparent activation energy required to oxidise the material using steam but when either was present on its own the material underwent sintering at a faster rate than for $Fe_2O_3$ alone but that the combination of the two additives was capable of lower the operating temperature while improving stability.

Work has also been carried out using transition metal ferrites for chemical looping $H_2$ production. The more notable of these include Kodama et al*'s* (2002) work using nickel, cobalt and zinc ferrites for cycling using methane as the reducing agent and steam as the oxidising agent. This work produced high carbon-content syngas and $H_2$ as the product streams but required high energy inputs due to the endothermic nature of the process. The authors intended for the use of solar energy to account for this. Of the ferrites studied nickel ferrite performed best and when supported on zirconia showed high stability.

Copper ferrite was also studied by Kang et al (2008) for methane reforming reactions. It was found that the addition of the copper inhibited the decomposition of methane decreasing carbon depositions but enhancing kinetics for the reaction. It was also found that supporting the material on ceria or zirconia improved reactivity, with ceria having the larger impact, with increased selectivity for CO formation and increased $H_2$ production during the oxidation half cycle.

*1c.iii.b Nickel oxide*

In chemical looping combustion for electrical power generation, nickel oxide is often used due to high redox reactivity, high melting point and large oxygen capacity. These properties are also useful for chemical looping $H_2$ production. However, these nickel oxide OCMs have

been found to have lower reactivity with $H_2O$ for $H_2$ production compared to iron oxide based systems (Mattisson et al 2001).

In the regime of interest nickel oxide can only exist in two oxidation states, metallic nickel and nickel oxide (NiO), this limits the potential oxygen content of the OCM. The necessity of forming a metallic phase also increases the chance of carbon deposition in the system. Additionally, Cho et al (2004) found that this material promotes methane cracking, causing OCM deactivation. The material also suffered from sulphur poisoning and thermal sintering, which would adversely affect the materials ability to perform as an OCM.

Nickel oxide is particularly vulnerable to sulphur poisoning; Jerndal et al (2006) and Wang et al (2008) both found that the presence of small quantities of $H_2S$ causing the formation of nickel sulphides. This destroys the oxygen capacity and reactivity of the material, decreasing redox activity. Garcia-Labiano et al (2009) found that unless the concentration of $H_2S$ was keep below 100 vppm there would be an unacceptable loss of redox activity in a chemical looping plant using nickel oxide as the OCM.

Nickel oxide is often supported on inert materials like $Al_2O_3$ to form spinel $NiAl_2O_4$ to increase the rate of both reduction and oxidation reactions. It has also been shown to lower the rate of thermal sintering which occurs in the reactor. Supported nickel oxide has been reduced with sulphur containing CO, this was seen to limit the poisoning effect when unsupported material was used. It was found that the OCM was unaffected after 10 redox cycles. (Shen et al 2010)

Murugan et al (2011 and 2012) tested supported nickel oxide (20 wt%) using cyclic temperature programmed reduction and temperature programed oxidation experiments between steam as the oxidising agent and CO as the reducing agent. These confirmed the presence of only one possible phase change in the system, due to the presence of only one peak in the temperature programed oxidation experiment. During the reduction carbon was deposited onto the OCM, which increases the $H_2$ production but decreased the product purity. Although there is high reactivity the presence of carbon deposition and the thermodynamic limitations for $H_2O$ splitting makes nickel oxide based OCMs unsuitable for chemical looping $H_2$ production processes.

*1c.iii.c Copper oxide*

Copper oxide has also attracted interest as an OCM, given its capacity for high conversion of methane when compared to nickel or iron oxide. Its high redox activity and thermodynamic properties make it an attractive option.

Copper oxide has an increased lifetime in chemical looping systems when supported $SiO_2$ or $ZrO_2$. Unsupported copper oxide has been shown to suffer from 90% drop in performance over three cycles, while the supported copper oxide had a much larger survivability. Additionally, the supporting materials increases the oxidation rate and the material stability by decreasing carbon deposition. (Diego et al 2004) These increases were found to not be a strong function of the preparation methods, with co-perception and mechanical mixing performing equally well and wet impregnation performing fractionally better.

The redox reactivity of copper oxide supported on $Al_2O_3$ and $SiO_2$ was studied using synthetic syngas (1:1 CO:$H_2$) as the reducing agent and 20 mol% $H_2O$ in nitrogen as the oxidation agent. The material supported on $Al_2O_3$ was found to achieve a higher conversion rate than that supported on $SiO_2$ when at 923 K. Increasing the temperature above this point led to the formation of $CuAl_2O_4$ spinel decreasing the conversion. At temperatures below 923K the kinetics of reaction were found to drop as expected by the authors. The oxidation reactivity was found to be more favourable at lower temperatures but the domination of kinetic effects meant that by 623K the $H_2O$ conversion had dropped to 2%. (Son et al 2009)

*1c.iii.d Manganese oxide*

Manganese oxide has a low melting point, 733 K for $MnO_2$ and 1093 K $Mn_2O_3$. This limits its use in chemical looping processes to those at low temperatures. At these low temperatures Mattisson et al (2001) found that manganese oxide out performed nickel and iron oxide. For chemical looping $H_2$ production this low temperature threshold is non-ideal.

*1c.iii.e Iron containing perovskites*

Recent studies on chemical looping $H_2$ production have concentrated on the use of iron containing perovskites (Schouten 2008, Dudukoic 2009, Kappagantula et al 2018). Perovskites-type material have an $ABO_3$ cubic structure. The B site is conventionally occupied by a transition metal ion while the A site is occupied by an alkali, rare earth or alkaline earth metal. The material is often in a cubic structure with the A ions in the

dodecahedral sites and the B ions sit in octahedral sites (Abazari and Sanati 2013, Bhalla et al 2000, Vasala et al 2014, Xu et al 2010). This structure can be seen in Figure 1.8.

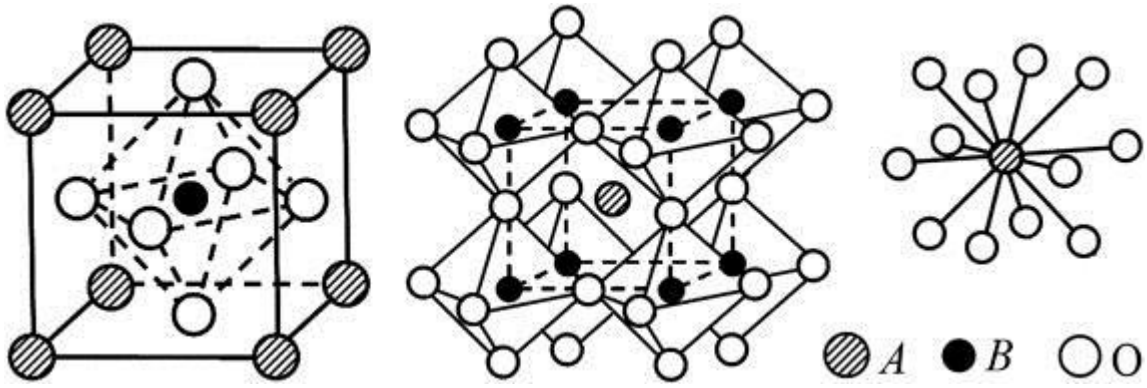


Figure 1.8 – $ABO_3$ structure of cubic perovskite (Xu et al 2010)

This class of material shows particular promise for chemical looping technologies due to their ability to store, release and transport oxygen. This oxygen mobility is due to oxygen vacancies formed when the A and/or B site of the material is doped with ions of different radii or valances. (Kim et al 2014, Shen et al 2014, Sun et al 2014). If the total charge of the A and B sites does not equal 6, the system cannot maintain a perfect crystal structure and charge neutrality. If the sites are doped correctly the structure rejects oxygen ions to balance the charge, forming oxygen vacancies (Xu et al 2010, Abazari and Sanati 2013). This causes mixed valence states in the material and causes the material to be a mixed ionic electronic conducting material.

The nature of these oxygen vacancies results in perovskite materials exchanging oxygen with the gas phases in contact with them without undergoing phase changes in the lattice structure. This differs from more conventional OCMs, like iron which changes phase to release oxygen. This lack of a phase change during oxygen release or take up allows for the oxygen content of the material to change at any partial pressure of oxygen and with a decreased energy barrier stopping oxygen release from the material. This is a useful property for chemical looping $H_2$ production as lower energy barriers to oxygen release lowers activation energy decreases costs or increases rate constants.

The nature of the movement of the oxygen in the lattice is often explained using a defect chemistry model. Point defects in the perovskite are used to determine the electrical and oxygen conductivity of the material. Point defects can be defined as either stoichiometric or non-stoichiometric. Stoichiometric point defects are often found in ionic solids and maintain

charge neutrality, they can be further classified into Schottky and Frenkel defects. These can then be used to predict the oxygen transport properties of perovskite materials (Kittel 2005 and Fierro 2005). Schottky defects form in perovskites when there are equal concentrations of cations and anions with the same charge. These defects maintain the charge neutrality and causes the density of the solid to decrease. Schottky defects often form in crystal structures with similar sized cations and anions. In comparison Frenkel defects occur when there is a large difference in the sizes of the anions and cations and does not change the density of the solid. Frenkel defects form when a small ion in the matrix moves from its normal position into an interstitial site creating a vacancy in the original location of the ion.

A wide range of ions that can be doped on the A and B site have been studied in the literature (Benamira et al 2014, Emmerlich et al 2014, Franca et al 2012, Feng et al 2014, Karen 2006, Kim et al 2014,Lankhorst et al 1997, Nagai and Iro 2014, *Shen* et al 2014, Smyth 2000, Stolen et al 2006, Vasala et al *2014,* Wang et al 2014, Xu et al 2010). Dopants in a perovskite change the nature of the relationship between the oxygen content and the $pO_2$ that it is in equilibrium with. Dopants also change the structure of the material increasing residence to sintering and attriction or change the melting point of the material allowing for the use of hotter reactors. Dopants can also help to catalysis the reduction or oxidation half reactions improving rate constants. Different dopants increase the suitability for some applications while decreasing the suitability for others. The use of the correct dopant, to the precise degree necessary, can give optimal properties for a chemical looping system. For example: the use of strontium on the A site or Cobalt on the B site can increase the oxygen transport properties but decreases lifetime due to a reduced resistance to phase segregation in reducing gas atmospheres (Martin 2003).

Iron containing perovskites have been shown to have good cyclic stability and to be resistant to carbon deposition (Murugan et al 2011). Of particular interest for chemical looping $H_2$ production is the lanthanum strontium ferrite series (LSF). This series has general formula $La_{1-x}Sr_xFeO_{3-\delta}$ and has only iron ions on the B site while the A site is doped with a ratio of $La^{3+}$ and $Sr^{2+}$. The iron ions, for the LSF series, are stable in a variety of different valences which gives a high oxygen ion conductivity, providing a wide electron distribution in the crystal structure. This helps with the reaction rates and stability of the material.

$La_{0.6}Sr_{0.4}FeO_{3-\delta}$ (LSF641) has attracted technological interest as a chemical looping oxygen carrier material for $H_2$ production (Murugan et al 2011; Metcalfe et al 2019), SOFC cathode

material and as a ceramic membrane. LSF641 is of particular interest as it is consistently single phase in the oxygen partial pressures and temperatures of interest to looping and sensor technologies. (Dann et al 1994)

The relationship between oxygen content and $pO_2$ of LSF641 was studied in the literature at a variety of temperatures and partial pressures of oxygen ($pO_2$) (Kuhn et al 2011, Mizuzaki et al 1985, Sogaard et al 2007). However, the thermochemical expansion of this material obtained in these studies concentrated on the solid oxide fuel cell application so that the range of $pO_2$'s investigated has been largely limited to ~ $10^{-7}$ bar. For chemical looping applications, the relevant $pO_2$ extends to ~$10^{-22}$ bar and as part of this thesis it is intended to extend previous investigations into this lower range.

To understand how a non-stoichiometric perovskite behaves in a chemical looping $H_2$ production scheme, a knowledge of the governing thermodynamics controlling the interaction between the material and reducing or oxidising potentials is required. (Murugan et al 2011, Sogaard et al 2007, Mizuzaki et al 1985). The oxygen non-stoichiometry (3-$\delta$) has been found with good reproducibility in literature (Kuhn et al 2011, Mizuzaki et al 1985, Sogaard et al 2007). The defect chemistry model used in these studies assumed that the gain and loss of oxygen of the solid is accompanied by a change in oxidation state of the iron ions through the linear combination of the oxidation reaction and the disproportionation reaction near an oxygen vacancy site:

$$2Fe^{3+} + 0.5O_2 + V_O^{\bullet\bullet} \rightleftharpoons 2Fe^{4+} + O^{2-}, \qquad \text{1.b.6}$$

$$2Fe^{3+} \rightleftharpoons Fe^{4+} + Fe^{2+}. \qquad \text{1.b.7}$$

Here $V_O^{\bullet\bullet}$ is the oxygen vacancy in the lattice as denoted in the Kröger-Vinc notation.

Combining material balance with conservation of cationic and anionic sites in the lattice and charge neutrality, the equilibrium partial pressure of oxygen, $P_{O_2}^*$, can be related to the degree of non-stoichiometry of the solid, $\delta$, *via*

$$\frac{\delta^{0.5}(2\delta - x + 1)}{(3-\delta)^{0.5}(2\delta - x)} \times {P_{O_2}^*}^{0.25} = \frac{K_{Fe}}{K_{ox}} \times \frac{(3-\delta)^{0.5}(x + 1 - 2\delta)}{\delta^{0.5}(2\delta - x){P_{O_2}^*}^{0.25}} - K_{ox}^{-0.5} \qquad \text{1.b.8}$$

where $x$ is the extent of substitution of La by Sr, in this case 0.4; $K_{ox}$ and $K_{Fe}$ are the equilibrium constants for Equations 1b.6 and 1b.7, respectively (Mizusaki et al 1985). The

oxygen non-stoichiometry of the material as a function of the equivalent oxygen partial pressure that would be in equilibrium with it for LSF641 at 1093K can be seen in Figure 1.9

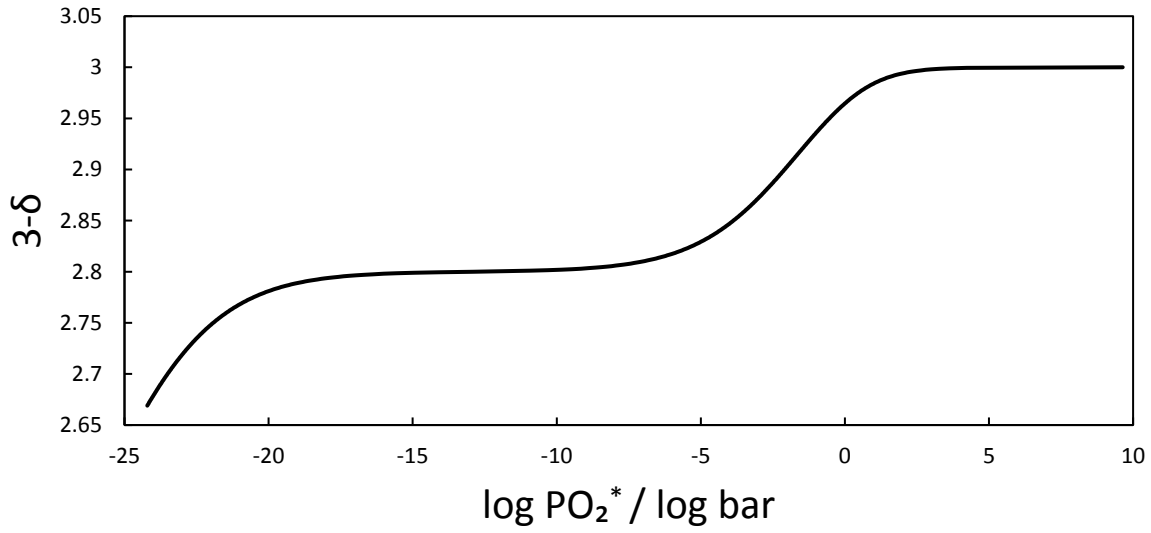


Figure 1.9: Oxygen non-stoichiometry of $La_{0.6}Sr_{0.4}FeO_{3-\delta}$ as a function of equivalent oxygen partial pressure at 1093K

As is exemplified by Figure 1.9, perovskites vary continuously in non-stoichiometry with changing chemical potential. This characteristic of the material can increase the life time of the material as the OCM must maintain integrity and be stable over prolonged operation. Operational life time can be increased if phase transition and segregation are both minimized, since phase segregation can cause significant changes in the chemical and electrical activity of the material (Lein et al 2006).

Studies of electronic conductivity of perovskite materials at different temperatures have been carried out by Singh et al (2013) who found that strontium doped lanthanum ferrite perovskites as the temperature increased the electronic conductivity also increased. This indicates that the transportation of oxygen most likely relies on vacancy diffusion as opposed to interstitial diffusion. Elshof et al (1997) found that for LSF641 the bulk diffusivity of oxygen through the material was not a function of oxygen pressure and that the equilibrium process between the gas and solid phase was governed by the surface exchange for low oxygen partial pressures.

Another advantage for strontium doped lanthanum ferrite perovskites (LSF) is that they are highly stable. Murgan et al (2011) showed that this class of material has showed a greatly increased lifetime when compared to alumina stabilised iron. Both LSF641 and alumina stabilised iron oxide were cycled 150 times between CO and $H_2O$, initially the stabilised iron

oxides higher oxygen capacity allowed it to produce more $H_2$ but over time the material degraded until by the 150th cycling is was very similar to the LSF731 and still showed a strong negative trend, in comparison after the first 10 cycles the LSF731 showed very stable $H_2$ production without significant degradation.

*1c.iii.f Manganese containing perovskites*

Another perovskite material of interest is strontium doped lanthanum manganite (LSM). This material has a larger oxygen capacity, in the $pO_2$ regime of interest, than the LSF series. Mizusaki et al (1991) compared $La_{0.6}Sr_{0.4}MnO_{3-\delta}$ LSM641 and LSF641. As can be seen in Figure 1.10 that the oxygen content of the LSM641 goes through a much larger change than that seen in LSF641 for the range of $pO_2$ used in $H_2$ production, $10^{-8}$ to $10^{22}$ bar. However, it was also found that the material underwent phase segregation and decomposition at a much higher $pO_2$. This means that it would be expected to decompose into a Brownmillerite phase, potentially irreversibly, well before the reducing conditions expected at the reducing gas feed location in a packed bed chemical looping reactor system for $H_2$ production ~$10^{-22}$ bar. This decomposition would limit the life time of the material either increases operation costs to replace the material or limit the profitability of the plant due to decreased conversions and yields.

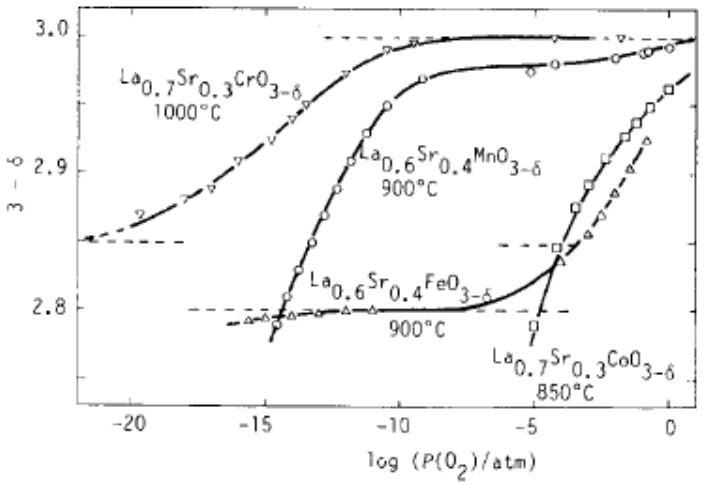


Figure 1.10: Comparison of oxygen non-stoichiometry in $La_{1-x}Sr_xMO_{3-\delta}$ (M= Cr, Mn, Fe, Co) from Mizusaki et al (1991)

It is important to note that the study of $La_{0.7}Sr_{0.3}CrO_{3-\delta}$ was not carried out in detail as studies my Meadowcroft (1969) and Mizusaki et al (1984) showed that this material requires temperature above 1273 K to be suitably reactive. This high a temperature would not be

limits the effectiveness of the system and increases operational heating costs and capital costs for insulation.

However, Manganese ions in LSM are only stable in oxidation states of 3+ and 4+, and hence its oxygen ion conductivity is significantly lower than that of LSF. (Noh et al 2013). This would adversely affect the rate of reaction in both the reduction and oxidation half cycles. Additionally, the oxygen stored deeper in the looping material would be unable to interact with the gas environment decreasing the viable oxygen content of the material.

Wang K et al (2000) also showed that this manganese based materials can catalyse carbon deposition which would decrease the number of active sites and lead to carbon containing compounds contaminating the $H_2$ product stream.

*1c.iii.g Thermodynamic advantages of non-stoichiometric oxides*

As well as the increased life time and fast kinetics, due to the high conductivity of oxygen through the lattice, variably non-stoichiometric oxides offer thermodynamic advantages to chemical looping systems when compared to simple metal/metal oxide systems.

A variably non-stoichiometric oxide has a range of $pO_2$s where there is a one to one relationship between oxygen content and $pO_2$, so it is possible to design a reverse flow packed bed system where each end of bed has an oxygen content that would be in equilibrium with one of the two feeds. In such a system, with rapid enough kinetics to approach the thermodynamic limitation, the gas leaving the reactor during a half cycle would be in equilibrium with the OCM at the outlet which is in equilibrium with inlet feed of the other half cycle. With the use of suitably pure inlet feeds, it would be possible to achieve arbitrarily high conversions. Without a one to one relationship between oxygen content and $pO_2$ a conventional metal/metal oxide OCM is not capable of achieving these high conversions, with the conversions limited by the $pO_2$ at which the phase changes occur.

The methodology and theory underpinning the thermodynamic limitations of chemical looping systems using different OCMs is detailed and examined in Chapter 3.

By circumventing the limitations of a conventional reactor large savings can be achieved. These savings come from reduced feed costs, as less feed is required to produce the same amount of high value products, and reduced capital costs as there is less need for the design and operation of the complex separation systems required to purify products.

## 1.d Purpose of study

A chemical looping reaction allows for the separation of the reduction and oxidation half reactions resulting in $H_2$ production in a separate outlet stream to that of the carbon containing products and reactants.

Before a chemical looping technology could be implemented at an industrial scale a better understanding of the reactions and the system would be required. The main objective of this thesis is to study a chemical looping reactor for $H_2$ production. This will concentrate on the comparison between a steam methane reforming or conventional water-gas shift reactor, as the current main industrial methodology of $H_2$ production, and a chemical looping system.

The comparison with conventional reactor systems seeks to demonstrate how and why the thermodynamic limitations of a chemical looping reactor with a non-stoichiometric OCM reaction allows an arbitrarily high conversion. This would also circumvent the limitations of a chemical looping reactor using a stoichiometric OCM like iron oxide.

The chemical looping system studied will consist of a non-stoichiometric oxygen carrier like LSF or LSM using CO or $CH_4$ as the reducing agent. The material will be oxidised using steam, to increase $H_2$ production.

The system will be studied by analysing the reactor outlet gas and using synchrotron *operando* x-ray diffraction (XRD). *Operando* x-ray diffraction allows for the internals of the reactor system to be studied as it undergoes reaction. The reactor system will also be studied through the use of mathematical modelling. Both the gas analysis and the reactor internal conditions, as probed using XRD techniques, will be compared to the model to aid validation. A fully validated model will aid scale up and help to optimize the reactor system.

# Chapter 2: Experimental set up

This chapter details the design and operation of the different process systems used as part of this thesis. This includes the flow system used at Newcastle University and on beam line ID22 at the European Synchrotron Research Facility (ESRF), the *in-situ* neutron detectors on the High Resolution Powder Diffractometer (HRPD) at the ISIS neutron and muon source, and the *in-situ* x-ray diffraction detector crystals on beam line ID22 at ESRF. Additionally the methodology for material synthesis are also detailed along with the methodology used to analyses the outlet gas composition.

## 2a Reactor flow system

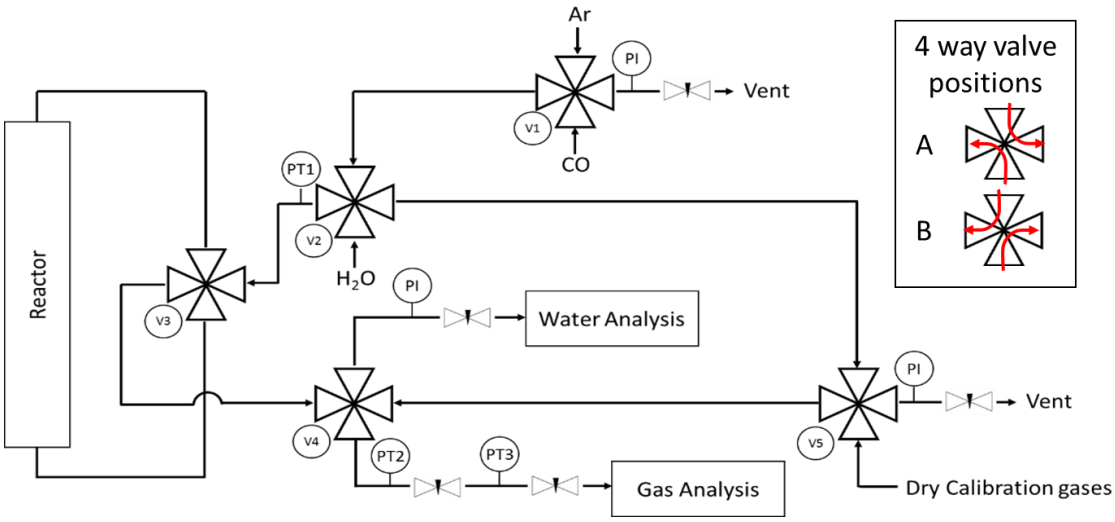


Figure. 2.1. Flow diagram of the fixed bed reverse flow integral reactor. Flow is continuous for all reactive gases and the type of gas introduction to the reactor is governed by two electronic 4-way valves V1 and V2. Flow direction in the reactor is directed by V3. V4 and V5 are used for gas analysis calibrations bypassing the reactor. Flow rate is set and regulated by computer at 3.4 $\times 10^{-5}$ mol $s^{-1}$ (+/- 3.4$\times 10^{-7}$ mol $s^{-1}$).or 50 ml/min NTP (+/- 0.5 ml/min).

The flow system consists of five automatic 4-way valves (VICI) to control flow direction and seven mass flow controllers (MFC) were used to control the flow rates of the feed gasses, these consisted of four for calibration with three feeding reacting gasses to the reactor in the furnace. Pressure transducers (Omega, PG309-100GV) were used to measure and monitor the pressures in various positions throughout the system. PT1 records the inlet pressure to the reactor while PT2 measures the outlet pressure. PT3 is used in conjunction with PT2 to obtain a measure of how the flowrates through the system change as different gases are fed to the reactor.

The mass flow controllers are connected to a computer controlled central unit which governed their set points, additionally this controlled a gas shut off solenoid valve attached at their outlet. This was present as the MFCs are not able to act as on/off valves, so when the flow rate through a MFC was set to zero this valve would shut off ensure no flow would pass through. Additionally these solenoid valves would shut off in the event of an interlock shutdown when a failure was diagnosed by the system or if the system is disconnected for more than 5 minutes.

The 4-way valves V1 and V2 were used to control whether Ar, 5±0.025 mol% CO in Ar, or 5±0.025 mol% steam in Ar was being fed to towards the bed and were connected to and controlled by the central unit. The reacting gases were then sent to V3 which controls the gas feeding direction towards the bed, this ensures that the system was running in a counter current configuration. The outlet gasses then go to V4, this then feeds the reacted gas stream towards the gas analysis system (QGA, Hiden Analytical). In order to calibrate the gas analysis system, calibration gasses are feed through V5, either Ar, 5±0.025 mol% CO in Ar, 5±0.025 mol% $CO_2$ in Ar, and 5±0.025 mol% $H_2$ in Ar through the calibration gasses inlet or $H_2O$ from the outlet of V2. Additional experiments changed the reducing and oxidising gasses fed to the reactor. The CO in Ar was replaced with 5±0.025 mol% methane in Ar to test the materials ability to achieve methane activation. Also the CO in Ar was replaced with $H_2$ in Ar and the steam in Ar was replaced with $CO_2$ in Ar. All the gasses were supplied by BOC.

All metal pipe lines which had contact with $H_2O$ moisture were wrapped in trace heating lines, this prevented $H_2O$ condensation in the system. $H_2O$ condensation leads to incorrect moisture contents reaching the bed and being recorded by the gas analysis system. This would have led to the recorded value for the $H_2O$ conversion being much lower that the reactor actually achieved.

In order to achieve a stable stream of 5 mol% steam in Ar a Liquid Filled Permeation Tube (LFPT) was used. This consists of a $H_2O$ filled reservoir separated from the flow of Ar by a $H_2O$ permeable membrane. The use of a membrane results in steady $H_2O$ diffusion regardless of the laboratory temperature as the system can be fit inside an external computer controlled furnace. The diffusion rate, and therefore the total amount of $H_2O$ transferred across the membrane, is a function of only the oven set point, as long as the

reservoir still contains adequate quantities of $H_2O$, so the percentage of $H_2O$ in the gas feed can be controlled by varying the furnace temperature or the gas flow rate.

The $H_2O$ analysis system is used to ensure the $H_2O$ stream consists of the correct proportion of $H_2O$. It consists of a chilled $H_2O$ hygrometer (the $H_2O$ analysis system in Figure 2.1). This measured the dew point of the gas between 228 K and 323 K with an uncertainty of 0.2 K.

In order to ensure consistent flowrates through the system computer controlled mass flow controllers (SLA5850, Brooks Instrument) were used. In order to avoid pressure heads passing through the system needle values were added to the end of vent lines and before the analysis systems. These were used to make sure the pressure drop between gas feed locations and the bed were consistent regardless of gas. This was carried out by comparing the different pressure indicators values with the pressure transducers (PG309-100GV, Omega), PT1, PT2and PT3. PT1 and PT2 were used to measure the pressure drop across the bed while PT2 and PT3 were compared to each other to determine the ratios of the molar flowrates through the bed. This was done by applying Equation 2b.1. This allows for an oxygen balance to be carried out comparing half cycles.

$$\frac{n_1}{n_2} = \sqrt{\frac{PT2_1^2 - PT3_1^2}{PT2_2^2 - PT3_2^2}} \qquad \text{2a.1}$$

$n$ is the molar flowrate, PT2 is the pressure by PT2 and PT3 is the pressure recorded by PT3.

The reactor itself was a 5 mm inner diameter quartz tube plumbed into the flow system using Ultra Torr fittings (Swagelok). The oxygen carrier material (OCM) used in each experiment was packed into the bed between two plugs of quartz wool, which are used to fix the bed in place. Additionally, quartz rods were paced inside the tube, on either side of the bed, to minimise the dead volume of the reactor. These rods also prevented the bed moving when the flow direction changed. Figure 2.2 shows a packed bed, note that the OCM was loaded from the left causing that plug to be darker in colour from picking up residual particles left on the side wall of the quartz wool

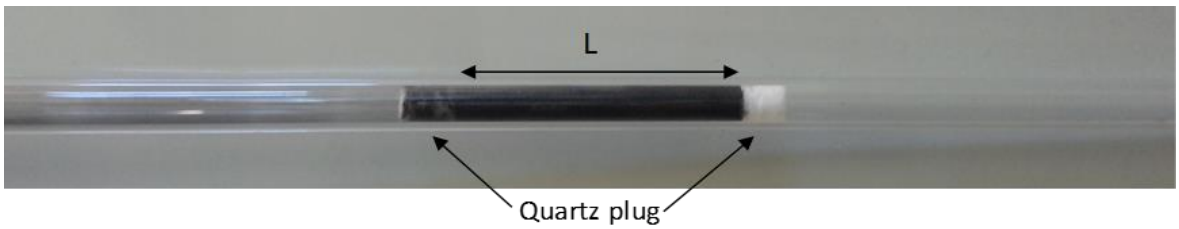


Figure 2.2: Photograph of a packed bed reactor. This packed bed is 5.97 g of $La_{0.6}Sr_{0.4}FeO_{3-\delta}$ and is 60 mm long.

*2a.i Leak detection*

Air leaking into the system or reacting gasses leaking out of the system was a major cause of experimental failure. The failures can take the form of high partial pressures of oxygen from the air reaching the bed causing over oxidation of the oxygen carrier material or the reacting gasses not reaching the mass spectrometer. As a result, leak detection and minimisation were of vital importance as part of this project. Snoop leak detection fluid was applied to all connections to check for large leaks, while small leaks were identified by pressure testing immediately before the experiment. This was done by pressurising the system to 2 bar-a using Ar and sealing the ends using shut off valves. Any drop in pressure over time was attributed to the presence of leaks in the system, and was used to determine the leak rate. The leaks in the system were deemed negligible once the change in pressure was less than 100 Pa (the detection limit of the pressure indicators) over one hour.

During experiments the mass spectrometer data can be used as an indication of leaks in the system. The presence of a 4:1 ratio of m/z= 28 ($N_2$) to 32 ($O_2$) indicates there is a leak in the system if other gasses with these ratios are not being fed into the system at the time. However this can also occur should the flowrate through the system drop below the draw rate of the mass spectrometer (16 ml(STP)/min) as this causes air to be pulled up the exhaust line. Additionally spraying helium towards the pipe connections can aid leak detection, where its small radius allows it to penetrate into leaking areas and can be used to pinpoint leak locations as this helium would then be picked up by the mass spectrometer.

*2a.ii Laboratory reactor system*

While the reactor flow system was used at Newcastle University it was used in conjunction with a tubular horizontal furnace (Lenton). This furnace acted as a heat source, heating the reactor to the 1093 K required to achieve equilibrium unity for the mixed water-gas shift reaction. This furnace has a 100 mm isothermal zone making this the maximum bed length.

The ends of the tubular furnace were plugged using quartz wool to prevent heat loss and the condensation of $H_2O$.

### 2b Gas analysis

All gas analyses were carried out using data collected from a quadrupole mass spectrometer (QGA, Hiden Analytical). It has a heated flexible silica capillary inlet to ensure no $H_2O$ condensation occurs blocking the inlet or damaging the internals of the mass spectrometer and to ensure the accurate measurement of steam in the outlet stream. The system has an input stream flow rate of 20 ml/min (STP), an inlet pressure of 1 bar and has a sampling rate of 8 measurements per second. The filament used in the system was oxide coated iridium. Oxide coated iridium allows lower temperature analysis than either tungsten/rhenium filaments allowing for residual gas analysis, additionally tungsten filaments produce carbon oxides by products when exposed to oxidising gasses which are important gasses to record in this work. Lanthanum hexaboride filaments were not used due to the decreased life time when used for continuous gas analysis.

The high sampling rate of the QGA was achieved using a Secondary Electronic Multiplier (SEM) detector, this allows for small ion currents to be detected by physically amplifying ion signals. This is achieved by applying a positive voltage to the electrons entering the mass spectrometer, which increases the sensitivity and lowering the partial pressure that can be detected. However use of the SEM required the operating pressure to be less than $10^{-6}$ torr to prevent pyrolysis of the dynodes by the $H_2O$ vapour in the system.

The mass spectrometer produces a constant background current for each mass to charge ratio when it is not being fed with a gas with that ratio. A zero point reading was taken where only the Ar was fed, this was then subtracted from the data to get a true current.

To account for the splitting of larger molecules such as $CO_2$ into smaller molecules a splitting factor was applied to the currents. The proportion of the current measured with mass to charge ratio 28 that is due to CO is equal to the total current for 28 minus 0.19 of the current for mass to charge ratio 44. The proportion of the current measured with mass to charge ratio 2 that is due to $H_2$ is equal to the total current minus 0.02 of the current for mass to charge ratio 18. These splitting factors were found and based on currents that had had the background value subtracted.

A calibration factor is then applied to take into account that the gasses sampled each have different sensitivities so are more or less likely to interact with the system. The calibration factors drifted constantly throughout the experiment. To ensure accurate results, molar concentrations of each gas were fed to the mass spectrometer directly, bypassing the reactor, and linear interpolation was then used to determine the calibration factor as a function of time.

In order to convert the calibrated currents into the molar percentages, they are divided by the total calibrated current. This means the molar percentages can be found using Equations 2b.1 to 2b.4.

$$y_{CO} = \frac{\frac{I_{28} - 0.19 \times I_{44} - I_{CO\ zero\ value}}{CO\ calibration}}{\frac{I_{28} - 0.19 \times I_{44} - I_{CO\ zero\ value}}{CO\ calibration} + \frac{I_{44} - I_{CO2\ zero\ value}}{CO_2\ calibration} + \cdots \frac{I_2 - 0.02 \times I_{18} - I_{H2\ zero\ value}}{H_2\ calibration} + \frac{I_{18} - I_{H2O\ zero\ value}}{H_2O\ \ calibration} + \frac{I_{40}}{Ar\ calibration}} \quad \text{2b.1}$$

$$y_{CO2} = \frac{\frac{I_{44} - I_{CO2\ zero\ value}}{CO_2\ calibration}}{\frac{I_{28} - 0.19 \times I_{44} - I_{CO\ zero\ value}}{CO\ calibration} + \frac{I_{44} - I_{CO2\ zero\ value}}{CO_2\ calibration} + \cdots \frac{I_2 - 0.02 \times I_{18} - I_{H2\ zero\ value}}{H_2\ calibration} + \frac{I_{18} - I_{H2O\ zero\ value}}{H_2O\ \ calibration} + \frac{I_{40}}{Ar\ calibration}} \quad \text{2b.2}$$

$$y_{H2} = \frac{\frac{I_2 - 0.02 \times I_{18} - I_{H2\ zero\ value}}{H_2\ calibration}}{\frac{I_{28} - 0.19 \times I_{44} - I_{CO\ zero\ value}}{CO\ calibration} + \frac{I_{44} - I_{CO2\ zero\ value}}{CO_2\ calibration} + \cdots \frac{I_2 - 0.02 \times I_{18} - I_{H2\ zero\ value}}{H_2\ calibration} + \frac{I_{18} - I_{H2O\ zero\ value}}{H_2O\ \ calibration} + \frac{I_{40}}{Ar\ calibration}} \quad \text{2b.3}$$

$$y_{H2O} = \frac{\frac{I_{18} - I_{H2O\ zero\ value}}{H_2O\ \ calibration}}{\frac{I_{28} - 0.19 \times I_{44} - I_{CO\ zero\ value}}{CO\ calibration} + \frac{I_{44} - I_{CO2\ zero\ value}}{CO_2\ calibration} + \cdots \frac{I_2 - 0.02 \times I_{18} - I_{H2\ zero\ value}}{H_2\ calibration} + \frac{I_{18} - I_{H2O\ zero\ value}}{H_2O\ \ calibration} + \frac{I_{40}}{Ar\ calibration}} \quad \text{2b.4}$$

Where $y$ denotes the mole fraction of each gas and $I$ denotes the current for the given mass to charge ratio.

In order to calculate a molar flowrate through the system these mole fractions would then be applied to Equation 2b.5.

$$n = \frac{y\ F}{60\ \times 22400} \quad \text{2b.5}$$

F is the total volumetric flow rate ml/min (STP), y is the mole fraction of the gas and n is the outlet molar flowrate (mol/s). From the ideal gas law it is known that 1 mole of gas has a volume of 22.4 L at standard temperature and pressure.

Each of the variables in Equations 2b.1 to 2b.4 have an associated uncertainty. As the values for the zero points and calibration factors for CO $CO_2$ $H_2$ and $H_2O$ are calculated as part of the data analysis by taking the average of values when fed with gasses of known concentrations. The standard error can then be found as part of the calculation. For the other variables in the equation the precision is used as a measure of the uncertainty.

The uncertainty is then propagated through the system using the following equations assuming that the covariance is zero:

$$\mathrm{f} = \mathrm{aA} \qquad \sigma_f^2 = a^2\sigma_A^2 \tag{2b.6}$$

$$\mathrm{f} = \mathrm{aA} + \mathrm{bB} \qquad \sigma_f^2 = a^2\,\sigma_A^2 + a^2\,\sigma_B^2 \tag{2b.7}$$

$$\mathrm{f} = \mathrm{AB} \qquad \sigma_f^2 = A^2B^2\left(\left(\frac{\sigma_A}{A}\right)^2 + \left(\frac{\sigma_B}{B}\right)^2\right) \tag{2b.8}$$

$$\mathrm{f} = \mathrm{A} \div \mathrm{B} \qquad \sigma_f^2 = \frac{A^2}{B^2}\left(\left(\frac{\sigma_A}{A}\right)^2 + \left(\frac{\sigma_B}{B}\right)^2\right) \tag{2b.9}$$

By applying Equations 6 to 9 to Equations 1 to 4 to get an equation for the uncertainty for the molar concentrations. Where f is the result of the operation, a and $b$ are constants without uncertainties, A and $B$ are measured variables with known uncertainties and $\sigma_x^2$ is the variance of variable x.

To calculate the conversions of $H_2O$ into $H_2$ and of CO into $CO_2$ the mole fractions of the products and unreacted reactants were integrated over each of their feed times. The conversion was then found using equations 2b.9 and 2b.10, as the molar flow rate is constant.

$$\frac{\int_{Start\ of\ Cycle}^{End\ of\ Cycle} y_{H2}\,dt}{\int_{Start\ of\ Cycle}^{End\ of\ Cycle} y_{H2}\,dt + \int_{Start\ of\ Cycle}^{End\ of\ Cycle} y_{H2O}\,dt} \tag{2b.9}$$

$$\frac{\int_{Start\ of\ Cycle}^{End\ of\ Cycle} y_{CO2}\,dt}{\int_{Start\ of\ Cycle}^{End\ of\ Cycle} y_{CO}\,dt + \int_{Start\ of\ Cycle}^{End\ of\ Cycle} y_{CO2}\,dt} \tag{2b.10}$$

In order to propagate the uncertainty through the integration the results were offset by one standard deviation before repeating the integration to obtain upper and lower bounds for the uncertainty.

### 2c In-situ x-ray diffraction

X-Ray Diffraction (XRD) is a technique that is used to determine the atomic structure of a crystalline material. The regular spaces between the atoms, seen in crystalline solids, because a beam of incident x-rays to diffract into specific directions. Through measuring the intensity and angles of these transmitted rays the structure can be obtained.

The work detailed here involves *in-situ* XRD, this is when the sample is measured while in the environment of interest, as opposed to *ex-situ* XRD where the sample is measured at ambient conditions. *In-situ* XRD has many advantages over *ex-situ* experiments. *In-situ* has the advantage that it allows for how and when the changes in structure occur during reaction and therefor an understanding of the kinetics involved to be obtained. The disadvantage is that the sample needs to be maintained at a set temperature and gas environment for the duration of the experiment, and the geometry of a given piece of equipment can limit the degrees of freedom when planning an experimental campaign.

*In-situ* x-ray diffraction was carried out on ID22 of the European Synchrotron Research Facility (ESRF). ESRF consists of an 844 m circumference electron particle accelerator that operates at an energy of 6 GeV. The source for ID22 is an in-vacuum undulator, sitting on a curve in the particle accelerator, which is capable of producing x-rays with energies from 6 keV to 80 keV. This beam is then monochromated before passing though the sample to the diffractometer. The diffractometer consists of nine silicon 111 crystals, which due to their very small acceptance angle act as a filter removing rays not parallel to the detector, and nine detectors. The filtering crystals and detectors are all mounted on a single rotational stage that moves through the 2θ angle allowing for peaks in the range of 0 to 25° to be recorded. The nine detector system is arrayed in fan like geometry meaning that a large selection of 2θ angles can be recorded while moving the stage a much smaller amount, this can be seen in Figure 2.3.

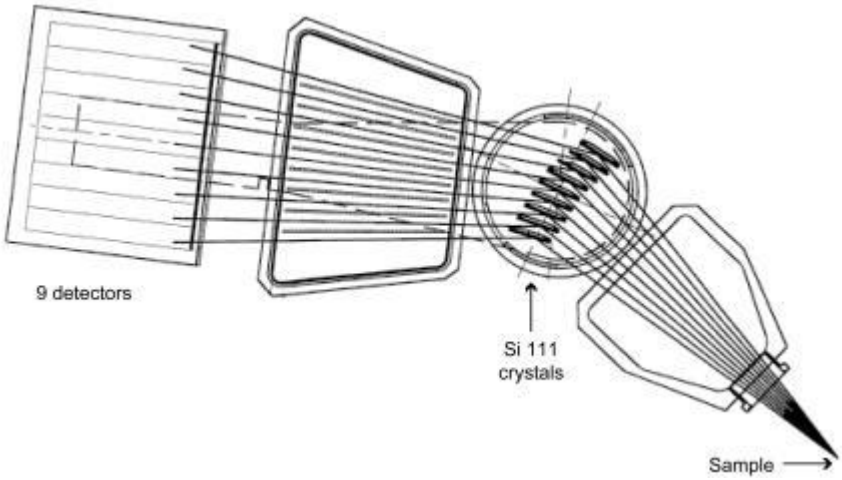


Figure 2.3: Schematic drawing of the mulianalyser stage, from Hodeau et al (1998)

This facility is uniquely suited for this experiment. It is optimized for the x-ray energies necessary for this experiment, due to the need to operate at high energies to overcome the large, for XRD experiments, sample size while avoiding the lanthanum K edge of 39 keV. It also gives high fluxes of x-rays allowing for the peak structure to be determined to within high levels of certainty rapidly.

The quality of its analyser crystals allows for high resolution, giving the sharp peaks necessary to monitor the small shifts in peak positions expected when the material is oxidised and reduced without going through a phase change. They also allow the evolution of peak splitting due to phase changes to be detected. In order to test a working reactor bed a reactor tube with a diameter on the order of 5 mm is necessary, which would make a conventional area detector unpractical as diffraction from the front and the back of the sample would broaden the beam and obscure subtle changes to the peak shape and shifts. There are very few facilities in the world with either enough flux at the required x-ray energy or the analyser resolution necessary for this experiment, and ID22 at ESRF has both.

For the experimental campaign detailed here the x-ray source was calibrated for 35 keV operation with a spot size of 1 mm x 1 mm. The dectrors moved at a rate of up to 30 degrees/minute and moved through 2.2 ° to cover 18.2° due to the fan of 9 detectors.

The flow system used on the beamline is the same as that detailed in Section 2b with the addition of a vertical split furnace and a smaller inner diameter tube. This custom manufactured vertical split furnace (IGI systems) achieved an isothermal zone of 200 mm at a maximum temperature of 1273 K. The furnace also had a thin vertical window on either

side to allow x-rays to pass through the bed so that the *in-situ* XRD measurements can be made at different points along the reactor. The furnace was wrapped in a thin layer of aluminium foil, this is used to minimise the radiative heat loses through these windows and due to the thinness of the sheet the contribution to the diffraction pattern picked up by the detectors is smaller than the detectible limit of the system.

The quartz tubes used for these experiments had an inner diameter of 4 mm, this smaller diameter was used as it reduces the amount of material that the x-rays must pass through before reaching the detectors, increasing the count rate for the detectors, ensuring that high quality fits can be achieved. It was decided to keep the sample mass consistent between laboratory and in-situ studies as this keeps the ratio of moles of the reactants to moles of OCM the same, meaning that optimization of cycle duration did not need to be carried out by Mak (2017) need to be carried out again. This leads to a longer bed length when compared to the beds detailed in Section 2b as can be seen in Figure 2.4.


Figure 2.4: (Left) Photograph of a packed bed reactor for use in the vertical split furnace used for *in-situ* XRD studies. This packed bed is 2.2 g of $La_{0.6}Sr_{0.4}FeO_{3-\delta}$ and is 170 mm long. (Right) Vertical split furnace used for *in-situ* XRD studies in use at ID22 with the x-ray detectors.

The *in-situ* studies carried out in this campaign were focused on $La_{0.6}Sr_{0.4}FeO_{3-\delta}$ (LSF641) however for some experiments, yttrium oxide, sieved to 10 – 20 μm, was added to the bed in a mass ratio of 1:5. Yttrium oxide does not have diffraction peaks that overlap with those of LSF641 and remains inert at the temperatures and oxygen partial pressures involved, more details are available in Section 2f. Using the yttrium oxide's expansivity it is possible to determine the *in-situ* temperature of the sample rather than the furnace wall. Also should the ratio of the LSF641 phase and yttrium oxide phase deviate from the known ratio, it implies than one of the materials has become amorphous and lost its crystalline structure.

The recorded diffraction patterns were analysed using the Rietveld method (Young 1995) using TOPAS software (Coelho 2012). A Rietveld refinement consists of minimising the difference between a theoretical diffraction pattern and the measured results. The refinement system used was a least squares approach.

The theoretical diffraction pattern is based on different crystal structures present, as well as the temperature and stress on them. The angle at which the different peaks are recorded are defined by the size and symmetry of the unit cells present in the system, while their intensities are dependent on where the atoms interacting to give that peak are located inside the structure, giving the internal structure. The strain on the system as well as the size of the crystallites define the peak widths.

By starting with an estimate based on literature values, through knowing the expected crystalline material present in the sample, it is then possible to carry out a refinement varying the size of the unit cell and the stresses present in the cell to minimise the least squares difference between the theoretical pattern and the recorded one. Additionally the relative intensities of the peaks associated with different phases for the quantity of theses expected phases to be determined. This refinement technique also gives a measure of error for the fit which can be used to determine if other crystalline phases not predicted are present. For each of these phases the unit cell parameters that define the structure are determined along with the uncertainty.

### 2d In-situ neutron scattering

Neutron scattering differs from XRD because neutrons and x-rays have different scattering properties and provide complementary information. X-rays interact primarily with the electron cloud surrounding the atoms, so interact more strongly with the atoms with larger

atomic numbers and therefore more electrons, for LSF641 this is the lanthanum and strontium, while the neutrons interactions are more complex as they interact directly with the nucleus of the atoms. This means that each isotope of an element would interact differently. For LSF641 the oxygen interacts strongly when compared to the metal ions, this means that as well as determining the size of the unit cell in the sample the quantity of oxygen is also obtainable to a reasonable level of certainty. This is carried out during the refinement process by varying the crystal structure based on the presence of an oxygen to determine the optimal fit.

*In-situ* neutron elastic scattering was carried out on the High Resolution Powder Diffractometer (HRPD) at the ISIS neutron and muon source. The neutrons used are produced by the bombardment of a tungsten target with high energy $H_2$ ions. The produced neutrons are then pass through a moderator, slowing them. The neutrons then travel down a 96 m supermirror neutron guide, this long primary flight path allows for one of the highest-resolutions possible on neutron powder diffractometers in the world. The wavelength of the neutrons is controlled using 'time of flight' by opening the shutter a set length of time after the target is hit and closing shortly after that only neutrons that travelled the 96m in the correct length of time, thereby defining their speed and energy, make it to the sample.

The neutrons then pass through the sample environment and are scattered. The scattered neutrons are then detected by the three banks of detectors. These three banks are the backscattering, $90^o$ bank and low angle bank. The backscattering and $90^o$ banks use ZnS scintillator fibre coupled to photomultiplier tubes and the low angle bank uses $^3$He gas tubes. These banks mean that scattering pattern of the material can be fully captured decreasing uncertainty in the shape of the curves. These different detectors convert neutron fluxes into currents. $^3$He gas tubes detects neutrons by adsorbing thermal neutrons producing $^1$H and $^3$H ions while the ZnS scintillator fibre produces tritium ions and an alpha particle when neutron adsorption occurs.

HRPD was used for this campaign due to its high resolution, the highest in the world as of 2009 (Ibbserson 2009). This high resolution allows for the very small changes in the unit cell parameter to be determined with a high degree of certainty, while also obtaining its oxygen occupancy straight from the refinement.

The flow system used consists of a manifold connecting the different gasses used to control oxygen partial pressure of the sample environment. Each mass flow controller is paired with an on/off valve that is used to ensure that when the mass flow controller is shut no flow enters the system

Five different gas environments at atmospheric pressure were used to vary the equivalent oxygen partial pressure the sample was exposed to, a pure Ar feed was also used to purge the whole system. These gasses were 5±0.025% oxygen, 5±0.025% $CO_2$ with 0.05±0.00025% CO, 5±0.025% $CO_2$ with 0.5±0.0025% CO, 2.5±0.0125% $CO_2$ with 2.5±0.0125% CO and 0.5±0.0025% $CO_2$ with 5±0.025% CO, with the balance being Ar in all cases (These gases were supplied by BOC). $CO_2$ and CO buffer gasses were used both because these gasses are expected to be produced by a working chemical looping reactor and because the reduction of LSF641 by CO or the oxidation by $CO_2$ is almost heat neutral between these buffer gasses. The consequence of this is that in a given buffer gas the oxygen content of the sample remains constant over a large temperature range, which can be exploited to determine the thermal expansivity whilst the oxygen vacancy remains constant.

In each case, the inlet gas was supplied from the bottom of the sample environment with a flowrate of 70 ml/min at 293 K and 1 bar. The outlet gas conditions were recorded and measured using the mass spectrometer set up detailed in Section 2a, this was used to define when the system had reached equilibrium conditions. Equilibrium conditions were defined for when the gradient of the gas analysis was zero and the values were the same as the feed gas.

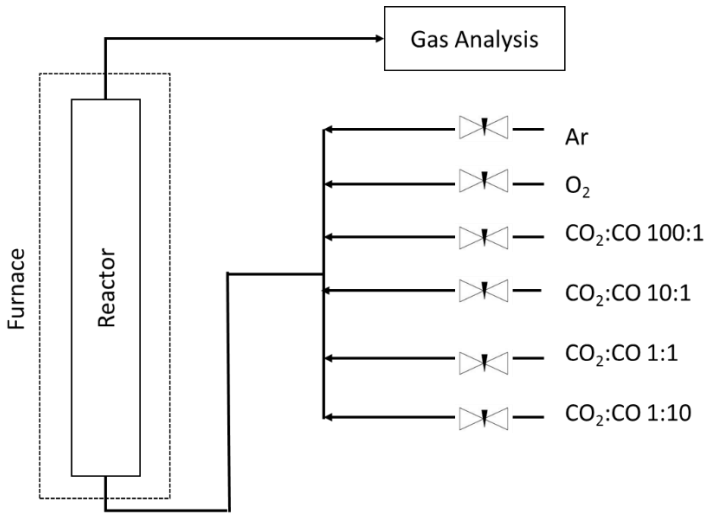


Figure 2.5: Flow diagram of the *in-situ* neutron elastic scattering reactor. Flow is not continuous and the type of gas introduction to the reactor is governed by the mass flow controllers and needle valves. Flow direction in the reactor is always top down. Flow rate is set at 70 ml/min (+/- 0.5 ml/min).

The total mass of sample studied was 2.96 g of LSF641 and the sample had particle sizes in the range 80-160 µm. The sample was placed inside a specialist 10 mm inner diameter double quartz tube cell with a sintered quartz plate to support the sample. The sample sat on the quartz plate and formed a 30 mm tall bed.

The sample environment was plumbed into the flows system and placed inside a vacuum furnace. The furnace internals are held under vacuum to minimise neutron interactions that are not related to the sample being studied. The furnace used was a Risø furnace with a vanadium element with maximum temperature of 1273 K allows for the sample. The sample was studied over a temperature range of 973 K and 1173 K in each of the five gas environments. The temperature was controlled using two K-type thermocouples, one inside the cell 10 mm above the sample and the other is in-between the double walled quartz tube.

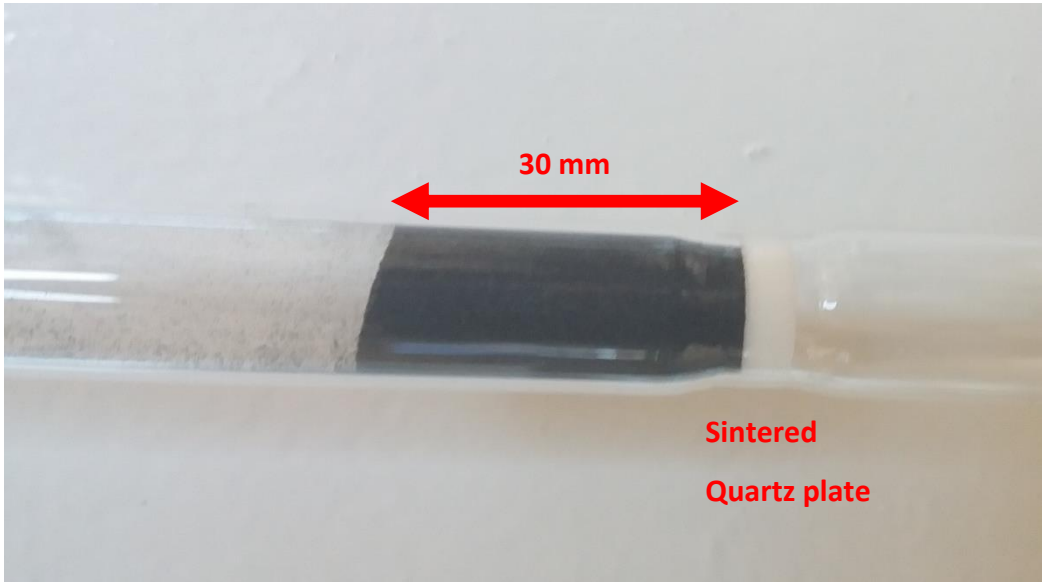


Figure 2.6: Photograph of the sample environment used for *in-situ* elastic scattering of neutrons studies. This packed bed is 2.96 g of $La_{0.6}Sr_{0.4}FeO_{3-\delta}$ and is 30 mm long.

Two different types of experiment were undertaken using this set up, the main type was carried out when the system had reached equilibrium conditions both chemically and thermally. Once this had been achieved the interaction between the neutrons and the sample was recorded until the total current produced by the detectors was 20 µA, this was repeated until 5 such files had been produced before changing either the temperature or the gas environment. The other type of experiment was carried out while the system was reaching equilibrium with the diffraction pattern being recorded in set 5 minute intervals continuously until the system had once again reached equilibrium. For both of these experiments the 'time of flight' for the neutrons was 10-110 ms, this was used to optimise the data collection in the range of interest from both the 90° and backscattering detectors.

The recorded diffraction patterns were then analysed using the Rietveld method (Young 1995) using TOPAS software (Coelho 2012). This gives the same advantages as detailed in Section 2c as well as allowing for the oxygen content of the material to be calculated.

### 2e Material Synthesis

Single phase LSF641 was synthesised via the Pechini sol-gel method using stoichiometric ratios of Fe $(NO_3)_3$ $(H_2O)_9$ (>99.95% Sigma Aldrich 216828), La $(NO_3)_3$ $(H_2O)_6$ (>99.99% Sigma Aldrich 61520), and Sr $(NO_3)_2$ (>99.995% Sigma Aldrich 243426) mixed with citric acid (>99.5% Sigma Aldrich 791725) and ethylene glycol (>99.8% Sigma Aldrich 324558) in molar ratios to the total cations present of 1:1 and 1.2:1 respectively. Deionized $H_2O$ is then added in a mass ratio of 4.5:1 to the mixture to produce a homogeneous solution which was

subsequently dried at 373 K for 48 hours. The resulting precursor was lightly crushed and placed in a covered alumina high form crucible (700 mL) and calcined to 1323 K at 1 K/min and held for 18 hours. The resulting powder underwent controlled cooling at 1 K/min to room temperature. The composition of the sample was then analysed using the experimental set up detailed in Section 2c. This can be seen in Figure 2.7.

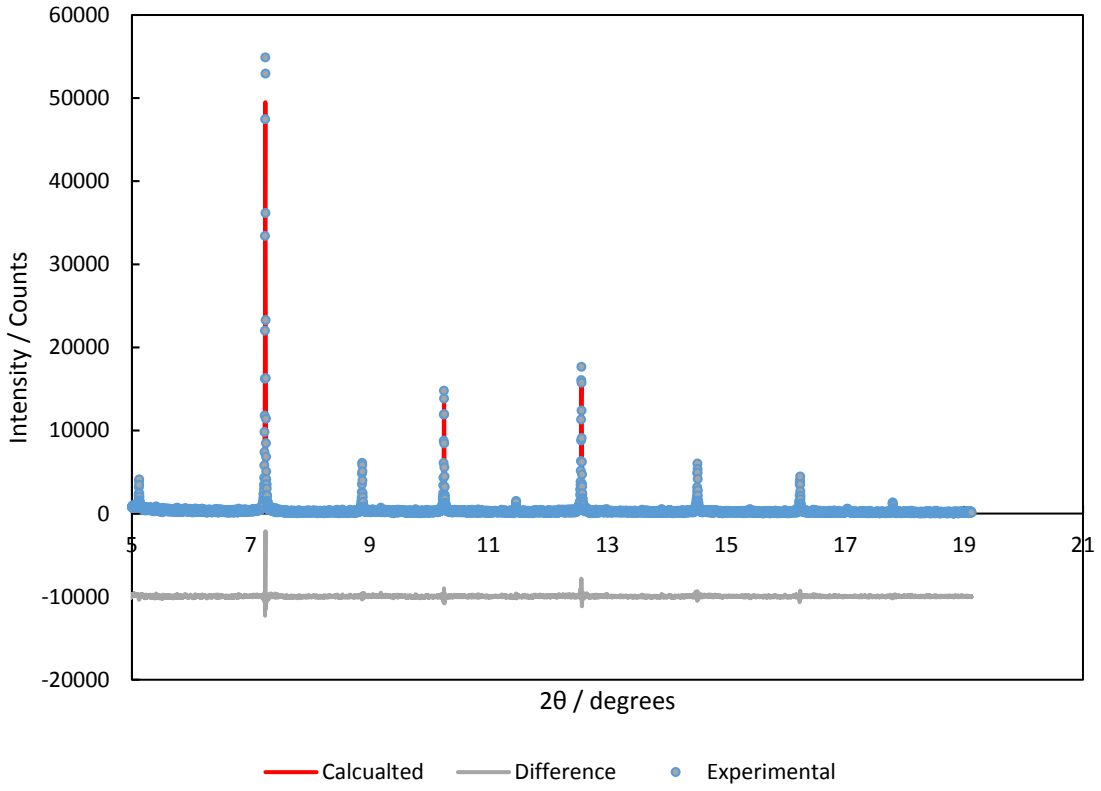


Figure 2.7: (Top) X-ray diffraction patterns of synthesised material at room temperature after synthesis in air, the data was collected using the experimental set up detailed Section 2c. The refinement carried out found the value of $a_{hex}$ to be 5.5 Å and $c_{hex}$to be 13.5 Å. (Bottom) Difference between X-ray diffraction scan and expected peaks shapes from the Rietveld refinement of synthesised material at room temperature after synthesis in air.

### 2f. Thermogravimetric Analysis

Thermogravimetric analysis was carried out using a Rubotherm dyntwo THERM unit with Brooks mass flow controllers. Two experiments were carried out using this equipment.

The first of these was carried out to confirm the thermodynamics of LSF641 in the temperature and $pO_2$ ranges detailed in the literature (Mizusaki et al 1985, Søgaard et al 2007, Kuhn et al 2011 and for comparison to those recorded as part of the neutron scattering experiments. Full discussion and results can be seen in Chapter 3The sample consisted of 0.25 g of LSF641 sieved to 80–160 µm and placed in the cradle. The sample was

exposed to 8.8x10$^{-3}$ mol/min of 5±0.025 mol% oxygen in Ar (BOC) and heated at 1 K/min then held at 973 K, 1013 K, 1053 K, 1093 K, 1133 K, and 1173 K. To ensure that the sample had reached equilibrium conditions the sample was held until the mass change was less than 5x10$^{-5}$ g/min. The sample mass change was recorded between each of these temperatures, this was then equated to the variation in oxygen content $\Delta\delta$ by Equation 2f.1.

$$\Delta\delta = \frac{M_s \cdot \Delta m}{M_o \cdot m} \qquad \text{2f.1}$$

With $M_s$ the molar mass of the sample, $M_o$ the molar mass of oxygen and m the sample mass. The gas buoyancy effect on the sample was negligible when compared with the mass changes resulting from oxygen release so was omitted from the calculations.

The second experiment was to ensure that yttrium oxide remains unreactive when exposed to the reducing gases and the temperatures that occur in chemical looping $H_2$ production, so that it can be used as an *in-situ* temperature gauge for XRD experiments. This experiment consisted of 0.53 g of yttrium oxide sieved to 10 – 20 µm. This sample was heated at 20 K / min in Ar until it reached 1093 K when it was exposed to 8.8E-3 mol/min of 5±0.025 mol% CO in Ar (BOC) for 1.5 hours. The sample mass change was recorded over this period and any mass change observed was expected to be due to a combination of carbon deposition or reduction on the material. No increase in mass greater than the uncertainty variation in measurement from the machine was found. The material is an adequate choice for *in-situ* temperature measurement during XRD experiments.

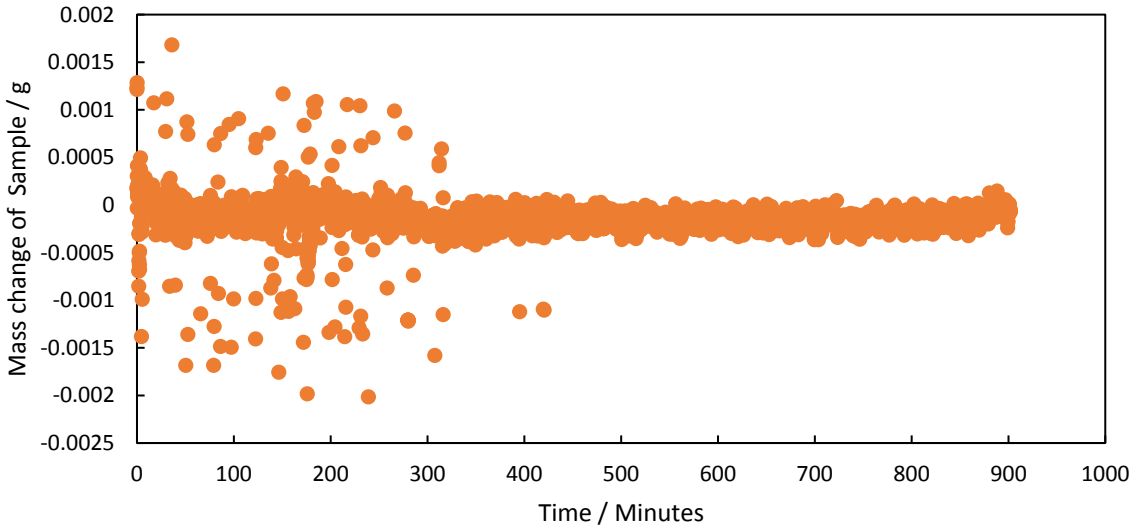


Figure 2.8: Mass change of 0.53 g of yttrium oxide during a 5±0.025 mol% CO in Ar. The noise in that data is much larger than any trend that can be seen over the 15 hours. The first five hours have a larger scatter as they were recorded during the day when larger number busses and cars driving past the laboratory can affect the mass measurement.

# Chapter 3: Thermodynamic studies of $La_{0.6}Sr_{0.4}FeO_{3-\delta}$

The strontium doped lanthanum ferrite $La_{0.6}Sr_{0.4}FeO_{3-\delta}$ (LSF641) was selected as the oxygen carrier of choice for study using *operando* x-ray diffraction (XRD). It is a non-stoichiometric material which offers a variety of advantages for packed bed chemical looping $H_2$ production.

The aims of this chapter are two fold; to show how the thermodynamics of suitable non-stoichiometric material increase reactor conversions and to show that the non-stoichiometry of LSF641 fulfils these criteria to ensure that the material is capable of achieving these high conversions.

## 3a Thermodynamic advantages of using a non-stoichiometric material

Metcalfe et al (2019) showed that a packed bed chemical looping system achieves higher conversions of $H_2O$ and CO than a conventional water-gas shift reactor when operated using a non-stoichiometric oxygen carrier. Metcalfe et al (2019) show that using a chemical looping reactor, where the product streams are not mixed, means that it is possible to achieve these conversions without requiring energy intensive separation processes.

This section concentrates on the chemical looping water-gas shift reaction using CO as the reducing agent. This makes it possible determine how a packed bed chemical looping reactor can be used to circumvent the thermodynamic limitations of a conventional reactor due to the relative simplicity of overall reaction, Equation 3a.1. The underlying principles would still govern chemical looping reactors regardless of the different oxidising or reducing agents involved.

$$H_2O + CO \rightleftharpoons H_2 + CO_2 \qquad \text{3a.1}$$

The base case that any improvements must be compared to would be that of a conventional reactor. These operate by mixing the reactants, $H_2O$ and CO, then co-feeding them into the reactor. Assuming that the kinetics are fast enough, these reactants would then undergo reaction until equilibrium is achieved. As these systems are normally operating below 10 bar it can be assumed that the products, reactants and any inert carrier gasses behave as ideal gasses. Which means that if equilibrium is achieved the partial pressure of the outlet gases would be described by, (Demirel and Azcan 2012, Finlayson 2012, Yeo 2017)

$$\frac{1}{K_{WGS}}\left(\frac{p_{CO_2}}{p_{CO}}\right)_{outlet} = \left(\frac{p_{H_2O}}{p_{H_2}}\right)_{outlet} \quad \text{3a.2}$$

where $K_{WGS}$ is the water-gas shift equilibrium constant and *p* is the partial pressure of the gas components.

At an operating temperature of 1093 K the water-gas shift equilibrium constant becomes unity (Callaghan 2006). This results, if a feed made up of equal parts CO and $H_2O$ without $CO_2$ or $H_2$ was fed to the reactor, in a 50% conversion of both CO and $H_2O$. That is to say that the outlet would contain a 1:1:1:1 ratio of $CO_2$:CO:$H_2O$:$H_2$. This means that, at this temperature, it is easier to compare a conventional reactor with a chemical looping reactor as it is easier to quantify the effect of the increase in CO and $H_2O$ conversions.

Any improvement on these conversions without using expensive separation steps, carrying out temperature changes or changing the ratio of the reactant's individual flowrates would indicate that the thermodynamic limitations of a conventional reactor has been circumvented. It is worth noting that as Reaction 3a.2 is equimolar with equal number of moles of gas on both sides of the reaction changing the pressure would not improve conversions while the system reaches its thermodynamic limit.

Throughout this chapter the thermodynamics of the reactor system are compared to that of heat exchange to highlight how the changes to reactor design circumvent the limitations of a conventional reactor. In such a comparison temperature can be thought of as equivalent to oxidising potential and energy as oxygen capacity. An equivalent system to a conventional reactor is a co-current heat exchanger, with both feeds entering at the same location then over the length of the reactor exchanging heat until both are at the same temperature.

*3a.i Single phase change materials*

The simplest chemical looping system would use an oxygen carrier that would only be able to be in one of two phases, i.e. a metal/metal-oxide system. In such a system the reduction and oxidation half cycles would involve the following reactions.

$MO + CO \rightleftharpoons M + CO_2$ Reduction 3a.3

$H_2O + M \rightleftharpoons H_2 + MO$ Oxidation 3a.4

Here M represents a metal and MO that metal's oxide.

The $CO_2$ acts as a reducing agent, changing the MO into a metallic form as it is oxidised to $CO_2$, then the feed is changed to that of $H_2O$ which then acts as an oxidising agent, returning the M back to its oxide form, MO, while being converted to $H_2$.

The equilibrium gas composition which would leave the reactor is defined by the M/MO system. During reduction the metal and metal oxide must coexist while reduction proceeds, and if the gas phase is at equilibrium conditions, the ratio of $CO_2$:CO must be one that is in equilibrium with the phase transition. This means that at the phase transition the ratio of $CO_2$:CO is set by the equilibrium relationship of Reaction 3a.3.

$$\left(\frac{p_{CO_2}}{p_{CO}}\right)_{PT} = K_{3a.3}\frac{[MO]}{[M]} = K_{3a.3} \qquad \text{3a.5}$$

Where $[MO]$ and $[M]$ are the thermodynamic activities of the metal oxide and metal, PT denotes the value associated with the phase change and $K_{3a.3}$ is the equilibrium constant for Reaction 3a.3.

The thermodynamic activities of stoichiometric solids is unity, resulting in the ratio of $CO_2$:CO in equilibrium with the phase change remaining constant for a given temperature. This then leads to the outlet gas composition depending on this ratio when equilibrium conditions dominate the gas-solid interactions. This gives the outlet composition of the reactor during the reduction half cycles as,

$$\left(\frac{p_{CO_2}}{p_{CO}}\right)_{outlet} = \left(\frac{p_{CO_2}}{p_{CO}}\right)_{PT} = K_{3a.3} \qquad \text{3a.6}$$

Carryout out the same analysis for the oxidation half cycle leads to,

$$\left(\frac{p_{H_2O}}{p_{H_2}}\right)_{outlet} = \left(\frac{p_{H_2O}}{p_{H_2}}\right)_{PT} = \frac{1}{K_{3a.4}} \qquad \text{3a.7}$$

with $K_{3a.4}$ being the equilibrium constant of 3a.4

If the outlet gas for both the oxidation and reduction half cycles are in equilibria with the respective phase transition, then they must be in equilibrium with each other. It follows that the outlet compositions must also be in equilibrium with each other. This means that such a system would have the same thermodynamic limitation as the mixed reactor.

For the analogy of heat exchange there is an equivalent system using a theoretical gas-liquid system as the energy vector to exchange heat between two separate streams. The gas-liquid system would have an infinitesimally small heat capacity but a boiling point at a set

temperature (T K) when at a pressure of 1 bar. As the cold stream is heated using the enthalpy of condensing the saturated gas it would be heated to T K but could not be heated further as the energy vector of the gas/liquid system has no more potential to donate energy to the stream even if the vector's temperature was decreased further. The inverse is true during the cooling of the hot stream which would also be limited to being cooled to T K. If T K is correctly chosen then such a system could achieve the same temperature change as the co-fed heat exchanger detailed earlier, but if the temperature of the phase change is not optimal then this system would underperform compared to a conventional reactor.

It would appear that selecting a material with a phase change at a ratio that favoured the oxidation half cycle, one with a $H_2O$:$H_2$ or $CO_2$:CO ratio in equilibrium with the phase change being smaller than 1:1, would increase the amount of $H_2$ produced. Such a methodology would not increase $H_2$ production or conversion if the system was to be operated with symmetrical cycles. Under such a sytem by the end of the oxidation half cycle the material had returned to the same state as before the preceding cycle.

To illustrate this, imagine a material with a phase transition associated with a low ratio of $H_2O$:$H_2$, 1:4. Assuming that the operating temperature is 1093 K such that the water-gas shift equilibrium is unity and that the feeds contain negligible quantities of the product gasses for the purposes of calculating the reactant conversions, which shall be assumed from here on. The more reducing nature of the phase transition will result in high conversions of $H_2O$ into $H_2$ resulting in the outlet gas compositions being given by:

$$\left(\frac{p_{H_2O}}{p_{H_2}}\right)_{outlet} = \frac{1}{4} \qquad \text{3a.8}$$

Which is a conversion of 80% of the feed $H_2O$ into $H_2$. The problem arises in the conversion of CO to $CO_2$ during the reduction half cycle where:

$$\left(\frac{p_{CO_2}}{p_{CO}}\right)_{outlet} = \frac{1}{4} \qquad \text{3a.9}$$

Which is a conversion of only 20% of the fed CO into $CO_2$.

This would increase $H_2$ production above that of a mixed reactor, however when an oxygen balance is carried out on the oxygen carrier material (OCM), it becomes clear that the amount of O taken in by the OCM during oxidation half cycle must equal the amount of O removed during the reduction half cycle.

To achieve the conversions above only 1 in 5 moles of CO fed to the reactor remove oxygen from OCM while 4 in 5 moles of $H_2O$ donate oxygen to the OCM. This means that for the conversion above to be realised then 4 times more CO would have to be fed to the reactor to satisfy the oxygen balance, requiring more CO to be fed to the reactor when compared $H_2O$ and most of that CO would pass through the reactor without reacting. This would increase the operational costs and not allowing for symmetrical cycles. Symmetrical cycles allow for simpler plant control and operation schemes and allows for continuous production using only two reactors, if this was to be achieved using asymmetrical cycling more than two rectors would be required.

The optimal case for a reactor is when both outlet streams are in equilibrium with the OCM and neither the $H_2O$ nor CO conversion is limited by the oxygen balance. This would maximise the product of the two conversions.

*3a.ii Multiple phase change materials*

However, when a more complicated system is used, where multiple phase changes exist, it becomes possible to overcome this limitation. For example: a metal/metal-oxide system that undergoes two phase changes, an M/MO and an MO/$MO_2$ transition. This allows for the design of a system that uses the former phase transition (M/MO) to produce a low $H_2O/H_2$ ratio and the latter (MO/$MO_2$) to produce a high $CO_2$/CO ratio. This system would need to undergo reverse flow such that an axial composition profile can be developed. Such a system can be seen in Figure 3.1. The axial composition profile can be seen to be present in both the oxidation and reduction stages. The left hand side, where the CO feed enters, remains metallic while the right hand side, where the $H_2O$ feed enters, remains fully oxidised. Such a composition profile results in the CO feed passing over the reduced M phase before passing across the MO phase and being partially oxidised then exiting in equilibrium with the $MO_2$ phase. In contrast the $H_2O$ feed would flow in the opposite direction, with the feed entering over the $MO_2$ then passing over the MO phase and being partially reduced as it come into contact with the MO phase, then being converted to a low ratio of $H_2O$:$H_2$ as it comes into contact with the M phase and leaves the reactor.

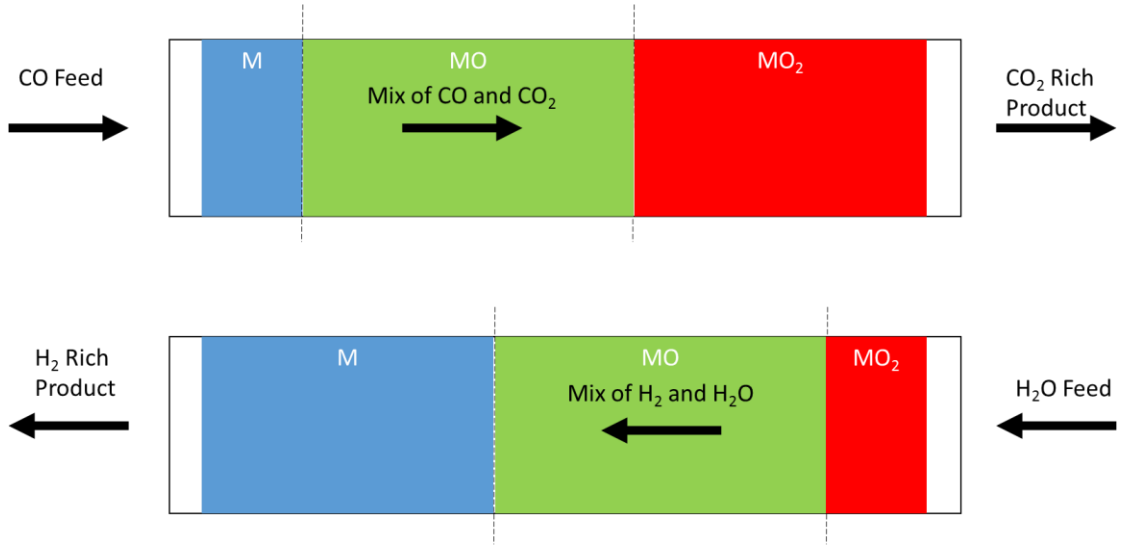


Figure 3.1: Inlet and outlet of a reverse feed chemical looping reactor making use of a 2 phase change OCM. As the system undergoes reaction the location in the reactor of the transitions between the different metallic phases will move, during reduction these locations will move to the right and under oxidation they would return to the left. While the material is operating cyclically high conversions can be obtained as long as the locations of the phase transitions do not reach the outlet of the reactor.

The conversion of such a system would be dependent on the gas ratios associated with the phase changes. An example case would be the transition at the more reduced conditions, M/MO, being at

$$\left(\frac{p_{H_2O}}{p_{H_2}}\right)_{PT,red} = \left(\frac{p_{CO_2}}{p_{CO}}\right)_{PT,red} = \frac{1}{4} \qquad 3a.10$$

while the transition at the more oxidised conditions, MO/$MO_2$ being

$$\left(\frac{p_{H_2O}}{p_{H_2}}\right)_{PT,ox} = \left(\frac{p_{CO_2}}{p_{CO}}\right)_{PT,ox} = 4 \qquad 3a.11$$

It can be seen that if the gas leaving the reactor is always in equilibrium with the optimal phase transition, then the outlet compositions for the oxidising half cycle would be 80% $H_2$ and 20% $H_2O$ while the outlet composition leaving the reduction half cycle would be 80% $CO_2$ and 20% CO. Which would equate to conversions of 80% for both half reactions, considerably higher than the 50% limitation imposed in a conventional reactor. This does not suffer from the same issue that a one phase change system has due to the oxygen balance as long as the equilibrium of the two phase changes are reciprocals of each other. Both half cycles exchange the same amount of oxygen with the OCM.

Returning to the analogy of heat exchange, with temperature being paralleled to oxidising potential and energy being equivalent to oxygen capacity. Adding an additional phase

change to the OCM, is equivalent to utilising an additional phase change to the heat exchange system, utilising the liquid/solid phase change in addition to the gas/liquid. If the liquid/solid phase change occurred at 273 K, it would then be possible to cool the hot stream further. If the system was operated counter currently the hot stream would come into contact with the gas phase, where it would be unable to exchange heat, meaning that it would keep the same temperature, it would then come into contact with the saturated liquid, which would be capable of exchanging heat, boiling the liquid and cooling the stream to 373 K. The stream would then come into contact with the solid phase, which could once again exchange heat, further cooling the product stream to 273 K as the solid melts. The cold stream would then undergo the opposite effect, passing first the solid with which it is unable to interact, then the liquid with which it starts to react, increasing its temperature to 273 K as it freezes the liquid. Before finally reaching the gas and being heated to 373 K as it condenses the gas.

In this system it becomes clear that for such a chemical reactor the maximum achievable conversion, assume an ideal material with optimal phase changes would be limited by the nature of the feed gasses. Until now it has been assumed that the feed gasses are pure but in reality a $H_2O$ feed would also have small quantities of $H_2$ present and a CO feed would have small quantities of $CO_2$. To maximise conversion the oxidising potential of the phase changes should match the potential of the feeds. If phase change required a gas ratio either more reducing than the CO rich feed or more oxidising than the $H_2O$ rich feed then the phase change would be unable to occur inside the reactor as the feeds would not be capable of reducing or oxidising the material into the new phase.

$$\left(\frac{p_{H_2O}}{p_{H_2}}\right)_{inlet} = \left(\frac{p_{H_2O}}{p_{H_2}}\right)_{PT\,,ox} = \left(\frac{p_{CO_2}}{p_{CO}}\right)_{PT\,,ox} \qquad \text{3a.12}$$

$$\left(\frac{p_{CO_2}}{p_{CO}}\right)_{inlet} = \left(\frac{p_{CO_2}}{p_{CO}}\right)_{PT\,,red} = \left(\frac{p_{H_2O}}{p_{H_2}}\right)_{PT\ red} \qquad \text{3a.13}$$

The outlet compositions of each feed would then also be dictated by these phase changes giving,

$$\left(\frac{p_{CO_2}}{p_{CO}}\right)_{oulet} = \left(\frac{p_{CO_2}}{p_{CO}}\right)_{PT\,,ox} = \left(\frac{p_{H_2O}}{p_{H_2}}\right)_{PT\,,ox} = \left(\frac{p_{H_2O}}{p_{H_2}}\right)_{inlet} \qquad \text{3a.14}$$

$$\left(\frac{p_{H_2O}}{p_{H_2}}\right)_{oulet} = \left(\frac{p_{H_2O}}{p_{H_2}}\right)_{PT,ox} = \left(\frac{p_{CO_2}}{p_{CO}}\right)_{PT,ox} = \left(\frac{p_{CO_2}}{p_{CO}}\right)_{inlet} \quad \text{3a.15}$$

It can be seen that the $CO_2$:CO and $H_2O$:$H_2$ ratios in the product streams are then limited only by solid equilibrium opposite end which has been selected to be equal to the inlet ratio of the other feed stream allowing for very high conversions to be achieved. Applying an oxygen balance to these equations shows that average conversions of both the reducing and oxidising streams must be equal, when using symmetrical cycling. This means that the conversions of both half cycles would be limited to the worse of the two conversions that can be calculated using Equations 3a.14 and 3a.15.

It is therefore theoretically possible, using suitably pure gas feeds, to achieve arbitrarily high conversions when using an OCM that has at least two phase transitions at the appropriate oxidising and reducing potentials. The complication with such a system is the difficulty of finding a "perfect" OCM for each reaction. Furthermore should the conditions inside the reactor deviate from the prescribed conditions, either a small change in feed conditions or a change in the temperature of the reactor, the system would cease to operate optimally reducing the conversions. If the inlet purity of the system drops below the first phase change, or the changing temperature of the reactor changes the $pO_2$ of the phase change beyond the inlet purity then the phase transition would no longer occur in the reactor converting the material into either a single phase change material or removing the capability for phase change at all. This could lead to the conversion of such a reactor dropping below that of a conventional reactor, or even in extreme cases down to zero.

*3a.iii Non-stoichiometric materials*

Building on the potential of a multiple phase change material to theoretically overcome the limitations of a conventional reactor, the next step would be to select a material capable of remaining flexible to changing inlet conditions and external temperature effects change the $pO_2$ of the phase changes in the system. Non-stoichiometric oxides can be used to this effect. Non-stoichiometric oxides have the property that they accommodate a continuously variable amount of oxygen according to the oxygen chemical potential that they are in equilibrium with. This continuous variability can be thought of as being effectively the same as having an infinite number of phase transitions, each with a small change in oxidation state at arbitrarily small differences in oxidising potential.

Within the analogy of heat exchange such a material would be equivalent to using a solid with a high heat capacity, but which did not undergo any phase changes, to exchange the heat between the two streams. When the energy vector comes into contact with the hot stream it is capable of heating up to the point where it is at the same temperature as the stream. The metal then comes into contact with the cold stream, which if operated counter currently and assuming a thermodynamically ideal system, is then heated up to the temperature the metal started at, which is the temperature of the hot stream. This would lead to the metal being the temperature of the cold stream when it then subsequently meets the hot stream again, cooling that hot stream to the temperature of the cold stream. It is clear that such a system would be resilient to changes in the temperature of the hot and cold streams, always exchanging energy between them and giving outlet temperatures for each stream equivalent to the inlet temperature of the other.

When comparing to the analogy of heat exchange, a system comparable to a counter current heat exchanger would be a better option, like a membrane reactor. However for the temperatures required in the water-gas shift, organic membranes would struggle to operate and ceramic membranes are brittle and prone to cracking. As the duration of each feed decreases or the total heat capacity of the reactor increases the chemical looping system detailed here approaches the same limitation as a counter current heat exchanger. This means that a chemical looping system is the best option to achieve these aims. For the chemical system this indicates that for the chemical looping water-gas shift reactor the reactor should have as a large an oxygen capacity as possible, as opposed to heat capacity, or very short feed durations. As longer feeds can simplifying plant operation and minimise wear on parts required to change flows it is therefore necessary to increase the oxygen capacity of the system.

The ideal non-stoichiometric material for such a purpose would remain non-stoichiometric in the full range of equivalent oxygen partial pressures present in the reactor. That is no ratio of $H_2O$:$H_2$ that could be present in the reactor that should cause the material to undergo a phase change. It is also important that no ratio of $H_2O$:$H_2$ causes the material to deactivate. The material would ideally have a large capacity for oxygen per mole of OCM in the expected range of $pO_2$'s to reduce the capital cost of the reactor and the total mass of OCM that requires purchasing.

### 3b Defect chemistry model of LSF641

Understanding if LSF641 is an adequate choice for use in a chemical looping $H_2$ production, requires knowledge of the materials non-stoichiometry and the oxidising potential of the gas phases in equilibrium with it.

The interaction between the oxygen partial pressure of the gas environment in equilibrium with LSF641 and its oxygen content, that is to say its degree of non-stoichiometry is commonly, in the literature, understood through the use of defect chemistry models. The defect models are described using the Kröger-Vink notation, where the superscript denotes the electronic charge, • describes one positive charge, $x$ denotes a null charge and ′ denotes one negative change, the subscript denotes the lattice site the species is on and *V* indicates a vacancy.

Studies by Kuhn et al (2011), Søgaard et al (2007) and Mizusaki et al (1991) have detailed the interactions between the different ions and defects present in the lattice. It was found that the thermodynamics were dominated by $[V_O^{\bullet\bullet}]$,$[Sr'_{La}]$, $[Fe'_{Fe}]$and $[Fe^{\bullet}_{Fe}]$. Where the effects of $[Fe'_{Fe}]$ or $[Fe^{\bullet}_{Fe}]$ dominate is dependent on the oxygen potential in the crystal. When under oxidising conditions $[Fe'_{Fe}]$ is found to dominate while under reducing conditions $[Fe^{\bullet}_{Fe}]$ has a larger impact. It was further shown that the La and Sr ions on the A site are only found in single valance states while the individual Fe ions are only present in 2+, 3+ or 4+.

For any strontium doped lanthanum ferrite only the oxygen in the system is in a state of non-stoichiometry. As the A site and B site ions are of a set stoichiometry and the A site ions do not change charge the following equations are defined.

$$[La^x_{La}] + [Sr'_{La}] = 1 \qquad \text{3b.1}$$

$$[Fe^x_{Fe}] + [Fe^{\bullet}_{Fe}] + [Fe'_{Fe}] = 1 \qquad \text{3b.2}$$

Where $[Fe^{\bullet}_{Fe}]$, $[Fe^x_{Fe}]$ and or $[Fe'_{Fe}]$ are the molar concentrations of Fe(IV), Fe(III) and Fe(II) respectively and $[La^x_{La}]$ and $[Sr'_{La}]$ are the molar concentrations of La(III) and Sr(II) which are known from the stoichiometry to be 0.6 and 0.4.

While the concentration of oxygen in the unit cell is not constant the maximum oxygen capacity per mole of material is capped at 3 mol, meaning that the sum of the oxygen present and the holes in the structure must obey:

$$[O^x_O] + [V_O^{\bullet\bullet}] = [O^x_O] + \delta = 3 \qquad \text{3b.3}$$

The reduction or oxidation of the material is adequately described by two equations. The first of these is the change in the valence of the Fe on the B site associated with the incorporation of oxygen into the material structure. This incorporation of the oxygen results in the destruction of an oxygen vacancy. This is shows in Equation 3b.4. The second reaction is the disproportionation of $Fe_{Fe}^{X}$ into $Fe_{Fe}^{\bullet}$ and $Fe_{Fe}^{\prime}$ which can be seen in Equation 3b.5.

$$\frac{1}{2}O_2 + V_O^{\bullet\bullet} + 2Fe_{Fe}^{X} \rightleftharpoons O_O^{x} + 2Fe_{Fe}^{\bullet} \quad \text{3b.4}$$

$$2Fe_{Fe}^{X} \rightleftharpoons Fe_{Fe}^{\bullet} + Fe_{Fe}^{\prime} \quad \text{3b.5}$$

These reactions therefore have the following equilibrium constants.

$$K_{ox} = \frac{[O_O^{x}][Fe_{Fe}^{\bullet}]^2}{pO_2^{0.5}[Fe_{Fe}^{X}]^2} \quad \text{3b.6}$$

$$K_{Fe} = \frac{[Fe_{Fe}^{\prime}][Fe_{Fe}^{\bullet}]}{[Fe_{Fe}^{X}]^2} \quad \text{3b.7}$$

Using Equations 3b.1 to 3b.7 it is then possible to eliminate all Fe terms and derive the following expression linking the oxygen non-stoichiometry of LSF641 to the equivalent oxygen partial pressure that it would be in equilibrium with.

$$\frac{\delta^{0.5}(2\delta + 0.6)}{(3-\delta)^{0.5}(2\delta - 04)} \times pO_2^{0.25} = \frac{K_{Fe}}{K_{ox}} \times \frac{(3-\delta)^{0.5}(1.4 - 2\delta)}{\delta^{0.5}(2\delta - 0.4)pO_2^{0.25}} - K_{ox}^{-0.5} \quad \text{3b.8}$$

Kuhn et al (2011), Søgaard et al (2007) and Mizusaki et al (1991) have experimentally found the enthalpy and entropy of reaction for Equations 3b.4 and 3b.5 allowing for the calculation of $K_{ox}$ and $K_{Fe}$ for a given temperature. The values obtained by each of them can be seen in table 3.1.

Table 3.1: Standard enthalpy and entropy change for the oxygen incorporation reaction and standard enthalpy and entropy change of the disproportionation reaction of $Fe_{Fe}^{X}$. Data by Kuhn et al (2011), Søgaard et al (2007) and Mizusaki et al (1991).

| | *Kuhn* et al *2011* | *Søgaard* et al *2007* | *Mizusaki* et al *1991* |
|---|---|---|---|
| $\Delta H_{ox}$ *(kJ mol$^{-1}$)* | -95.62±4.18 | -90.0±9.5 | 98.79±11.17 |
| $\Delta S_{ox}$ *(J mol$^{-1}$ K$^{-1}$)* | -54.27±4.43 | -57.7±7.6 | -65.39±8.26 |
| $\Delta H_{Fe}$ *(kJ mol$^{-1}$)* | 95.75±2.05 | 114.8±13.4 | 127.50±24.76 |
| $\Delta S_{Fe}$ *(J mol$^{-1}$ K$^{-1}$)* | -21.63±2.13 | -10.2±10.8 | -4.02±16.52 |

These data show good agreement with the values all agreeing to within a 95% confidence interval. Combining these values with Equation 3b.8 it is possible to predict the oxygen content of a sample of LSF641 at a given temperature and gas environment. For 1093 K the $\delta$ state of the material was plotted as a function of $pO_2$ using the thermodynamics extracted from Kuhn et al (2011), Søgaard et al (2007) and Mizusaki et al (1991)..

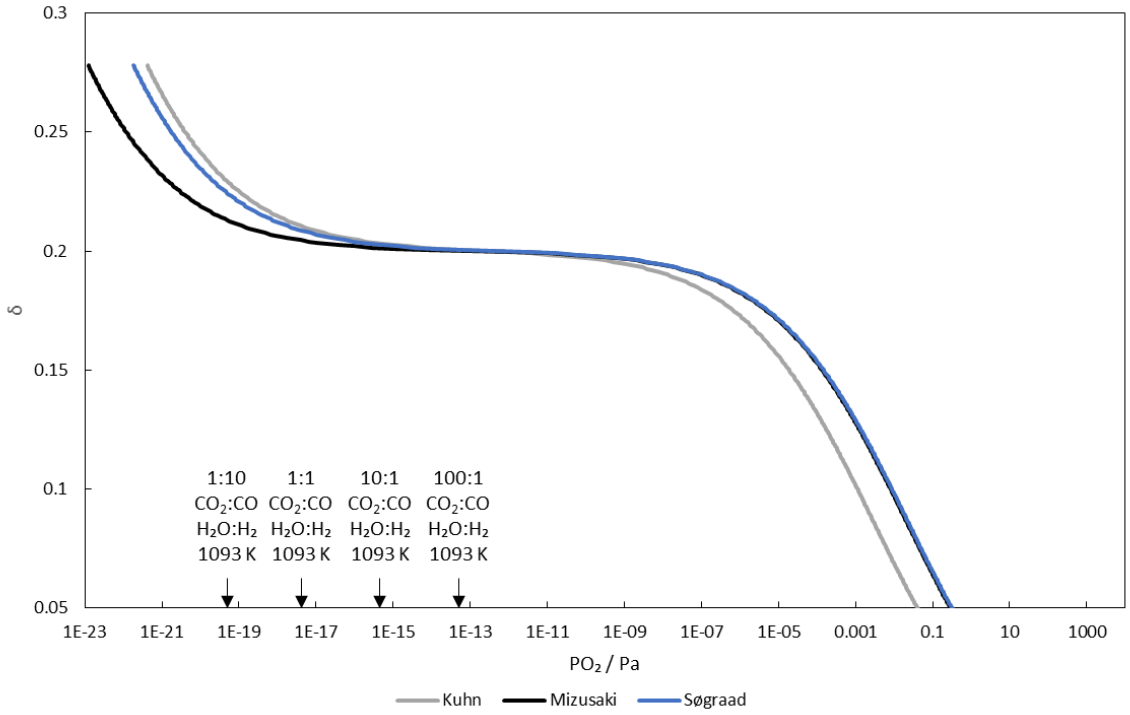


Figure 3.2: A plot of $\delta$ as a function of pO2 at 1093 K. With ratios of $CO_2$ to CO and $H_2O$ to $H_2$ that are expected to be present in the reactor. (Kuhn et al (2011), Søgaard et al (2007) and Mizusaki et al (1991) and Burgess (2018)).

In Figure 3.2 key ratios of $CO_2$ to CO and $H_2O$ to $H_2$ are marked. At 1093 K the Gibbs free energy of reaction of the water-gas shift reaction is 0 KJ/mol so at a set ratio, one of these pairs will be in equilibrium with the same set ratio of the other (Burgess 2018). The material theoretically remains variably non-stoichiometric in the range of interest at this temperature showing capability to be used to overcome the equilibrium limitations of a conventional water-gas shift reactor.

To ensure that the synthesised material behaves as expected from the literature the oxygen non-stoichiometry of LSF641 as a function of temperature in 5% oxygen (at atmospheric pressure) was investigated using three different methods: thermogravimetric analysis, Rietveld fit of occupancy parameters of *in situ* neutron diffraction patterns and oxygen balance calculated from the outlet gas composition measured in the neutron diffraction experiment. These results are shown in Figure 3.3 and compared to the values predicted

using Equation 3b.8 and the enthalpy and entropy of reaction reported by Kuhn et al (2011), Søgaard et al (2007) and Mizusaki et al (1991).

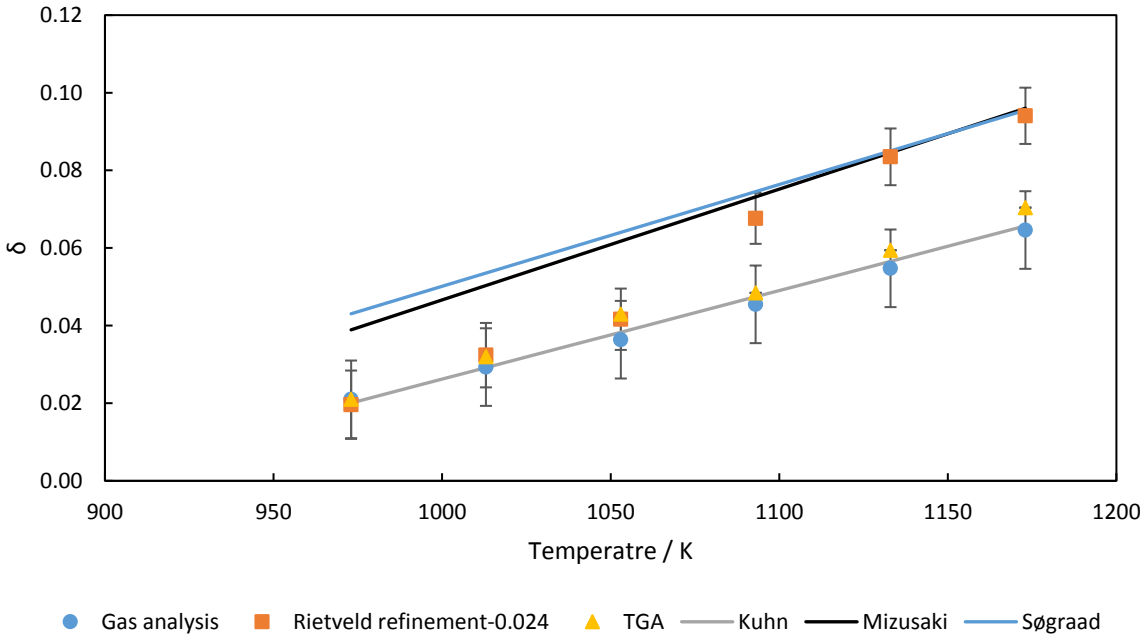


Figure 3.3: $\delta$ state of $La_{0.6}Sr_{0.4}FeO_{3-\delta}$ as a function of temperature in 5% oxygen calculated from the Rietveld refinement and outlet gas conditions, both with one standard deviation, compared to predicted values obtained from thermodynamics in the literature (Mizusaki et al 1985, Søgaard et al 2007, Kuhn et al 2011) and TGA results with one standard deviation being less than the size of the marker. The gas and chemical expansion methods are only capable of obtaining relative values so the results for 973 K is used as a reference.

The outlet gas analysis and TGA results only measure the change in oxygen content between two states. In order to compare these results, it was assumed that the oxygen vacancy content ($\delta$ in the molecular formula $La_{0.6}Sr_{0.4}FeO_{3-\delta}$) at 973 K was 0.021, the value derived from literature (Mizusaki et al 1985, Søgaard et al 2007, Kuhn et al 2011) under the same conditions.

It is worth noting that, with this assumption, the starting stoichiometry of oxygen in the material used in the TGA experiment was found to be 3.001 at room temperature, slightly higher than the expected value of 3.000 predicted by literature (Mizusaki et al 1985, Søgaard et al 2007, Kuhn et al 2011). As shown in Figure 3.2 the $\delta$ state of the material increases with increasing temperature, as the total amount of oxygen in the material decreases under a constant $pO_2$. This difference is larger than standard deviation in the measurement of the mass, which is of the order of $10^{-5}$.

An offset of 0.024 has been applied to the oxygen content data obtained through the Rietveld refinement Figures 3.3, and throughout the rest of this thesis, to account for an underestimation found in the Rietveld refinement. This offset was applied because the average value of the oxygen content for the fully oxidised sample was found it be 2.96 (standard uncertainties on individual values ~0.017 and the standard deviation was 0.024). Evidence from Kuhn et al (2011), Dann et al 1994 and Sogaard et al 2007 suggests that the true oxygen content under these conditions should be 3.0; that is that the $\delta$ value should be 0. The average corrected oxygen content for data collected between 868 and 1093 K was 2.76. Schmidt and Campbell (2001), who studied the crystal and magnetic structures of $Sr_2Fe_2O_5$, also found that Rietveld refinement of oxygen content from neutron diffraction experiments under predicted the expected oxygen content in these temperature ranges.

It can be seen that the values of $\delta$ determined from the TGA, gas analysis from the neutron diffraction and the predictions from based on the work of Kuhn *et al* (2011) are in good agreement. The results from Mizusaki et al (1985) and Søgaard et al (2007) over predict the absolute values from the TGA work, but as the gradient of the curves are consistent with the gas analysis from the neutron diffraction studies but have a constant offset. Additionally the refined oxygen occupancy yielded higher oxygen vacancies above 1100 K even after the offset discussed previously was applied, although the relative change in oxygen vacancy with temperature, away from the 1100 K transition, was similar to that obtained from other methods. This step increase does bring the results into line with the values predicted by Mizusaki et al (1985) and Søgaard et al (2007) but the step increase does not agree with the TGA work and the oxygen balance from the neutron diffraction gas analysis. Additionally the thermodynamic constants from Mizusaki et al (1985) and Søgaard et al (2007) were calculated for data above 1073 K so require extrapolation to this regime.

The discontinuity in the values of $\delta$ for the higher temperatures is most likely due to uncertainties in the fitting or the vibrations of the oxygen decreasing the interaction with the neutrons. It may also be due to the presence of disordered oxygen in the sample that fails to be quantified using purely crystallographic measures as in Oswald and Bruckner (2004).

The atomic displacement parameters found from the Rietveld refinement for the O ions were found to increase linearly with increased temperature in this regime. In the O-O-O direction the atomic displacement increases with temperature, starting at 0.018 $Å^2$ at 973 K then increasing to 0.021 $Å^2$ at 1173 K. The displacement in the direction of the Fe-O-Fe bond is more

complex with the value of $\delta$ have a greater effect. Increasing the temperature still increases the degree of displacement. The displacement is 0.061 $Å^2$ at 973 K then increasing to 0.071 $Å^2$ at 1173 K.

To confirm the thermodynamics in a lower range of $pO_2$ Figure 3.4 shows how the $\delta$ state of the material changes as a function of $pO_2$ for the $Fe^{3+}/Fe^{2+}$ transition at a set temperature of 1093 K. The values for the $\delta$ state are obtained using the Rietveld refinement. This was then compared to expected values based on the model values obtained from literature sources (Mizusaki et al 1985, Søgaard et al 2007 and Kuhn et al 2011) Additionally the outlet gas analysis of the system can show the change in $\delta$ state during the changes in gas analysis, through the assumption that Kuhn et al's (2011) thermodynamics of the system are correct for a $pO_2$ of 0.05 bar the expected and measured differences can be compared. The gas analysis and model results agree very well while the occupancy from the Rietveld refinements shows less agreement but for the values with a $\delta < 0.2$ they agree to within the uncertainty.

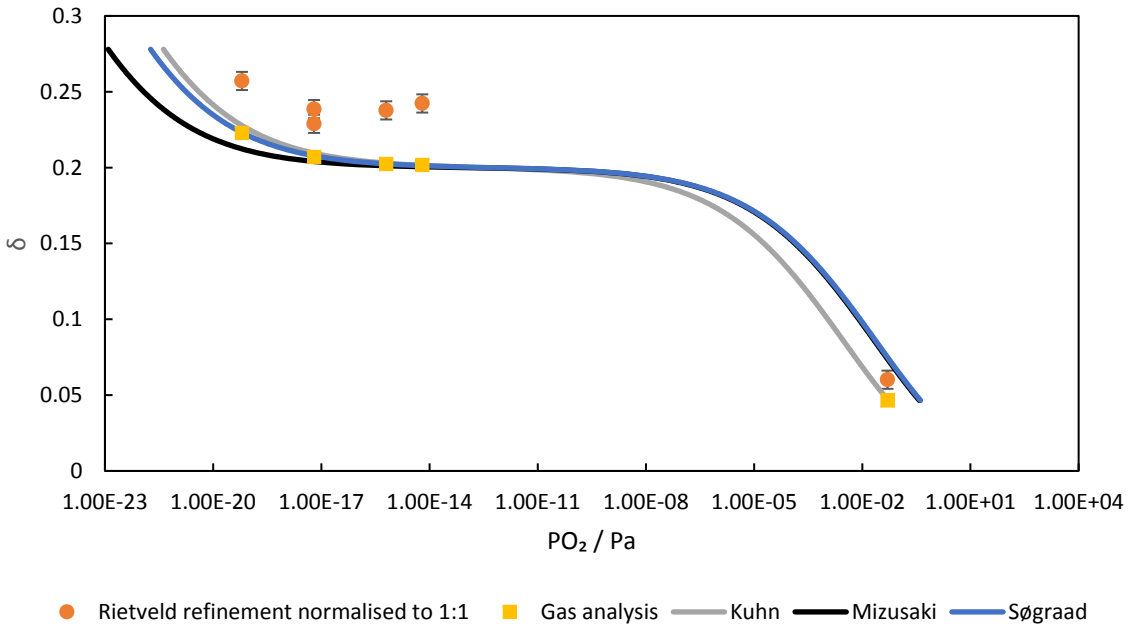


Figure 3.4: $\delta$ state of the material calculated using the Rietveld refinement from neutron diffraction data (with error bars showing one standard deviation) and the outlet gas conditions compared to predicted values obtained from thermodynamics from literature (Mizusaki et al 1985, Søgaard et al 2007, Kuhn et al 2011). The outlet gas composition method is only capable of obtaining relative values so the results for $5x10^{-2}$ Pa obtained using Kuhn et al (2011) is used as a reference, and both have error bars smaller than their markers. Values are for 1093 K and gas atmospheres of 1:10, 1:1, 10:1, 100:1 $CO_2$:CO ratios and 5% $O_2$ all in a balance of Ar at atmospheric pressure.

This shows that Kuhn et al (2011) extracted thermodynamic data can be used to accurately predict the $\delta$ state of the material used here and throughout this thesis based on the material's temperature and the $pO_2$ of the gas environment that is in equilibrium with it. This allows for the direct comparison between the $\delta$ state and the crystal structure. However both Mizusaki et al (1985) and Søgaard et al (2007) fail predict the changes seen due to the outlet gas results or the rietveld refinement meaning that for further analysis the thermodynamics detailed by Kuhn et al (2011) will be used.

### 3c Summary of Chapter 3

It has been shown that it is possible for a chemical looping reactor to achieve conversions higher than the thermodynamic limits of a conventional reactor. When a variably non-stoichiometric OCM is used and the reactor is operated under ideal conditions the outlet gas compositions of each half cycle is limited to the same $pO_2$ as the inlet gas compositions of the other half cycle.

The variable non-stoichiometry of LSF641 has been detailed and it has been shown that this material is suitable for the use in a chemical looping water-gas shift reactor capable of achieving higher conversions than a conventional water-gas shift reactor.

It has also been shown that of the available literature thermodynamics governing the behaviour of LSF641 the work by Kuhn et al (2011) best describes the material

# Chapter 4: Chemical and Thermal Expansivity of LSF641

LSF641 was selected as the OCM of interest for the chemical looping $H_2$ production using the WGS reaction undertaken in this thesis. An understanding of the material's properties is of vital importance in overcoming key challenges in its uses. One particular challenge is that the material must maintain integrity over prolonged operation. This requires phase segregation to be minimised, which is minimal if no phase transitions occur, since it can cause significant changes in the chemical and electrical activity of the material (Lein 2006).Additional as a non-stoichiometric material it is possible to relate its structure to it oxygen content if the temperature and the thermal and chemical expansivities are known. This would allow for the study of how the internals of a chemical looping reactor change as the reducing and oxidation half cycles occur. Also knowledge of how the material changes is important for plant design as if the material's increase in volume is larger than expected this can cause reactor vessels to rupture.

LSF641 has been shown to have a rhombohedral structure at low temperatures and as the temperature increases the material begins to transform into cubic structure, with the exact temperature of these transitions dependant on the $\delta$ state of the material. How this change transpires can be seen in Figure 4.1, with the iron sites tilting until the system is equivalent to a cubic unit cell. Literature has shown that the material is commonly in the cubic structure when at the temperatures and partial oxygen pressures ($pO_2$s) chosen as the basis for this research work. (Dann et al 1994)

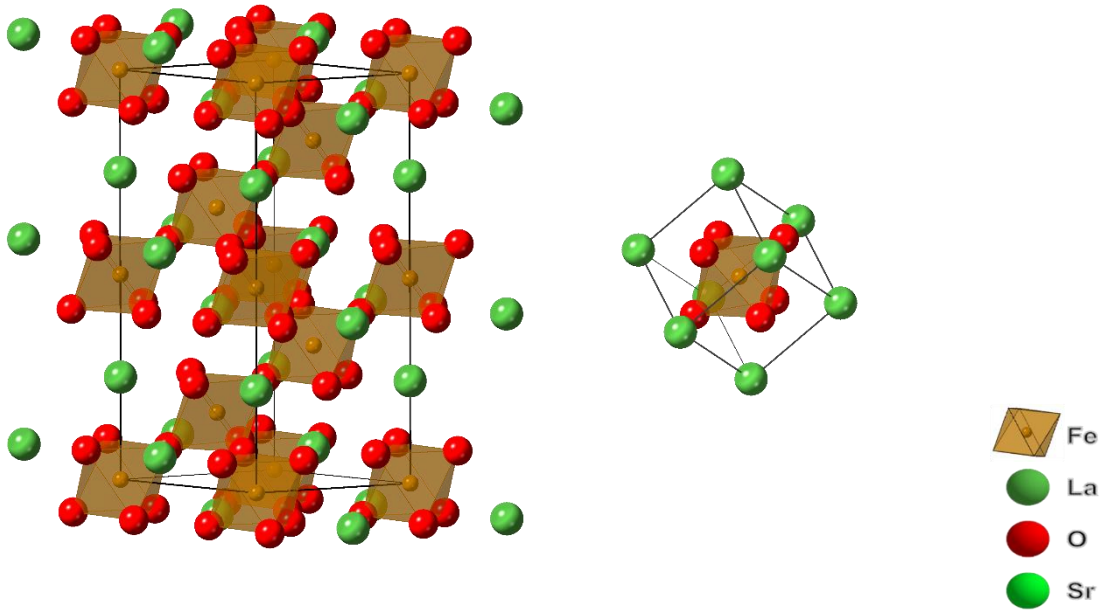


Figure 4.1: Crystal structure of LSF641, at 298 K (left) and 1098 K (right) in a 1:1 $CO_2$:CO buffer gas. The scale and orientation of the material is the same in both images to ease comparison between the two temperatures.

In addition to minimising phase segregation it is important that the expansion of the material under different oxygen chemical potentials is understood. Bishop et al (2014) reviewed the effect of structural changes to a material based on changing chemical conditions. They found that the expansivity of the material can have a direct effect on the elastic modulus of the material and its ionic and electronic conductivity confirming the importance of a complete knowledge of how this material's properties vary at different oxidising potentials. Additionally, large changes in the unit cell parameter due to chemical changes during operation can lead to decreased operational life time due to decreased mechanical integrity.

Thermal stresses also compromise the mechanical integrity of the material; these weaken oxygen carrier materials (Ryden et al 2008). Therefore, knowledge of the phase stability and the thermochemical expansion, under relevant operation conditions, underpins the appropriate design and implementation of functional chemical looping reactors.

LSF641 is well studied in the literature due to the many applications that it has shown promise for. These previous works have investigated the oxygen non-stoichiometry and the thermochemical expansion of this material at a variety of temperatures and partial pressures

of oxygen ($pO_2$) (Kuhn et al 2011, Mizuzaki et al 1985, Sogaard et al 2007). However, these studies concentrated on SOFC cathode applications so that the range of $pO_2$s investigated has been largely limited to ~ $10^{-7}$ bar. For chemical looping applications, the relevant $pO_2$ extends to ~$10^{-22}$ bar.

Of additional interest is the use of chemical and thermal expansivities to relate the unit cell parameter of LSF641 to the value of $\delta$. Bishop et al (2014) shows that the conversion of unit cell parameter to information about the chemical nature of a system is possible. This would allow for *operando* studies of the chemistry of a working reactor to be carried out if the unit cell parameter is measured.

The thermal and chemical expansivities of a material are defined by how the unit cell parameter changes as a function of temperature and the material's $\delta$ state. The relationship can be seen in Equations 4.1 and 4.2.

$$\alpha_{thermal} = \left.\frac{\partial a}{\partial T}\right|_{\delta} \quad 4.1$$

$$\alpha_{chemical} = \left.\frac{\partial a}{\partial \delta}\right|_{T} \quad 4.2$$

Where $a$ is the unit cell parameter, $T$ is the temperature, $\alpha_{thermal}$ is the thermal expansivity and $\alpha_{chemical}$ is the chemical expansivity.

For the range of pO2s previously studied (approximately between $10^{-5}$ to 1 bar), both the chemical and thermal expansivity were found to be independent of temperature and $\delta$ state (Kuhn et al 2011). However, extrapolating these results into regions of lower pO2s, well beyond the area of study is inadvisable. In particular, It is expected that due to the different Fe ions present in the lattice that the expansivities when $\delta$<0.2 (where $Fe^{4+} \rightarrow Fe^{3+}$ dominates) would be different from when $\delta$>0.2 (where $Fe^{3+} \rightarrow Fe^{2+}$ dominates) (Søgaard et al 2007).

Neutron diffraction experiments are ideally suited to explore the thermal and chemical expansivity of LSF641 as it allows for both the $\delta$ state of the material and the lattice parameter to be determined at the same time, through the Rietveld refinement of the diffraction pattern. Combining neutron diffractions studies with off gas analysis allows for confirmation of the expected $\delta$ state of the material. However, to collect statistically significant results high counts of interactions are required, which given the low fluxes

associated with the neutron sources require lengthy experiments. These longer experiments mean that *operando* studies cannot be carried out and that the nature of how the material changes as it undergoes changes in gas environment or temperature cannot be determined.

X-ray diffraction (XRD) experiments allow for more rapid data collection than that achievable using neutron sources due to the high flux of synchrotron radiation sources. This allows for the structure of the material to be determined as it undergoes changes in $\delta$ state and temperature. However, XRD cannot unambiguously measure $\delta$ but its change can be inferred from the change in the unit cell parameter and the knowledge of the chemical and thermal expansivity. This can further be confirmed with outlet gas analysis of the reactor. This means that this technique can be used to confirm the values obtained from neutron diffraction but relies more heavily on the outlet gas analysis and thermodynamic results to extract thermal and chemical expansivities. XRD also allows for *operando* studies where the internal structure and oxygen content of a working reactor are studied.

### 4a Chemical expansivity theory

To understand how the material behaves at higher $\delta$, knowledge of how the material changes as it undergoes chemical and thermal expansion is required. Whilst the factors contributing to the thermal expansion are similar for non-stoichiometric perovskites and stoichiometric solids, the oxygen non-stoichiometry also has effects on the lattice structure and size.

In the case of LSF641, the material remains a perovskite structure over a wide range of oxygen non-stoichiometry ($0<=\delta<=0.3$). In this window, any reduction or oxidation of the material only changes the amount of oxygen vacancy in the lattice and the oxidation number of the Fe ions while the oxidation number of O, La and Sr remains constant. This means that as the material is reduced or oxidised, the coordination and oxidation number of the Fe ions change and these twin effects affects the size of the Fe ions and hence the size of the unit cell of the perovskite structure.

Assuming that the ions remain in a high spin state throughout this reduction and that the material remains in a perovskite structure regardless as to the coordination of the Fe ions, it is possible to create simple analytical models to determine how the unit cell parameter varies with $\delta$.

The Fe ions in $La_{0.6}Sr_{0.4}FeO_{3-\delta}$ can undergo two changes in oxidation number while the material remains a perovskite (Kuhn et al 2011) $Fe^{4+}$ to $Fe^{3+}$ and $Fe^{3+}$ to $Fe^{2+}$. The Fe ions in the stoichiometric compound $La_{0.6}Sr_{0.4}FeO_3$ have an average oxidation number of +3.4, which may be considered as a mixture of 40% $Fe^{4+}$ and 60% $Fe^{3+}$ (Mizusaki et al 1984) both of which have an octahedral coordination. From a geometric perspective, it can be seen that as the material is reduced, $Fe^{4+}$ is converted to $Fe^{3+}$ first, accompanied with a reduction in the coordination number for the same amount of the $Fe^{3+}$ ions to form square pyramids with the neighbouring $O^{2-}$. The average coordination of the Fe ions must be equal to twice the number of $O^{2-}$ present, as each oxygen interacts with two Fe ions.

This means that as the value of $\delta$ increases from 0 to 0.2 the unit cell length of the perovskite structure is equal to its value in the stoichiometric state, $a_0$, plus an additional term accounting for the average change in the radius of Fe ions:

$$a = a_0 + 2\Delta r_{Fe_{VI}^{4+}\rightarrow Fe_{VI}^{3+}} \cdot y_{Fe_{VI}^{3+}} + 2\Delta r_{Fe_{VI}^{4+}\rightarrow Fe_{V}^{3+}} \cdot y_{Fe_{V}^{3+}} \quad \text{4a.1}$$

$$a = a_0 + 2\left(r_{Fe_{VI}^{3+}} - r_{Fe_{VI}^{4+}}\right) \cdot y_{Fe_{VI}^{3+}} + 2\left(r_{Fe_{V}^{3+}} - r_{Fe_{VI}^{4+}}\right) \cdot y_{Fe_{V}^{3+}} \quad \text{4a.2}$$

Here $a$ is the unit cell parameter, $a_0$ is the unit cell parameter at $\delta$=0, r is the radius of a Fe ion with a set oxidation number and coordination and x is the fraction of Fe ions in the given state.

The total proportion of iron ions changed is twice the number of oxygen atoms changed, as each oxygen removes 2 electrons with it.

$$y_{Fe_{VI}^{3+}} + y_{Fe_{V}^{3+}} = 2\delta \quad \text{4a.3}$$

$$a = a_0 + 2\Delta r_{Fe} = a_0 + 2y_{Fe_{VI}^{3+}} \cdot r_{Fe_{VI}^{3+}} + 2 \cdot \left(2\delta - y_{Fe_{VI}^{3+}}\right) \cdot r_{Fe_{V}^{3+}} - 4\delta \cdot r_{Fe_{VI}^{4+}} \quad \text{4a.4}$$

The total coordination of the iron ion present must equal the amount of oxygen coordinating with each molecule, but each oxygen coordinates with 2 iron atoms, so half the sum of the coordination numbers must be equal to the amount of oxygen present.

$$0.5\left(6 \cdot y_{Fe_{VI}^{3+}} + 5\left(2\delta - y_{Fe_{VI}^{3+}}\right) + 6 \cdot (1 - 2\delta)\right) = 3 - \delta \quad \text{4a.5}$$

$$y_{Fe_{VI}^{3+}} = 0 \quad \text{4a.6}$$

Combining Equation 4a.6 with 4a.4 gives

$$a = a_0 + 4 \cdot \delta\left(r_{Fe_{V}^{3+}} - r_{Fe_{VI}^{4+}}\right) \quad \text{4a.7}$$

This process becomes more complicated once $\delta$>0.2 where the $Fe^{3+}$ ions are reduced to $Fe^{2+}$. As more oxygen vacancies are created, Fe ions form a square planar coordination. This coupled with the 2+ ions forming either octahedral or square planar depending on the local conditions, gives 5 different coordinations available for a given Fe ion. Repeating the above set of calculations is more complex, Equation 4a.8 has five unknowns but there is still only the electron balance and the oxygen coordination to remove these unknowns. It is not possible to determine these without complete knowledge of the formation energies of each state to determine what configuration is most favourable but it is clear that the system does change after the $\delta$ state passes beyond 0.2. Indicating that to understand this regime and therefore a chemical looping system using LSF641 further work must be carried out.

$$a = a_0 + \Delta r_{Fe_{VI}^{4+}\rightarrow Fe_{VI}^{3+}} \cdot y_{Fe_{VI}^{3+}} + \Delta r_{Fe_{VI}^{4+}\rightarrow Fe_{V}^{3+}} \cdot y_{Fe_{V}^{3+}} + \Delta r_{Fe_{VI}^{4+}\rightarrow Fe_{IV}^{3+}} \cdot y_{Fe_{IV}^{3+}} \quad \text{4a.8}$$
$$+\Delta r_{Fe_{VI}^{4+}\rightarrow Fe_{VI}^{2+}} \cdot y_{Fe_{VI}^{2+}} + \Delta r_{Fe_{VI}^{4+}\rightarrow Fe_{V}^{2+}} \cdot y_{Fe_{V}^{2+}} + \Delta r_{Fe_{VI}^{4+}\rightarrow Fe_{IV}^{2+}} \cdot y_{Fe_{IV}^{2+}}$$

As the bond lengths and electrostatic forces change in the regime it is expected that the thermal effects will also change, as these forces govern how the kinetic energy of the atoms associated with the increased temperature are dissipated.

To determine how the chemical and thermal expansivity changes in this new regime *in-situ* neutron diffraction and X-ray diffraction experiments were carried out on LSF641.

## 4b Material characterisation

The material was tested to determine if it remained a single-phase perovskite and the nature of the unit cell at these temperatures and oxygen partial pressures. To achieve this the dimensions of the unit cell of the material was recorded at a variety of temperatures in a 1:1 $CO_2$:CO buffer gas, Figure 4.2. At low temperatures the material is rhombohedral but as the temperature increases the crystal structure changes, approaching a true cubic cell. A rhombohedral model ($R\bar{3}c$) was also used to fit some of the experimental data and results compared with the cubic model. For conversion between hexagonal and cubic unit cells the value of "$a_{cub}$" and "$c_{cub}$" are given in Equations 4b.1 and 4b.2. These are derivable from the interaction between the unit cells seen in Figure 4.1. Doing this allows for a more direct comparison between the values obtained based on a rhombohedral or cubic fitting parameter.

$$a_{cub} = \frac{a_{hex}}{\sqrt{2}} \quad \text{4b.1}$$

$$c_{cub} = \frac{c_{hex}}{\sqrt{12}} \qquad 4b.2$$

Where $a$ and $c$ are perpendicular directions in the unit cell of the cubic ($cub$) and hexagonal ($hex$) unit cells.

This change in structure was expected as at higher $pO_2$s Dann et al (1994) had similar findings. It was also observed as part of that study that with increased temperature the structure changed from rhombohedral to cubic. Once the temperature has reached 800 K the deviation from the cubic structure was minimal with less than 0.1% difference between the transformed rhombohedral cell dimensions. Once the temperature rose to 1000 K the crystal structure was better fit using a cubic rather than a rhombohedral structure.

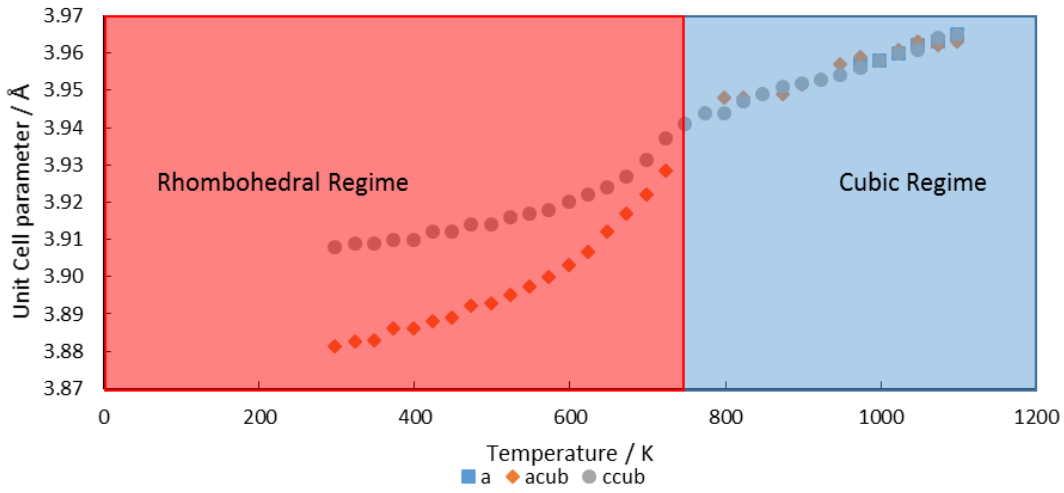


Figure 4.2: Unit cell parameter of LSF641in a 1:1 $CO_2$:CO feed as a function of temperature. In this figure "a" is the unit cell parameter of a cubic material and $a_{cub}$ and $c_{cub}$ are transformed values from the rhombohedral cell to compare with the cubic cell, as they transit the cell shape becomes cubic. It can be seen that at high temperatures the material starts to approximate a cubic material before becoming indistinguishable from one. The uncertainty in the unit cell parameter from the rietveld refinement is smaller than the symbols.

Another comparison between the cubic and rhombohedral unit cell parameter is the angle in the rhombohedral cell. This is given by Equation 4b.3 and as it tends towards 60° the rhombohedral cell becomes equivalent to a cubic cell. This can be seen in Figure 4.3 with the gradual increase in the internal angle of the rhombohedral cell until it jumps to a value of 60°

$$\theta = \cos^{-1}\frac{2{c_{hex}}^2 - 3{a_{hex}}^2}{2{c_{hex}}^2 + 6{a_{hex}}^2} \qquad 4b.3$$

Where $a$ and $c$ are perpendicular directions in the unit cell of the cubic ($cub$) and hexagonal ($hex$) unit cells. $\theta$ is the rhombohedral cells' internal angle.

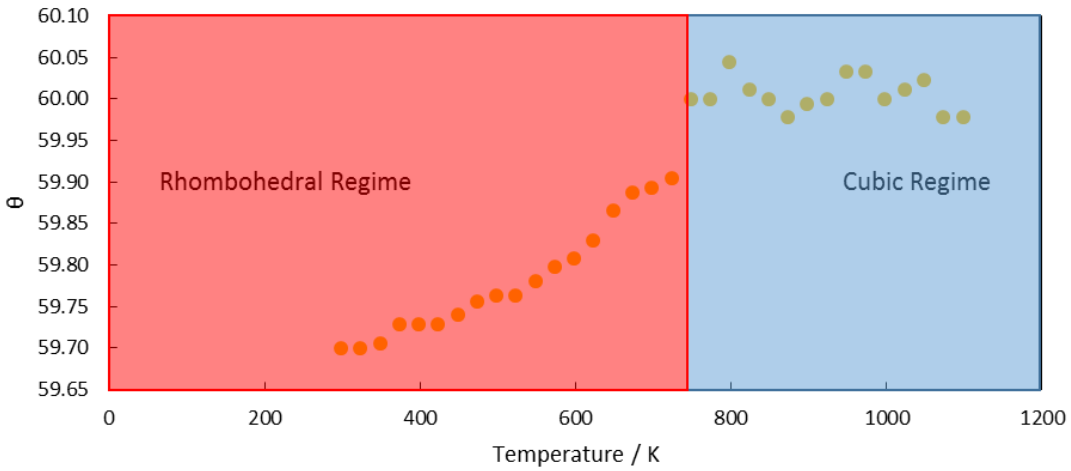


Figure 4.3: Calculated angle of the rhombohedral cell LSF641in a 1:1 $CO_2$:CO feed as a function of temperature. As this parameter becomes 60° the rhombohedral cell becomes equivalent to a cubic one. The uncertainty in its value based on the uncertainty in the rietveld refinement is less that the size of the markings.

### 4c Chemical and thermal expansivity for $\delta$<0.2

In order to determine the chemical and thermal expansivity of LSF641 with a $\delta$<0.2 a series of experiments was carried out using synchrotron *in-situ* XRD at a variety of $pO_2$s.

LSF641 was studied at 1%, 5% and 20% $O_2$ in Ar at a pressure of 1.1 bara in a temperature range of 932 K to 1050 K. When the unit cell parameter was plotted as a function of $\delta$ for the different temperatures studied it was found that the chemical expansivity was linear in this regime which was expected based on the calculations found in Section 4a. The extracted chemical expansivity was found to be 0.144±0.009 Å (using the thermodynamic model of Kuhn et al 2011 to obtain the values of $\delta$) and largely independent of temperature, as shown in Figure 4.4. This contrasts with a chemical expansivity of 0.0777 Å in the same temperature and $\delta$ range reported by Kuhn et al (2011). This difference could be linked to the different temperature measurement techniques used by Kuhn et al (2011) when compare to this work. Kuhn et al (2011) used a thermocouple to record the temperature of a Pt heater rather than an internal sample temperature technique. If the system was consistently at a lower temperature than expected then for a given $pO_2$ the $\delta$ in equilibrium with it would be different. With a lower temperature the changes is $\delta$ would be smaller than the recorded value giving a smaller expansivity.

The uncertainties in $\delta$ seen in Figure 4.4 were dominated by the uncertainty in the pressure reading which was ±0.1 bar, as the relationship between $\delta$ and $pO_2$ is non-linear, causing the error bars to be asymmetrical.

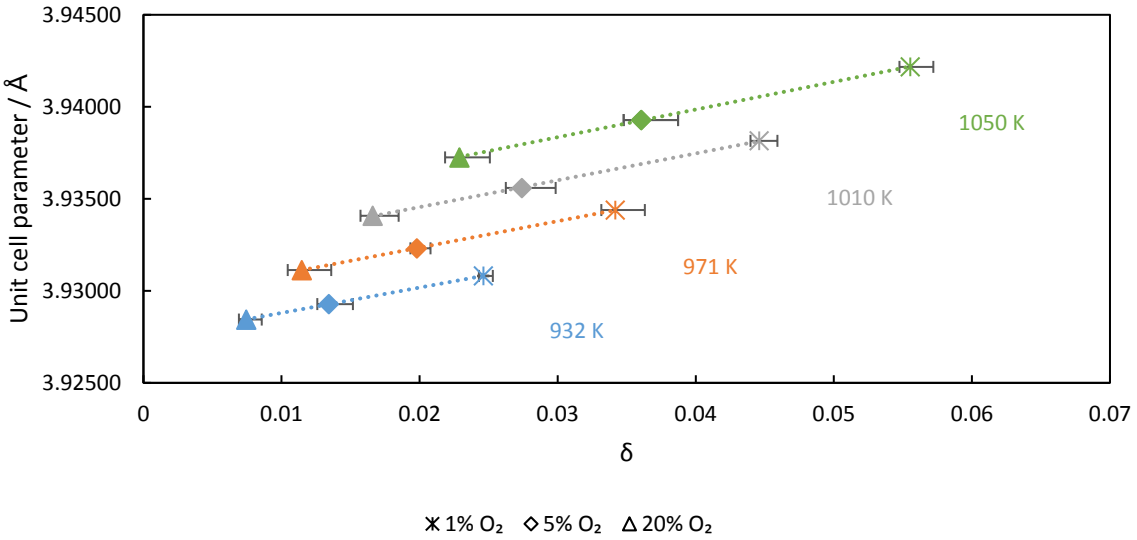


Figure 4.4: Plot of unit cell parameter as a function of predicted $\delta$ state based on the thermodynamics by Kuhn (2011) used in Figure 3.3, three different $pO_2$s were used to obtain a changing $\delta$ value. These were 1%, 5% and 20% $O_2$ in Ar at a total pressure of 1.1 bara. The data was collected at temperatures in the range of 932 to 1050 K. Unit cell parameter was calculated from Rietveld refinement of the XRD data. The uncertainty in the unit cell parameter is smaller than the marked points, the x direction uncertainty is dominated by the uncertainty in the pressure reading which was ±0.1 bar, as the relationship between $\delta$ and $pO_2$ is non-linear this causes the error bars to be asymmetrical.

In order to extract the thermal expansivity the effect of the change in $\delta$ as the temperature changes was removed to obtain a pure thermal expansivity plot, Figure 4.5. This was carried out by plotting the unit cell parameter for $\delta$=0 predicted by each line. This gave the pseudo-linear thermal expansivity to be 5.70±0.05 $\times 10^{-5}$ Å/K compared with 4.307 x$10^{-5}$ Å/K from literature (Kuhn et al 2011).

The chemical and thermal expansivities were found to be linear in this regime which is expected based on the calculations found in Section 4a.

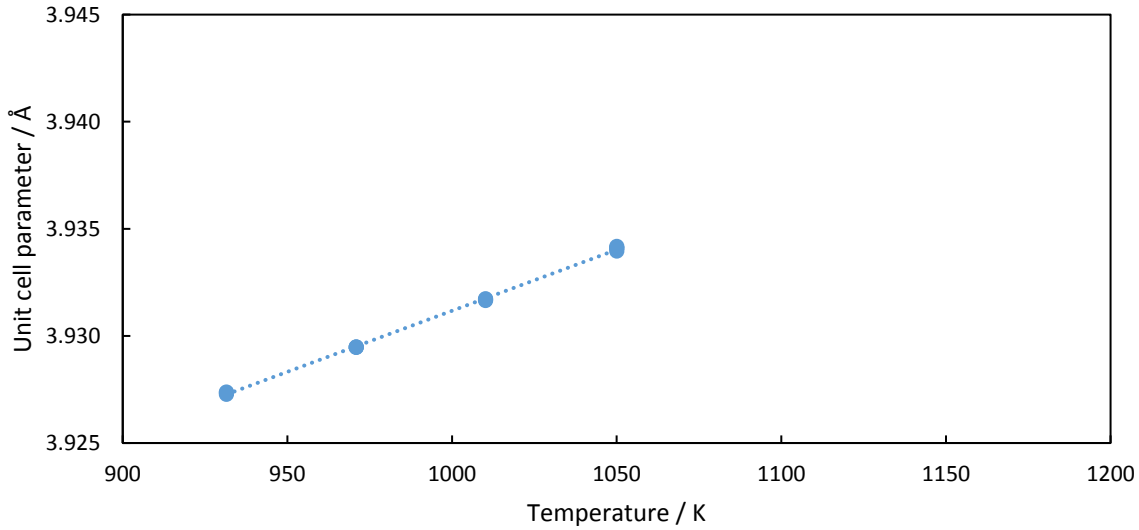


Figure 4.5 Plot of unit cell parameter with the effect of the change in delta removed as a function of temperature as obtained from the Rietveld refinement of the yttrium oxide. The data was collected at temperatures in the range of 932 to 1050 K. Unit cell parameter was calculated from Rietveld refinement of the XRD data. The uncertainty in each point was of the order of 0.00001 and the temperature uncertainty was smaller than the marked points.

The data collected using neutron diffraction in 5% $O_2$ was used to test the extracted values for chemical and thermal expansivity. This required the use of Equation 4c.1 and the extrapolation of the data up to a temperature of 1193 K.

$$a_{calculated} = a_{reference} + \alpha_{thermal}(T - T_{reference}) + \alpha_{chemical}(\delta - \delta_{reference}) \qquad 4c.1$$

Where $a_{calculated}$ is the calculated unit parameter, $a_{reference}$ is the unit cell parameter at a known temperature and $pO_2$, here the value at 1050 K and 5% $O_2$ at 1 bara was used, $T$ is the temperature, $T_{reference}$ was 1050 K, $\delta_{reference}$ was $\delta$ at 1050 K and 5% $O_2$ at 1 bara, $\alpha_{thermal}$ was the thermal expansivity and $\alpha_{chemical}$ is the chemical expansivity.

In Figure 4.6 the unit cell parameter obtained from the Rietveld refinement was plotted as a function of the temperature and compared with the expected value for each temperature, and its corresponding $\delta$. The expected unit cell parameter was calculated using the parameters extracted from Figure 4.4 and 4.5 and the $\delta$ was calculated using the thermodynamics from Kuhn et al (2011).

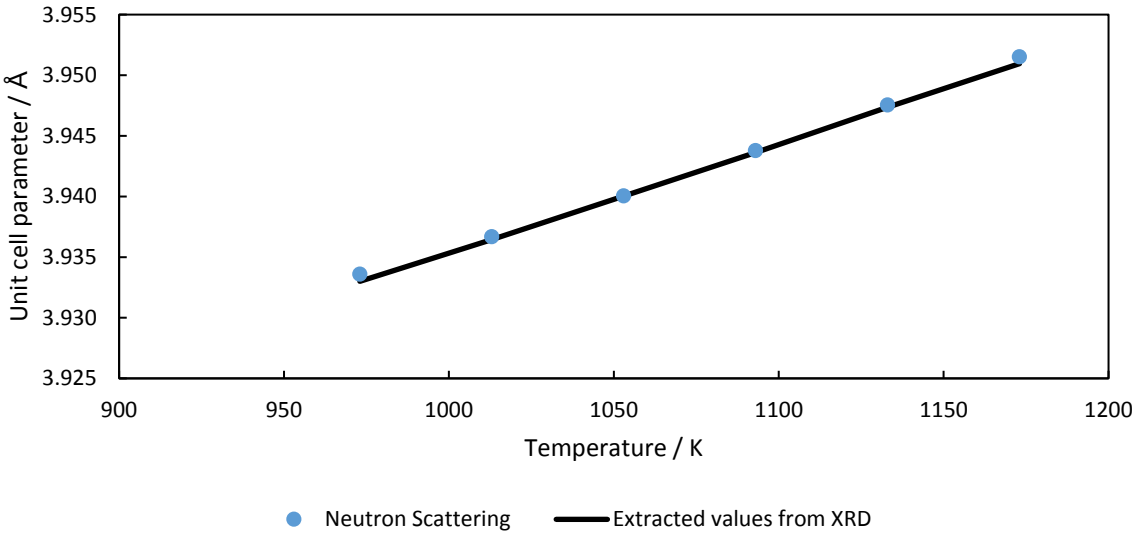


Figure 4.6: Unit cell parameter as a function of temperature at a $pO_2$ of 0.05 at 1.0 bara as calculated from values extracted from Figure 4.3 and as measured during the neutron diffraction experiment under 5% $O_2$ in Ar at atmospheric pressure; the error was less than the size of the markers.

For this short range of temperatures an assumption of a linear dependence between $\delta$ and temperature was applied to better compare Kuhn's (2011) results with those found in this work. The gradient from the neutron scattering results was $8.99 \times 10^{-5}$ Å/K, the predicted gradient based on the XRD results was $9.01 \times 10^{-5}$ Å/K while previous literature (Kuhn et al 2011) predicts $6.07 \times 10^{-5}$ Å/K when accounting for both the thermal expansion and the chemical expansion associated with that temperature change. The results here show good agreement to the data collected using other techniques but differ from those found in the literature. From this point onwards the experimentally determined expansivities will be used, due to their ability to more accurately predict the properties of the materials when compared to the values in the literature.

### 4d Chemical and thermal expansivity for $\delta$>0.2

As detailed in the section on chemical expansivity theory (Section 4a) it was expected that for $\delta > 0.2$ the chemical and thermal expansivities would change due to the addition of $Fe^{2+}$ to the lattice at these increased $\delta$ states. In order to obtain $\delta > 0.2$ for $La_{0.6}Sr_{0.4}FeO_{3-\delta}$ low $pO_2$'s (typically $<10^{-10}$ bar) are required. Redox buffers such as $CO_2$/CO couples or $H_2O/H_2$ couples would be required to maintain such low $pO_2$s as using oxygen environments requires very low leak rates. In this work, the $CO_2$/CO redox couples have been used because the reaction

$$\varepsilon CO + La_{0.6}Sr_{0.4}FeO_{3-\delta} \rightarrow \varepsilon CO_2 + La_{0.6}Sr_{0.4}FeO_{3-\delta-\varepsilon} \qquad 4d.1$$

is almost heat neutral for $\delta$> 0.2 (Kuhn et al 2011, Burgess 2018). As a result, the value of $\delta$ remains constant over a large temperature range for a given $CO_2$/CO buffer and the thermal expansivity can be measured without accounting for the influence of the chemical expansivity.

In order to obtain a $\delta$ state of 0.2, the point at which the material is expected to change expansivity regime, a $CO_2$:CO buffer of $10^{10}$:1 would be necessary so studies were carried out at more reducing atmospheres than this as to achieve this ratio very small quantities of CO, of the order of parts per billion, would need to be added to a $CO_2$ rich stream. With mole fractions this low the uncertainty is large enough that ensuring the correct ratio is present problematical.

The thermal expansion of $La_{0.6}Sr_{0.4}FeO_{3-\delta}$ measured under various $CO_2$/CO buffers are shown in Figure 4.7. Similar to when $\delta$<0.2, the thermal expansivity of $La_{0.6}Sr_{0.4}FeO_{3-\delta}$ did not vary with $\delta$. The thermal expansivity found for each individual buffer gas are found in Table 4.1. The differences between these values are small enough for the data set as whole to be used for determining the thermal expansivity. The thermal expansivity was found to be 6.18±0.08x$10^{-5}$ Å/K, larger than the value of 5.72±0.04x$10^{-5}$ Å/K found for a $\delta$<0.2.

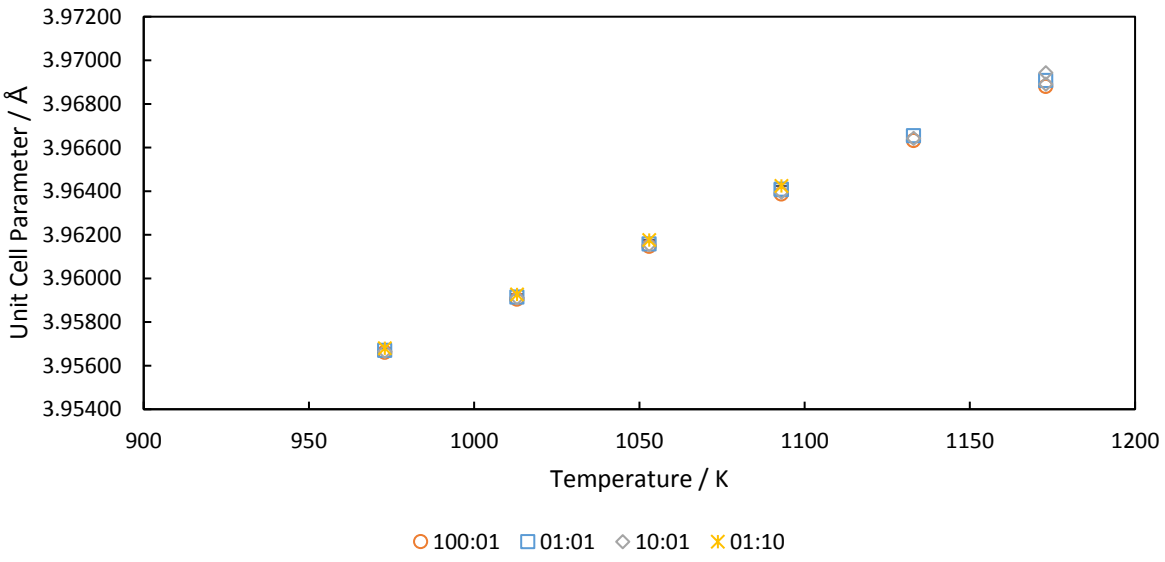


Figure 4.7: Unit cell parameter of the LSF641 as a function of temperature determined using a thermocouple situated 10 mm above the sample. The unit cell parameter was calculated from the Rietveld refinement of the neutron scattering experiments in 100:1, 10:1, 1:1 and 1:10 $CO_2$:CO buffer gasses. The uncertainty in each point was less than the data points.

Table 4.1: Thermal expansivity of LSF641 from neutron diffraction in 100:1, 10:1, 1:1 and 1:10 $CO_2$:CO buffer gasses

| $CO_2$:CO BUFFER GAS | THERMAL EXPANSIVITY (Å/K) | STANRDARD UNCERTAINTY(Å/K) |
|---|---|---|
| **100:1** | $6.20\times10^{-5}$ | $0.02\times10^{-5}$ |
| **10:1** | $6.18\times10^{-5}$ | $0.01\times10^{-5}$ |
| **1:1** | $6.25\times10^{-5}$ | $0.10\times10^{-5}$ |
| **1:10** | $6.08\times10^{-5}$ | $0.04\times10^{-5}$ |

Experiments were also carried out to determine the chemical expansivity in this regime. Figure 4.8 shows how the $\delta$ state of the material changes as a function of $pO_2$ for the $Fe^{3+}/Fe^{2+}$ transition at a set temperature of 1093 K. The values for the $\delta$ state are obtained using the Rietveld refinement and the outlet gas analysis of the system. These are then compared to expected values based on the model values obtained from Kuhn et al (2011). The gas analysis and model results agree well, while the occupancy from the Rietveld refinements shows less agreement but for the values with a delta state less than 0.2 they agree to within the uncertainty analysis.

The $\delta$ state of the material, for a given $CO_2$:CO ratio, was taken and plotted as a function of unit cell parameter, shown in Figure 4.8. For $\delta$ values above 0.2 the chemical expansion becomes nonlinear, decreasing for increasing values of $\delta$. Additionally, the expansivity is consistently smaller than the values for $\delta$<0.2

For $\delta$ > 0.2 an estimate of the linear chemical expansion was found to 0.0148±0.0037 Å per change in $\delta$ compared with 0.144±0.009 Å per change in $\delta$ for $\delta$<0.2.

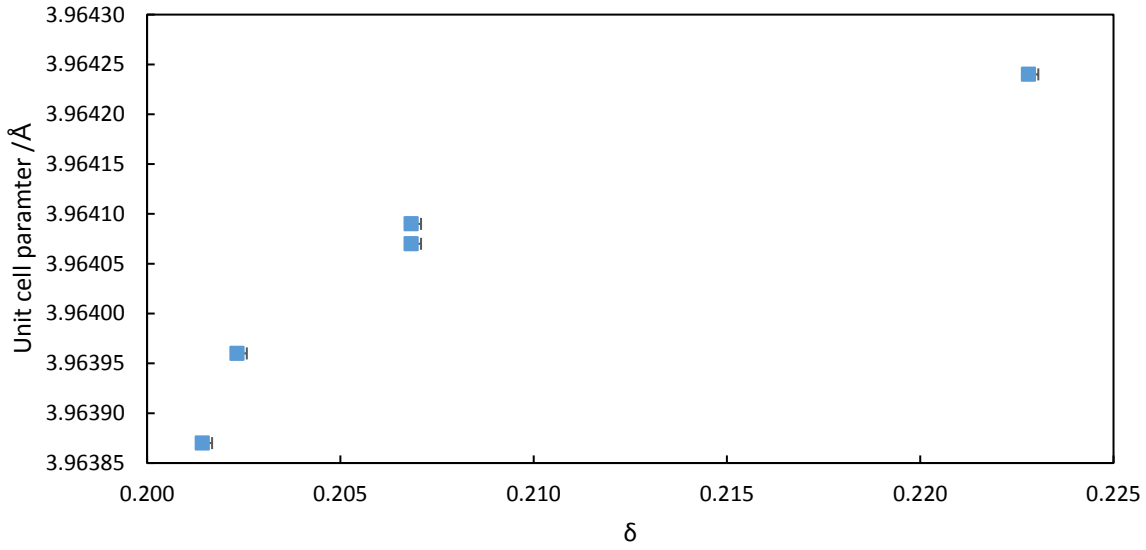


Figure 4.8: Unit cell parameter calculated by *in-situ* neutron scattering as a function of expected $\delta$ state of the material for a given $pO_2$. This was carried out at 1093 K using gas atmospheres of 1:10, 1:1, 10:1 and 100:1 $CO_2$:CO ratios in a balance of Ar at 1 bara. Showing that the chemical expansivity is non-linear for this section and decreases for increasing $\delta$ state. With error bars of one standard deviation which are smaller than the markers in the y direction.

Comparing the shape of the curve on either side of the $\delta$=0.2 transition, in Figure 4.9, it is clear that the material properties change as the material transitions between the two regimes. The unit cell parameter no longer has a linear dependence on the $\delta$ state of the material.

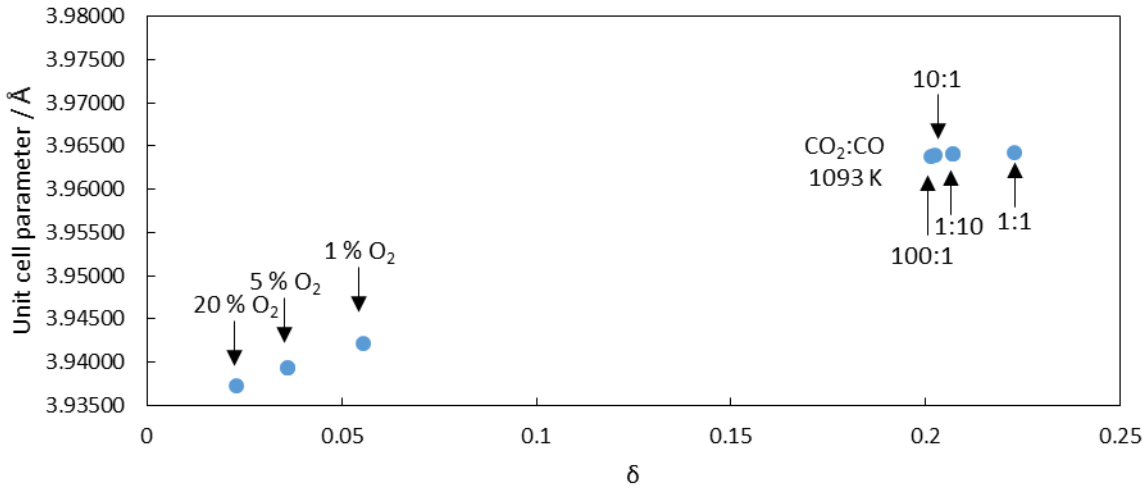


Figure 4.9: Unit cell parameter as a function of $\delta$ state. The different $\delta$ states were achieved via different gas conditions. These were 1%, 5% and 20% $O_2$ in Ar at a total pressure of 1.1 bara and 1:10, 1:1, 10:1 and 100:1 $CO_2$:CO ratios in a balance of Ar at 1 bara. The data was collected at temperatures in the range of 1093 K. Unit cell parameter was calculated from Rietveld refinement of the XRD data. The uncertainty is smaller than the marked points for all points shown.

This new approximation for the value of the chemical expansivity was confirmed for a small range of $pO_2$ using X-ray diffraction experiments; for these experiments the measured oxygen leaving or entering the solid phase based on the outlet gas analysis from the XRD experiments showed good agreement with the delta values predicted using the literature values for the thermodynamics from Kuhn et al (2011). The linear expansivity also fits the data reasonably well inside this short range of $pO_2$ but does under predict then over predict the results, which is expected given the non-linear relationship between $\delta$ and unit cell parameter inside this range.

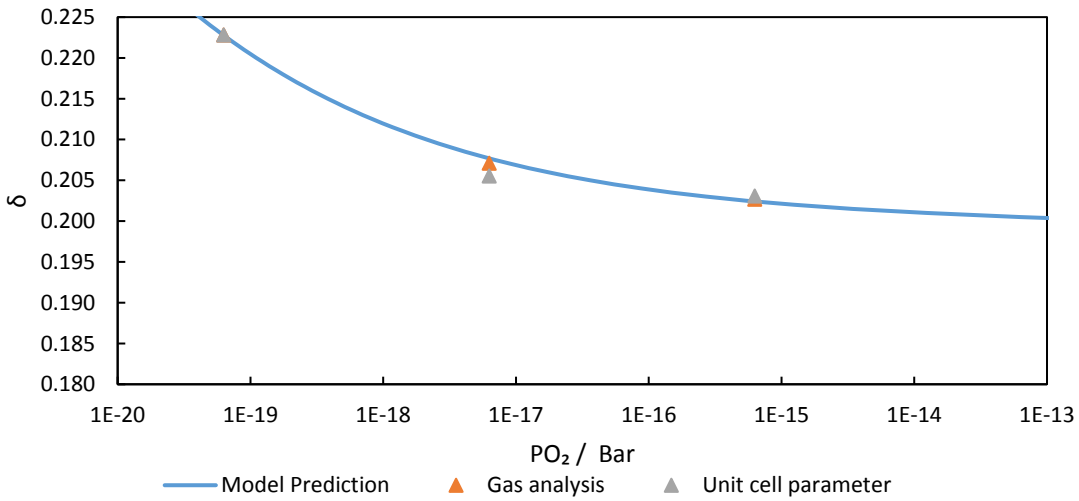


Figure 4.10: $\delta$ state of the material calculated using the chemical expansivity extracted from Figure 4.8 and outlet gas conditions are compared to predicted values obtained from thermodynamics in the literature (Kuhn et al 2011). This was carried out at 1093 K using gas atmospheres of 1:10, 1:1 and 10:1 $CO_2$:CO ratios in a balance of Ar at 1 bara. The gas analysis results are only capable of obtaining relative values so the results for $6.3x10^{-20}$ Pa is used as a reference, this point was chosen as it is the most reduced. The error bars of one standard deviation were smaller than the markers so are not included

### 4e Summary of Chapter 4

The $Fe^{3+}$ to $Fe^{2+}$ regime is characterised with different physical properties to the previously studied $Fe^{4+}$ to $Fe^{3+}$ regime. These changing properties are expected to be due to the changing nature of the bonds in the perovskite. As the number of holes or defects, caused by the vacancies of oxygen atoms, in the structure increase the bonds' strengths will increase making the thermal effects smaller. While the increased chemical expansivity when the sample is mainly in the $Fe^{3+}$ state with only small amounts in the $Fe^{2+}$ stage is most likely due to the formation of $Fe^{2+}$ octahedral co-ordination iron ions which have much larger atomic radii (0.78 Å) than the octahedral $Fe^{3+}$ and $Fe^{4+}$ (0.645 Å and 0.58 Å, high spin values) respectively

increasing the unit cell parameter quickly. However, after this change as more oxygen atoms are removed the unit cell parameter cannot increase to the same degree due to the formation of increasing quantities of the smaller lower coordination iron ions (Shannon, 1976). However even though the material's thermal and chemical expansivity change in this reduced state it continues to have perovskite structure.

Additionally the neutron scattering experiments raised issues with the refinement fit for oxygen density disagreeing with the thermodynamic model and previous work. The measurement of the $\delta$ being above that expected for temperatures above 1100 K in 5 mol% oxygen is probably due to the thermal movement of the oxygen atoms. The oxygen atoms interact strongly with the incoming neutrons (Kamitakahara 2013) so the shape of the elastic scattering pattern depends on their locations. If the oxygens are constantly vibrating, due to the high temperatures and large defects in the structure it is possible that their interactions with the neutrons will be smaller than the refinement software would expect for a given $\delta$ so would be equivalent to a smaller number of stationary oxygen molecules.

For $\delta$ states below 0.2 the chemical and/or thermal expansivity were found to be under predicted by the literature with a chemical expansivity of 0.144±0.009 Å per unit change in $\delta$ and a thermal expansivity of $5.72\pm0.04\times10^{-5}$ Å/K.

For $\delta$ states of greater than 0.2 the material's thermal expansivity was seen to increase compared with the previous regime to $6.18\pm0.08\times10^{-5}$ Å/K. The changes to the chemical expansivity were more complex, with the value becoming a function of the $\delta$ state. The values for the chemical expansivity decrease with increasing $\delta$. The chemical expansivity for this regime remains smaller than the value obtained for a $\delta$ value of less than 0.2 for all measured results but close to the expected transition point it may increase, varying from 0.140 Å at $\delta$=0.202 to 0.011 at $\delta$=0.215 Å. This shows the chemical expansivity around this transition point is complex and requires further study for a complete understanding of the material to be obtained. If a linear fit is put on all the data collected in this regime then the chemical expansivity is found to be 0.0148±0.0037 Å per change in $\delta$.

It was found that regardless of $\delta$, for chemical looping $H_2$ production the material's structure remains a perovskite and does not undergo phase segregation. That is that operating at lower oxygen partial pressure will not negatively affect the material's usefulness as chemical looping oxygen carrier.

Additionally, using these chemical and thermal expansivities it is possible to determine the material's $\delta$ state using XRD. Given the fast fluxes, and that this technique does not interfere with the chemical processes undertaken as part of a chemical looping reactor, it is possible to carryout *operando* studies on a working chemical looping reactor. This allows for an understanding of how the chemical properties of the material change during use. This can be used to confirm the thermodynamics or kinetics of the system and aids the validation of simulations as they would not need to rely solely on outlet gas composition or the study of spent reactor beds.

# Chapter 5: Experimental studies on chemical looping $H_2$ production

Chapter 3 has shown that, theoretically, using $La_{0.6}Sr_{0.4}Fe_{3-\delta}$ (LSF641) in a counter current chemical looping water-gas shift (WGS) reactor would allow for conversions that are higher than the thermodynamic limit of a conventional WGS reactor. The time averaged conversions of the reducing and oxidising feeds were used to indicate that the system had overcome these limitations. A conversion above 50% for both feeds would show that a system had achieved this aim.

While Chapter 4 has shown that it is possible to relate the oxidation state of LSF641, through its oxygen content, to the unit cell parameter of the material. This is possible due to the structure distorting as the oxygen content of the material changes during oxidation and reduction. This would allow for the internals of the reactor to be visualised during reaction, determining how the oxygen content of the oxygen carrier material (OCM) changes at different points inside the bed.

Chapter 4 showed that the material remains single phase in the range of $pO_2$s expected in the reactor. This indicates that LSF641 would not undergo degradation while cycling between the oxidation and reduction stages leading to an increased material life time when compared to other OCMs. A prolonged OCM lifetime would decrease operational costs of the reactor system improving the viability of chemical looping $H_2$ production.

The purpose of the studies detailed within was to prove experimentally in a working reactor that LSF641 can be used as an OCM in a chemical looping reactor achieving higher conversions than those expected from a conventional reactor. The activity of LSF641 in mixed and unmixed reactions as well as the long-term stability of the material are determined and the effect of varying the temperature of the system was explored.

To increase the understanding of such a system the oxygen content of the bed was probed using *operando* XRD during reduction and oxidation of the material. This allows for how the oxygen content of each point in the bed varies are a function of time during reaction to be determined; increasing the knowledge of the system and aiding scale up.

## 5a Conventional WGS reaction

The thermodynamics detailed in Chapter 3 indicate that a mixed reactor is not capable of achieving conversions above 50% for both $H_2O$ and CO at 1093 K. That is that in a mixed WGS reactor, where CO and $H_2O$ are co-fed in equimolar concentrations, equilibrium

conditions would be achieved limiting the outlet composition to a 1:1:1:1 $CO_2$:CO:$H_2O$:$H_2$ ratio at an operating temperature of 1073 K where the WGS equilibrium constant is close to unity. The outlet gas compositions as a function of time during a mixed WGS experiments using LSF641 is shown in Figure 5.1. During synthesis the material is formed in an oxidised state as air has a much larger oxidising potential than the gasses used in this experiment. This causes full oxidation of 2.5 mol% CO feed gas to $CO_2$ while the 2.5 mol% $H_2O$ remains unreacted for the first six minutes of reactive gas flow. After this initial stage the LSF641 present in the reactor would have reached an equilibrium state. Once this is achieved the conversions of both the $H_2O$ and CO reaches 50%, with an equal quantity of $CO_2$, CO, $H_2O$ and $H_2$ present in the outlet composition. During the reduction of the packed bed 850 µmol of oxygen had been removed from the LSF641. This highlights the maximum conversion that a mixed reactor could achieve at this temperature to be 50%.

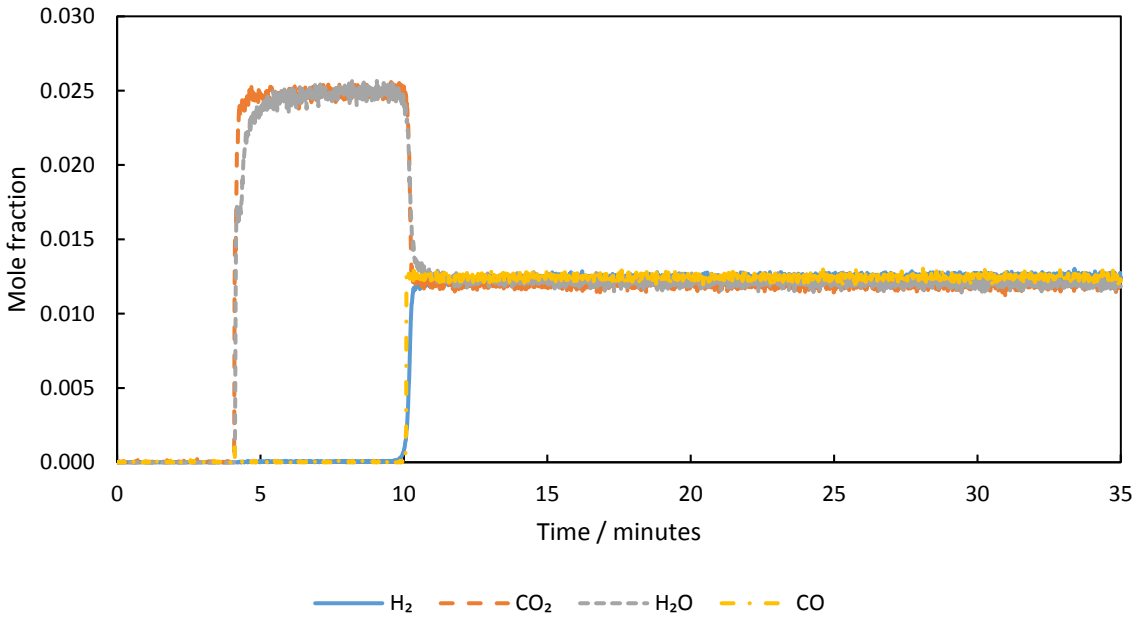


Figure 5.1: Outlet gas composition verses time for a conventional WGS reactor using LSF641 as a catalyst. This experiment used a mixed flow of 2.5 mol% $H_2O$ and 2.5 mol% CO in Ar. The flow of reactive gas began after four minutes of inert feed and lasted for 31 minutes. The nominal flowrate was $3.4 \times 10^{-5}$ mol $s^{-1}$ (50 ml/min NTP) and a sample mass of 2.08 g was used. The uncertainty in any measurement was less than ±100 ppm based on the analysis from Chapter 3.

### 5b Temperature optimisation

As this thesis concentrates on creating an underlying understanding of packed bed chemical looping systems, the work was focused on isothermal reactors. Isothermal reactors are where the whole bed is kept at a constant temperature for the duration of each cycle. The

temperature that the reactor is operated at affects the expected conversions for both a chemical looping reactor and a conventional one.

In order to determine the optimal temperature to compare the two systems a packed bed of 2.39 g of 80-160 µm LSF641 was cycled between 5% CO and 5% $H_2O$ until steady cycling had occurred at five temperatures ranging from 993 K to 1193 K. The temperature range was centred on 1093 K as this temperature has been used in multiple other studies of the material, (Mak 2017 and Metcalfe et al 2019). 1093 K also serves as a useful benchmark for determining if such a system can overcome the limitations of a conventional reactor as if a water-gas shift reactor was operated in these conditions the reactants would both have conversions of 50%. The reactor set up and the methodology for the calculation of the conversions for each cycle is detailed in Chapter 2.

Figure 5.2 shows both CO and $H_2O$ conversion as a function of cycle number at a variety of temperatures, regardless of the temperature chosen the time averaged conversion both the $H_2O$ and CO were found to exceed 50% once steady cycling had been achieved. Confirming that this reactor system is capable of exceeding the thermodynamic limitations of a conventional reactor.

Initially the material began fully oxidised due to its synthesis in air, this means that the conversion of CO was close to 100% and the conversion of $H_2O$ was very low. As the cycle number increased the conversion of $H_2O$ gradually increased until it reached its steady cycling value. In comparison the CO conversion remained steady with high conversion for 15 cycles before rapidly dropping to its steady cycling value. As the temperature increased so did the conversion; this indicates that the use of a higher temperature would be more profitable. The system rapidly reached a new steady cycling value after each temperature change, taking no more than three cycles.

An oxygen balance on the system accounting for the differing flowrates of the $H_2O$ and CO streams was found to close to within 5% due to $H_2O$ feed having a flowrate that was larger. Carrying out carbon and $H_2$ balances on each of the half cycles to within 5% indicated good calibration values and that no carbon deposition is occurring during cycling.

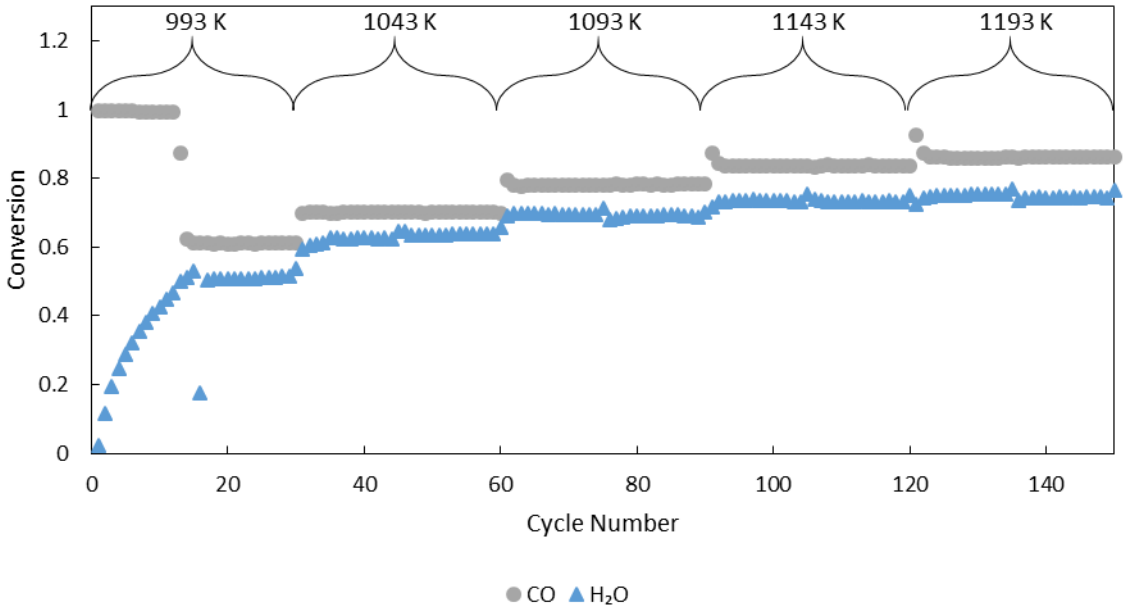


Figure 5.2: Conversion versus cycle number for 150 cycles. $H_2O$ (blue) and CO (grey) conversion as a function of cycle number with 60 seconds feeds of 5 mol% CO and 5 mol % $H_2O$ in Ar. The experiment was carried out with nominal molar flowrates of $3.4x10^{-5}$ mol $s^{-1}$ (50 ml/min NTP) with a mass of 2.39 g LSF641. Over the course of the experiment the temperature was held for every 30 cycles, for the first 30 cycles its was 993 K, then it increased by 50 K every cycle until the final set of 30 which were carried out at 1193 K.

While the conversion data indicates that operating at a higher temperature could be the most beneficial when scaling up, examination of the outlet gas conditions for the steady cycling data complicates this assessment. The shape of the curves for the reduction half cycle follows a pattern, with each half cycle starting with an effectively pure $CO_2$ before rapid breakthrough of CO at some point later in the cycle, with the hotter temperatures exhibiting breakthrough later. This results in both the selectivity and the conversion increasing as the temperature increases.

This is not the case for the oxidation half cycle, where even though the overall conversion increases with temperature, the quality of the $H_2$ feed changes. At higher temperatures there is an immediate breakthrough of $H_2O$ with the quantity in the feed at the beginning of the cycling increases at higher temperature. As the cycles continue the amount of $H_2O$ increases, but the rate of this increase decreases hence the larger conversions at these high temperatures. This lowering of product quality with temperature increase is most likely linked to the degrading equilibrium constant for CO oxidation at high temperatures. This is because the $H_2$ outlet conditions are defined by the inlet CO conditions, as the equilibrium constant degrades for CO oxidation by the OCM the end point reached by that half of the reactor is less reduced so cannot achieve the same degree of reduction of the $H_2O$ feed .

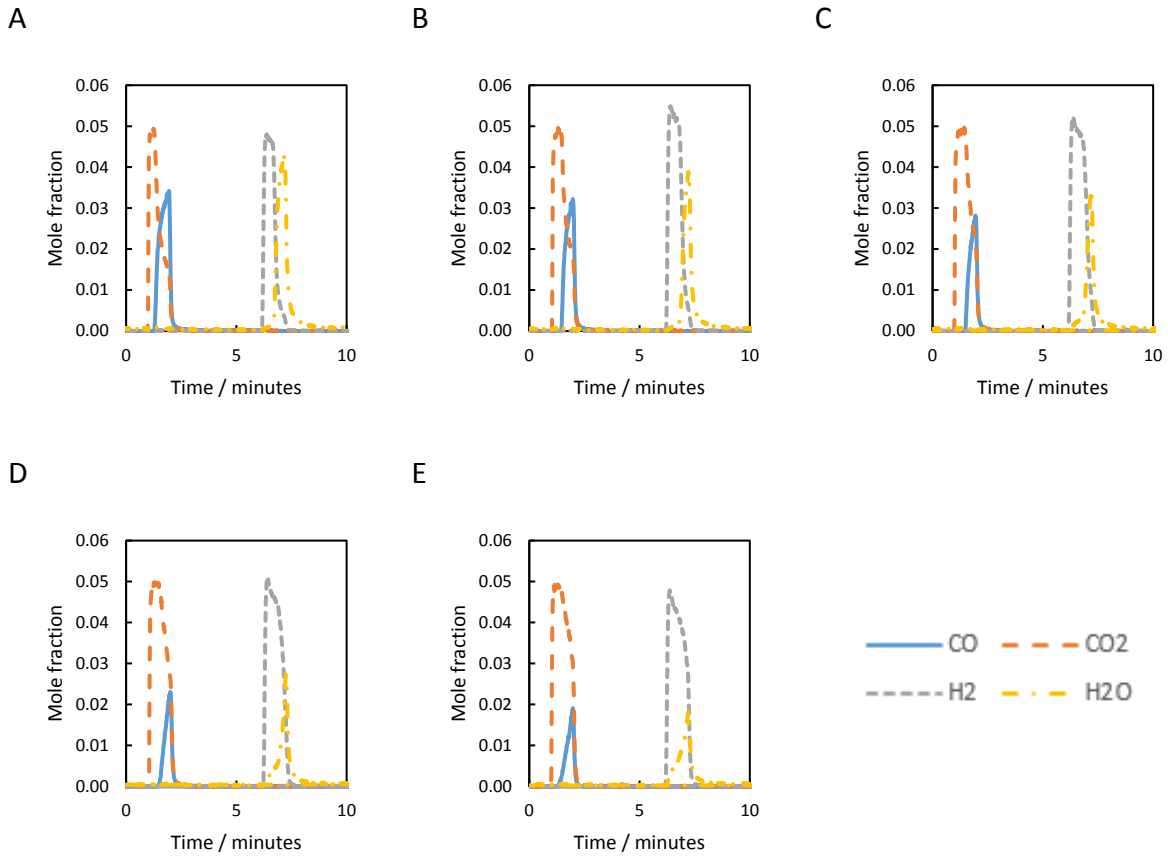


Figure 5.3: Outlet composition versus time from the long-term stability experiment. Six oxidation and reduction cycles indicating the effect of reactor temperature on the outlet gas compositions (A) 993 K, B) 1043 K, C) 1093 K, D) 1143 K and E) 1193 K) are shown. The experiment used 5% mole fraction of reactive gas in a balance of Ar with nominal molar flowrates of $3.4 \times 10^{-5}$ mol $s^{-1}$ (50 ml/min NTP) with an OCM mass of 2.39 g at a variety of temperatures. The uncertainty in any measurement was less than ±100 ppm mole fraction based on the analysis Chapter 2.

Due to the combination of a loss in product quality and the increased cost for operating at high temperatures commercially, the furnace was set to 1093 K for future work.

## 5c Half cycle duration optimisation

Another parameter in the operation of a packed bed chemical looping system is the duration of the half cycles termed redox duration. Adjusting this redox duration has a direct effect on the conversions of $H_2O$ and CO, with shorter durations expected to increase conversion as there is a smaller change in the oxygen content of the material and vice versa. To test this hypothesis 1.43 g of LSF641 was cycled using 60 s feeds (Region A) before decreasing the duration to 48 s (Region B) and increasing to 120 s (Region C). Each region lasted 15 cycles to confirm that the system had reached a new steady cycling state. The conversions of $H_2O$ and CO for each cycle are shown in Figure 5.4 and the outlet gas compositions from representative cycles can be seen in Figure 5.5.

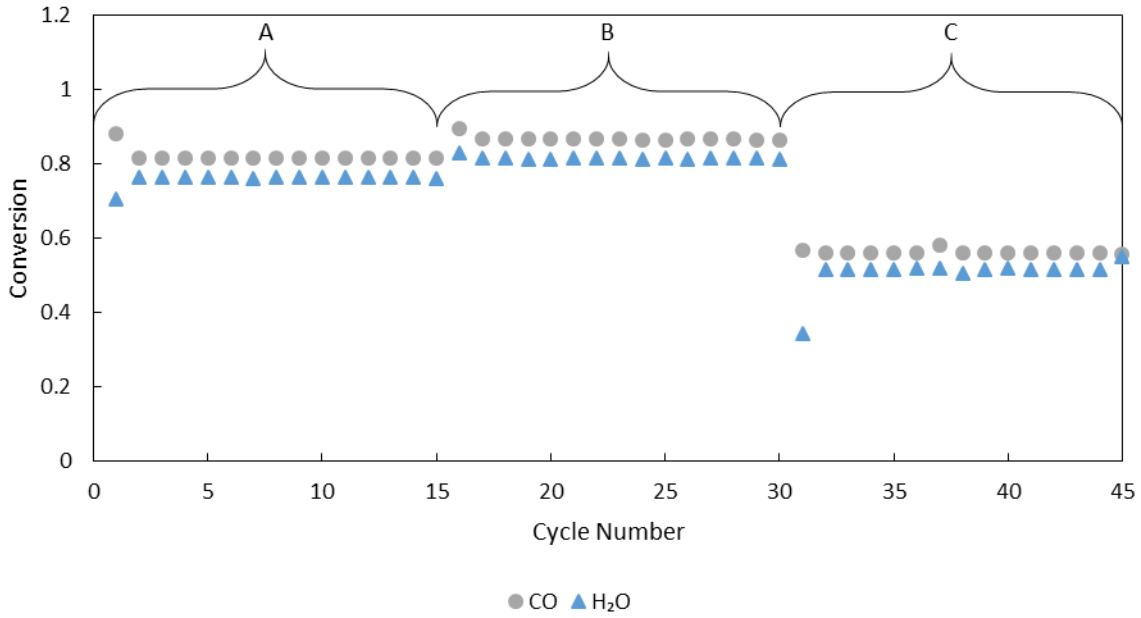


Figure 5.4: Conversion of CO and $H_2O$ as a function of cycle number. This was carried out in the counter-current chemical looping reactor using 1.43 g of LSF641 as the OCM. The reactive feeds were of 5 mol% CO and 5 mol% $H_2O$ with 120 s inert purges between reactive gas flows. The experiment was carried out with nominal molar flowrates of $3.4x10^{-5}$ mol $s^{-1}$ (50 ml/min NTP) and at a temperature of 1073 K. The duration of the reactive feeds was varied, with 60 s feeds being used for the first 15 cycles (Region A) 48 s for cycles 16 to 30 (Region B) and 120 s feeds for the final 15 cycles (Region C).

The system responded quickly to the changes in redox duration, achieving a new steady cycling state within two cycles. This rapid adaptation to new operating conditions is expected to be due the fact that the bed is operating in similar $pO_2$ range regardless of the cycle duration. As each end of the beds were already in equilibrium with one of the two feeds the extremes of the bed were largely unaffected by cycle duration. This flexibility to changes in the systems operational parameters and the ability to respond and adjust quickly to these changes would allow for the system to be adjusted to meet the needs of different applications. The system could be operated to maximise purity of $H_2$ and then be rapidly changed to maximise the conversion of $H_2O$ should the need arise.

The system had been used previously for cycling so was close to steady state operation at the beginning of Region A, for this reason steady operation begins after two cycles. The system achieved 81% conversion of CO and 76% conversion of $H_2O$ in Region A. This difference in the conversions was accounted for due to differing flowrates of the $H_2O$ and CO feeds, the flowrate of $H_2O$ was found to be 105% of the CO feed based on the pressure transducers detailed in the Chapter 2. The leads to the oxygen balance closing to within 2%.

When the redox duration was changed to 48 s the system reached a new steady cycling profile within two cycles highlighting the speed at which the system can respond to changing operating conditions. This change, as expected, increased the $H_2O$ and CO conversions to 81% and 86% respectively. Once the differing flowrates were accounted for the oxygen balance closed to within 1%.

In Region C, where the redox duration was 120 s, the conversions dropped significantly to 52% and 56% for $H_2O$ and CO respectively. This, once again, occurred over only two cycles showing that the packed bed configuration would adjust to new conditions quickly and without lasting effects on the system. The oxygen balance for the system was found to close to within 3%. Throughout all three regions, the carbon and $H_2$ balances carried out on the system close to within 3% which in combination with the lack of carbon containing compounds during the oxidation half cycles indicates a lack of carbon deposition or leaks in the system.

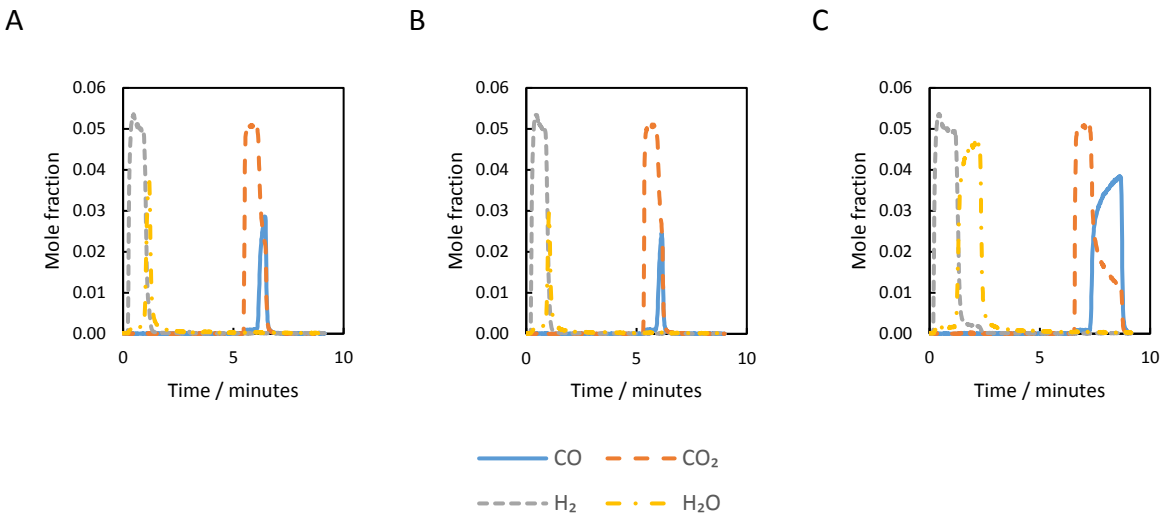


Figure 5.5: Representative outlet gas composition as a function of time for the half cycle duration optimisation experiment. Three oxidation and reduction cycles indicating the effect of redox duration on the outlet gas compositions (A) 60 s, B) 48 s and C) 120 s) are shown. The experiment used 5% mole fraction of reactive gas in a balance of Ar with nominal molar flowrates of $3.4 \times 10^{-5}$ mol $s^{-1}$ (50 ml/min NTP) with an OCM mass of 1.43 g at 1073 K. The uncertainty in any measurement was less than ±100 ppm based on the analysis from Chapter 2.

Comparing the outlet gas compositions of representative cycles from each region, shown in Figure 5.5, it can be observed that shortening the duration of a half cycle does not result in a truncated form of the half cycles of a longer duration. As the length of the half cycles increase so does the duration of the half cycle with high purity product, with increased cycle

duration the time until reactant break through increases. When the duration was shortened unreacted gas passes through the reactor considerably earlier. Achieving a 100% conversion using LSF641 in a commercial reactor would be more complex than just shortening the redox duration. Consequently, longer duration leads to higher production, whilst the longest duration produces the most $H_2$ it does not have the highest production rate. The concentration profile of the outlet gas implies that with long enough feed durations to would be possible to wash out the gradient in the bed, so that by the end of a cycle all of the reactive gas would pass through the reactor unreacted. These are both important considerations when undertaking scale up calculations.

In Region B the system showed very high conversions with very little of the reactants passing though the reactor unconverted with only sudden spikes at the end of the half cycles being detected. These spikes were observed in the 60 s durations redox cycling in Region A but were considerably reduced in size for Region B. These high conversions and small mole fractions of the reactants in the outlet gases make study of the systems kinetics or limitations difficult as with only small quantities of the product being detected the outlet concentration can be more easily impacted by the uncertainty in its measurement.

The cycles from Region C show that change in oxidation and reduction half cycles behave differently. During the oxidation half cycle high conversions are achieved initially, very little $H_2O$ reaches the outlet of the reactor, then the conversion drops very rapidly, with little $H_2$ at the outlet of the reactor. The system swings from high conversion to low conversion rapidly. This is contrasted by the reduction half cycle, where while the system starts with high conversion of CO, the amount of CO in the product stream increases quickly but that rate slows before the end of the half cycle with the feed at the end having both $CO_2$ and CO present. It appears that should the redox duration be increased further then eventually all of the CO would pass through the reactor unconverted.

The difference between the two half cycles outlet gas composition as a function of time is expected to be due to the non-symmetry of the relationship between $pO_2$ and oxygen content of LSF641, with the curve almost plateauing at the $pO_2$s associated with a $H_2O$ stream and the gradient increasing at an increasing rate as $pO_2$ becomes more reducing. With large amounts of oxygen content available at similar $pO_2$s for the reduced end of the bed, the outlet from the $H_2O$ half cycle can remain almost constant until that capacity is used up and the composition has moved down the curve to the flatter section where the lack of

capacity means that the system rapidly reaches the point where the system is unable to reduce the $H_2O$ to $H_2$. In comparison for the reduction half cycle the outlet is at the oxidised end of the bed where there is little oxygen capacity between different $pO_2$s. This capacity is used up more rapidly so the system starts to show CO passing through the reactor earlier than $H_2O$ would but once the CO begins passing through the reactor the curve relating oxygen content and $pO_2$ becomes steeper so the system continues to produce $CO_2$ is diminishing mole fractions as the OCM approaches a state in equilibrium with the reducing feed gas.

All three of these regions overcome the WGS equilibrium of a conventional reactor based on the conversions achieved. All the systems showed the high purity $H_2$ production throughout operation with low concentrations of $H_2O$ when $H_2$ was produced. There was little to no carbon containing compounds produced with the $H_2$ simplifying and reducing the costs for downstream separation processes.

Region A and B showed that the $CO_2$ produced would have little to no CO present under these regimes. However, during Region C a mixed feed of CO and $CO_2$ was produced which would require processing before it would be utilised or stored.

It was decided to use 60 s durations for the rest of the experiments carried out in this thesis as this produced high conversions compared to conventional reactors. Additionally, some unreacted reactants pass through the reactor which allows for better comparisons between other changes occurring in the system.

### 5d Chemical looping for reverse WGS

An implication of the thermodynamics detailed in Chapter 3 is that for a given gradient in the chemical potential as long as the chemical potential of the reactants remain the same the chemical composition of the reactants can change. Consequently, using feeds of $H_2$ and $CO_2$ high purity $H_2O$ and CO can be produced from a bed that had been developed into a steady cycling system for $H_2$ and $CO_2$ production. This is the same as reversing the direction of Reaction 3a.1 giving 5d.1.

$$H_2 + CO_2 \rightleftharpoons H_2O + CO \qquad \text{5d.1}$$

This is commonly referred to as the reverse water-gas shift (RWGS) reaction. It is used commercially for the sustainable production of CO (Yoshihara et al 1996, and Wenzel et al

2017). Operating a chemical looping reactor for these purposes would have similar advantages to those of the conventional WGS reaction; allowing for high purity without energy intensive separation processes downstream.

The conversion of a reverse flow packed bed chemical looping reactor carrying out the WGS reaction to one carrying out the RWGS reaction would require only a switch of feed gas, without the need to alter the reactors overall design. This would allow for a reactor to be used for $H_2$ or CO production without large capital costs.

This flexibility in design is not present in other $H_2$ or CO production reactors. For example membrane or adsorbent based processes are specifically designed with the performance of only one reaction. This would require increased capital cost to change the system or would suffer from low conversions or purity in the outlet streams when the alternative reaction was desirable.

To test the system's ability to alternate between a set up for $H_2$ production to one for CO production, 2.98 g of LSF641 was initially cycled using 5 mol% $H_2O$ and 5mol% CO for 20 cycles to reach steady state operation. During this stage 62 % conversion of $H_2O$ and 69% of CO was achieved. Indicating that at steady state this packed bed was achieving high conversions in comparison to a conventional WGS reactor. Once the differing flowrates of the reactant streams was accounted for, a 12% larger flowrate of the oxidising gas, the oxygen balance was found to close to within 1%. Carrying out a carbon and a $H_2$ balance both were found to close to within 4% indicating that carbon deposition was not occurring and that the gas flow fed to the system reaches the outlet of the reactor, with limited ingress of $O_2$ and $N_2$ from the atmosphere. This lower conversions when compared to the other experiments is most likely due channelling occurring in the bed, allowing the reactants to bypass the OCM.

Once the oxidising and reducing gasses were changed to 5 mol% $CO_2$ and 5 mol% $H_2$ the steady cycling conversions became steady at 70%. The pressure data collected indicated that the flowrates of the gasses became equal, showing a closed oxygen balance. The carbon and $H_2$ balance continue to close to within 4%.

Once the reactor was converted to operate the reverse water-gas shift reaction, the system returned to steady cycling within three cycles. This interruption to steady cycling is expected to be based on the lack of a difference in flowrate between the reactant feed rates.

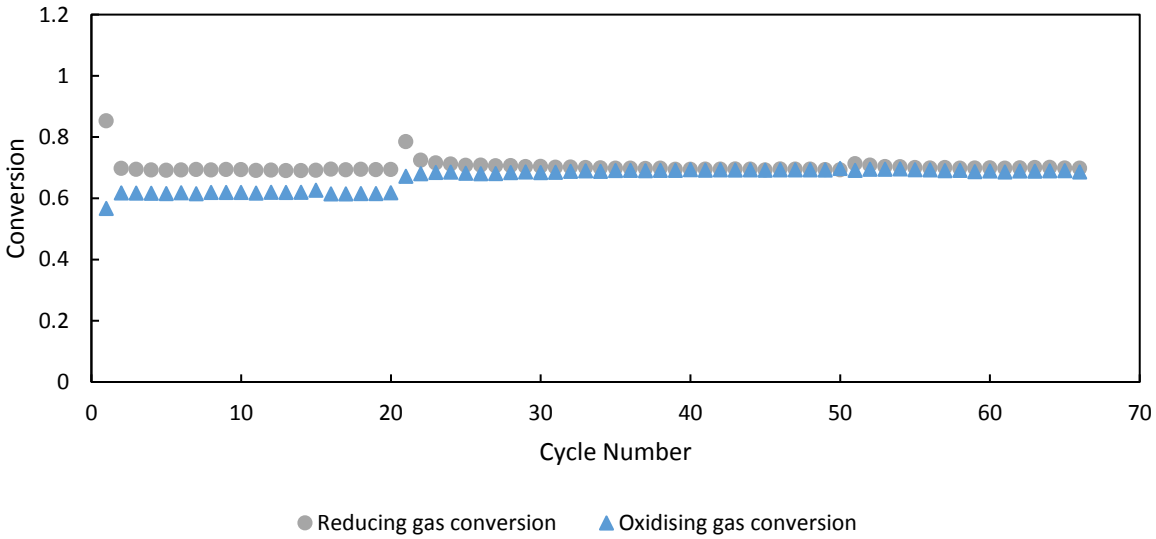


Figure 5.6: Conversion of reduction (grey) and oxidation (blue) half cycles using a counter current flow reactor using 2.98 g of LSF641 as the OCM. For the first 20 cycles 5 mol% $H_2O$ and 5 mol% CO were used as the reactive gasses, from then for the duration of the experiment 5 mol% $H_2$ and 5 mol% $CO_2$ were used. The experiment was carried out with nominal molar flowrates of $3.4x10^{-5}$ mol $s^{-1}$ (50 ml/min NTP) at 1093 K.

Figure 5.7 shows the outlet compositions of representative cycles from Figure 5.6. One representative cycle (cycle 15) from steady cycling of the WGS reaction and three representative cycles (cycles 21, 50 and 80) from steady-cycling with the RWGS reaction were selected. Cycle 15 gives the outlet composition of the system during WGS cycling, while 21 shows how the system responds to the switch to RWGS initially. Cycles 50 and 80 show how the system reaches a new steady cycling behavior giving high purity CO as a product.

The outlet composition versus time of the representative cycle from steady-cycling of the WGS reaction is similar to the representative cycles from steady-cycling of the RWGS, with $CO_2$, CO, $H_2$, and $H_2O$ replaced with $H_2O$, $H_2$, CO, and $CO_2$ respectively. This can be seen in Figure 5.7, with C and D have the same form as A with the gas changed as detailed above. The nature of the half cycle, either reducing or oxidizing, as opposed to the gas pair involved in the reaction, is the important feature for defining the shape of the outlet gas compositions curves. This highlights that is the relationship between the oxygen content and equivalent $pO_2$ of the OCM not the difference in the gas phase equilibrium constants or the gas-solid interactions that causes the differences between the outlet gas composition curves for the reducing and oxidizing half cycles.

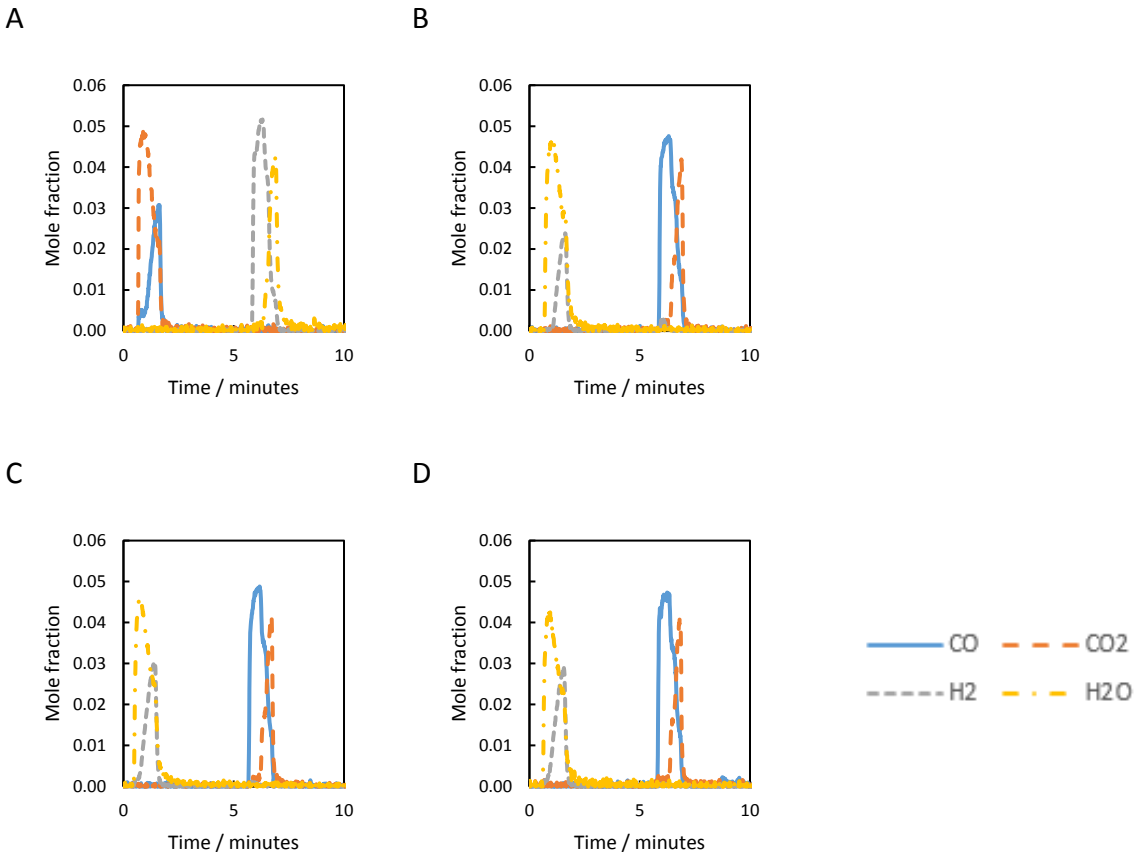


Figure 5.7: Outlet composition versus time for four representative cycles of WGS followed by RWGS operation. The four cycles shown are; A) cycle 15 during WGS operation, B) cycle 21 overall and cycle 1 of RWGS, C) cycle 50 overall or 30 of RWGS and D) cycle 80 overall or 50 of RWGS. The experiment was performed using 5 mol% reactive gas in a balance of Ar, CO and $H_2O$ for WGS and $H_2$ and $CO_2$ for RWGS. The nominal flowrate was $3.4x10^{-5}$ mol $s^{-1}$ (50 ml/min NTP) with an OCM mass of 2.98 g. The uncertainty in any measurement was less than ±100 ppm based on the analysis from Chapter 2.

This experiment shows that the system can be operated as either a WGS or RWSG reactor without changes to plant design, increasing the flexibility of such a system. A counter current fixed bed chemical looping reactor could be designed to be operated either for $H_2$ production, using $H_2O$ and CO as feed stocks, or CO, using $H_2$ and $CO_2$ as feed stock without compromising on product quality or reactant conversion. In fact, such a system could react to market changes, producing the more economically or socially valuable chemical, without requiring the reactor system to cool down once an oxygen potential gradient has been formed along the reactor.

### 5e Long term material stability

The stability of an OCM is always an important property when designing a chemical looping reactor for industrial purposes. The factors that affect the deactivation of OCMs are varied but all eventually lead to diminishing production of $H_2$ or $CO_2$ to the point that the system is

no longer cost effective. When the OCM is considered cheap it can often be more economical to regularly replace the OCM, but with the increased cost and material preparation time of LSF641 when compared to conventional OCMs like Fe or Cu this method becomes less effective. (Bohn et al 2010 and Mattison et al 2001)

In order to test the material's long-term stability for the WGS reaction, fresh 2.79 g (approximately 0.013 mol) $La_{0.6}Sr_{0.4}FeO_{3-\delta}$ was subjected to 1100 cycles of redox reactions with 5±0.025mol % CO and 5±0.025mol % $H_2O$ in the packed bed system following the protocol detailed in the experimental section.

Figure 5.8 shows how the conversions evolved with cycle number. The overall conversion of $H_2O$ increased from a very low initial value in cycle 1 to a steady value of 92.4% at cycle 25 and this value remained largely unchanged for the remainder of the experiment. In contrast, the CO is almost completely converted at the beginning of the experiment before changing to its steady-cycling value of 84.5% over a small number of cycles (Cycles 10-15). The difference in the steady cycling conversion of CO and $H_2O$ was due to the slightly different flowrates of the $H_2O$ and CO used. Once this was considered, the oxygen balance between the gas streams closed to within 2%. During each half cycle 85 µmol of oxygen was exchanged between the solid material and gas stream; this is only equivalent to 2.2% of the total oxygen capacity of the material. This difference between the maximum oxygen capacity of the solid and the quantity exchanged is due to most of this material's capacity is at $PO_2$'s high than that of $H_2O$ (~ $10^{-8}$ bar).

There is a maximum absolute deviation from the average conversion of both the $H_2O$ and CO of 1.5% once stable cycling has begun indicating good material stability. A linear regression on conversion against cycle number over the steady cycling regime showed a slightly positive gradient, which was less than the standard error from the regression, showing that there was no obvious change in conversion with repeated cycling.

Figure 5.9 shows the gas compositions measured at the outlet of the reactor from selected cycles. The material initially started in equilibrium with air as part of the synthesis process leading to an initially high CO conversion. First the CO fully oxidises before reaching the end of the reactor. The oxidation half cycle fails to return the system back to its original state, when it was in equilibrium with air. Over progressive cycles more and more of the bed moves to a condition where chemical potential gradient is between that of the $H_2O$ feed and

the CO feed. This continues until the whole of the reactor has reached its steady cycling gradient.

The bed will have developed an oxygen chemical potential gradient along its length. Achieving this takes a number of cycles as the bed must be reduced from its initial conditions. During this time the gas conversions changed and through study of these changes an understanding of the chemistry involved was achieved. The nature of how the gas composition changes for each cycling as the bed approaches steady cycling can be seen in Figures 5.9 A-5.9 D.

Once steady cycling had occurred (Figure 5.9 E and F) the reduction half cycle started with almost 100% conversion, for the first 40 seconds, before dropping gradually to a final value of 50% at the end of the minute. The oxidation cycle followed the same pattern with almost pure $H_2$ production before some $H_2O$ was present in the outlet gas.

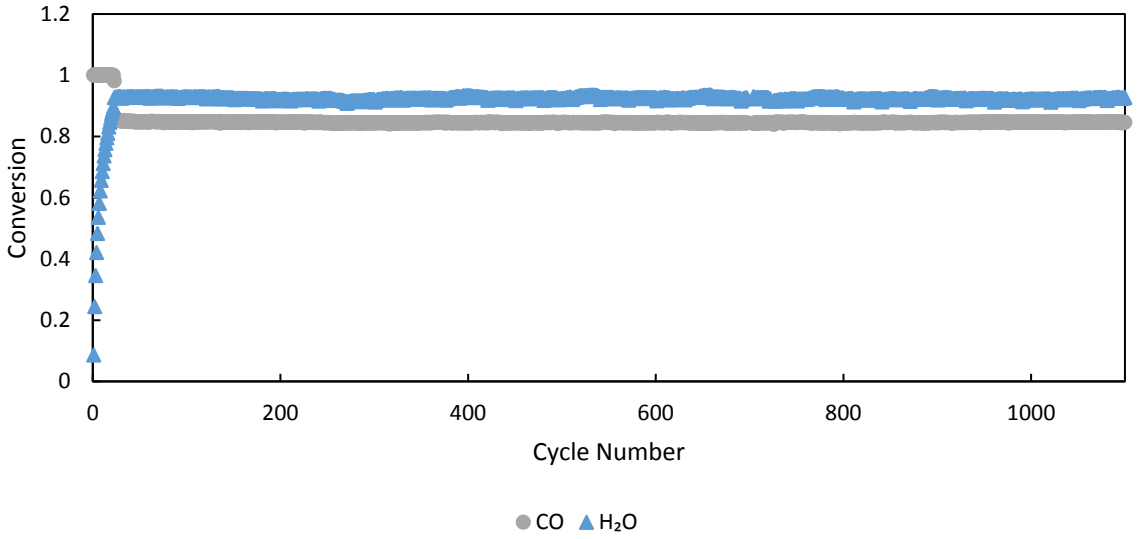


Figure 5.8: Conversion versus cycle number for 1100 cycles. $H_2O$ (blue) and CO (grey) conversion as a function of cycle number with 60 seconds feeds of 5 mol% CO and 5 mol% $H_2O$. The bed consisted of 2.79 g of 80-160 µm LSF641 and a molar feed rate of $3.4x10^{-5}$ mol $s^{-1}$ (50 ml/min NTP) was used.

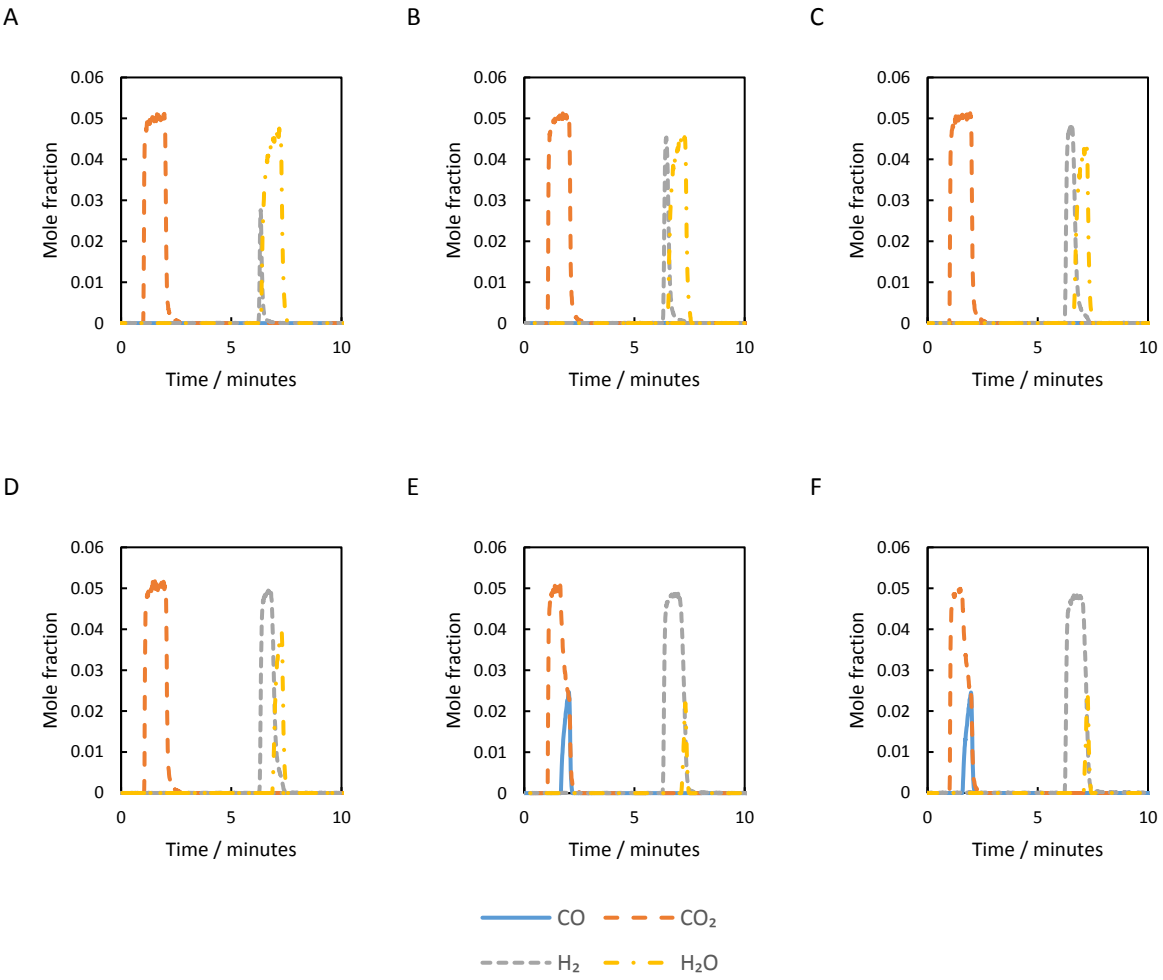


Figure 5.9: Outlet composition versus time from the long-term stability experiment. Six oxidation and reduction cycles indicating the evolution of the bed into a steady-cycling regime (Cycles 1 (A), 2 (B), 5(C), 10(D), 50(E) and 1000(F)) are shown. The system used 60 second feeds of 5 mol% CO and 5 mol% $H_2O$. The bed consisted of 2.79 g of 80-160 µm LSF641 and a molar feed rate of $3.4x10^{-5}$ mol $s^{-1}$ (50 ml/min NTP). The uncertainty in any measurement was less than ±100 µmol based on the methodology detailed previously.

Solid samples were taken after the 1100 cycles of reaction and examined by SEM and XRD to investigate if any significant structural changes and/or phase segregation had occurred. SEM images of the fresh and cycled material (Figure 5.10) showed that the material retained its structure with no significant morphological change. The material did not undergo macro structural changes as the cycling occurs, this is most likely due to the packed bed geometry minimising attrition. The material did not increase in porosity as it underwent cycling, this is expected to be due to the lack of phase changes in the material. The material only underwent small changes in structure and cell size which minimises stress on the material.

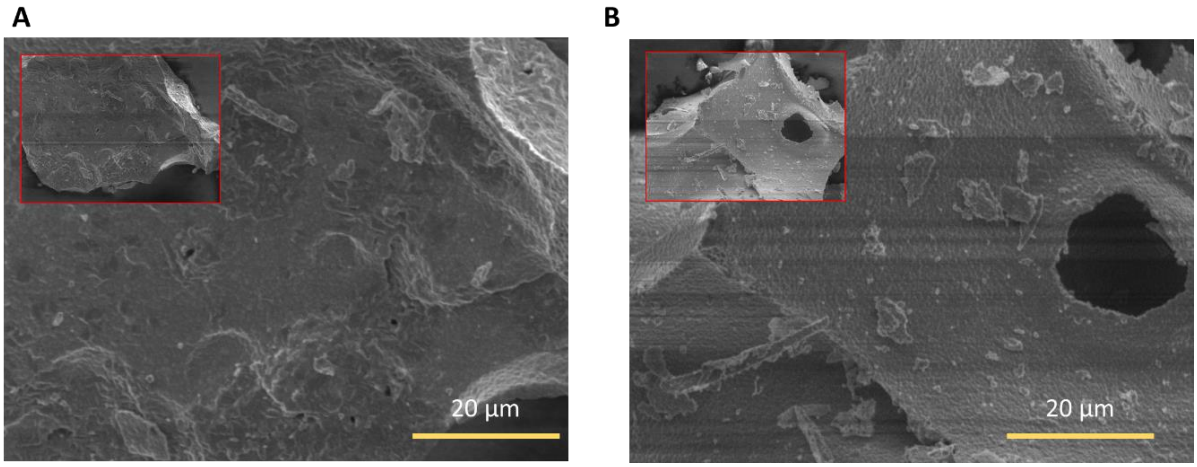

Figure 5.10: SEM micrographs of LSF641. A) fresh (before cycling) and B) used (after 1100 cycles)

After cycling the reduced end of the bed underwent *ex-situ* XRD. The reduced end was selected as this is the most likely to undergo phase segregation. Comparing the X-ray diffractograms of the sample before and after cycling shows that the major peaks all occur at the same points, being only slightly shifted to lower angles. This was due to the material being in a more reduced state, the direction of this shift is consistent with the expected results from Chapter 4. Direct calculation of the oxygen content of the material was not carried out as the ambient temperature of the reactor is much lower than the temperatures that were studied so considerable extrapolation of the results would be required.

The small change in the shape of the diffractogram shows that the material has not undergone phase segregation during the cycling. The background pattern for the two sets of peaks differ due to different *ex-situ* XRD machines being used to analyse the crystal structure and not due to any changes in the structure of the material.

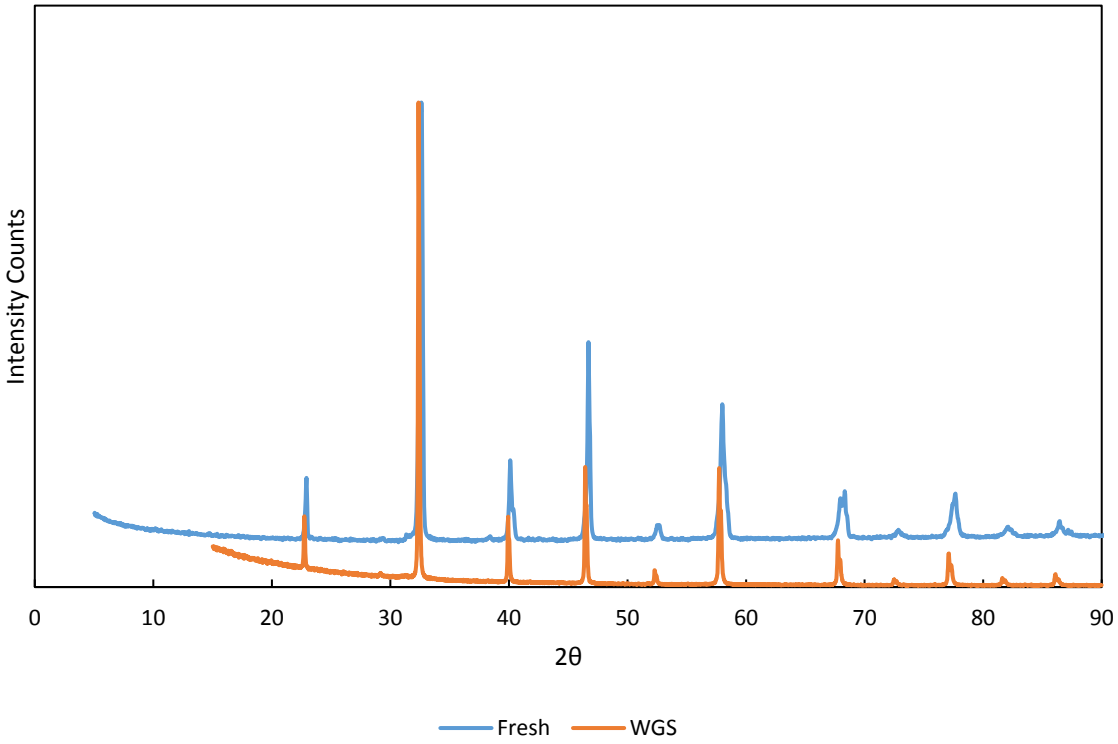


Figure 5.11: X-ray diffractogram of LSF641 (A) fresh (before cycling and (B) used from the reduced end of the bed (after 1100 cycles)

There is no evidence of carbon deposition in the reactor during the WGS. Carbon balances, using the outlet gasses, closed with the total amount of carbon entering and leaving the reactor agreeing and no carbon containing molecules exiting the reactor during the oxidation half cycle. Carbon deposition would lead to OCM deactivation lowering yield or to CO or $CO_2$ leaving the reactor during the oxidation half cycle lowering the purity of the products.

The material allows for high conversions consistently without physical degradation. This was shown through the outlet gas compositions, *ex-situ* XRD and SEM images. The material is a good OCM for the WGS reaction and does not suffer from short life time. The high conversions were as expected from previous work (Metcalfe et al 2019).

### 5f Oxygen profile of a LSF641 bed

The conversions achieved by the packed bed counter current flow chemical looping reactors using LSF641 as the OCM have demonstrated that these systems are capable of overcoming the thermodynamic limitations of conventional mixed feed reactors. The exact nature of the profile of the oxygen state of the material inside the reactor is not known. Determining how this profile changes over cycling can be investigated which would aid scale up and determination of the optimum operating conditions. As detailed in Chapter 3, the formation

of an oxygen potential gradient along the reactor is vital if the system is to operate with higher conversions than a conventional reactor. This gradient would form unless the whole capacity of the bed was used during each half cycle. That is if a half cycle duration well above that of Region C in Figure 5.4 was utilised. This gradient would form with a reduced end in equilibrium with an almost pure CO feed producing almost pure $H_2$ and an oxidised end with an almost pure $H_2O$ feed producing an equivalent ratio of $CO_2$.

This gradient can form in a packed bed reactor as the packing of the material restricts the movement of the particles. Transportation of oxygen through the solid limited due to the small particle diameter when compared to the bed length and in the gas phase the low equivalent $pO_2$s of the OCM, when used for the water-gas shift, reduces the potential for a gas phase oxygen partial pressure sufficient to redistribute oxygen in the timescale of these experiments. This combination of the particle being unable to move and the oxygen being unable to pass between particles enables a gradient in the $\delta$ state of the material, and therefore the oxygen chemical potential, to form along the bed.

Using the lattice expansivities detailed in Chapter 4 it is possible to extract chemical data from *operando* XRD studies of working reactors. Given the nature of this chemical looping system, with its non-stoichiometric OCM and rapid changes in oxygen content, high fluxes of X-rays are required if the nature of the material is to be ascertained during the reaction. In order to have high confidence in the structure of the material high count rates are required. Given the short half cycle duration, for a XRD study, in order to collect results at during the reaction often enough to gain an understanding of how the system operates a much higher flux than a laboratory scale source is required. This necessitates the use of a synchrotron radiation source.

Studies where the chemistry and structure of the internals of a working reactor are measured cut down on development time between laboratory scale and pilot plant developments. This allows for the determination of how the material changes structurally as it undergoes reaction, while at a scale more indicative of large scale reactors.

*5f.i Temperature determination*

As the unit cell parameter is a function of both temperature and the material's $\delta$ state a complete understanding of the thermal conditions of the reactor is required. To ensure that the temperature of each part of the bed studied was known $Y_2O_3$ was added to the bed. In

Chapter 2 it was found that $Y_2O_3$ would not react with the carbon containing compounds used nor would it react with CO. The inert nature of $Y_2O_3$ in the range of $pO_2$ studied together with its Bragg reflections not coinciding with LSF641 major peaks makes this useful for internal temperature determination. The temperature was obtained as part of the Rietveld refinement using empirical equations linking the unit cell parameter to temperature according to Rebber (1975) and Wang K et al (2000).

It is essential to know the temperature gradient along the reactor. To this end the temperature of 15 evenly distributed points in the bed was determined with the furnace set to 1093 K in three different states. The three different states were measured: while the OCM was not reacting (in equilibrium with 1:1 $CO_2$:CO buffer gas), while the OCM was cycled between 5% CO and 5% $H_2O$ and while the system was cycled between 1:1 $CO_2$:CO and 1:10 $CO_2$:CO. The bed consisted of 2.2 g of LSF641 and 0.40 g of $Y_2O_3$ and was 170 mm long and had an internal diameter of 2 mm. The temperature without reaction is seen in Figure 5.12A and the variation from this temperature during buffer gas cycling and during WGS cycling is present in Figure 5.12B.

It is also important to know if the temperature of the reactor changes as a function of time during reaction, as in order to calculate the $\delta$ state of the material the temperature must be known, so that it is possible to determine how much of the change in unit cell parameter is due to chemical, as opposed to thermal, effects. In Figure 5.12C how the temperature of a single point in the bed varies during reaction is recorded as the bed cycles between 5% CO and 5% $H_2O$, with one minute feeds separated by 4 minutes of inert Ar. The same packed bed from Figure 5.12A was used

A

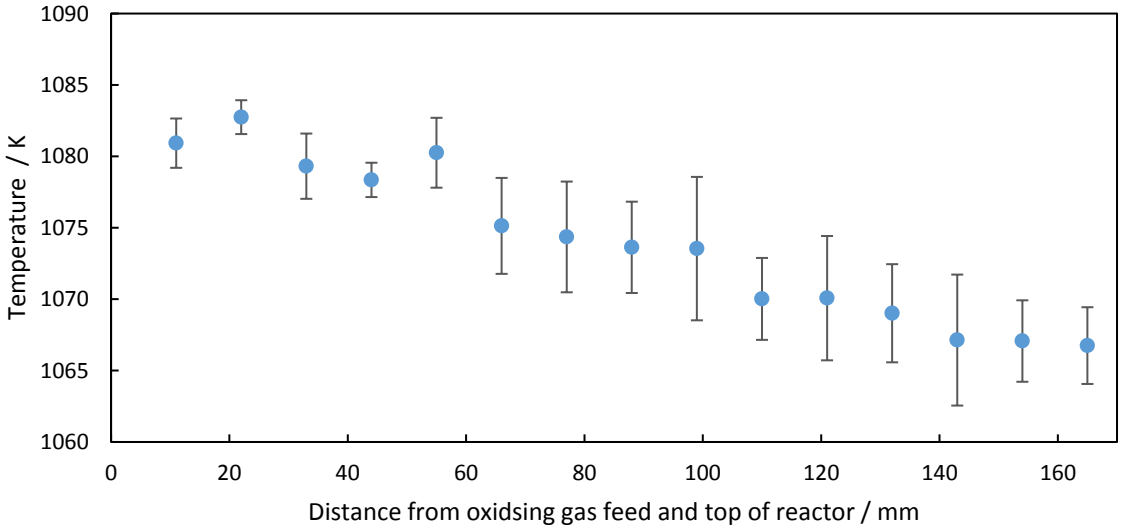
1090
1085
1080
1075
1070
1065
1060
Temperature / K
0
20
40
60
80
100
120
140
160
Distance from oxidsing gas feed and top of reactor / mm

B

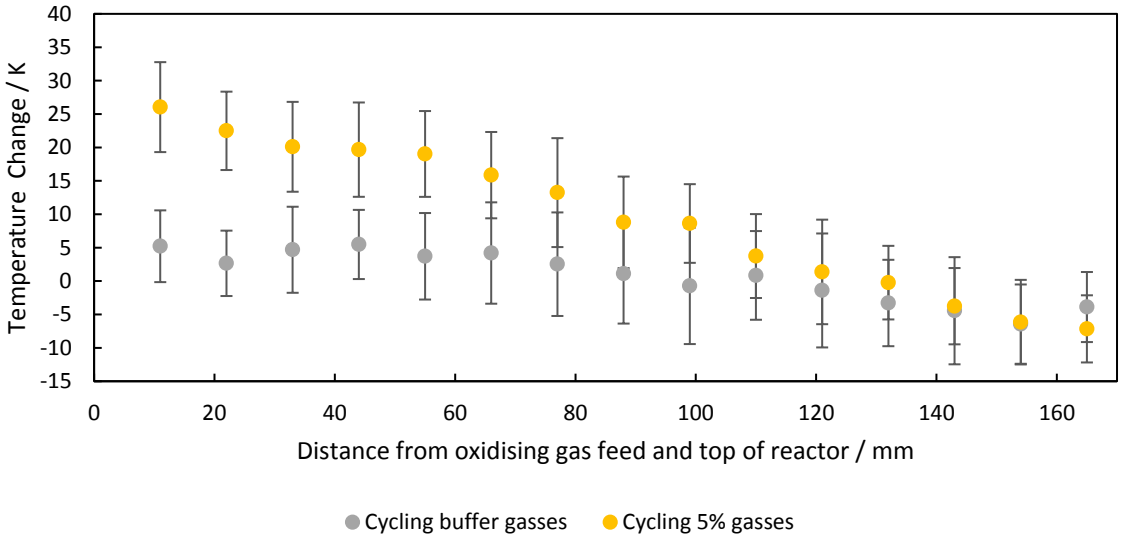
40
35
30
25
20
15
10
5
0
-5
-10
-15
Temperature Change / K
0
20
40
60
80
100
120
140
160
Distance from oxidising gas feed and top of reactor / mm
Cycling buffer gasses
Cycling 5% gasses

C

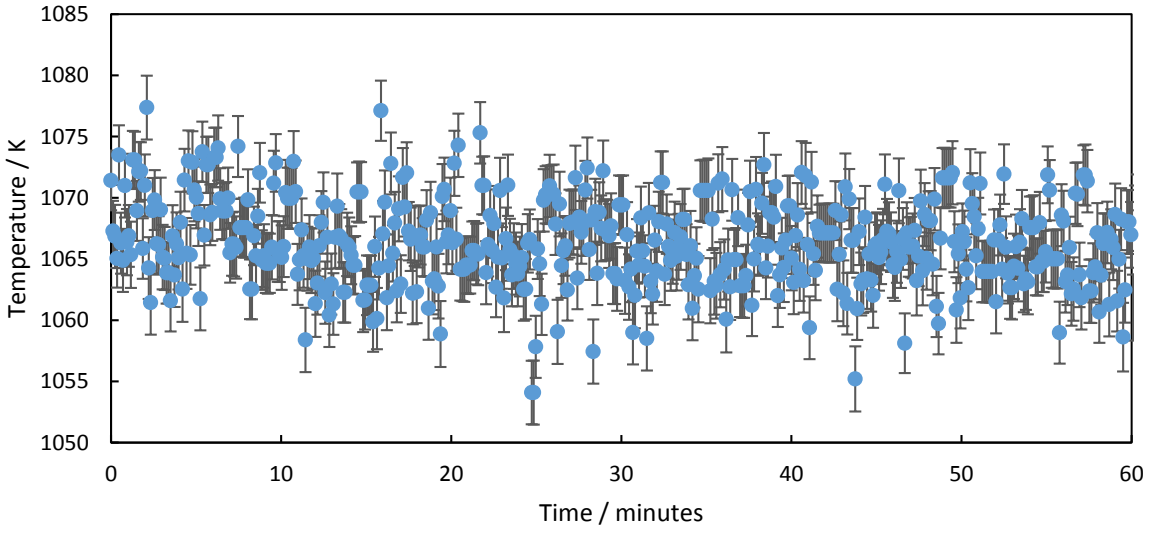
1085
1080
1075
1070
1065
1060
1055
1050
Temperature / K
0
10
20
30
40
50
60
Time / minutes

Figure 5.12: A (top), time averaged temperature, calculated using the rietveld refinement of the $Y_2O_3$, of sections of the bed with no reaction. The error bars are equal to the one standard deviation as found by the rietveld refinement. The oxidising feed end is the top of reactor B (middle), time averaged temperature difference between temperature measurement with no reaction compared with that measured during cycling between 5% CO and 5% $H_2O$ in Ar and between and 1:10 and 1:1 $CO_2$:CO buffer gas feeds. The error bars are equal to the standard deviation of the data collected over a cycle. C (bottom), Temperature of a point 40 mm from the bottom of the reactor as a function of time over three cycles of 1 minute feeds of 5% CO and 5% $H_2O$ in Ar, no noticeable changes or trends are present. The error bands are one standard error based on the rietveld refinement.

It can be seen in Figure 5.12B that the temperature of the solid changes when the reactor is being cycled and when it is not. This is due to the exothermic nature of the oxidation half cycle (Reaction 3a.4). As the cycling occurs the majority of the reaction for each half cycle occurs near its feed end causing the exothermic oxidation half cycle to heat the $H_2O$ feed while during the heat neutral reduction half cycle the temperature of the CO feed drops due to the lack of an exothermic reaction and the requirement to heat the incoming gas stream.

Figure 5.12C shows that while the average temperature changes between buffered steady feeds and cycling it does not change within a cycle once steady cycling is achieved. There are no noticeable harmonic components over multiple cycles.

The rietveld refinement gives a low uncertainty for the temperature of the reactor but the data has a greater scatter than the uncertainty in the measurement. This is due to the nature of the rietveld refinement which finds a local minimum for the fit. If there is uncertainty in the raw data this will not propagate through the calculation to the final values. This effect can lead to the actual uncertainty being larger than that calculated.

While the bed is not isothermal along its length, during cycling each point remains at a constant temperature. The bed has a 43 K variation in temperature along its length. To determine the $\delta$ of the material, this difference in temperature at different points in the bed must be account for.

*5f.ii Buffer gas reaction*

To test the ability to determine the $\delta$ state profile inside the bed the system was cycled between 1:1 $CO_2$:CO and 1:10 $CO_2$:CO counter currently as detailed in Chapter 3. While the system underwent oxidation and reduction the unit cell parameter was probed as a function of time for 15 evenly distributed points in the bed. Also, with the relatively small shifts in $\delta$ expected between these two buffer gasses the chemical expansivity was assumed to be

constant for this regime as was calculated to be 0.020 Å, using the gradient between the points corresponding to 1:1 and 1:10 $CO_2$:CO ratios on Figure 4.8A.

The use of these buffer gasses as the reducing and oxidising agents have the advantages of the $\delta$ state remaining larger than 0.2. Ensuring that the transition between the two regimes detailed in Chapter 4 is avoided resulting in only one chemical and thermal expansivity being required.

Analysis of the outlet gas composition and calculated conversions of $CO_2$ from the 1:1 feed and conversion of CO in the 1:10 feed can be seen in Figure 5.13. Before cycling the bed, the system was reduced using a 1:10 $CO_2$:CO ratio, resulting in the 1:10 half cycle having an initial conversion close to zero. Over time this conversion increases until it reaches steady cycling at a value of about 40%. In contrast the 1:1 cycle achieves a much better conversion up near 80%.

The 1:10 conversion is lower than the 50% expected from a conventional mixed feed water-gas shift reactor system with pure feed gasses, due to the limitations of the system when using low quality feeds. In fact, should the WGS reaction be carried out in a conventional reactor using equimolar feeds of 1:1 $H_2O$:$H_2$ and 1:10 $CO_2$:CO the threshold conversions to exceed, found using the methodology from Chapter 3, was 40% for $H_2O$ and 23% for CO. The chemical looping reactor continues to outperform a conventional reactor.

The difference between the conversion of the reducing and oxidising feeds is because they are not symmetric. The 1:1 ratio is limited by the oxygen capacity of the gas. The maximum change in the 1:1 stream would when the outlet stream is an almost pure CO stream; converting all of the $CO_2$ into CO. This would result in each mole of the gas donating 0.025 moles of oxygen. In comparison, the 1:10 stream can accept much more due to the increased fraction of the feed being able to undergo reaction. If all of the CO feed into the reactor was converted to $CO_2$ then each mole of gas would be able to accept 0.05 moles of oxygen because the feed under ideal conditions consists of 5% CO initially. As the reducing feed has twice the capacity for change as the oxidising feed it would be expected that the conversions for the 1:10 half cycle would only be half that of the 1:1 stream. This is seen in the conversion data shown in Figure 5.13

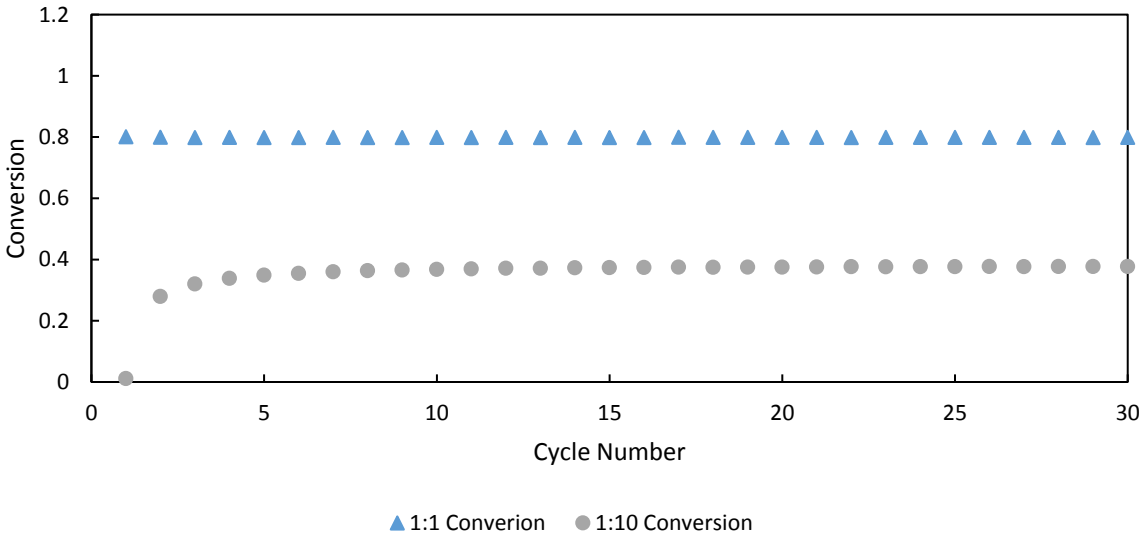


Figure 5.13: Conversion versus cycle number *operando* buffer gas feed experiment. 1:1 $CO_2$:CO (blue) and 1:10 $CO_2$:CO (grey) conversion as a function of cycle number with 60 seconds feeds of 5% 1:1 $CO_2$:CO and 5.5% 1:10 $CO_2$:CO in a balance of Ar. The bed consisted of 2.2 g of 80-160 µm LSF641 and 0.4 g $Y_2O_3$. A molar feed rate of $3.4x10^{-5}$ mol $s^{-1}$ (50 ml/min NTP) was used.

The gas leaving the reactor during a representative cycle of the buffer gas experiment is shown in Figure 5.14. The 1:1 feed is fed into the reactor just before the one minute mark and last for one minute. Looking at the 1:1 feed, it is almost completely converted to 1:10. This indicates the high conversions achieved during the cycling. The 1:10 feed begins just after the six minute mark and is initially converted to a 1:1 ratio but over the cycle this conversion decreases with more CO passing through the reactor unreacted, this is due to the stream's higher capacity to change the oxygen content of the solid, it can accept twice as much oxygen as the same amount of the 1:1 would be capable of. This data closes the oxygen balance between the half cycles and the total carbon entering and leaving the reactor during each half cycle also closes showing that no carbon deposition occurs.

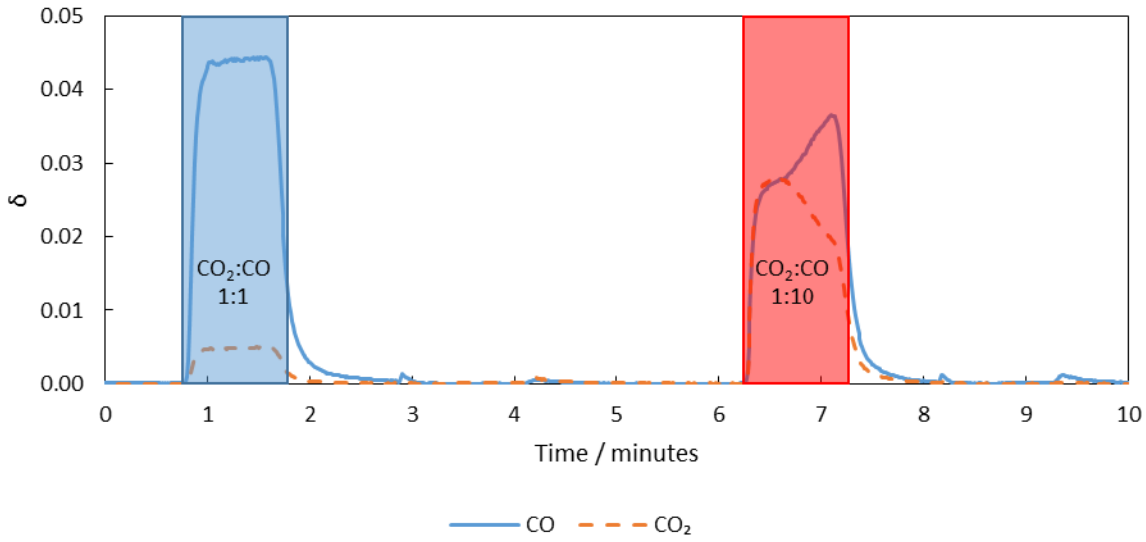


Figure 5.14: Outlet composition versus time from *operando* buffer gas feed experiment. One representative cycle from steady state conditions is shown. The system used 60 seconds feeds of 2.5% $CO_2$ and 2.5% CO (a 1:1 ratio of $CO_2$:CO), fed from 50 s to 1 minute 50 s and 0.5% $CO_2$ and 5% CO (a 1:10 ratio of $CO_2$:CO) in a balance of Ar, fed from 6 minute 10 s till 7 minutes 10 s. The bed consisted of 2.2 g of 80-160 µm LSF641 and 0.4 g $Y_2O_3$ and a molar feed rate of $3.4 \times 10^{-5}$ mol $s^{-1}$ (50 ml/min NTP)was used. The uncertainty in any measurement was less than ±100 µmol based on the methodology detailed previously.

The lattice parameter recorded every 7 s as part of the *operando* synchrotron XRD experiment was converted into the $\delta$ state using the chemical expansivity and thermal expansion coefficients. By recording the changes in temperature due to cycling of the material it is possible to determine the change in the unit cell parameter that is due to changes in the oxygen content. This can then be used to determine the $\delta$ state of the different points in the bed. By averaging the results measured when the material was not undergoing reaction, which is during the inert purges, it is possible to determine the state of the bed before and after the reducing and oxidising half cycles. The state of the bed before and after the buffer gases were fed is shown in Figure 5.15.

Figure 5.15 indicates that over a cycle the change in the lattice parameter, due to the different gas environments, is very small at the reduced end of the bed and is larger towards the oxidised end. The majority of the used oxygen capacity was found between 20 to 80 mm from the oxidising gas feed location. Most of the bed remains in equilibrium with the reduced feed of 1:10 $CO_2$:CO. This is expected as the feed's larger capacity for oxygen exchange results in it dominating the reactor bed.

The small changes in $\delta$, and therefore unit cell parameter, are dominated by the high uncertainty in their measurement, especially towards the reduced end of the bed. However, a clear gradient is visible along the bed due to the reducing gas and oxidising gasses' different feed locations. The data in Figure 5.15 represents the chemical changes along the length of the bed normalised for the temperature gradient.

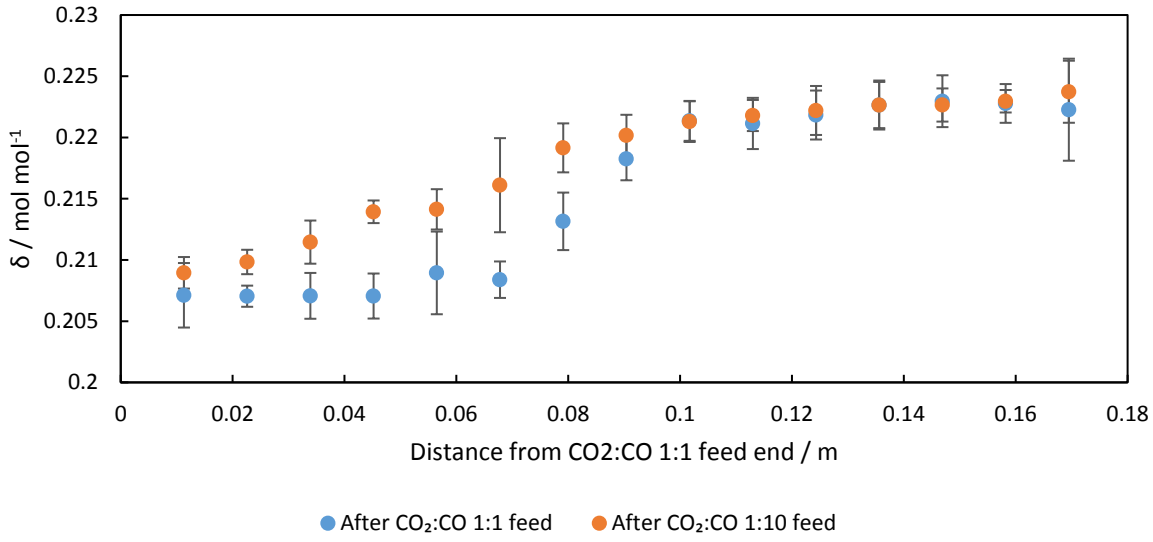


Figure 5.15: The delta state of the bed as recorded using *operando* XRD during cycling between buffer gas feeds. The system used 60 seconds feeds of 5% 1:1 $CO_2$:CO and 5.5% 1:10 $CO_2$:CO in a balance of Ar. The bed consisted of 2.2 g of 80-160 µm LSF641 and 0.4 g $Y_2O_3$ and a molar feed rate of $3.4x10^{-5}$ mol $s^{-1}$ (50 ml/min NTP)was used. The uncertainty in these measurements is one standard error based on the averaging of values recorded after each half cycle. The oxidising gas is fed from the left hand side whilst the reducing is from the right. The bed is 170mm long and 4mm in diameter.

The oxygen balance for the outlet gasses is compared with that measured for the solids. The gas analysis shows that $3.61x10^{-5}$ moles of oxygen leave the material compared with the $2.63x10^{-5}$ moles being exchanged based on the calculation based on the solids. These results show reasonable agreement, being of the same order of magnitude.

In Figure 5.16 a single point in the bed 45 mm from the oxidising feed is studied over a full cycle. This point is plotted as it shows the largest change in $\delta$ so is the least dominated by the uncertainty in the unit cell parameter from the Rietveld refinement. From this it becomes clear that the scatter in the points is large enough to obscure some of the change in $\delta$ recorded, making extraction of kinetics or the exact nature of the change difficult to quantify. For these small changes in the oxygen content this technique has little success, with small changes in

unit cell parameter caused by the chemical changes being masked by the white noise and uncertainty in the measurements.

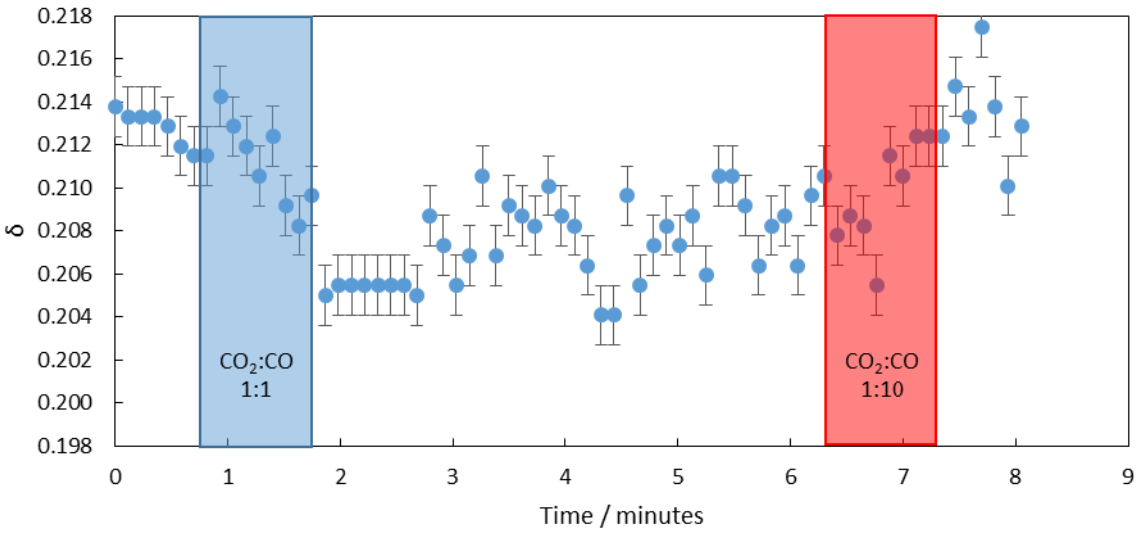


Figure 5.16: Delta state of one point in the bed 45 mm from the oxidising feed end verses time for a representative steady cycle, for a reverse-flow reactor being fed 0.5% $CO_2$ and 5% CO in Ar as the oxidising gas and 2.5% $CO_2$ and 2.5% CO in Ar as the inert gas with inert purging between cycles. The bed is a 2.2 g, 170mm length and 4mm diameter packed bed of LSF641 with 0.4 g of $Y_2O_3$. A molar feed rate of $3.4 \times 10^{-5}$ mol $s^{-1}$ (50 ml/min NTP)was used. The errors bands are equal to the effect of one standard deviation from the rietveld refinement.

*5f.iii WGS reaction*

It has been shown that using *operando* XRD techniques have had moderate success in detailing the changes in the bed over complete half cycles for small ranges of $\delta$. Next it was shown that such a technique can be used to determine the internals of an operating laboratory scaled WGS reactor. The experiment was repeated using 5% $H_2O$ and 5% CO in Ar. Given the work to date it was expected that the change in unit cell parameter would be larger with a similar magnitude noise thence being able to show more clearly how the bed changes over a cycle. However, the expected $\delta$ changes would be much larger and cross over the $\delta$=0.2 transition meaning that the assumption of a constant chemical expansivity would not hold true. The data was processed under the assumption that the chemical and thermal expansivities were constant but different on both sides of the $\delta$=0.2 transition. For $\delta$>0.2 a value of 0.0148 Å and $6.18 \times 10^{-5}$ Å/K was used and for $\delta$<0.2 0.144 Å and $5.73 \times 10^{-5}$ Å/K. The difference between the value for the expansivity for $\delta$>0.2 when compared to that used in Section 5f.2 is due to the non-linearity of the chemical expansion in this regime, here the expansivity covers a larger range of $\delta$ which changes the value for the best linear fit.

The whole bed initially had a low $\delta$ as it had been synthesised in air and was not pre-treated as in previous experiments. This resulted in initial high conversions of CO, near 100%, for the first 24 cycles before reaching steady cycling at cycle 25. This change occurs very quickly, whilst in contrast the conversion during the oxidation half cycle changed more gradually, initially starting low due to the over oxidised state of the bed (due to its initial pre-treatment with air). This is apparent in the drop in conversion seen after cycle 24 of Figure 5.17. This behaviour is consistent with the previously detailed experiments and has the same explanation.

Once steady cycling is reached 88% conversion is achieved in both the reducing and oxidising half cycles. In this experiment the flowrates were very close to equal meaning that the oxygen balance between half cycles continues to close. The carbon and $H_2$ balances for each half cycle close to within 2% and 1% respectively, showing a lack of carbon deposition or leaks in the system.

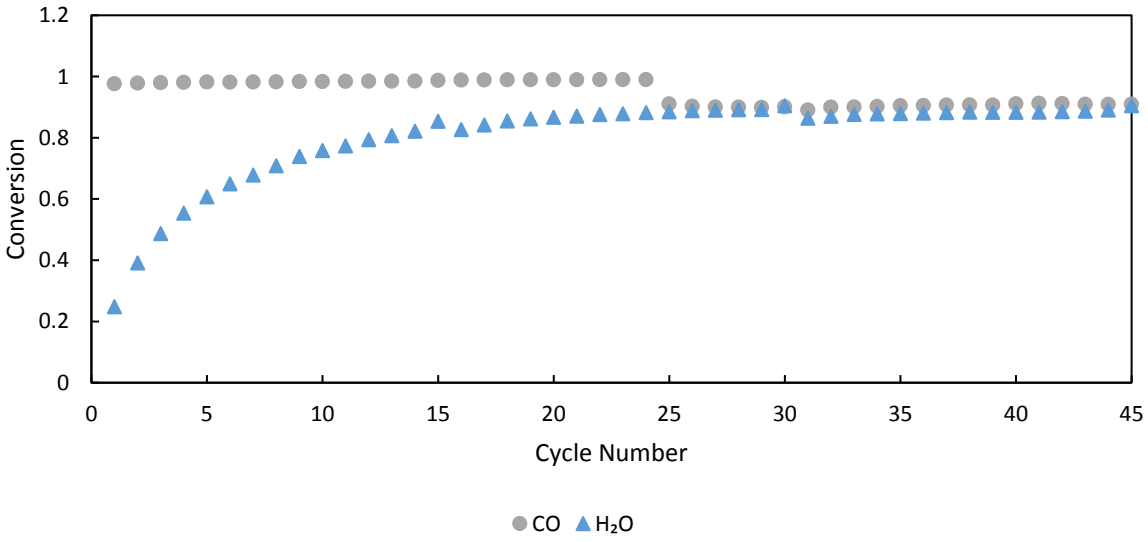


Figure 5.17: Conversion versus cycle number *operando* WGS experiment. The system used 60 seconds feeds of 5 mol% $H_2O$ and 5 mol% CO in a balance of Ar. The bed consisted of 2.2 g of 80-160 µm LSF641 and 0.4 g $Y_2O_3$. A molar feed rate of $3.4x10^{-5}$ mol $s^{-1}$ (50 ml/min NTP) was used.

In Figure 5.18 a representative cycle from the steady state operation was studied. The outlet gas shows similar patterns to those seen in previous sections with the high conversions seen throughout this thesis. The $H_2O$ feed is initially almost completely converted to $H_2$ but this decreases slowing over the half. The quantity of $CO_2$ recorded stays steady for most of the cycle before rapidly dropping 50 s before the reactive feed is stopped. This data closes the

oxygen balance between the half cycles and the total carbon and $H_2$ entering and leaving the reactor showing that no carbon deposition occurs.

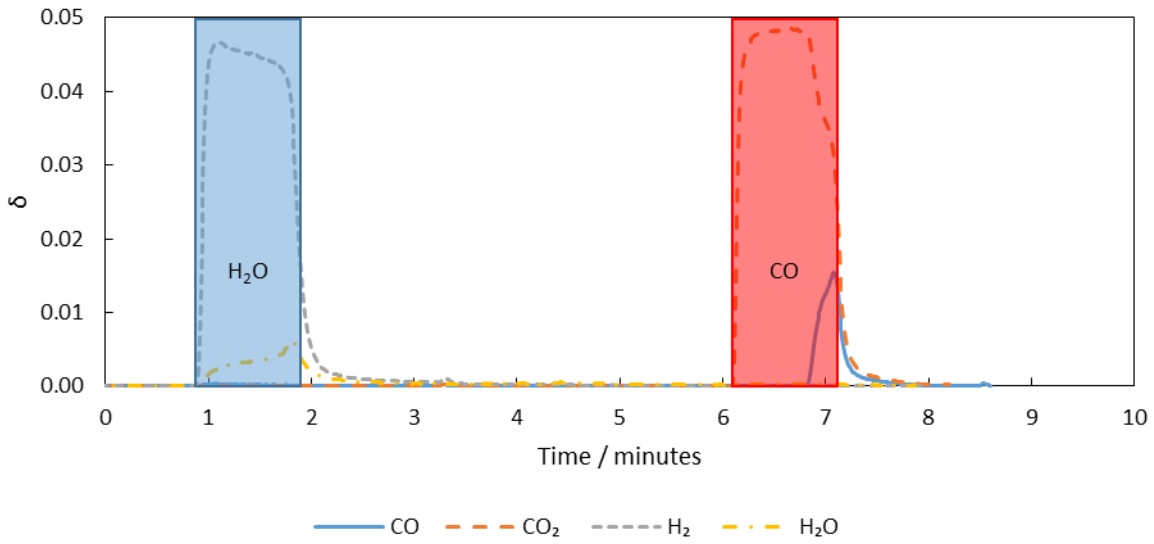


Figure 5.18: Outlet composition versus time from *operando* WGS experiment. One representative cycle from steady state conditions is shown. The system used 60 seconds feeds of 5 mol% $H_2O$ and 5 mol% CO in a balance of Ar. The bed consisted of 2.2 g of 80-160 µm LSF641 and 0.4 g $Y_2O_3$ and a molar feed rate of $3.4x10^{-5}$ mol $s^{-1}$ (50 ml/min NTP). The uncertainty in any measurement was less than ±100 µmol based on the methodology detailed previously.

Carrying out the same analysis as Section 5f.2 on the *operando* synchrotron XRD data collected every 7 s during this operation of the WGS reactor allowed for the $\delta$ state of the bed to be calculated as a function of time. By averaging the results from the inert purges it is possible for the $\delta$ state of the bed to be mapped after each half cycle. This can be seen in Figure 5.19. In contrast to the buffer gas experiments previously the whole bed undergoes a noticeable reaction here. This change is most likely due to both the increased reducing and oxidising potential of the feeds and their increased capacity for oxygen exchange with the solid.

It is noted that the gradient in the bed is not constant, with the reduced end of the bed having a more rapid change in $\delta$ per unit depth than the oxidising feed end. This is expected to be due to the non-linearity in the relationship between $\delta$ and $pO_2$. At the $pO_2$s of interest to chemical looping WGS reactions LSF641 undergoes larger changes in $\delta$ per unit change in $pO_2$ at reducing potentials associated with a CO stream than at the oxidising potentials of a mainly $H_2O$ stream, this means that the reduced end of the bed would be expected to have a steeper gradient at these reducing potentials as the small changes in $pO_2$ as the gas reacts

while it passes through cause large changes in $\delta$ while at the oxidised end these same changes in $pO_2$ would not results in a changing $\delta$ as is seen here.

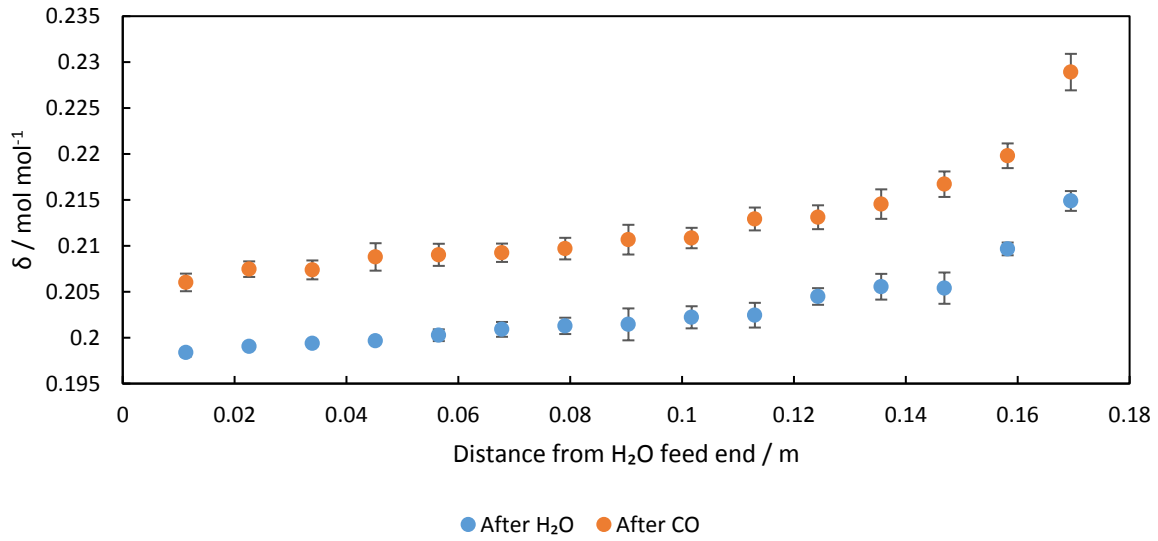


Figure 5.19: The delta state of the bed as recorded using *operando* XRD during WGS cycling. The system used 60 seconds feeds of 5 mol% $H_2O$ and 5 mol% CO in a balance of Ar. The bed consisted of 2.2 g of 80-160 µm LSF641 and 0.4 g $Y_2O_3$ and a molar feed rate of $3.4x10^{-5}$ mol $s^{-1}$ (50 ml/min NTP). The uncertainty in these measurements is one standard error based on the averaging of values recorded after each half cycle. The oxidising gas is fed from the left hand side whilst the reducing is from the right. The bed is 170mm long and has a 4mm diameter.

This technique allows for the changes over a cycle to be recorded at a given point in the bed during steady cycling. A representative point in the bed was observed as a function of time over one complete cycle, this is shown in Figure 5.20. The $H_2O$ half cycle begins after 1.5 minutes, and causes this point in the bed to begin to undergo oxidation at the 1.6 minute mark, the feed then stops after 2.5 minutes at which point this reaction at this point in the bed ceases. Then after 4 minutes of the flow of inert Ar, the feed of CO begins which after a brief pause as the CO passes through the reactor causes the reducing of this section of the bed back to its original $\delta$ state, 7.5 minutes after the start of the half cycle.

It can be seen that when the results are not averaged the uncertainty in each measurement from the Rietveld refinement dominates. This makes the gaining a complete understanding of how the material changes during reaction directly from this method impossible. The changes observed using the WGS reaction were much larger than those observed during the buffer gas experiment showing that this larger change in oxygen potential, between the half cycles, makes it easier to distinguish changes in the internal conditions of the bed. However,

it is expected that by using a simulation of the bed it may be possible to determine kinetics fitting the overall changes viewed at each point of the end.

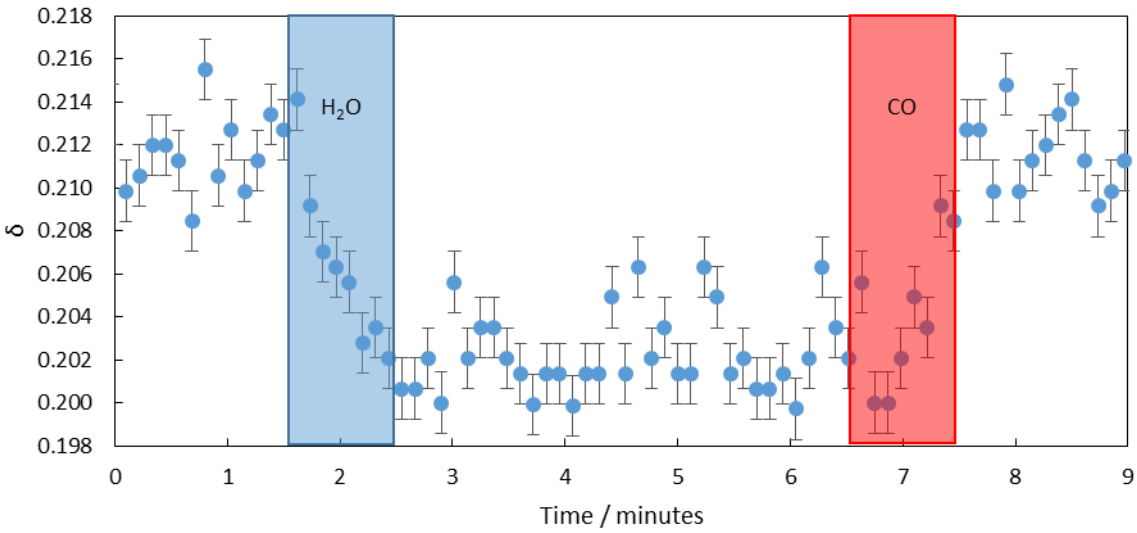


Figure 5.20: Delta state of one point in the bed, 40 mm from the $H_2O$ feed end verses time for a representative steady cycle, for a reverse-flow reactor being fed 5% CO and 5% $H_2O$ in Ar with inert purges between feeds. The bed is a 2.2 g of LSF641 and 0.4 g $Y_2O_3$, 170mm length and 4mm diameter packed bed of LSF641. The errors bands are equal to the effect of one standard deviation from the rietveld refinement.

Finally, the assumptions used in the production of this data were tested by comparing the total oxygen into and out of the system as measured by outlet gas analysis with that calculated by the change in the lattice parameter. The gas analysis shows $9.48 \times 10^{-5}$ moles of oxygen leave the sample on reduction and the lattice parameter data, using the chemical expansivity shows that $9.28 \times 10^{-5}$ moles of oxygen left material on reduction. These values are within 5% of each other while using different detection methods. This shows that the expansivity's dependence on oxygen content can be neglected for these changes and still achieve an increased understanding of the system.

### 5g Preliminary LSM821 experiments

LSM821 offers increase oxygen capacity when compared to LSF641. To test its appropriateness as an OCM for chemical looping $H_2$ production initial were carried out using the system detailed in the experimental methods section. The 5±0.25% CO in Ar was used as the reducing agent and 5% $H_2O$ in Ar was used as the oxidiser. The feed times were 1 minute for each half cycle. The packed bed consisted of 1.15 g of 80-160 µm LSM821. This bed was 95 mm long. The shorter bed was selected due to the increased capacity of the LSM821 and

the increased pressure drop experienced when attempting to achieve parity with the LSF641 beds.

In Figure 5.21 it can be seen that a LSM821 system can continue to achieve the high conversions exhibited by LSF641, with a conversion of 94% of the CO fed to the reactor and 71% of the $H_2O$. This difference in conversions is consistent with the differing flowrates of the $H_2O$ and CO feeds seen throughout. These high conversions are similar or larger to those seen in the LSF641 experiments highlighting the larger capacity of LSM821, as these are achieved when using half as many moles of OCM. The experiment was run until the system had reached a steady cycling but long term stability tests were not carried out so the expected life time of the system is unknown.

The total amount of oxygen recorded to have been removed during reduction and accepted during oxidation are equal to within 5% and results in 0.000084 mole of oxygen entering and leaving the OCM each half cycle this is 5.6% of the total oxygen capacity of the material. The higher value compared with the WGS reaction, is due to more of the oxygen capacity of the material being inside the range of $pO_2$ of the feed gasses, indicating this material's suitability for the process. The $H_2$ and carbon balances both close to within 5% indicating that the fed $H_2O$ all reaches the reactor and that there is no carbon deposited on to the OCM during cycling.

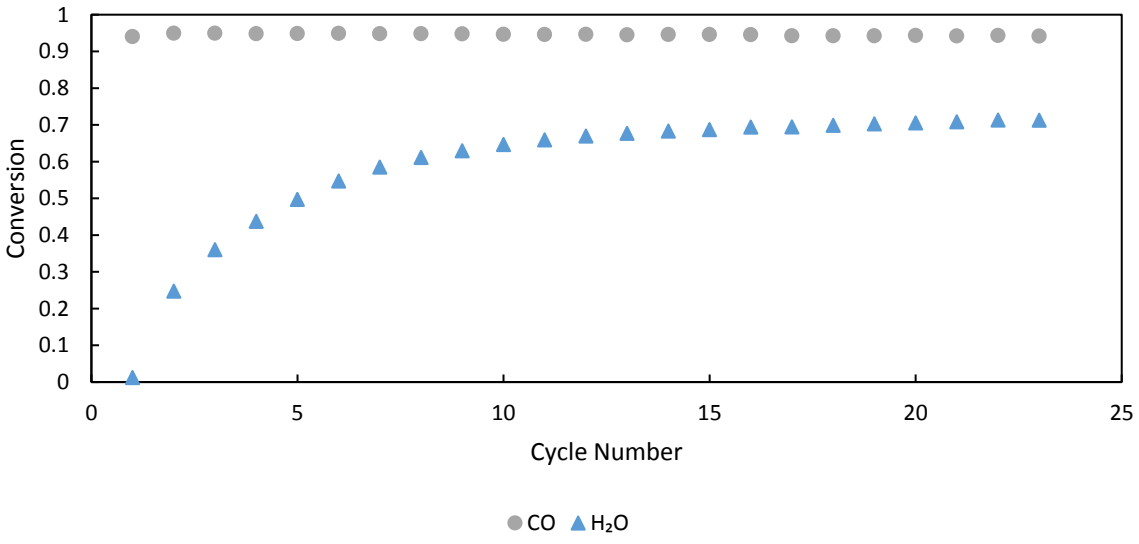


Figure 5.21: Conversion versus cycle number for 23 cycles. $H_2O$ (blue) and CO (grey) conversion as a function of cycle number with 60 seconds feeds of 5% CO and $H_2O$ in Ar. The

experiment was carried out with nominal molar flowrates of $3.4x10^{-5}$ mol $s^{-1}$ (50 ml/min NTP) with a mass of 1.15 g LSM821 and a temperature of 1093 K

As with the LSF641 the system starts with the OCM fully oxidised so initially shows complete conversion of the CO to $CO_2$ and no conversion of $H_2O$ to $H_2$ as the cycle number increases more of the $H_2O$ is converted to $H_2$ but the high conversion of CO remains throughout. This high conversions of CO to $CO_2$ is clear in Figure 5.22 where little to no CO is seen during exiting the reactor.

It can be seen that as system approached steady cycling the $H_2O$ mole fraction towards the beginning of the cycle exceeds 5 mol%. This is inconsistent with the results for LSF641 and shows that a secondary effect or experimental error must be occurring. This is because the maximum mole fraction of $H_2O$ fed to the reactor is 5%, so if axial dispersion is minimal, it should not be possible to achieve a $H_2$ mole fraction of greater than 5%. However, as the $H_2$ balance closes for the system this is most likely due to the $H_2O$ adsorbing to the material before desorbing towards the end of the cycle. This is problematic for plant operation as the spikes in $H_2$ production at the beginning of the oxidation half cycle could cause inconsistent flowrates would could complicate downstream processes. Analysis of components during the oxidation half cycle showed no carbon containing compounds confirming little to no carbon deposition occurred during the reduction half cycles.

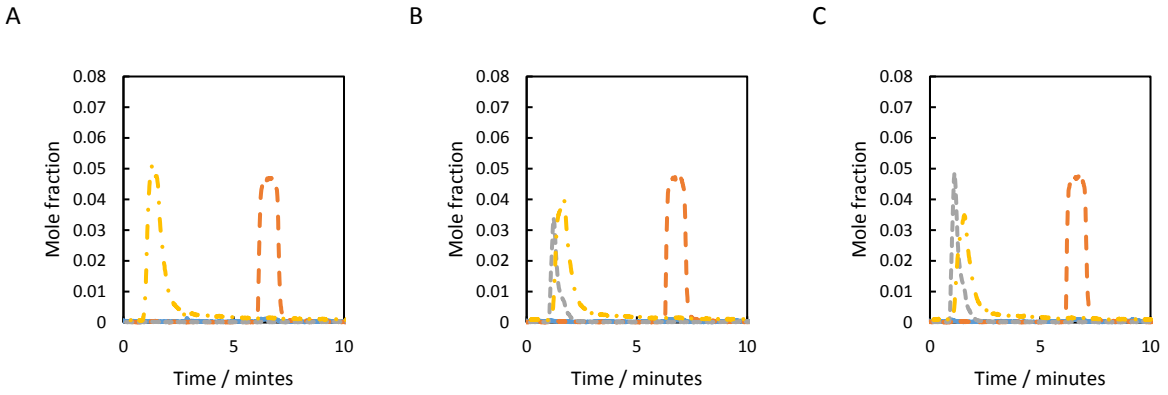

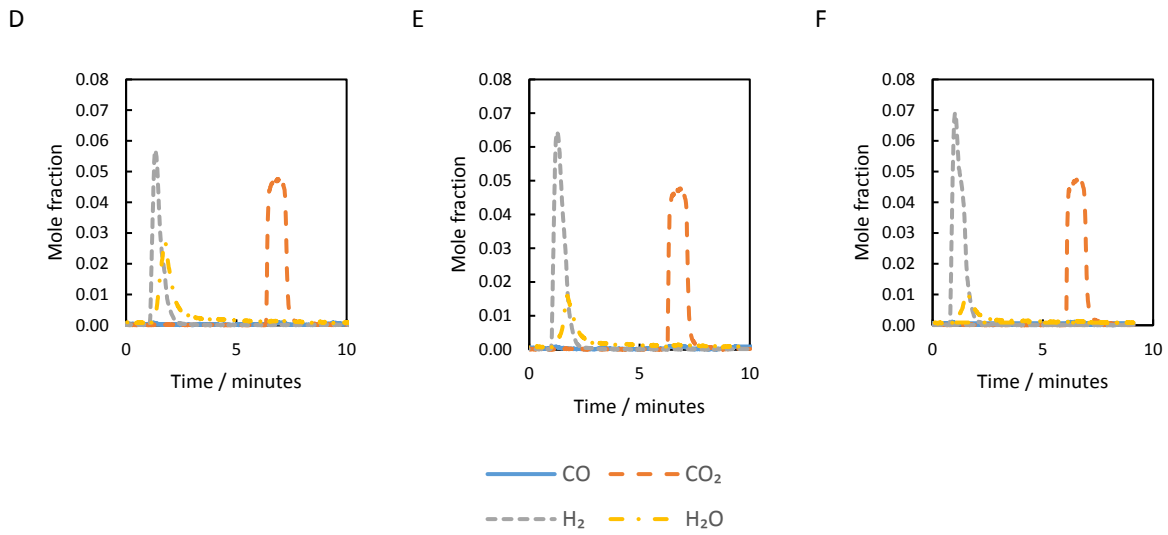


Figure 5.22: Outlet composition versus time from the long-term stability experiment. Six oxidation and reduction cycles indicating the evolution of the bed into a steady-cycling regime (Cycles 1 (A), 2 (B), 3(C), 5(D), 10(E) and 23(F)) are shown. The experiment used 5% mole fraction of reactive gas in a balance of Ar with nominal molar flowrates of $3.4x10^{-5}$ mol $s^{-1}$ (50 ml/min NTP) with an OCM mass of 1.15 g at a temperature of 1093K.

Despite the more complex nature of the relationship between the oxygen content and equivalent $pO_2$ of the OCM the outlet gas curves shows a very similar shape. As the material has the potential to be reduced out of the perovskite phase there was the possibility of seeing phase change behaviour in the outlet gas composition, with a consistent amount of $H_2O$ passing through the reactor without reacting. The lack of such a baseline concentration points either to the material not undergoing phase segregation, the formation of this new phase being slow enough that the effect was not seen over the small cycles in this experiment or that the new phase formed continues to have non-stoichiometric properties conserving the high purity $H_2$ production.

LSM821 was capable of carrying out the WGS reaction. The system did achieve the same high conversions as LSF641 chemical reactors but required only 50% of the OCM to achieve the same volume of $H_2$ production. The system suffered from unusual oxidation half cycles which were expected to be due to the LSM821 causing the $H_2O$ to adsorb to the surface to a greater degree causing a spike in $H_2$ production. This has potential to impact industrialisation of the process as additional equipment may be required to guarantee flow equalisation for downstream processes.

Further investigations would be to carryout long term stability tests on the material, to determine whether the material can sustain these conversions and product quality. Also a

system for simulating such a reactor should be developed to aid scale up such that an optimal plant design can be achieved.

### 5h Preliminary methane work

Whilst chemical looping water-gas shift generally exhibits fast kinetics, (Metcalfe et al 2019 and Mosleh et al 2009) one of the reactants, CO, has to be produced from $CH_4$ or the gasification of coal. This would require an additional onsite reactor, increasing plant foot print and costs. Should the OCM be capable of direct oxidation of methane with reasonable kinetics, it would be possible to replace the entirety of a steam methane reforming (SMR) plant with a chemical looping reactor system.

Initial experiments to were carried out to determine the effectiveness of using LSF641 as the OCM for a chemical looping reactor using 5±0.25% $CH_4$ in Ar as the reducing agent and 5% $H_2O$ in Ar as the oxidising agent. This was carried out using the same set up as that detailed in the experimental methods section and utilised a packed bed of 2.79g of LSF641 and the system was cycled 115 times.

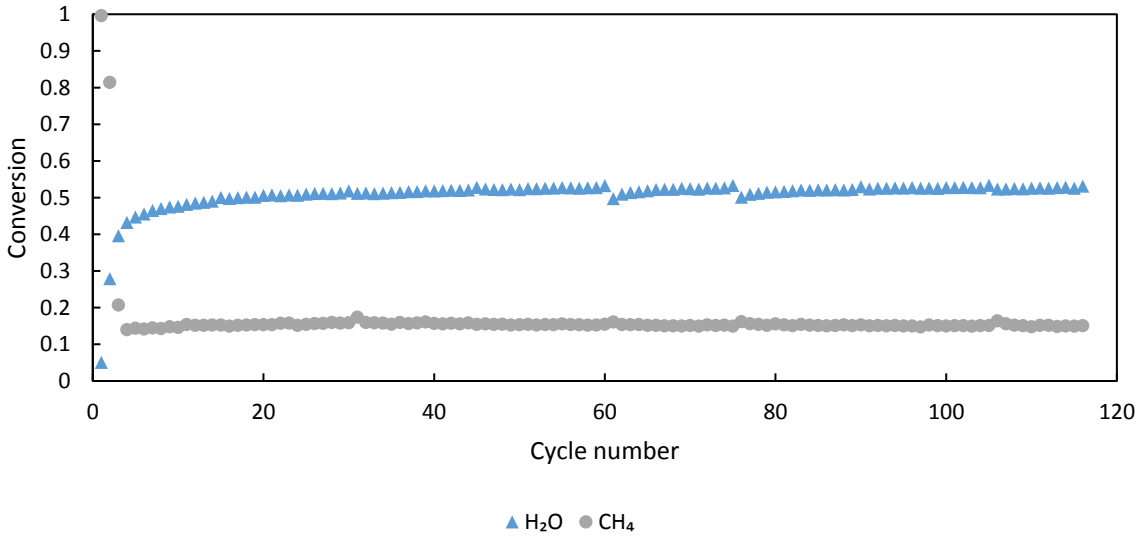


Figure 5.23: Conversion versus cycle number for 115 cycles. $H_2O$ (blue) and $CH_4$ (grey) conversion as a function of cycle number with 60 seconds feeds of $CH_4$ and $H_2O$. The experiment was carried out with 5% mole fraction of reactive gas in a balance of Ar with nominal molar flowrates of $3.4 \times 10^{-5}$ mol $s^{-1}$ (50 ml/min NTP) with an OCM mass of 2.79 g and a temperature of 1093 K

Figure 5.23 shows how the conversions develop with cycle number. The system rapidly reaches steady cycling conditions with the $H_2O$ conversion increasing from Cycle 1 to Cycle 5 and is then steady for the remainder of the experiment. The $CH_4$ is almost completely converted for the first cycle before quickly changing to its steady-cycling value (Cycles 1-5).

Once steady cycling has occurred, in contrast with the WGS reaction, the average conversions of methane and $H_2O$ were not similar to each other, 15.4% and 52.1% respectively. This difference between the methane and $H_2O$ conversions was due to stoichiometry of the reaction where it takes four moles of $H_2O$ converting to $H_2$ to convert one mole of methane into $CO_2$ and $H_2O$. Additionally, the differing mass flowrates of the $H_2O$ stream and methane stream which has been seen previously in the WGS experiments has an additional contribution. The oxygen balance carried out closes to within 2% and results in $5.8x10^{-5}$ mole of oxygen entering and leaving the OCM each half cycle this is 1.5% of the total oxygen capacity of the material. The low value is due to the oxygen capacity being outside the range of $pO_2$ of the feed gasses. As the capacity used is smaller for SMR than for the WGS studies, 1.5% compared to 2.2%, this indicates that there is an additionally limitation of using $CH_4$ over CO as the reducing gas. Despite the increases reducing potential of $CH_4$ and its greater oxygen capacity compared with CO the $CH_4$ failed to reduce the material to the same extent. It is expected that this is due to the kinetics for $CH_4$ reduction being slower than those of CO, pushing the system out of the thermodynamically limited regime.

Both the carbon and hydrogen balances for each half cycle close to within 5% indicating that carbon deposition did not occur and that the system remained leak free.

There was only a small, 2.2%, deviation in the time averaged conversion over the course of these cycles. Once steady cycling state was achieved regression on the conversion data show a slight negative gradient for the $CH_4$ conversation and a slight positive gradient for the $H_2O$ conversion. These gradients were less than the standard error indicating the material was stable.

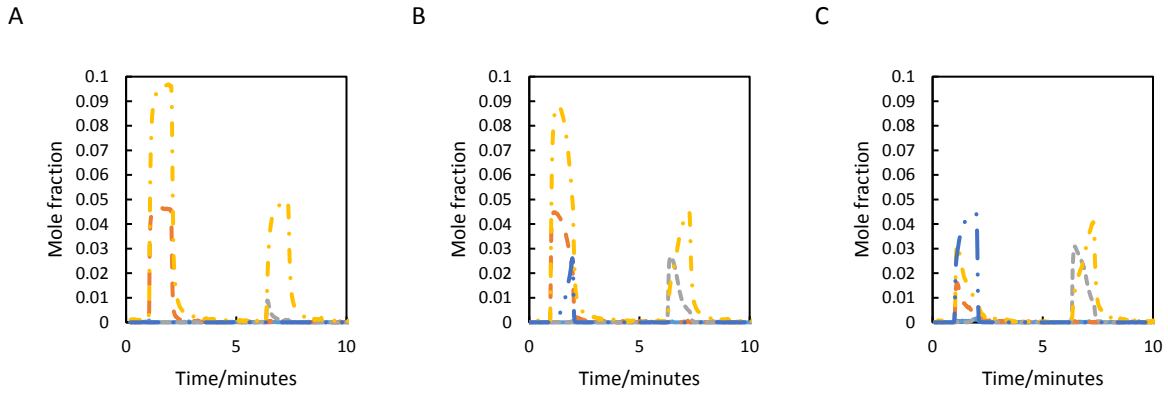

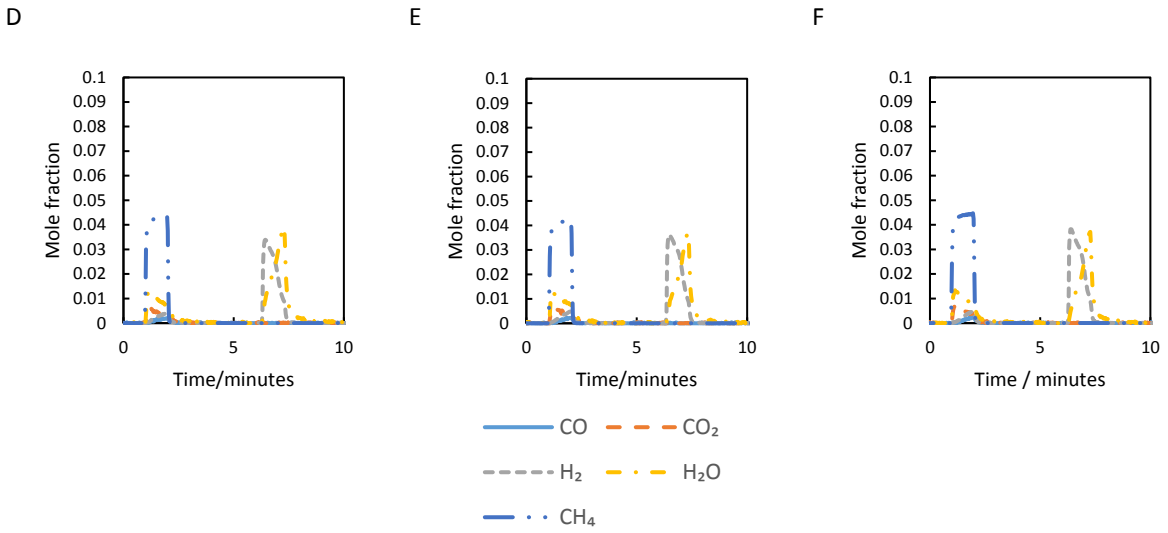


Figure 5.24: Outlet composition versus time from the long-term stability experiment. Six oxidation and reduction cycles indicating the evolution of the bed into a steady-cycling regime (Cycles 1 (A), 2 (B), 3(C), 5(D), 25(E) and 100(F)) are shown. The experiment used 5% mole fraction of reactive gas in a balance of Ar with nominal molar flowrates of $3.4x10^{-5}$ mol $s^{-1}$ (50 ml/min NTP) with an OCM mass of 2.79 g at a temperature of 1093K.

For the first cycle while the material is still fully oxidised from its synthesis in air almost complete conversion of methane to $CO_2$ and $H_2O$ is achieved. However, this conversion rapidly decreases as cycling number increases. Even at high cycle numbers the methane that undergoes reaction, is fully oxidised by the OCM. Small amounts of CO and $H_2$ are being produced by the reactor by the end of the reduction half cycle. This conflicts with a conventional SMR reactor where most of the methane is only partially oxidised maximising $H_2$ production because $H_2O$ cannot oxides $CH_4$ to $H_2O$ again. An additional issue with this chemical looping system is that a lower conversion is achieved when compared to a conventional optimised reactor.

Once steady cycling had occurred, the reduction half cycle consist of the majority of the methane passing through without reacting, that which does react, initially is fully oxidised to $CO_2$ and $H_2O$. As the half cycle continues the amount of methane reacting drops and some CO and $H_2$ is produced. These effects combine to reduce the amount of $H_2O$ and $CO_2$. During the reduction half cycle the ratio of $CO_2$ to $H_2O$ and CO to $H_2$ remains at 1:2.

The oxidation half cycle starts with almost complete conversion to $H_2$. As the cycle continues the amount of $H_2$ produced drops much more rapidly than seen in the water-gas shift reaction.

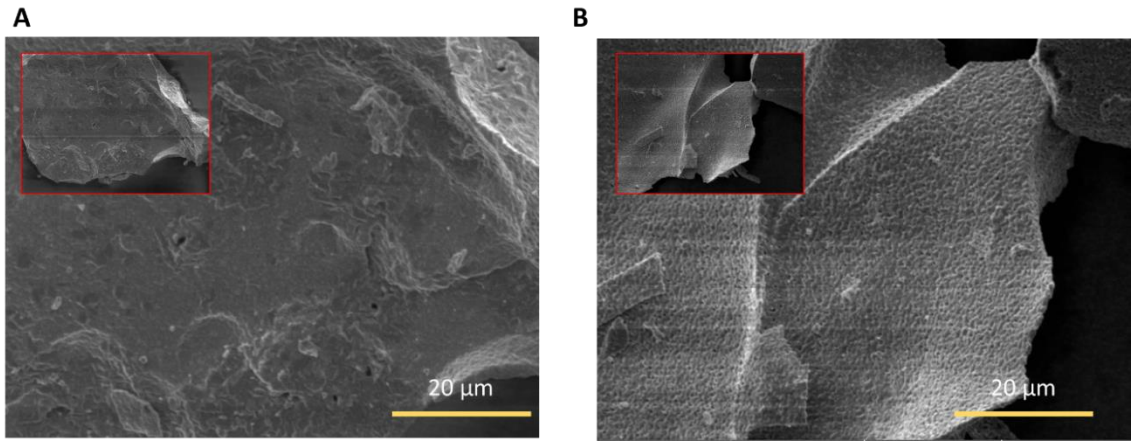


Figure 5.25: SEM micrographs of LSF641. (A) fresh (before cycling) and (B) used (after 115 cycles).

Scanning electron microscope images of the material before and after the 115 cycles (Figure 5.25) show that the material continues to maintain its macro structure, with the particle size and shapes not noticeably changing. The surface material seems to increase in porosity as it undergoes cycling with the surface appearing to roughen. Yet, it does not undergo macro structural changes as the cycling occurs, this is most likely due to the packed bed geometry minimising attrition. The material also does not appear to undergo agglomeration. This combination of a lack of attrition or agglomeration highlights that the material is capable of being cycled between the different states for this number of cycles without structural failure.

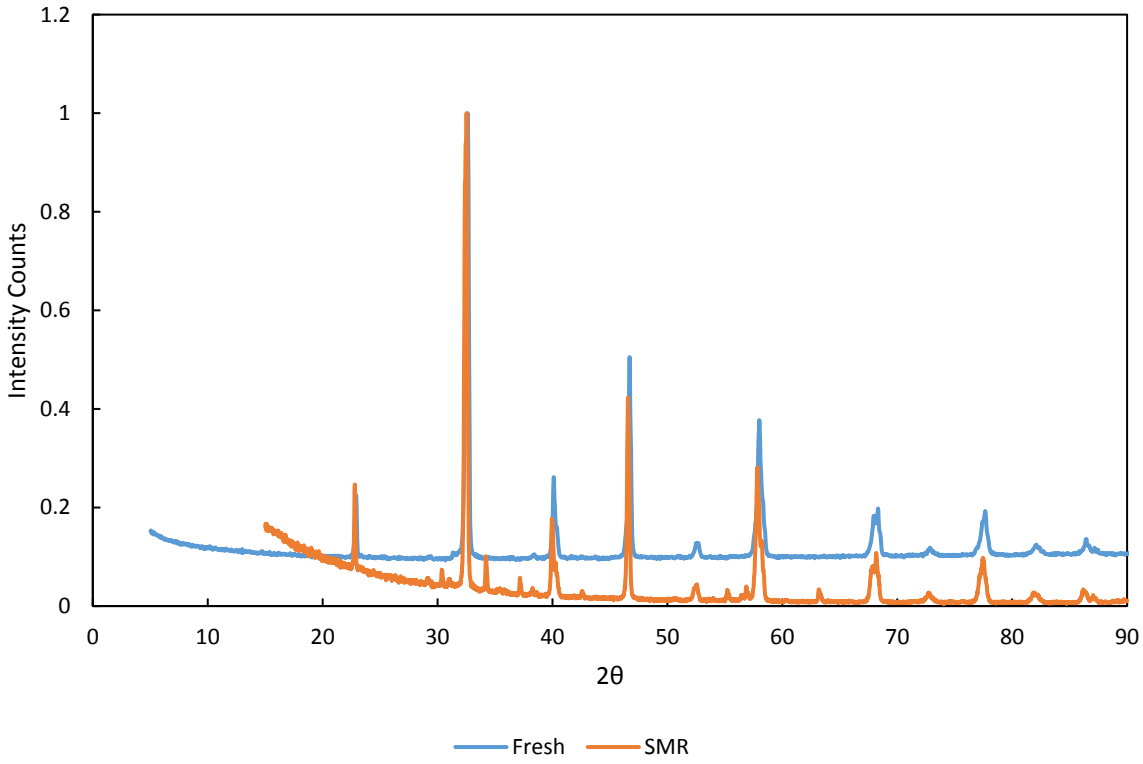


Figure 5.26: X-ray diffractogram of LSF641 (A) fresh (before cycling and (B) used from the reduced end of the bed (after 115 cycles of SMR)

After cycling the reduced end of the bed underwent ex-situ XRD. The reduced end was selected as this is the most likely to undergo phase segregation. Comparing the X-ray diffractograms of the sample before and after cycling (Figure 5.26) shows the addition of small peaks after reduction using methane, these peaks can be seen mainly between 30-40° but can also be seen between 55-60°. However, the majority of the peak locations and sizes remain similar. Carrying out phase identification shows that these peaks are most likely due to small amounts of the material decomposing into strontium iron oxide and lanthanum iron oxide. This phase segregation could lead to the material suffering from a shorter life time when used as an OCM for SMR than when used for the WGS. The small size of these peaks in the diffractogram at different 2θ angles implies these effects could be small and gradual; further work should be carried out where the material is cycled for longer to determine the effect of this decomposition on conversion and OCM lifetime.

When comparing the number of cycles before steady cycling for the WGS seen in previous chapters and SMR, it is clear that steady cycling is achieved much quicker for methane reforming. This effect is due to the methane requiring more oxygen to undergo oxidation, complete oxidation requiring four moles of oxygen atoms while the CO requires only one.

The high capacity for oxygen removal from the methane gas would be expected to result in a lower methane conversion than CO conversion with similar $H_2O$ conversion if the kinetics were fast for methane activation. Due to the respective oxygen stoichiometry of the reactions, $CH_4$ oxidation requiring more oxygen atoms than CO oxidation does.

This is not the case with both the $H_2O$ and methane conversions being much lower than the water-gas shift. This points to the activation of methane being a slower process when compared to that of the WGS. Additionally, it can be seen that the activation of the methane is kinetically limited due to the water-gas shift gases being in equilibrium to each other but not to the methane causing the mixed gases being more reduced than expected.

The methane reforming cycling OCM, when compared to the WGS cycling OCM, has undergone more surface changes, as indicated by the surface roughening. This is most likely due to methane being more reducing than the CO therefore causing increased reduction in the material destroying the surface geometry. This could point towards this material having a shorter life time when used as an OCM for SMR than it has for the WGS reaction.

The XRD diffractograms for the material also shows this increased reducing power of the methane with greater phase segregation for methane reduction than the CO reduction. This greater phase segregation for the methane reduction additionally indicates the potential of a decreased life span of the material when used for methane reduction.

However, the outlet gas analysis showed no degradation in product quality with this structural change nor was there a change in particle size. This change may not have an effect on the materials integrity so it may still be capable of sustaining the reaction for prolonged periods of time. This merits the further study where the material is subjected to a greater number of cycles to test its long term viability for SMR chemical looping.

There is no evidence of carbon deposition in the reactor during the WGS or SMR. Carbon balances using the outlet gasses closed with the total amount of carbon entering and leaving the reactor agreeing and no carbon containing molecules exiting the reactor during the oxidation half cycle. Carbon deposition would lead to OCM deactivation lowering yield or to CO or $CO_2$ leaving the reactor during the oxidation half cycle lowering the purity of the products.

LSF641 was capable of splitting $CH_4$ using $H_2O$ as the oxidiser. The system did not achieve the selectivity that conventional SMR obtains, where full oxidation occurs. When used as an OCM for SMR LSF641 undergoes more structural changes than when used for the WGS as seen in the XRD and SEM. This causes the life time of the material to be shorter for SMR than for WGS. This is due to the greater reducing power of the methane feed when compared to that of the CO.

Should this material be carried forward for SMR the next steps would be to vary feed times or flowrates to the reactor with the aim of increasing $H_2$ production. Additionally, a study should be carried out to explore the use of a three stage looping system using air to increase the methane conversions and help ensure that the system is not overall an endothermic reaction.

A further option would be to explore the use of alternative oxygen carrier materials that would have increased life time under methane reduction.

### 5g Summary of Chapter 5

It has been shown that it is possible experimentally to achieve the high conversions predicted in Chapter 4 using a chemical looping reactor to carry out the water-gas shift reaction when using LSF641 as the OCM.

The effect of reactor temperature was studied and it was shown that increasing the temperature of the reactor increases conversion but decreases product quality. When the effect of half cycle duration was studied it was found that shortening the half cycle improved conversions but that shorter half cycles were not equivalent to truncated outlet gases from a system using longer half cycles.

It was also shown that a chemical looping system can be changed to produce different chemicals with the same $pO_2$ by changing the inlet gases and that the system responds to such changes quickly and without a drop in product quality.

A study was also carried out to determine the lifetime of LSF641 as an OCM for the water-gas shift reaction, it was found that there was no noticeable drop in product quality over 1000 cycles and that the OCM material did not seem to undergo any structural changes that are indicative of the material reaching the end of its life time. Additionally no carbon deposition was found on the material.

Additionally the internals of a working chemical looping reactor for the water-gas shift reaction were studied using *operando* XRD. The state of the $\delta$ state of the bed before and after the oxidation and reduction half cycle was measured. When buffer gas feeds were used these changes were small and hard to quantify but when the larger changes in structure associated with using 5% CO and 5% $H_2O$ feeds were recorded there was good agreement between outlet gas analysis and the change in $\delta$ state of the solid. It was not possible to detail how a given point in the bed changes during reaction due to the high uncertainty in the measurements but the changes recorded happened over appropriate time scales for each half cycle.

# Chapter 6: Modelling a chemical looping reactor

Even through the use of *operando* XRD techniques it is not possible to entirely understand a chemical looping reactor but the use of mathematical modelling can further increase the understanding of the system. Accurate model systems facilitate rapid predictive experimentation with varying process parameters, hence reducing laboratory time and shortening the time between experimentation and industrial scale operations.

A chemical looping reactor using a non-stoichiometric oxide like LSF641 has additional complications when compared to systems using more conventional OCMs. The dependence of the oxygen chemical potential of such non-stoichiometric oxides on their oxygen content, while useful in practice, means that there are no phase transitions at fixed oxygen potentials accompanying a gas-solid reaction. Thus, the reaction occurring in a pack bed system cannot be modelled as a wave propagating through the bed along with the phase change, which is commonly used for reactions limited by thermodynamic equilibrium (Heidebrecht and Sundmacher 2009; Zeng et al 2012). In terms of reaction kinetics, the rate law for reversible gas-solid oxygen exchange reaction, with two or more solid phases, (such as $CuO/Cu_2O$, $Fe_3O_4/FeO$ *etc*) can be described as

$$rate = k\left(P_{O_2}{}^{n} - P_{O_2}^{*}{}^{n}\right)f(X) \qquad 6.1$$

where $r$ is the rate of reaction, $k$ the rate constant, $P_{O_2}$ the operating partial pressure of oxygen (or its equivalent), $P_{O_2}^{*}$ the equilibrium partial pressure of oxygen, $n$ the order of reaction and $f(X)$ the dependence of the rate of reaction on the degree of conversion of the solid, $X$. However, this is not valid for non-stoichiometric materials such as $La_{0.6}Sr_{0.4}FeO_{3-\delta}$ because $P_{O_2}^{*}$ would be a function of the solid conversion, instead of being independent of it. As a result, it is more difficult to extract the rate constant $k$ from a non-stoichiometric oxide experimentally than from a stoichiometric one, and the computational cost for numerical models would be higher.

In this work, an equilibrium model was developed for chemical looping $H_2$ production using the non-stoichiometric oxide LSF641 in a packed bed reactor from first principles. Key results from the numerical model, such as solid conversion and gas concentration profiles at the outlets of the reactor were compared with their experimental counterparts to aid validation of the model. The internal solid state changes of a working reactor, studied using *operando* synchrotron XRD, were compared with the simulated results.

## 6a Model development

The packed bed reactor for $H_2$ production was modelled assuming idealised conditions. These were the reactor was isothermal and isobaric, and that the gas phase being plug flow with perfect radial mixing and no axial dispersion. Dispersion was not included for simplicity, since solving the equations without dispersion already required long computational time due to the complexity of the thermodynamics of the system. It was further assumed that the gas-solid reactions (Equation 6a.2 and 6a.3) are limited by thermodynamics rather than chemical kinetics or mass transfer processes. Side reactions such as the Boudouard reaction were not considered since preliminary investigations showed no carbon deposition in the system. The physical parameters of the numerical model were based on the corresponding experiments described in the Chapter 5.

$$CO + H_2O \rightleftharpoons CO_2 + H_2 \quad \text{6a.1}$$

$$m\ CO + La_{0.6}Sr_{0.4}FeO_{3-\delta} \rightarrow m\ CO_2 + La_{0.6}Sr_{0.4}FeO_{3-\delta-m} \quad \text{6a.2}$$

$$m\ H_2O + La_{0.6}Sr_{0.4}FeO_{3-\delta-m} \rightarrow m\ H_2 + La_{0.6}Sr_{0.4}FeO_{3-\delta} \quad \text{6a.3}$$

The defect chemistry model detailed in Chapter 3 was used to define the thermodynamics of the gas solid interactions. The governing equation can be seen in Equation 6a.4

$$\frac{\delta^{0.5}(2\delta - x + 1)}{(3-\delta)^{0.5}(2\delta - x)} \times P_{O_2}^{*\ 0.25} = \frac{K_{Fe}}{K_{ox}} \times \frac{(3-\delta)^{0.5}(x + 1 - 2\delta)}{\delta^{0.5}(2\delta - x) P_{O_2}^{*\ 0.25}} - K_{ox}^{-0.5} \quad \text{6a.4}$$

where $x$ is the extent of substitution of La by Sr, in this case 0.4; $K_{ox}$ and $K_{Fe}$ are the equilibrium constants for eq. 4 and 5, respectively (Mizusaki et al 1985). The dependence of $\delta$ on $P_{O_2}$ for $La_{0.6}Sr_{0.4}FeO_{3-\delta}$ (Equation 6a.4) was approximated by a 5th degree polynomial,

$$\delta\left(\frac{\log_{10} p_{O_2}}{10}\right) = -3.89761831 \times 10^{-2} \times \left(\frac{\log_{10} p_{O_2}}{10}\right)^5 - 0.235225805 \times \left(\frac{\log_{10} p_{O_2}}{10}\right)^4 - 0.591012724 \times \left(\frac{\log_{10} p_{O_2}}{10}\right)^3 - 0.782344918 \times \left(\frac{\log_{10} p_{O_2}}{10}\right)^2 - 0.551282238 \times \left(\frac{\log_{10} p_{O_2}}{10}\right) + 3.45065388 \times 10^{-2} \quad \text{6a.5}$$

to reduce the computational cost. The approximation was made over the range $0.186 < \delta < 0.3$ with $K_{ox} = 20.2$ and $K_{Fe} = 4.98 \times 10^{-7}$($K_{ox}$ and $K_{Fe}$ are the equilibrium constants for Equations 3b.5 and 3b.4, respectively as calculated using the thermodynamics detailed by Mizusaki et al 1985.) and yielded an $R^2 = 0.99993$.

The governing equations for the reduction and oxidation of the solid, *i.e.* Equations 6a.2 and 6a.3, in the packed bed can be written as

$$-r_{CO} = u\frac{\partial y_{CO}}{\partial z} + \varepsilon\hat{\rho}_g\frac{\partial y_{CO}}{\partial t} \quad \text{6a.6}$$

$$-r_{H_2O} = v\frac{\partial y_{H_2O}}{\partial z} + \varepsilon\hat{\rho}_g\frac{\partial y_{H_2O}}{\partial t} \quad \text{6a.7}$$

$r_{CO}$ and $r_{H_2O}$ are the rates of consumption of CO and $H_2O$ respectively (mol $m^{-3}$ $s^{-1}$); $u$ and $v$ are the molar fluxes of the gas streams (mol $s^{-1}$ $m^{-2}$); $y_{CO}$ and $y_{H_2O}$ are the mole fractions of CO and $H_2O$ in the gas streams (-); $\hat{\rho}_g$ is the molar density of the gases (mol $m^{-3}$); $\varepsilon$ is the voidage of the bed (-); $z$ is the axial position along the packed bed (m) and $t$ is the time (s). The oxygen balance between the gas and solid phases at any given $(z, t)$ is given by

$$r_{CO} = (1-\varepsilon)\hat{\rho}_s\frac{\partial\delta}{\partial t} \quad \text{6a.8}$$

$$r_{H_2O} = -(1-\varepsilon)\hat{\rho}_s\frac{\partial\delta}{\partial t}. \quad \text{6a.9}$$

Under the assumption that the system is equilibrium limited, $\frac{\partial\delta}{\partial t}$ can be related to the rate of change of the equilibrium chemical potential of oxygen, *i.e.*

$$\frac{\partial\delta}{\partial t} = \frac{d\delta}{\partial P^*_{O_2}}\frac{\partial P^*_{O_2}}{\partial t}, \quad \text{6a.10}$$

$\frac{d\delta}{\partial P^*_{O_2}}$ can be calculated from Equation 6a.5 and $\frac{\partial P^*_{O_2}}{\partial t}$ can be linked to the changes in gas phase composition. For example, during reduction of the solid, $P^*_{O_2}$ of the system can be linked to the equilibrium:

$$CO + 0.5\,O_2 \rightleftharpoons CO_2 \quad K_c = \frac{P_{CO_2}}{P_{CO}{P_{O_2}}^{0.5}} = \frac{y_{CO_2}}{y_{CO}{P_{O_2}}^{0.5}} \quad \text{6a.11}$$

Here $K_c$ is the equilibrium constant. As a result,

$$\frac{\partial P_{O_2}^*}{\partial t} = \frac{\partial}{\partial t}\left(\frac{y_{CO_2}}{y_{CO}}\frac{1}{K_c}\right)^2. \quad \text{6a.12}$$

Since no carbon deposition was observed during the experimental studies detailed in Chapters 4 and 5, carbon is conserved in the gas phase, so that $y_{CO_2} + y_{CO} = y_c$ remains constant throughout the reactor during the reduction phase under isothermal and isobaric conditions. Combining Equations 6a.6, 6a.8, 6a.10 and 6a.12 yields

$$(1-\varepsilon)\hat{\rho}_s \frac{d\delta}{\partial P_{O_2}^*}\left(-\frac{2}{{K_c}^2}\frac{y_c}{{y_{CO}}^2}\left(\frac{y_c}{y_{CO}}-1\right)\right)\frac{\partial y_{CO}}{\partial t} = u\frac{\partial y_{CO}}{\partial z} + \varepsilon\hat{\rho}_g\frac{\partial y_{CO}}{\partial t}. \quad \text{6a.13}$$

Similarly, for the oxidation reaction,

$$(1-\varepsilon)\hat{\rho}_s \frac{d\delta}{\partial P_{O_2}^*}\left(2{K_H}^2\frac{y_{H_2O}}{y_H}\right)\frac{\partial y_{H_2O}}{\partial t} = v\frac{\partial y_{H_2O}}{\partial z} + \varepsilon\hat{\rho}_g\frac{\partial y_{H_2O}}{\partial t} \quad \text{6a.14}$$

$K_H$ is the equilibrium constant for the reaction

$$H_2O \rightleftharpoons H_2 + 0.5\,O_2 \quad \text{6a.15}$$

and

$$y_H = y_{H_2} + y_{H_2O}.$$

Both $K_H$ and $K_c$ are readily available from thermodynamic databases such as (Burgess 2018).

In order to model the experimental set up used for the results in Chapter 5 the oxidation (Equation 6a.14) and the reduction (Equation 6a.13) half-cycle governing equations were solved sequentially for 60 s until the system reached steady cyclic operation, where the maximum difference in $P_{O_2}^*$ at any location in the packed bed in successive cycles after the CO feed and after the $H_2O$ feed was less than 0.001%. This was typically achieved after 5 to 15 cycles. Inert purge periods were not modelled here; the *operando* XRD studies carried out in Chapter 5 indicate that the state of the solid did not change during these periods.

For each half cycle the governing equation was transformed into a system of ordinary differential equations using the method of lines by discretisation along the length of the reactor using a backwards difference scheme. The resulting system of ordinary differential equations was solved with ode45 in MATLAB.

The initial condition of each half cycle was defined so that the $pO_2$ for the gas remaining from the purge in the reactor at the start of each half cycle was the same as that at the end

of the preceding half cycle (such that the gas is in equilibrium with the solid at the beginning of each half cycle). For the 1st half cycle the OCM was assumed to be in equilibrium with $pO2$=9.38×10$^{-8}$ bar (equivalent $pO_2$ of $H_2O$ at 1093 K). For the boundary conditions, the mole fractions $y_{CO}$ and $y_{H_2O}$ were set to 0.05 at the inlet for each half cycle when the WGS was simulated. For the buffer gas simulation, the inlet conditions matched that of the buffer gas being fed.

Additionally, in an attempt to account for gas mixing in the flow system downstream of the reactor, calibration gases (5% of $H_2$, $H_2O$, CO and $CO_2$ balanced in Ar, respectively) were fed to the flow system (bypassing the reactor) for a fixed period of time so that a "top-hat" concentration profile can be assumed for the input, this consists of a step increase in concentration which is held for a set amount of time before a step decreases back to a concentration of zero. The impulse responses for $H_2$, $H_2O$, CO and $CO_2$ were estimated by de-convolving the input signal for each gas from the respective outputs recorded by the mass spectrometer using the method of conjugate gradient. The impulse responses were then convolved with the simulated outlet gas profiles to produce the simulated outlet gas results.

*6a.i Addition of axial dispersion*

This simulation scheme was edited to allow for the effect of axial dispersion in the gas phase to be determined. The addition of a dispersion term to the material balance of the system, Equations 6a.6 and 6a.7, cause the system to become more complex. This means that the new material balances for the system become:

$$-r_{CO} = u\frac{\partial y_{CO}}{\partial z} + \varepsilon\hat{\rho}_g\frac{\partial y_{CO}}{\partial t} - \varepsilon\hat{\rho}_g D_{axCO}\frac{\partial^2 y_{CO}}{\partial z^2} \quad \text{6a.16}$$

$$-r_{H_2O} = v\frac{\partial y_{H_2O}}{\partial z} + \varepsilon\hat{\rho}_g\frac{\partial y_{H_2O}}{\partial t} - \varepsilon\hat{\rho}_g D_{axH_2O}\frac{\partial^2 y_{H_2O}}{\partial z^2} \quad \text{6a.17}$$

$D_{axCO}$ is the axial diffusivity of CO in Ar for the packed bed. The axial diffusivity through a packed bed was determined from literature (Levenspiel 1999). This requires knowledge of the geometry of the reactor and the physical properties of the fluid. The viscosity of the fluid was assumed to be that of Ar in the appropriate conditions (Yaws, 2011) and for the diffusion coefficients it was assumed that interactions between Ar and the gas of interest dominated, these were found using the technique developed by Fuller et al (1966).

With the addition of a dispersion term, the total amount of carbon or $H_2$ containing compounds is no longer constant, so to accurately model the system two addition material

balances are required for the product gasses. However, as the rate of consumption of CO or $H_2O$ is equal to rate of generation of $CO_2$ or $H_2$, these two equations that govern the other half reaction are found to be:

$$r_{CO} = u\frac{\partial y_{CO_2}}{\partial z} + \varepsilon\hat{\rho}_g\frac{\partial y_{CO_2}}{\partial t} - \varepsilon\hat{\rho}_g D_{axCO_2}\frac{\partial^2 y_{CO_2}}{\partial z^2} \quad \text{6a.18}$$

$$r_{H_2O} = v\frac{\partial y_{H_2}}{\partial z} + \varepsilon\hat{\rho}_g\frac{\partial y_{H_2}}{\partial t} - \varepsilon\hat{\rho}_g D_{axH_2}\frac{\partial^2 y_{H_2}}{\partial z^2} \quad \text{6a.19}$$

The oxygen balance between the solid and gas phase and the assumption of very fast kinetics are still in effect so equation 6a.8, 6a.9 and 6a.10 still hold.

$$r_{CO} = (1-\varepsilon)\hat{\rho}_s\frac{\partial\delta}{\partial t} \quad \text{6a.8}$$

$$r_{H_2O} = -(1-\varepsilon)\hat{\rho}_s\frac{\partial\delta}{\partial t}. \quad \text{6a.9}$$

$$\frac{\partial\delta}{\partial t} = \frac{d\delta}{\partial P^*_{O_2}}\frac{\partial P^*_{O_2}}{\partial t}, \quad \text{6a.10}$$

$\frac{d\delta}{\partial P^*_{O_2}}$ can be calculated from Equation 6a.5 and $\frac{\partial P^*_{O_2}}{\partial t}$ can be linked to the changes in gas phase composition as in the previous section, however as $y_{CO_2}$ and $y_{CO}$ are no longer linked by the carbon balance, Equation 6a.12 becomes:

$$\frac{\partial P^*_{O_2}}{\partial t} = \frac{\partial}{\partial t}\left(\frac{y_{CO_2}}{y_{CO}}\frac{1}{K_c}\right)^2 . = \frac{2}{{K_c}^2}\frac{y_{CO_2}}{y_{CO}}\left(\frac{1}{y_{CO}}\frac{\partial y_{CO_2}}{\partial t} - \frac{y_{CO_2}}{{y_{CO}}^2}\frac{\partial y_{CO}}{\partial t}\right) \quad \text{6a.20}$$

Combining Equations 6a.8, 6a.10, 6a.16 and6a.20 gives:

$$\frac{\partial y_{CO}}{\partial t} = \frac{u\frac{\partial y_{CO}}{\partial z} - \varepsilon\hat{\rho}_g D_{axCO}\frac{\partial^2 y_{CO}}{\partial z^2} . + (1-\varepsilon)\hat{\rho}_s\frac{d\delta}{\partial P^*_{O_2}}\frac{2}{{K_c}^2}\frac{{y_{CO_2}}^2}{{y_{CO}}^2}\frac{\partial y_{CO_2}}{\partial t}}{\left((1-\varepsilon)\hat{\rho}_s\frac{d\delta}{\partial P^*_{O_2}}\left(\frac{2}{{K_c}^2}\left(\frac{{y_{CO_2}}^2}{{y_{CO}}^3}\right)\right) - \varepsilon\hat{\rho}_g\right)} \quad \text{6a.21}$$

Combining 6a.8, 6a.10, 6a.18 and 6a.20 gives:

$$(1-\varepsilon)\hat{\rho}_s \frac{d\delta}{\partial P_{O_2}^*}\left(\frac{2}{{K_c}^2}\frac{y_{CO_2}}{y_{CO}}\left(\frac{1}{y_{CO}}\frac{\partial y_{CO_2}}{\partial t}-\frac{y_{CO_2}}{{y_{CO}}^2}\frac{\partial y_{CO}}{\partial t}\right)\right) \qquad \text{6a.22}$$

$$= u\frac{\partial y_{CO_2}}{\partial z}+\varepsilon\hat{\rho}_g\frac{\partial y_{CO_2}}{\partial t}-\varepsilon\hat{\rho}_g D_{axCO_2}\frac{\partial^2 y_{CO_2}}{\partial z^2}$$

Combining 6a.21 and 6a.22 to give equations which are not a function of the time differential of each other gives equations 6a.23 and 6a.24 respectively. This was carried out such that the model could be transformed into a system of ordinary differential equations using the method of lines by discretisation along the length of the reactor using a backwards difference scheme.

$$\frac{\partial y_{CO_2}}{\partial t} = \qquad \text{6a.23}$$

$$\frac{u\frac{\partial y_{CO_2}}{\partial z}-\varepsilon\hat{\rho}_g D_{axCO_2}\frac{\partial^2 y_{CO_2}}{\partial z^2}+\cdots}{(1-\varepsilon)\hat{\rho}_s\frac{\partial\delta}{\partial P_{O_2}^*}\frac{2}{{K_{3a.3}}^2}\frac{{y_{CO_2}}^2}{{y_{CO}}^3}\frac{u\frac{\partial y_{CO}}{\partial z}-\varepsilon\hat{\rho}_g D_{axCO}\frac{\partial^2 y_{CO}}{\partial z^2}}{(1-\varepsilon)\hat{\rho}_s\frac{\partial\delta}{\partial P_{O_2}^*}\left(\frac{2}{{K_{3a.3}}^2}\left(\frac{{y_{CO_2}}^2}{{y_{CO}}^3}\right)\right)-\varepsilon\hat{\rho}_g}}$$

$$(1-\varepsilon)\hat{\rho}_s\frac{\partial\delta}{\partial P_{O_2}^*}\left(\frac{2}{{K_{3a.3}}^2}\frac{y_{CO_2}}{y_{CO}}\left(\frac{y_{CO_2}}{{y_{CO}}^2}\frac{\frac{1}{y_{CO}}-\cdots}{\left((1-\varepsilon)\hat{\rho}_s\frac{\partial\delta}{\partial P_{O_2}^*}\left(\frac{2}{{K_{3a.3}}^2}\left(\frac{{y_{CO_2}}^2}{{y_{CO}}^3}\right)\right)-\cdots\right)}\right)\right)\cdots$$

$$\frac{(1-\varepsilon)\hat{\rho}_s\frac{\partial\delta}{\partial P_{O_2}^*}\frac{2}{{K_c}^2}\frac{y_{CO_2}}{{y_{CO}}^2}}{\varepsilon\hat{\rho}_g}$$

$$-\varepsilon\hat{\rho}_g$$

$$\frac{\partial y_{CO}}{\partial t} = \qquad 6a.23$$

$$u\frac{\partial y_{CO}}{\partial z} - \varepsilon\hat{\rho}_g D_{axCO}\frac{\partial^2 y_{CO}}{\partial z^2} + \cdots$$

$$u\frac{\partial y_{CO_2}}{\partial z} - \cdots$$

$$\varepsilon\hat{\rho}_g D_{axCO_2}\frac{\partial^2 y_{CO_2}}{\partial z^2} + \cdots$$

$$u\frac{\partial y_{CO}}{\partial z} - \cdots$$

$$(1-\varepsilon)\hat{\rho}_s\frac{d\delta}{\partial P^*_{O_2}}\frac{2}{{K_{3a.3}}^2}\frac{{y_{CO_2}}^2}{{y_{CO}}^3}\frac{\varepsilon\hat{\rho}_g D_{axCO}\frac{\partial^2 y_{CO}}{\partial z^2}}{(1-\varepsilon)\hat{\rho}_s\frac{d\delta}{\partial P^*_{O_2}}\left(\frac{2}{{K_{3a.3}}^2}\left(\frac{{y_{CO_2}}^2}{{y_{CO}}^3}\right)\right) - \varepsilon\hat{\rho}_g}$$

$$(1-\varepsilon)\hat{\rho}_s\frac{d\delta}{\partial P^*_{O_2}}\frac{2}{{K_c}^2}\frac{y_{CO_2}}{y_{CO}}\left(\frac{{y_{CO_2}}^2}{{y_{CO}}^4}\frac{(1-\varepsilon)\hat{\rho}_s\frac{d\delta}{\partial P^*_{O_2}}\frac{2}{{K_c}^2}}{\left((1-\varepsilon)\hat{\rho}_s\frac{d\delta}{\partial P^*_{O_2}}\left(\frac{2}{{K_{3a.3}}^2}\left(\frac{{y_{CO_2}}^2}{{y_{CO}}^3}\right)\right)\cdots\right)}\right)$$

$$\frac{1}{y_{CO}} - \cdots$$

$$-\varepsilon\hat{\rho}_g$$

$$-\varepsilon\hat{\rho}_g$$

$$\left((1-\varepsilon)\hat{\rho}_s\frac{d\delta}{\partial P^*_{O_2}}\left(\frac{2}{{K_{3a.3}}^2}\left(\frac{{y_{CO_2}}^2}{{y_{CO}}^3}\right)\right) - \varepsilon\hat{\rho}_g\right)$$

Due to the symmetry of the reduction the oxidation half reactions, the governing equations of the oxidation half cycle can be given by Equations 6a.23 and 6a.24 with $u$ replaced with $v$ $y_{CO}$=$y_{H_2}$, $y_{CO_2}$=$y_{H_2O}$ and the diffusivities changed accordingly. The initial conditions are kept the same between both this model and the previous one, but the boundary conditions were set using the inlet conditions from the previous section and using the outlet conditions recommended by Patankar (1980). This states that for a suitably high Peclet number local one-way behaviour exists at the outflow boundary.

The resulting system of ordinary differential equations was solved with ode45 in MATLAB.

## 6b Effect of diffusivity on the system

To determine the effect of including the axial dispersion scheme on the simulation, a packed bed of 2.2g of LSF641, in a reactor with an internal diameter of 4 mm and a length of 170 mm was simulated, using the original model and the dispersion model.

A

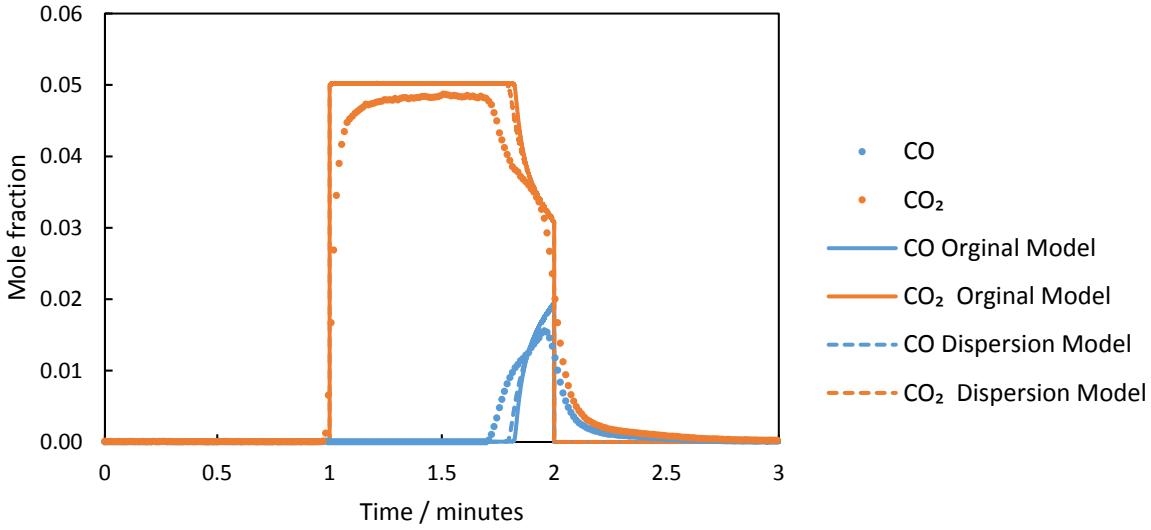


B

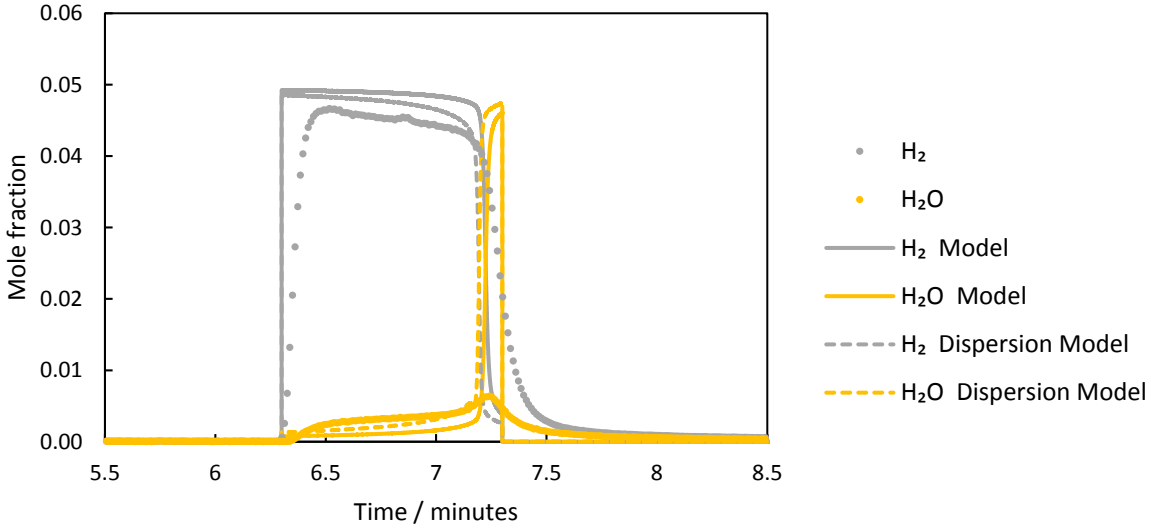


Figure 6.1: Experimental and simulated (outlet gas mole fractions verses time for a representative steady half cycles for a reverse-flow reactor. The reactive gas feeds were 5% CO (A) and 5% $H_2O$ (B) separated using inert purges. The bed is a 2.2 g, 170mm length and 4mm diameter packed bed of $La_{0.6}Sr_{0.4}FeO_{3-\delta}$. These simulations were carried out using the model detailed in Section 6a, and the model detailed in 6a.i with literature values for the diffusivities.

Neither model perfectly predicts the experimental results. With both failing to predict the nature of the rise nor the tail of the response after flow has stopped. Both models give much more square responses when compared with the experimental results.

Comparing the different simulated results in Figure 6.1 shows that upon the addition of the diffusion terms the nature of the oxidation half cycle changed. There was a minor increase in the quantities of $H_2O$ passing through the reactor and decreased $H_2$ production can be seen in the simulated outlet gas model fractions. The effect on the reduction half cycle is much smaller with little to no noticeable change with the addition of a diffusion term. This larger, but still minor, change for the oxidation half cycle is due to the larger diffusivity of $H_2$ compared with the other gasses present.

The inclusion of the diffusion term increased the computational time for each simulation by a factor of 20. This increased computational cost in conjunction with the fact that the change only had a small effect on the outlet gas composition means that when carrying out comparisons with laboratory results the diffusion term will not be applied.

It can additionally be noted that by setting the diffusivities in the system to zero both models give the same results, pointing to the stability of both reactor simulations increasing confidence in the results of the model where the assumption of no axial diffusion was made.

### 6c Simulation of *operando* XRD packed bed experiments

As Chapter 5 has shown the system can achieve high conversions, it should be operating close to its thermodynamic limit. Therefore, to test the appropriateness of this simulation scheme the *operando* XRD packed bed experiments were simulated.

Using the thermodynamic model, it was possible to predict the expected outlet gas concentrations as a function of time. These were compared to experimental results with the aim of validating the assumptions within the model. As the system is capable of maintaining consistent gas outlet conditions and conversions over prolonged operation, as detailed in Chapter 5, the study concentrated on the final state of the system. Comparing the predicted steady cycling values for the outlet gas measurements from the model with steady state experimental results.

A

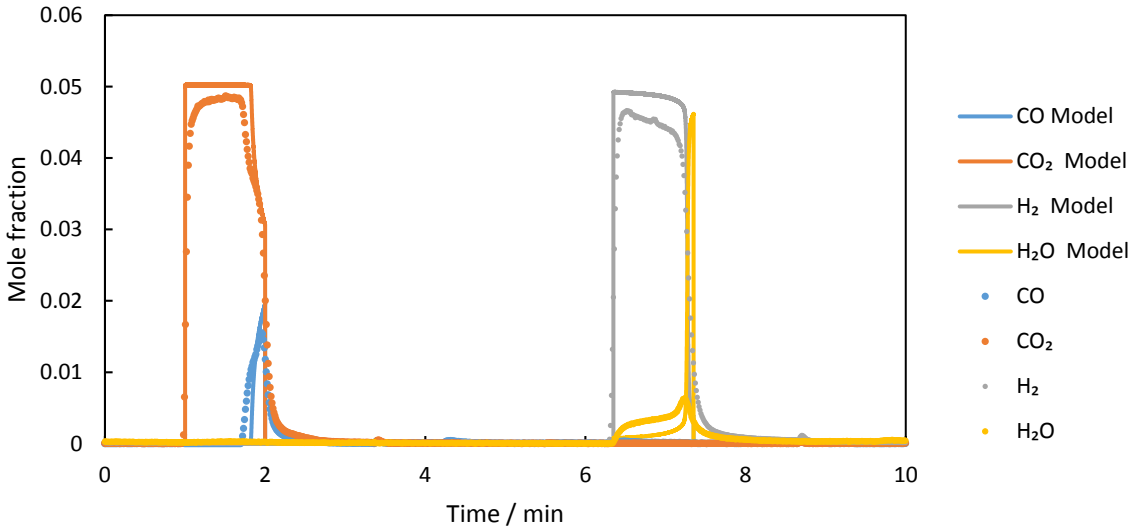


B

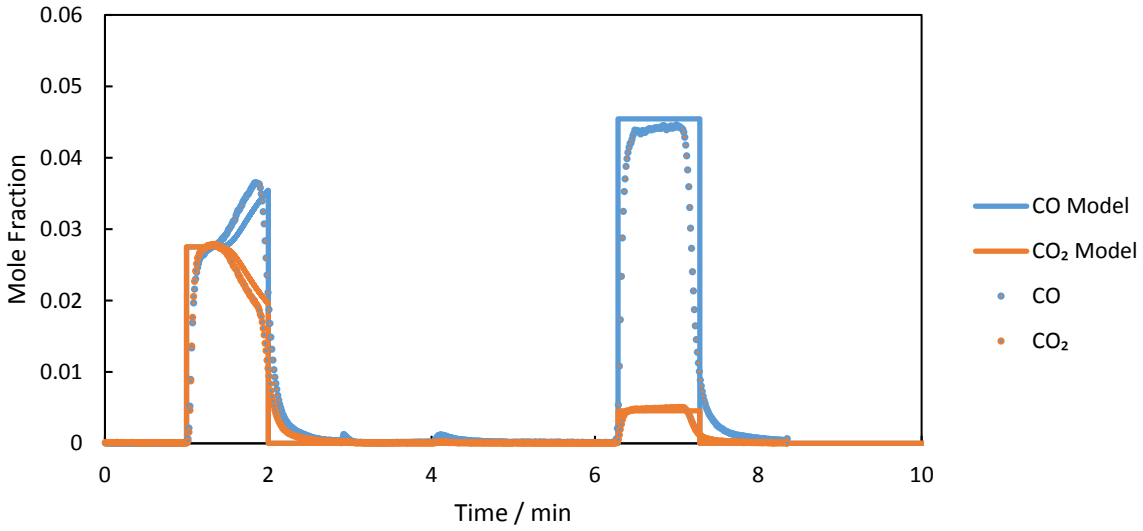


Figure 6.2: Effluent gas mole fractions verses time for a representative steady cycle for a reverse-flow reactor being A) fed 5% CO in Ar and 5% $H_2O$ in Ar or B) 5%CO with 0.5% $CO_2$ and 2.5%CO with 2.5% $CO_2$. These reactive gas feeds were separated using inert purges. The bed is a 2.2 g, 170mm length and 4mm diameter packed bed of $La_{0.6}Sr_{0.4}FeO_{3-\delta}$. The solid lines are the values predicted by the simulation of the bed while the points are the values obtained using a mass spectrometer for the lab based system.

The experimental gas analysis of the WGS reaction, Figure 6.2A, shows that the concentration of the $CO_2$ increases rapidly at 1 minute marker when the reactive gas feeds start. For the reduction half cycle, of both the WGS reaction and the buffer gas feeds, the mole fraction of the $CO_2$ holds steady for most of the half cycle before dropping after 50s in conjunction with a rise in unreacted CO being detected. This is caused by the capacity of the

OCM in the reactor becoming depleted. Once the feed has stopped, at the 2 minute mark, both gasses mole fractions decrease. The drop is instant for the model results but the gas results show a slight tail.

The oxidation half cycle shows that the mole fraction of $H_2$ rapidly increases at 6 minutes 20s. Over the half cycle the $H_2$ mole fraction drops steadily until 50s into the half cycle when the rate of decrease increases. Over the half cycle the $H_2O$ content increases so that the sum of $H_2O$ and $H_2$ stay constant at 0.05.

The gas leaving the reactor during the buffer gas experiment was analysed showing the high conversions achieved during the cycling. Both the model and experimental results show very similar results. The 1:1 feed being almost completely converted to 1:10 for the cycle and following a similar pattern to that of the WGS results. With under prediction of the product gas and over prediction of the reactant. The 1:10 feed is initially converted to a 1:1 ratio but over the cycle this conversion decreases with more CO passing through the reactor unreacted. This is due to the stream's higher capacity to change the oxygen content of the solid, it can accept twice as much oxygen as the same amount of the 1:1 would be capable of. This data closes the oxygen balance between the half cycles.

The model over predicts the amount of the products and therefore also under predicts the values for the reactants. It fails to predict the initial slope increase and the tails at the end. While these effects are small it is expected that they would be accounted for by the interactions between the solid and gas phases in the bed and the flow in the subsequent pipe work. The results from the models and experimentation do show very similar results in terms of the rest of the shape of the half cycles, with the $CO_2$ staying steady and dropping at the end of the half cycle while $H_2$ starts to decrease straight away at a smaller rate.

The similarities between the outlet gas compositions predicted by the simulation and the experimental results indicate that this system is operating close to its thermodynamic limits. The ability to predict the outlet conditions of both the buffer gas and the water-gas shift experiments using simulated results is useful for scale up. The simulation of the $H_2$ and $H_2O$ is worse than that of CO and $CO_2$ this is most likely due to the added complexity of hydrogen bonding and the smaller size of these molecules.

A

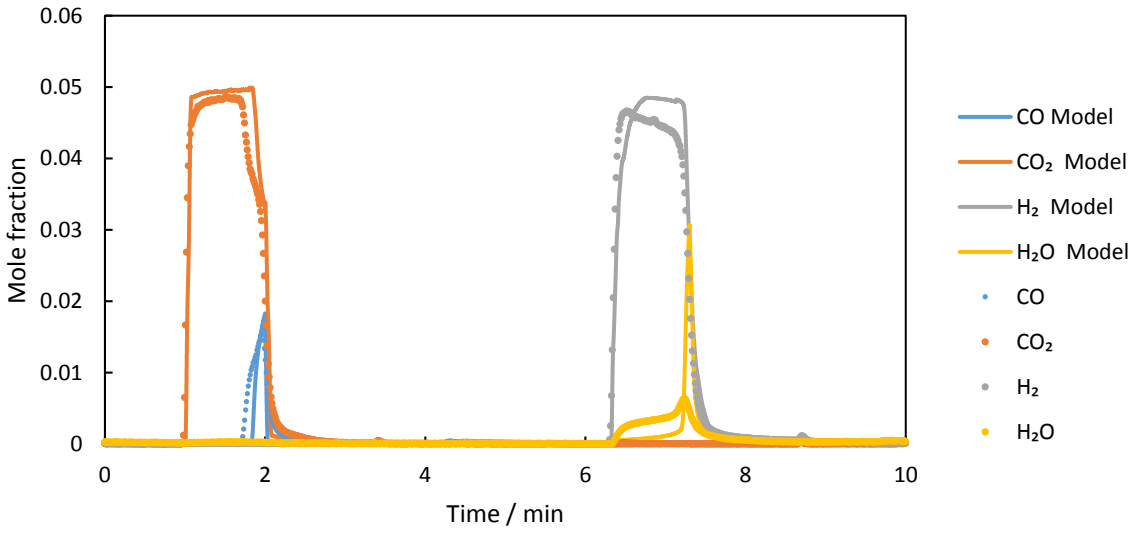


B

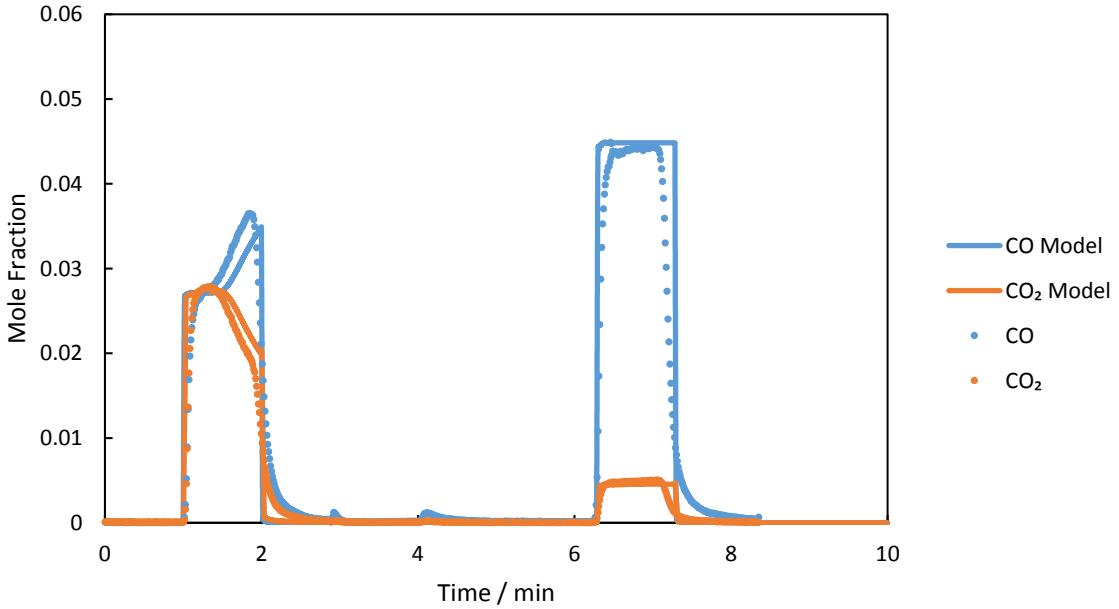


Figure 6.3: Effluent gas mole fractions verses time for a representative steady cycle for a reverse-flow reactor being fed A) 5% CO in Ar and 5% $H_2O$ in Ar or B) 5%CO with 0.5% $CO_2$ and 2.5%CO with 2.5% $CO_2$with inert feeds in-between. The bed is a 2.2 g, 170mm length and 4mm diameter packed bed of $La_{0.6}Sr_{0.4}FeO_{3-\delta}$. The solid lines are the values predicted by the simulation of the bed convoluted with the systems response to a step change, while the points are the values obtained using a mass spectrometer for a lab based system.

Convolving the model results with the impulse response of the mass spectrometer for each gas present in the system, as detailed at the end of Section 6a, as expected, smooths and changes the shapes of the curves. It does not however change the total amount of each product recorded meaning the integration of each gas over the cycle will remain the same.

For the CO half cycle this brings the results closer to those found experimentally, improving the shape of the increase at the beginning and of the middle of the cycle. However, the drop visible towards the end of the cycle no longer matches as closely. The convolution added the tails in the experimental results to the model's prediction but it does not fully account for the shape shown in the experimental results.

For the oxidation half cycle the addition of the convolution smoothed the initial increase in $H_2$ as well as adding the tails at the end of the cycle. However, the convolution failed to address the under prediction of the $H_2O$ content present initially and throughout the cycle. Additionally, the $H_2$ curve shape for the middle of the cycle no longer matches that of the experimental results. The $H_2$ plateaus in the middle of the cycle before dropping rapidly at the end rather than dropping continuously throughout the cycle before the gradient increases towards the end.

Adding the effect of the pipe work and flow inside the mass spectrometer does not cause perfect agreement between the modeled system and the experimental results, failing to completely explain the nature of the tail or the shape of the rise. Given that the addition of the convolution only achieves a slight improvement on the capability of the simulation to reflect the experimental results and its addition significantly increases the time required to simulate each packed bed it will not be included for further simulations.

The addition of the response of the mass spectrometer did not increase the accuracy of the simulation enough to reconcile the differences between the simulation and the experimental results. This indicates that there is another source for these differences it is expected that adding a term to account for adsorption and desorption from the solid phase to the governing equations would help to account for these differences. Such a term was not added here due to the increase in computational complexity that would be required.

The model detailed in Section 6a predicts the spatiotemporal variation of $\delta$ in the bed of $La_{0.6}Sr_{0.4}FeO_{3-\delta}$ under steady cyclic operation, where the $\delta$ state at the beginning and end of the cycle at any given point in space is the same. Snapshots of the expected $\delta$ state of the bed during the reduction and oxidation half-cycles of the WGS can be seen in Figures 6.4 and 6.5, while the buffer gas cycling is shown in Figures 6.6 and 6.7 respectively. These are compared to the values for the end points of the bed as obtained from *operando* XRD using the technique detailed in Chapter 5.

The system starts with the CO feeding from the left, reducing the material and increasing $\delta$. The feed end reduces first as expected, over time more of the bed starts to undergo reduction until the whole bed is being reduced as the gas flows. After 60 s, the flow of CO is stopped and $H_2O$ is fed in the reverse direction pushing the reaction front back through the bed, as well as lowering the oxidation state of the bed as a whole. This continues until the bed has returned to its original state.

The XRD data shows reasonable agreement to the model results but fails to obtain the extent of the reduction of the reducing feed end of the bed that the model predicts. It shows a greater gradient along the bed than the model predicts after the respective half cycles, this could be linked to the material at the reduced end of the bed failing to reach the $\delta$ the model predicts due to the formation of a new phase, as the end of the bed does not undergo as much reduction as expected, a more reducing feed enters the rest of the bed where it causes increased reduction, as the system still seems to return to the same state and does not undergo noticeable drop in product quality over repeated cycles the reduced end of the bed must reform the perovskite phase without degrading.

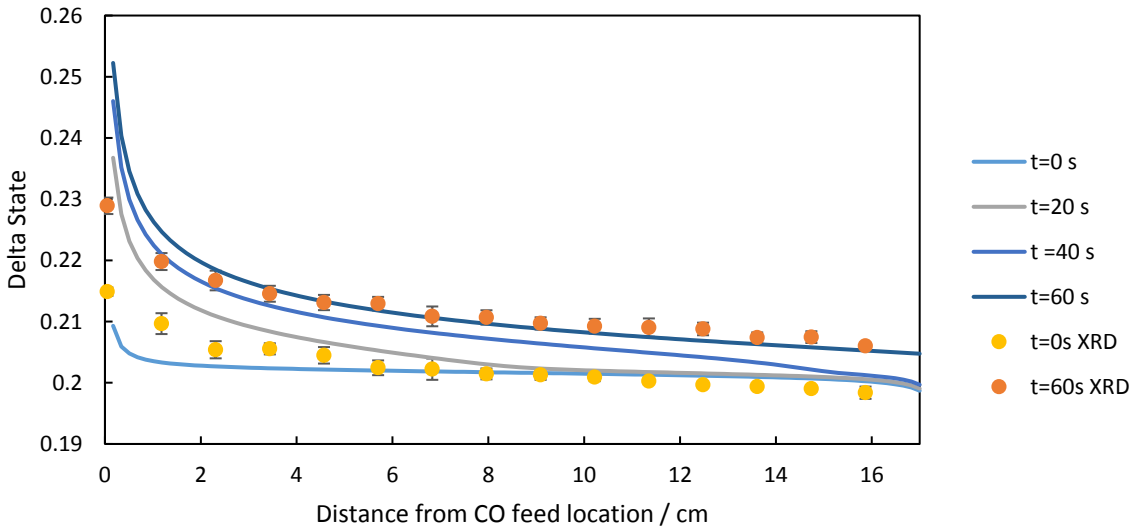


Figure 6.4: The delta state of the bed at 20s increments simulated using a thermodynamically limited model for a 60s feed of 5% CO in Ar to a bed that had reached steady cycling and as recorded using *operando* XRD. The uncertainty in these measurements is less than the marker size. The gas is fed from the left hand side. The bed is 170mm long, 4mm diameter and is 2.2g. The uncertainty of 1 standard deviation is plotted on the experimental data.

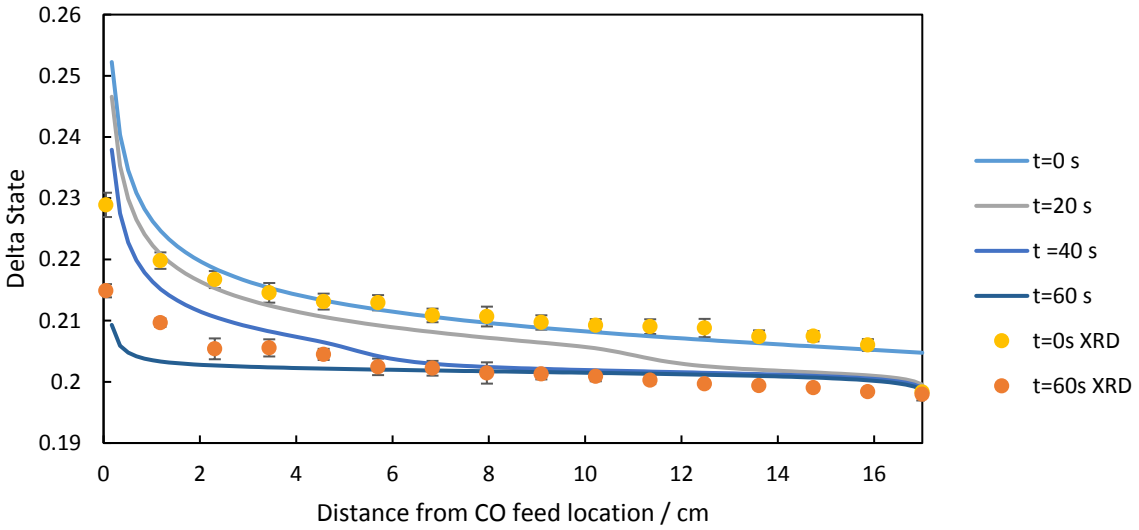


Figure 6.5: The delta state of the bed at 20s increments simulated using a thermodynamically limited model for a 60s feed of 5% $H_2O$ to a bed that had reached steady cycling as recorded using *operando* XRD. The uncertainty in these measurements is less than the marker size. The bed is 170mm long, 4mm diameter and is 2.2g. The uncertainty of 1 standard deviation is plotted on the experimental data.

An oxygen balance is carried out across a half cycle, the model predicts that $8.93 \times 10^{-5}$ mol of oxygen will leave the material during the reduction half cycle and enter during the oxidation half cycle. This was compared to the oxygen exchanged as measured using the X-ray diffraction and outlet gas recordings. Both these methods showed slightly more oxygen being exchanged in each half cycle but within the uncertainty of the measurements. The X-ray diffraction showed $9.21 \times 10^{-5}$ mol and the gas analysis saw $9.48 \times 10^{-5}$ mol. The model prediction, the X-ray diffraction measurement and the gas analysis all agree within 6%. This confirms the model's validity as it can closely predict the magnitudes of the changes occurring inside the beds as recorded using two separate methods.

Carrying out the same analysis using the buffer feed gasses gives similar results with a wave propagating through the bed. Here the lower capacity for oxygen transport by the gases results in the change only being seen in half of the bed.

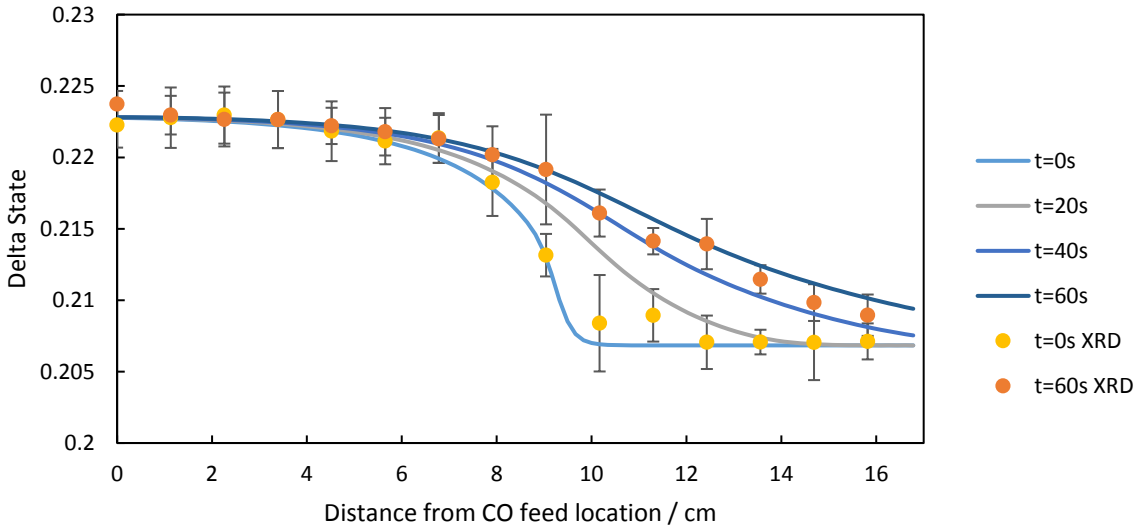


Figure 6.6: The delta state of the bed at 20s increments simulated using a thermodynamically limited model for a 60s feed of 2.5% $CO_2$ and 2.5% CO in Ar to a bed that had reached steady cycling and as recorded using *operando* XRD The uncertainty in these measurements is less than the marker size. The gas is fed from the left hand side. The bed is 170mm long, 4mm diameter and is 2.2g. The uncertainty of 1 standard deviation is plotted on the experimental data.

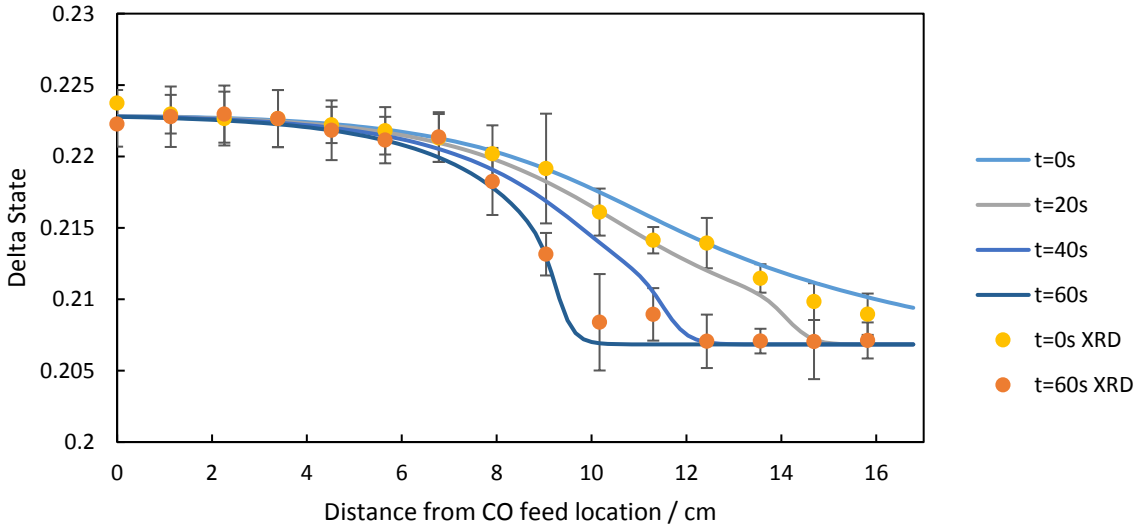


Figure 6.7: The delta state of the bed at 20s increments simulated using a thermodynamically limited model for a 60s feed of 5% $CO_2$ and 0.5% CO in Ar to a bed that had reached steady cycling and as recorded using *operando* XRD. The uncertainty in these measurements is less than the marker size. The bed is 170mm long, 4mm diameter and is 2.2g. The uncertainty of 1 standard deviation is plotted on the experimental data.

Repeating the oxygen balance on the bed shows that the model predicts that 4.18 $x10^{-5}$mol of oxygen will transfer between the gas and the solid each half cycle. This was compared to the oxygen exchanged as measured using the X-ray diffraction and outlet gas recordings. Both these methods showed more oxygen being exchanged in each half cycle. The X-ray diffraction showed 2.63 $x10^{-5}$mol and the gas analysis saw 3.62 $x10^{-5}$mol. For this system the

model results and the values measured using XRD have a larger discrepancy than for the water-gas shift reaction which is to be expected given the smaller total oxygen transfer. The model and the gas agree reasonably well to within 14% however, the higher uncertainty in the lattice parameter and smaller change in the value result in a larger discrepancy of almost 40%. This disagreement is much larger than for the WGS experiment, pointing to the smaller overall change reducing the effectiveness of the technique.

A

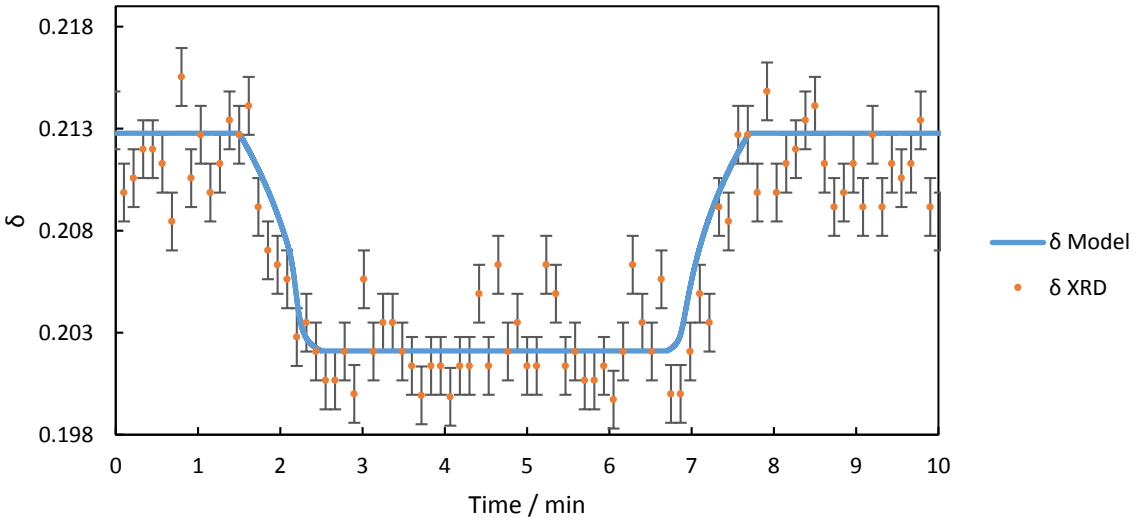


B

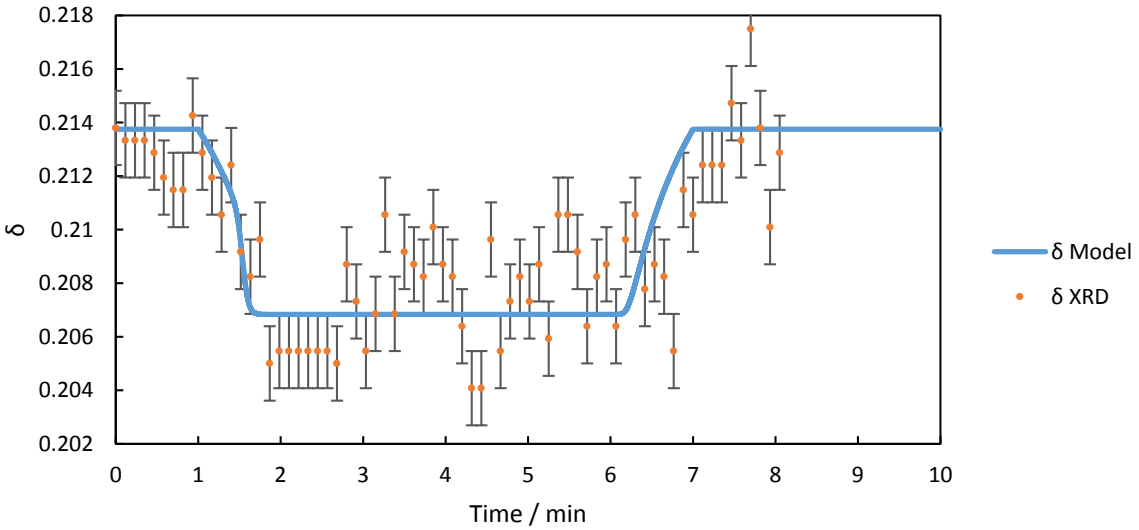


Figure 6.8: Delta state of one point in the bed, A) 40 mm from the $H_2O$ feed end verses time for a representative steady cycle, for a reverse-flow reactor being fed 5% CO in Ar and 5% $H_2O$ in Ar with inert feeds in-between. B) 128 mm from the oxidising feed end verses time for a representative steady cycle, for a reverse-flow reactor being fed 5% $CO_2$ and 0.5% CO in Ar as the oxidising gas and 2.5% $CO_2$ and 2.5% CO in Ar as the inert gas with inert feeds in-between. The bed is a 2.2 g, 170mm length and 4mm diameter packed bed of $La_{0.6}Sr_{0.4}FeO_{3-}$

$_{\delta}$. The solid line is the value predicted by the simulation of the bed while the points are the values obtained by analysis of the XRD results. The errors bands are equal to the effect of one standard deviation from the rietveld refinement.

When looking at how one point in the bed changes as a function of time whilst undergoing cycling. It can be seen that for both the WGS and buffer gas experiments the curves are not symmetrical but do return to the starting conditions after a full cycle. The size of the change is consistent with the model's prediction for both. The confirmation of the exact shape of the curve is not possible due to its rapidity. The limited number of data points describing the change along with the uncertainty and inherent noise within the data points exacerbates this problem.

Comparison of the outlet gas conditions from the simulations and experimental techniques show that the outlet conditions are predicted reasonably well with the simulation. The reactor underwent *operando* X-ray diffraction during cycling, studying the different points in the bed as they were reduced and oxidized. This allowed for multiple diffraction patterns to be obtained as the material underwent lattice expansion or contraction, investigating how the delta state of the material changes over cycling allowing for the confirmation of the internals of the system.

The changes in the cubic cell parameter is near the limit of what is measurable by the equipment used. The measuring changes are in the order of 0.0001 angstroms, resulting in the data having a large degree of scatter. It does have a clear quick increase and decrease at the correct time in the cycle, but the uncertainty in the results mean that while this data indicates that the model is suitable is not sufficient to fully validate the model. These results do however show good agreement for the extent of reaction at each point in the bed, with the $\delta$ state before and after each half cycle being consistent between the model and the experimental results.

### 6d Temperature optimization

The temperature optimization experiments detailed in Chapter 5 allow for further validation of the model, due to the different geometry of the reactor and the varying thermodynamics of the system due to the temperature changes. The packed bed used in this experiment had a larger internal diameter, 0.007 m rather than 0.004 m, this results in a similar mas of material having a shorter bed length.

Comparisons between the predicted outlet gas results from the model and the experimental results collected are seen in Figure 6.9.

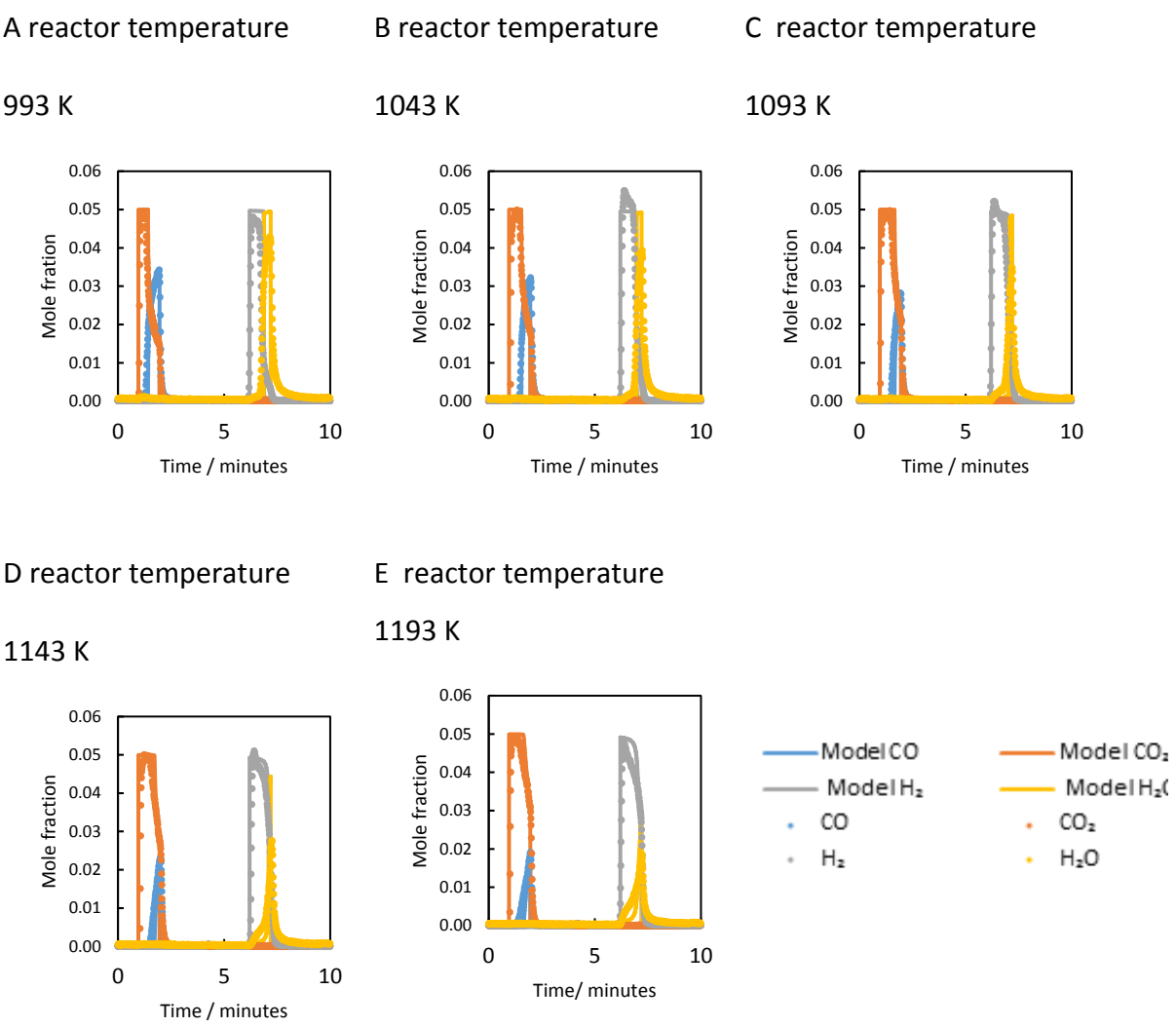


Figure 6.9: Outlet composition versus time from the long-term stability experiment. Six oxidation and reduction cycles indicating the effect of reactor temperature on the outlet gas compositions (A) 993 K, B) 1043 K, C) 1093 K, D) 1143 K and E) 1193 K) are shown. The experiment used 5% mole fraction of reactive gas in a balance of Ar with nominal molar flowrates of $3.4 \times 10^{-5}$ mol $s^{-1}$ (50 ml/min NTP) with an OCM mass of 2.39 g at a variety of temperatures. The packed bed had internal diameter of 0.007 m and a length of 0.06 m. The uncertainty in any measurement was less than ±100 ppm based on the analysis Chapter 2.

Comparison between the simulated and experimental results shows good agreement but at all temperatures the model continues to over predict product concentrations and under predict reactant concentration in the gas outlet. However, the timings of the drop in product mole fraction is consistently predicted using the model for both the oxidation and reduction half cycles. This shows that the system continues to operate near its thermodynamic limit in this range of temperatures considered. The model predicts the increased conversion and

drop in product quality as the temperature increases. The model is capable of accounting for the different geometry used here, accurately predicting outlet gas composition in this shorter, wider and horizontal packed bed, the aspect ratio of the bed changes from 42.5 to 8.6 a significant change in the geometry of the packed bed. The system can accurately simulate the system regardless of the temperature of the reactor, correctly predicting the outlet compositions of the gas. This indicates that the prediction made in Chapter 5 that the decreased product quality at higher temperature is due to the thermodynamics of the system and not related to side reactions or other effects is true.

### 6e Half cycle duration optimization

In Chapter 5 studies were undertaken to explore the effect of half cycle duration on product quality and quantity. These studies used a smaller mass of OCM in the bed than previously simulated but continued to use the 0.04 m inner diameter beds. Simulations were carried out to replicate these studies to further validate the model both for smaller quantities of OCM and for the changing half cycle duration.

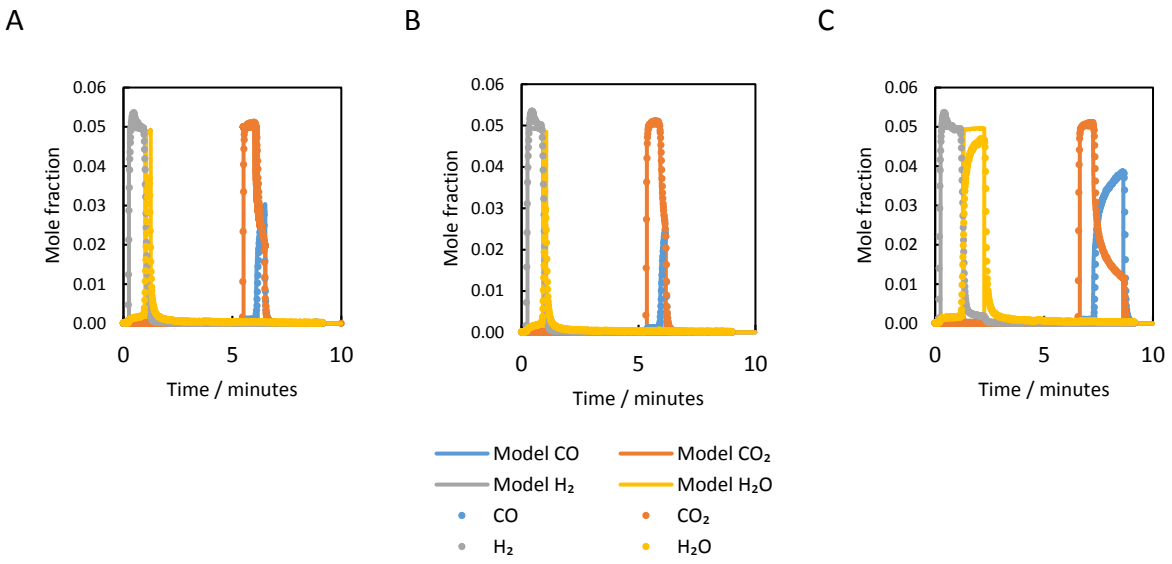


Figure 6.10: Representative outlet gas composition as a function of time for the half cycle duration optimisation experiment compared to the prediction of the thermodynamic model. Three representative oxidation and reduction cycles indicating the effect of redox duration on the outlet gas compositions (A) 60 s, B) 48 s and C) 120 s) are shown. The experiment used 5% mole fraction of reactive gas in a balance of Ar with nominal molar flowrates of $3.4 \times 10^{-5}$ mol $s^{-1}$ (50 ml/min NTP)with an OCM mass of 1.43 g at 1073 K.

The model continues to predict the outlet gas shapes for each of the different half cycle durations studied here. The initial spike above 5% observed in the $H_2$ is not predicted for any of the durations, this is because this spike is most likely due to condensation of the $H_2O$ in its

feed line causing an increased mole fraction of $H_2O$ at the beginning of the cycle while this condensation of evaporated before the bed. This initial increase mole fraction cannot be predicted by the model as the governing equations do not allow for it.

For this geometry the reduction half cycle is well predicted for all of the half cycle durations studied. The oxidation half cycle is less well predicted. The $H_2$ outlet gas follows a similar pattern in both the simulated and laboratory results but the $H_2O$ is under predicted at first and then over predicted. This discrepancy could be due to stronger adsorption interactions between the $H_2O$ and the solid phase than the other gasses. This would cause the $H_2O$ feed to both increase then decrease more slowly than the idealised model. $H_2O$ is more effected that the other gasses present in the system.

As the half cycle duration increases the degree to which the model accurately predicts the outlet gas composition decreases. The 48 s half cycle has the strongest correlation between the model and the laboratory results followed by the 60 s and then the 120 s. The shorter half cycle has a smaller quantity of $H_2O$ in the outlet so the effect of the interactions between the solid and the $H_2O$ inside the system is less pronounced and noticeable. The 120 s cycle exhibits the increased interaction with the $H_2O$ most clearly as there is the highest amount of $H_2O$ passing through the reactor unreacted.

### 6f Sensitivity analysis

Sensitivity analysis was carried out to determine the model's sensitivity to the uncertainty in the input conditions. Where well detailed uncertainties were known, values were taken from literature and the effect of a one standard deviation perturbation in that value was shown. Where the variable in question is a controlled variable a 10% perturbation was used to allow for an understanding of the effect on the reactor of changing these parameters. The packed bed used for the *operando* XRD studies was simulated and used as the base case. This consisted of 2.2 g of LSF641 in a 4 mm diameter reactor. It has a total length of 170 mm and was cycled between 5% CO and 5% $H_2O$ in Ar at 1093 K. The variation caused by each of the changes in indicated in Figure 6.11.

A $K_{ox}$ +/- 1 SD

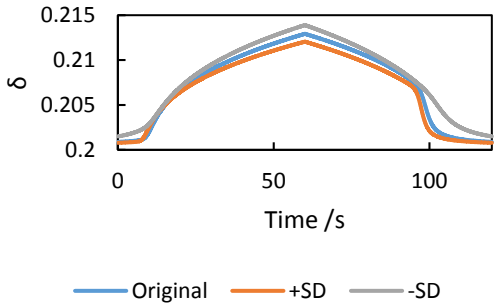


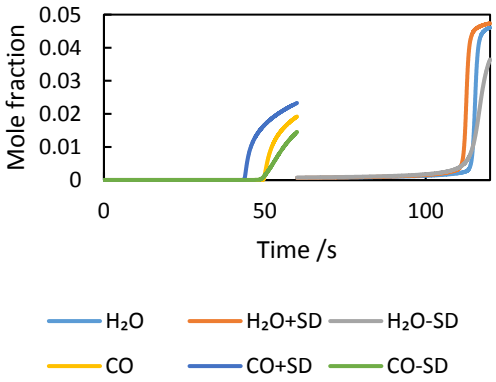


B $K_{Fe}$ +/- 1 SD

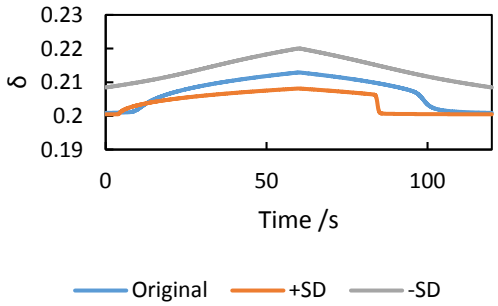


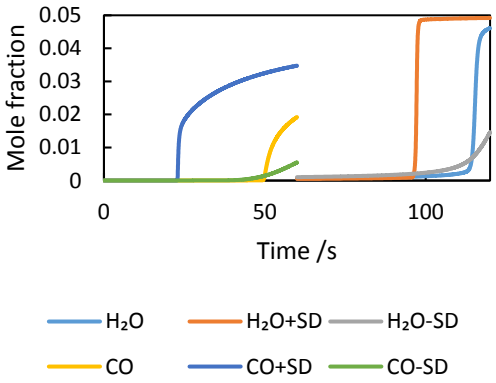


C $H_2O$, $H_2$ & $O_2$ +/- 1 SD

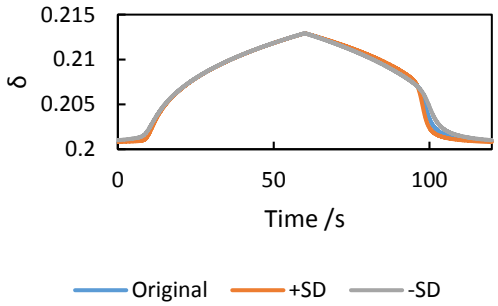


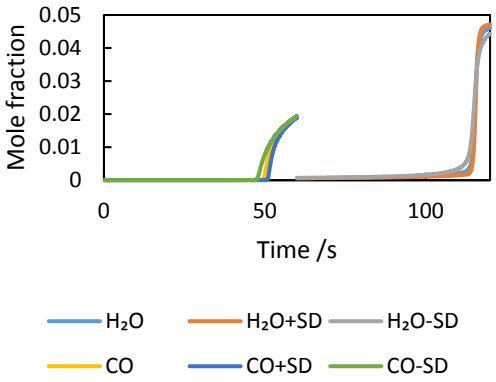


D $CO_2$, CO & $O_2$ +/- 1 SD

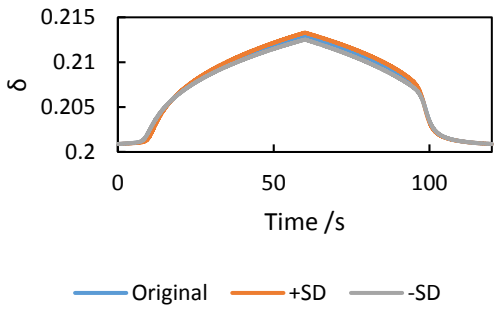


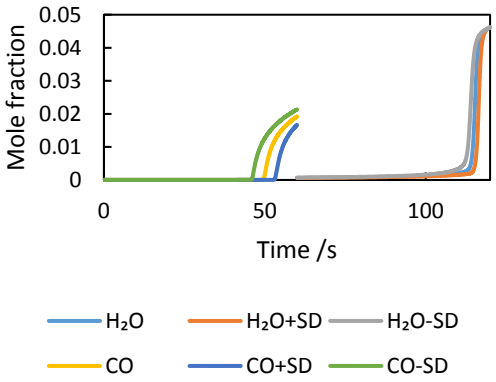

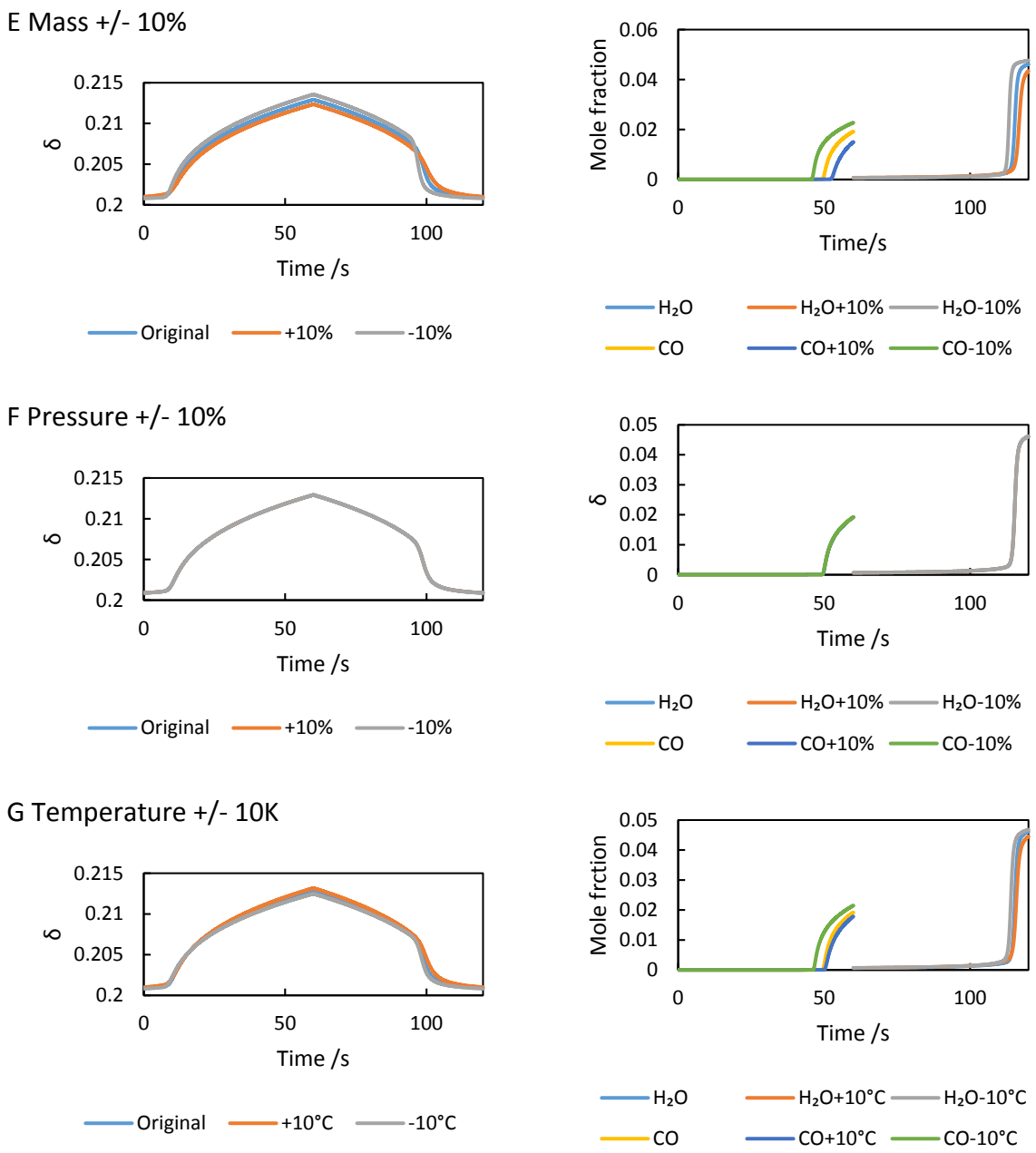


Figure 6.11: Sensitivity analysis of the delta state of one point in the bed, 40 mm from the $H_2O$ feed end (left) and $H_2O$ and CO outlet gas composition (right), without convolution, verses time for a representative steady cycle, for a reverse-flow reactor being fed 5% CO in Ar and 5% $H_2O$ in Ar with inert feeds in-between. The bed is a 2.2 g, 170mm length and 4mm diameter packed bed of $La_{0.6}Sr_{0.4}FeO_{3-\delta}$. A: The effect of changing the value of $K_{ox}$ by one standard deviation in either direction. B: The effect of changing $K_{Fe}$ by one standard deviation. C: The effect of varying the $H_2O$, $H_2$ and $O_2$ equilibrium constant by one standard deviation. D: The effect of varying the $CO_2$, CO and $O_2$ equilibrium constant by one standard deviation. E: the effect of varying the total mass of sample present by 10%. F: the effect of varying the pressure that the reactor is operated at by 10%. G: the effect of varying the temperature of the reactor by 10 K.

It can be seen in Figure 6.11A and B that of the thermodynamics it is the uncertainty in the $K_{Fe}$ variable that has the largest effect, while the $K_{ox}$ variable has a much smaller effect on the model. This is expected as $K_{Fe}$ is closely linked to the transition of $Fe^{3+}$ and $Fe^{2+}$ while

$K_{ox}$ is closer linked to the transition of $Fe^{3+}$ and $Fe^{4+}$ as explained in Chapter 3. In the regime that the system operates most iron is transitioning from the 3+ to the 2+ rather than 4+ to 3+ so it is expected that $K_{Fe}$would have a larger effect on the system.

Figure 6.11 C and D show the variation due to changes in the gas phase equilibrium constants have less of an effect. An increase in the $CO/CO_2$ equilibrium coefficient has a very similar effect to a decrease in the $H_2/H_2O$ equilibrium coefficient for the solid's interaction but in the gas phase this is less noticeable. It is expected that the weaker effect of a change in gas phase thermodynamics, when compared to the solids, is due to the solids higher oxygen capacity dominating the gas phase.

Of the gas phase equilibrium constants, the effect of the $CO_2$, CO and $O_2$ equilibrium constant is more pronounced; this is most likely due to the larger gradient in the $\delta$ $pO_2$ curve in reducing environments. Changing the extent to which the material is reduced has a much larger effect on oxygen capacity when compared to the effect of changing the oxidising power of the $H_2O$ feed.

Of the controlled variables the change in the total mass of sample has the largest effect of any change, whilst the change in gas phase pressure had little to no effect. This is due to the much larger oxygen capacity of the solid compared with the gas, associated with the order of magnitude difference in molar density. This indicates that the mass of the material is one of the most important controlled variables when designing a pilot or industrial sized system.

Temperature effects are small, this is because at the temperature of interest the reaction is almost heat neutral (Cox et al 1984). So small shifts in the temperature would only result is small shifts in the thermodynamics of the system. The shift in temperature was not large enough for the gas and solid densities to change dramatically.

### 6g Comparison and Discussion

The system can be successfully simulated using a thermodynamic model. It predicts that the system is capable of achieving the high conversions shown by Metcalfe et al (2019) experimental work.

This simulated work shows that the conversions are high, mirroring the experimental work, when the system is considered only from a thermodynamic stand point. Showing that this system can be operated in such a regime encourages the scale up of the system as it would

continue to result in these high conversions as long as the system can be designed to keep transfer processes suitably efficient.

This system has been shown to not obey the dissolution front model that Heidebrecht and Sundmacher (2009) created. Instead, while there is a front visible moving through the bed this is combined with the bed as a whole changing in tandem. This justifies returning to first principles for the creation of the model. The model manages to grasp the greater complexities of a variably non- stoichiometric OCM.

The assumption that the system is thermodynamic limited is justified as the model is able to accurately simulate the system, with respect to the outlet gasses for both WGS and buffer gas experiments. However, the system fails to achieve the purity and conversions that the model predicts even when convolved with the systems impulse response, as detailed at the end of Section 6a.

Due to the nature of the OCM it was expected that the simulation would be reasonably accurate without including kinetics, this has been confirmed as the largest deviations between experimental and theoretical results is the tails at the end of each half cycle.

The buffer gas feeds allowed for correlations linking the delta state of a given point in the bed to be linked directly to the unit cell parameters. The reactor is not isothermal, but as the system's sensitivity to temperature is low it is not expected to have a major effect on its behaviour.

The scatter in the XRD values means that the degree to which the data can be used to validate the model is limited, but the timings and magnitude of the changes do confirm the model. The delta of a single point in the bed changes in line with the model, increasing and decreasing by a consistent amount over the same time scale and with the same magnitude as the model predicts.

The closeness of the system to its thermodynamic limit is encouraging for scale up. It is expected that during scale up the surface area to volume ratio will decrease which may move the system towards either surface or solid state diffusion limitation regimes.

# Chapter 7: Conclusion

The work carried out during this thesis focused on proving that a chemical looping $H_2$ reactor is capable of overcoming the thermodynamic limitations of a conventional water-gas shift reactor. The operation of such a system would improve $H_2$ production yield and product quality, minimising the need for pressure swing adsorption or other expensive downstream separation processes when the production of pure $H_2$ is required commercially or for downstream processes.

It was shown from the thermodynamics that chemical looping reactor, is theoretically capable of achieving higher conversions and product quality than a conventional water-gas shift reactor. This was achieved via the use of either a material with multiple phase changes or a variably non-stoichiometric oxide as the OCM and counter current feeds. Then during cycling a gradient in oxygen chemical potential would form along the reactor which gives the high conversions. The material used in such a system must be capable of undergoing redox reactions in the $pO_2$ range of interest and remain stable in such a changing environment.

LSF641 is a material of interest due to its variable non-stoichiometry in the range of interest. However the material's structural properties had not been well studied in the literature in the $\delta$ range of interest to chemical looping $H_2$ production. It was shown that from first principles the material's chemical and thermal expansivity were expected to change once the material was reduced to a $\delta$ state above 0.2.

The chemical and thermal expansivities as a function of temperature and $\delta$ state were determined through the use of *in-situ* neutron and X-ray diffraction studies. These found that the material remains single phase in the $pO_2$'s expected in a reactor and that the thermal expansivity can have two different values depending on the material's $\delta$, $5.73 \times 10^{-5}$ Å/K for $\delta<0.2$ and $6.18 \times 10^{-5}$ Å/K for $\delta>0.2$, this contrasts with the literature value of $4.71 \times 10^{-5}$ Å/K found by Kuhn et al (2011). The chemical expansivity is linear for $\delta<0.2$ with a value of 0.144 Å and above 0.2 became a complex function of $\delta$, with increasing the $\delta$ state caused decreasing changes in unit cell parameter. The values for the chemical expansivity decreases with increasing $\delta$ state and with the largest expansivity recorded at smallest $\delta$ measured in this range ($3.10 \times 10^{-2}$ Å at 0.204) and was seen to decrease as the value of $\delta$ increased (increasing to $1.06 \times 10^{-2}$Å at a $\delta$ of 0.215).

Through the use of these expansivities it was possible to determine the nature of the oxygen chemical potential in a functioning WGS reactor through the use of *operando* x-ray diffraction using a synchrotron source. This system was found to achieve the high conversions predicted by the thermodynamic studies exceeding the limitations of a conventional reactor. The internals of the bed were analysed and the gradient in the bed before and after cycling was determined. The amount of oxygen entering and leaving the bed was determined by both the analysis of the XRD data and the outlet gas compositions and found to agree.

The system also determined how different points in the bed change a function of time over cycling, this data was of a lower quality due to the uncertainty in the calculations and the degree of scatter. It was not possible due to rapid nature of the half cycles and the scanning speed to extract kinetic data using this technique.

A chemical looping system operating using $CO_2$:CO buffer gasses was also analysed in this way. This found that using buffer gasses resulted in a different gradient. The buffer gas feeds exchanged less oxygen with the solid with the difference before and after each half cycling being concentrated at one end of the reactor.

Additional studies on chemical looping systems were carried out to determine the effect of temperature and half cycle duration. It was found that lengthening the half cycle duration increased the quantity of product produced but at the expense of time averaged conversion and product quality. It was also determined that it would not be possible to achieve 100% conversion with such a system through shortening the half cycling duration.

As the temperature of the reactor was increased so did the time averaged conversion of $H_2O$ and CO but at the expense of decreased product quality. Given the increased operational and capital costs of operating a reactor at higher temperatures 1098 K was used for the other studies carried out, as this gave a good combination of product quality and reactant conversions while keeping the temperature low enough for ease of operation.

Long term experiments were also carried out of the use of LSF641 for $H_2$ production, the system was subjected to1100 redox cycles. The product quality and conversion did not degrade over these cycles. SEM images and XRD scans of the material before and after cycling also showed no degradation in the OCM. This points to the suitability of this material for scaled up tests and experiments.

A thermodynamic model of the system was also produced, with no fitted parameters. This model was successfully at predicting the systems response to temperature and half cycle duration changes but did not perfectly simulate the system. However, it over predicted the both the $CO_2$ and $H_2$ product quality. The difference between the simulated and experimental results was decreased by convolving the model results with the impulse response of the gas analysis system but this still failed to completely explain the system. It is expected that the addition of solid gas interactions, as well as relaxing the assumption of perfect radial mixing in the reactor, would improve the accuracy of the model.

The model also successfully predicts the chemical potential gradient in the reactor during both WGS operation and when operated using buffer gas feeds. Through the use of *operando* XRD it was possible to confirm that the model accurately predicts the gradient in $\delta$ seen experimentally, regardless of whether WGS or buffer feeds are used as reactants.

This all shows that through the use of a variably non-stoichiometric material it is possible to overcome the thermodynamic limitations of a conventional reactor. LSF641 is a good option of a chemical looping reactor for $H_2$ or CO production, due to its variable non-stoichiometry in the $pO_2$ range of interest and its long life time, making it a good option for further large scale experimentation. This can be supported through the use of the thermodynamic simulation here developed and the increased understanding of the system from *operando* XRD results.

Additional work looking at the use of this material using more industrial relevant reducing gases like $CH_4$ or syngas should be carried out due to the high cost of obtaining pure CO as a feedstock.

In the range of $pO_2$s used in the water-gas shift reaction LSF641 only has a small change in oxygen content. It is expected that the use of a different variably non-stoichiometric OCM with a higher oxygen content in this range may perform better; requiring less material to achieve the same time averaged conversions.

# Chapter 8: Future Work

This thesis has proven that a counter current packed bed chemical looping reactor utilising $La_{0.6}Sr_{0.4}FeO_{3-\delta}$ (LSF641) is capable of achieving conversions higher than the theoretical maximum of a conventional water-gas shift (WGS) reactor. This has been demonstrated theoretically, experimentally and through the use of a thermodynamic simulation of an operating reactor.

It has additionally been shown that the oxygen content as a function of position in a packed bed chemical looping reactor can be investigated and visualised using *operando* X-ray diffraction. When using LSF641 as the oxygen carrier material (OCM) it was possible to visualise the oxygen content of the material before and after cycling. It was also found while it was possible to visualise how each point in the bed changes during reaction. It was complicated by the rapid nature of the oxidation and reduction paired with the relatively small shift in unit cell parameter between scans, of the order of 1/10000 of an Angstrom.

The use of an OCM with a larger oxygen capacity in the $pO_2$ range of interest is expected to increase the shift in unit cell parameter. It is also expected that by increasing the oxygen capacity of the reactor it would be possible to increase the half cycle duration. With longer half cycles the oxygen content of each point in the bed can be recorded more times as it undergoes reduction and oxidation, which in turn allows for the modelling of the complexities of each half cycle to be more easily confirmed.

In tandem this increased capacity would also make the operation of a commercial chemical looping reactor more viable due to lower costs to pack the reactor and the increased half cycle durations would decrease the frequency of valve manipulations and changes in operation. This would decrease the operational burden of the plant management.

However an increased change in the unit cell parameter of the material over each cycle can also decrease the materials life time, in turn increasing the shutdown burden to plant management. This would increase operating costs and can potentially lead to degradation in product quality over time.

$La_{0.8}Sr_{0.2}MnO_{3-\delta}$ (LSM821) shows promise as a potential replacement for LSF641. This is because it has larger oxygen capacity in the range of interest. However its lower stability in reducing conditions may lead to phase segregation and OCM deactivation. Additionally LSM821 has a more complex relationship between its oxygen content and the $pO_2$ that

would be equilibrium with it (Darvish et al 2015, Mizusaki et al 2000). This would make determination of a relationship between unit cell parameter and oxygen content more challenging.

Another method to increase the oxygen capacity of the bed is to vary the material in the bed, using sections of variably non-stoichiometric OCMs at the ends of the bed to give the high conversions seen in this work but have the majority of the change be carried out by a more conventional OCM, like supported iron oxide, form a middle section between the non-stoichiometric end sections of the bed. The optimum nature of each section of the bed both in terms of its material and its size would require extensive modelling and experimental work.

Additionally in order to use the thermodynamic model detailed previously at an industrial level the assumption of an isothermal reactor would need to be relaxed. This would be carried out by adding a heat balance to the reactor, initially it is suggested that the assumption of isothermal behaviour be changed to an assumption that the reactor operates adiabatically. As this assumption only energy to enter the system through reaction or from the temperature of the gas feeds this would allow for an understanding of the heating costs for an industrial plant to be better understood. The assumption that the system was thermodynamically limited could also be relaxed, requiring experimental work to extract the kinetics of each reaction.

An additional limitation of this work is the use of CO as the reducing gas. As detailed in Section 1c.ii CO is rarely used industrially for such a purpose with most $H_2$ production systems using natural gas or syngas. With this being the case further work should be carried out on the use of alternative reducing agents like methane or natural gas. This thesis concentrated on using the WGS reaction for $H_2$ production, where CO is used as the reducing agent. This was to avoid complications due to carbon deposition and the selectivity of methane. For industrial purposes natural gas is a more commercially relevant reducing agent for $H_2$ production due to it low price and existing infrastructure. Future work should be carried out to assess the capabilities of LSF641 and other OCMs to crack $CH_4$ and determine its effectiveness as an OCM for a chemical looping steam methane reforming (SMR) plant.

# References


Abazari R and Sanati S, *Perovskite $LaFeO_3$ nanoparticles synthesized by the reverse microemultion Nano reactors in the presence of aerosol-OT: Morphology, crystal structure and their optical properties* Superlattices and Microstructure's 64 p148-157 2013

Ada´nez J, de Diego L F, Garcı´a-Labiano F, Gaya´n P, Abad A, Palacios J M "*selection of Oxygen carrier for chemical-looping Combustion*" Energy and Fuels 18 371-377 2004

Ahmed, S., Aitani A, Rahman F Al-Dawood, Al-Muhaish F., *Decomposition of hydrocarbons to $H_2$ and carbon.* Applied Catalysis A: General. 359(1-2): p. 1-24. 2009

Akiyama T, Miyazaki A, Nakanishi H, Hisa M and Tsutsumi *A Thermal and gas analyses of the reaction between iron carbide and steam with $H_2$ generation at 573 K* international journal of $H_2$ Energy 29(7) p 721-724 2004

Alamsar B, Torii S, Trianto A and Bindar Y *Heat and Mass Transfer in Reduction Zone of Sponge Iron Reactor* ISRN Mechanical Engineering 2011 page 1-12 2011

Andrade V., Caraballo-Vivas R.J., Costas-Soares T., Pedro S.S., Rocco D.L., Reis M., Campos A.P.C. and Coelho A.A. ,*Magnetic and structural investigationson La0.6Sr0.4MnO3 nanostructured manganite: Evidence of a ferrimagnetic shell* Journal of Solid State Chemistry, 219, p 87-92, 2014

Arakawa Arakawa T, Kurachi H, Shiokawa J *Physicochemical properties of rare earth perovskite oxide used as gas sensor material* J. Mater. Sci., 4 pp. 1207-1210 1985

Archbold, R. *Hindenburg: An Illustrated History*. Toronto: Viking Studio/Madison Press, 1994.

Balachandrana U Duseka J.T. Maiyaa P.S. Maa B. Mievillea R.L. Kleefischb M.S. Udovichb C.A. "*Ceramic membrane reactor for converting methane to syngas"* Catalysis Today **36**(3) pp 265-272 1997

Bandopadhyay A, Ganguly A, Gupta KN, ray HS *Investigations on the anomalous oxcidation behaviour of high-carbon gas based direct reduced iron (DRI)* Thermochimaica Acta 276 p 199-207 1996.

Barelli, L., Bidini G, Gallorini F, Servili S. *$H_2$ production through sorption-enhanced steam methane reforming and membrane technology: A review.* Energy, 33(4): p. 654-570. 2008.

Basu P, Butler J *Studies on the operation of loop-seal in circulating fluidsed bed boilers* Applied Energy **86(9)** pp1723-1731 2009

Bayraktar D, Diethelm S, Graule T, Van herle J, Holtappels P *Properties of B-site substituted La0.5Sr0.5FeO 3-δ perovskites for application in oxygen separation membranes* Journal of Electroceramics 22 pp 55-60 2009

Benamira, M., Thommy L, Moser F, Jouberrt O, Caldes MT., *New anode materials for IT-SOFC derived from the electrolyte BaIn0.3Ti0.7O2.85 by lanthanum and manganese doping.* Solid State Ionics,. 265(0): p. 38-45. 2014

Bishop SR, Marrocchelli D, Chatzichristodoulou C, Perry NH, Mogensen MB, Tuller HL and Wachsman ED *Chemical Expansion: implications for electrochemical energy storage and conversion devices* Annual Review of Material Research 44 pp205-239 2014

Bleeker M, Kresten S Veringa H *Pure $H_2$ from pyrolysis oil using the steam-iron process* Catalysis Today 127(1-4) p 278-290 2007

Bhalla, A.S., R. Guo, and R. Roy, *The perovskite structure – a review of its role in ceramic science and technology.* Material Research Innovations, 4(1): p. 3-26. 2000

Bleeker M, Gorter S, Kersten S, Ham L, Berg H, Veringa H, *Hydrogn production from pyrolysis oil using the steam-iron process: a process design study Clean Technologies and Environmental Policy* 12(2) p125-135 2010

Bleeker M, Kresten Veringa H *Pure $H_2$ from pyrolysis oil using the steam-iron process* Catalysis Today 127(1) p278-290 2007

Bohn CD *The production of pure $H_2$ with simultaneous capture of $CO_2$* PhD Dissertation, University of Cambridge 2010

Bohn CD, Cleeton JP, Müller CR, Chuang SY, Scott SA and Dennis J S *Stabilizing Iron Oxide Used in Cycles of Reduction and Oxidation for $H_2$ Production.* Energy & Fuels, 24(7): p. 4025-4033. 2010

Boudghene S. *Solid oxide fuel cells (SOFCs): a review of an environmentally clean and efficient source of energy.* Renewable and Sustainable Energy Reviews, Vol. 6, Issue 5, pp. 433–455, 2002.

Burgess D, R. *Thermochemical Data* in NIST Chemirsty WebBook, NIST Standard Reference Database Number 69" Eds. P.J. Linstrom and W.G. Mallard, National Institute of Standards and Technology, Gaithersburg MD, 20899 (retrieved 2018)

Callaghan *PhD Dissertation*, Worcester Polytechnic Institute 2006

Chiesa, P., Lozza G, Malandrino A, Romano M, Piccolo V, *Three-reactors chemical looping process for $H_2$ production.* International Journal of $H_2$ Energy,. 33(9): p. 2233-2245. 2008

Cho P, Mattisson T, Lyngfelt A *Comparison of iron- nickel- copper- and manganese – based oxygen carriers for chemical-looping combustion* Fuel 83(9) 2004

Chu S, Majumdat A, *Opportunities and Challenges for a Sustainable Energy Future'* Nature 488 p294-303 (2012)

Cleeton J, Bohn C, Muller C, Dennis J, Scott S, C*lean $H_2$ production and electricity from cola via chemical looping: Identfying a suitable operating regime* international journal of $H_2$ Energy 34(1) p1-12 2009

Coelho A A (2012). *TOPAS academic: general profile and structure analysis software for powder diffraction data* (Bruker AXS, Karlsruhe, Germany, 5th edition, 2012)

Czuppon, T.A., S.A. Knez, and J.M. Rovner, *Ammonia,* in Kirk-Othmer Encyclopedia of Chemical Technology. 2000, John Wiley & Sons, Inc.

Dann S, Currie D, Weller M, Thomas M, Al-Rawwas A, *The Effect of Oxygen Stoichiometry on Phase Relations and Structure in the System La1-xSrxFeO3-δ ($0 \leq x \leq 1$, $0 \leq \delta \leq 0.5$*) Journal of Solid State Chem 109, p. 134-144 1994

Darvish S, Sabarou H, Saxena S K, Zhong Y, *Quantitative Defect Chemistry Analysis and Electronic Conductivity Prediction of $La_{0.8}Sr_{0.2}MnO_{3\pm\delta}$* Journal of Electrochemical Society 162(9) p134-140 2015

. de Diego L F, Garcia-Labiano F., Adánez J., Gayán P., Abad A., Corbella B.and Palacios J., *Development of CU-based oxygen carrier for chemical-looping combustion* Fuel, 83(13), p. 1749-1757, 2004

de Diego, L.F Ortiz M, Garcia-Labiano F, Adanez J, Abad A, Gayan P. *$H_2$ production by chemical-looping reforming in a circulating fluidized bed reactor using Ni-based oxygen carriers.* Journal of Power Sources,. **192**(1): p. 27-34. 2009

Demirel E and Azcan N, *Processing of the Word thermodynamic Modelling or $H_2O$-gas shift Reaction in supercritical $H_2O$,* Congress on Engineering and Computer Science 2012(2) 2012

Dieges, P. *Vaporization of exhaust products in $H_2$-oxygen engine* US 3844262. 1974

Dincer I, (2015) "Review and evaluation of $H_2$ production methods for better sustainability" International Journal of $H_2$ Energy 40(34) pp 11094-11111

Ding, Y. and Alpay E., *Adsorption-enhanced steam-methane reforming. Chemical Engineering Science,*. 55(18): p. 3929-3940. 2000

Dissanayake D, Rosynek M P, Kharas K C C, Lunsford J H. *Partial oxidation of methane to CO and $H_2$ over a $Ni/Al_2O_3$ catalyst* Journal of Catalysis 132 1 117-127 1991

Dudukovic M. P "*Frontiers in Reaction Engineering*". Science 325, pp 698-701., 2009

Emmerlich, J., Linke BM, Music S, Schneider JM, *Towards designing La1-xSrxCoyFe1-yO3-d with enhanced phase stability: Role of the defect structure*. Solid State Ionics. 255 p. 108-112. 2014

Enger B, Lødeng R. and Holmen A., *A review of catalytic partial oxidation of methane to synthesis gas with emphasis on reaction mechanisms over transition metal catalysts* Applied. Catalysis. A-General. **346**, pp 1-27 2008

Ermakova, M.A., Ermakov D Y, Chuvilin A, Kuvshinov GG., *Decomposition of Methane over Iron Catalysts at the Range of Moderate Temperatures: The Influence of Structure of the Catalytic Systems and the Reaction Conditions on the Yield of Carbon and Morphology of Carbon Filaments*. Journal of Catalysis, **201**(2): p. 183-197. 2001.

Elshof J. E., Lankhorst M. H. R. Bouwmeester H. J. M, *Oxygen Exchange and Diffusion Coefficients of Strontium-Doped Lanthanum Ferrites by Electrical Conductivity Relaxation* J. Electrochem. Soc. volume 144, issue 3, 1060-1067 1997

Fan LS, *Chemical Looping Systems for Fossil Energy Conversion*, Wiley-Blackwell, 2011

Feng, H.L., Arai M, Matsushita Y, tsujimoto Y, Yuan Y, Sathish C I, He J, Tanaka M, Yamaura K., *High-pressure synthesis, crystal structure and magnetic properties of double perovskite oxide Ba2CuOsO6.* Journal of Solid State Chemistry,. 217: p. 9-15. 2014

Fierro J, *Metal Oxides Chemistry and Applications*, CRC Press, 2005

Finlayson B, *Introduction to chemical Engineering Computing*, John Wiley & Sons, Inc., New Jersey, 2012

Franca, R.V., A. Thursfield, and I.S. Metcalfe, *La0.6Sr0.4Co0.2Fe0.8O3−δ microtubular membranes for $H_2$ production from $H_2O$ splitting.* Journal of Membrane Science. 389(0): p. 173-181. 2012

Fuller, E. N., Schettler, P. D. and Giddings, J. C. *A new method for the prediction of gas-phase diffusion coefficients* Industrial and Engineering Chemistry. 58 (5) 1966

Garcia-Labiano F, de Diego, Luis F, Gayan P, Adanez J, Abad A, Dueso C *Effect of fuel fas composition in chemical-looping combustion with Ni-based oxygen carriers. 1. Fate of Sulphur* Industrial & Engineering Chemistry Research 48(5) 2009

Gnanapragasam, N.V., Reddy B.V., and Rosen M.A., *$H_2$ production from coal using coal direct chemical looping and syngas chemical looping combustion systems: Assessment of system operation and resource requirements*. International Journal of $H_2$ Energy, **34**(6): p. 2606-2615. 2009.

Go, K.S., Son SR, Kim SD Kang KS, Park CS., *$H_2$ production from two-step steam methane reforming in a fluidized bed reactor*. International Journal of $H_2$ Energy, 2009. **34**(3): p. 1301-1309.

Gough, J.B. Charles The Obscure. Isis (70 (4): 576, 579. 1979

Graham, M.J. Channing D A, Swallow G A Jones R D. *A Mössbauer study of the reduction of hematite in $H_2$ at 535$^oC$*. Journal of Materials Science, 1975. 10(7): p. 1175-1181.

Grigoriev, S.A., V.I. Porembsky, and V.N. Fateev, *Pure $H_2$ production by PEM electrolysis for $H_2$ energy.* International Journal of $H_2$ Energy, 2006. **31**(2): p. 171-175.

Gupta, P., L.G. Velazquez-Vargas, and L.S. Fan, *Syngas redox (SGR) process to produce $H_2$ from coal derived syngas.* Energy and Fuels. 21(5): p. 2900-2908. 2007

Hacker V, Faleschini G, Fuchs H, Frankhauser R, Simader G, Ghaemi M, Spreitz B Friedrich K *Usage of biomass gas for fuel cell by the SIR process* Journal of Power Sources 71(1-2) p 226-230 1998

Hacker V, Frankhauser R, Faleschinia G, Fuchsa H, Friedicha K, Muhra M Kordeschb K *$H_2$ production by steam-iron process* Journal of Power Sources 80(1-2) p 531-535 2000

Hauch, A; Ebbesen, Dalgaard S; Jensen, S H; Mogensen, M *Highly efficient high temperature electrolysis*. Journal of Materials Chemistry **18** (20): 2331–40 2008.

Hamer HP, Gallucci F, Cobden PD, Kimball E, van Sint Annaland M *A novel reactor configuration for packed bed chemical-looping combustion of syngas* International Journal of Greenhouse Gas Control **16** p1-12 2013

Heidebrecht, P., C. Hertel, and K. Sundmacher, *Conceptual Analysis of a Cyclic water-gas shift Reactor*. International Journal of Chemical Reactor Engineering **6**. 2008

Heidebrecht, P. and K. Sundmacher, *Thermodynamic analysis of a cyclic $H_2O$ gas-shift reactor (CWGSR) for $H_2$ production*. Chemical Engineering Science. 64(23): p. 5057-5065. 2009

Helfferich, F.G., *The theory of precipitation/dissolution waves*. AIChE Journal 35(1): p. 75-87. (1989)

*Hemschemeier, A; Melis, A; Happe, T Analytical approaches to photobiological $H_2$ production in unicellular green algae. Photosynthesis Research 102 (2–3): 523–540. 2009*

Holladay, J.D., Hu J, King D L Wang Y *An overview of $H_2$ production technologies.* Catalysis Today, 2009. **139**(4): p. 244-260.

Hoogers G. *Fuel Cell Technology Handbook*. Boca Raton, FL: CRC Press. pp. 6–3. 2003

Hossain M and H. Lasa H, *Reduction and oxidation kinetics of Co–Ni/Al2O3 oxygen carrier involved in a chemical-looping combustion cycle*s Chemical Engineering Science, , 65(1), p. 98-106 2010

Hodeau, JL, Bordet P, Anne M, Prat A, Fitch AN, Dooryhee E, Vaughan G, Freund A K *Nine-crystal multianalyser stage for high-resolution powder diffraction between 6 keV and 40 keV* Proc. SPIE 3448, Crystal and Multilayer Optics, 1998

Huebler J, Johnson J, Schora F, Tarman P, *Production of $H_2$ via the steam-iron process utilizing dual solids recycle,* United States Patent Office, US3442619. 1969

Hurst, S., *Production of $H_2$ by the steam-iron method.* Oil & Soap, 16(2): p. 29-35. 1939.

Ibbserson, R. M. (2009) *Design and performance of the new supermirror guide on HRPD at ISIS*. Nucl. Instr. Methods A, 600, 47-49. (10.1016/j.nima.2008.11.066)

Jerndal E, Mattisson T, Lyngfelt A *Thermal Analysis of Chemical-Looping Combustion* Chemical Engieering research and Design 84(9) 2006

Jiang, SP *Development of lanthanum strontium manganite perovskite cathode materials of solid oxide fuel cells: a review,* Jounral of Materials Science, 43(21), p 6799-6833, 2008.

Kamitakahara B (2013) "NIST Centre for Neutron Research Resources" https://www.ncnr.nist.gov/resources/ accessed 25/06/2018

Kang KS Kim CH Cho WC Bae KK Woo SW Park CS *Reduction characteristics of CuFe2O4 and Fe3O4 by methane; CuFe2O4 as an oxidant for two-step thermochemical methane reforming*. International Journal of $H_2$ Energy, 2008. **33**(17): p. 4560-4568.

Kappagantula RV, Ingram GD and Vuthaluru HB, *Investigation into the Efficiencies of Steam Conversion in Three Reactor Chemical Looping* International Journal of Chemical and Molecular Engineering 12(2) 2018

Karen, P., *Nonstoichiometry in oxides and its control.* Journal of Solid State Chemistry, 2006. **179**(10): p. 3167-3183.

Kierzkowska AM, Bohn CD, Scott CD, Cleeton J P, Dennis JS Müller C R *Development of Iron Oxide Carriers for Chemical Looping Combustion Using Sol-Gel*. Industrial & Engineering Chemistry Research. 49(11): p. 5383-5391 2010

Kim, H., Kim S, Lee K-H, Lee H-L, Lee K-T *Oxygen ion conduction in barium doped LaInO3 perovskite oxides.* Journal of Power Sources,. 267(0): p. 723-730. 2014

Kittel C, *Introduction to Solid State Physics*, John Wiley & Sons, Inc., New York, 8, 2005

Kodama T, Shimizu T, Satoh Tm Nakata, Shimizu K *Stepwise production of CO-rich syngas and $H_2$ via solar methane reforming by using a Ni(II)-ferrite redox system.* Solar Energy, 73(5): p. 363-374. 2002.

Kolbitsch P, Bolhar-Nordenkampf J, Proll T, Hofbauer H *Operating experience with chemical looping combustion in a 120 kW dual circulating fluidized bed (DCFB) unit* International Journal of Greenhous Gas Control **4(2)** pp 180-185 2010

Koroneos C, Dompros A, Roumbas G, Moussiopoulos N *Life cycle assessment of $H_2$ fuel production processes.* International Journal of $H_2$ Energy, 29(14): p. 1443-1450. 2004

Kuhn M, Hashimotot S, Sato K, Yashiro K, Mizusaki J *Oxygen nonstoichiometry, thermos-chemical stability and lattice expansion of La0.6Sr0.4FeO3-δ* Solid state Ionics 195(1) p 7-15 2011

Lankhorst, M.H.R., H.J.M. Bouwmeester, and H. Verweij, *Thermodynamics and Transport of Ionic and Electronic Defects in Crystalline Oxides*. Journal of the American Ceramic Society,. 80(9): p. 2175-2198. 1997

Levenspiel O, *Chemical reaction engineering* 3rd ed. New York: Wiley, 1999. Print. p340

Li K Zhang R Bi J, *Experimental study on syngas production by co-gasification of coal and biomass in a fluidized bed international* Journal of $H_2$ Energy 35(7) 2722-2726 2010

Lein HL, Wiik K, Grande T, "*Kinetic demicing and ddecompostion of oxygen permeable membranes"* Solid State Ionics 177 pp 1587-1590 2006

Lin, H.-Y., Y.-W. Chen, and C. Li, *The mechanism of reduction of iron oxide by $H_2$*. Thermochimica Acta,. 400(1-2): p. 61-67. 2003

Lorente E, Pena J Am Herguido J *Kinetic study of the redoc process for spearing and storing $H_2$: Oxidation stage and aging of solid International* Journal of $H_2$ Energy 33(2) p. 615-626 2008

Luo H P and Xiao W D "*A reactive distillation process for a cascade and azeotropic reaction system: Carbonylation of ethanol with dimethyl carbonate*" Chemical Engineering Science **56**(2) pp 403-410 2001

Lv P, Yuan Z, Wu C, Ma L, Chen Y, Tsubaki N, *Bio-syngas production from biomass catalytic gasification Energy Conversion and Management* 48(4) p 1132-1139 2007

Mak C M, *Overcoming water-Gas-Shift Equilibrium via Chemical Looping* PhD Thesis Newcastle University 2017

Marda, JR, DiBenedetto J, McKibben S, Evans, RJ, Czernik S, French RJ, Dean A M *Non-catalytic partial oxidation of bio-oil to synthesis gas for distributed $H_2$ production* International Journal of $H_2$ Energy 34(20) p 8519-8534 2009

Martin, M., *Materials in thermodynamic potential gradients.* The Journal of Chemical Thermodynamics 35(8): p. 1291-1308. 2003

Mattisson T, Lyngfelt A, Cho P *The use of iron oxide as an oxygen carrier in chemical-looping combustion of methane with inherent separation of $CO_2$* Fuel 80(13) p1953-1962 2001

Mayer, W. and Tamura, H. *Propellant injection in a liquid oxygen/gaseous $H_2$ rocket engine*. Journal of Propulsion and Power,. 12(6): p. 1137-1147. 1996

Meadowcroft D B, *Some properties of strontium doped lanthanum chromite* Journal of Physics D: Applied Physics 2(9) 1969

Messerschmitt A, US Pat., US971206, 1910

Metcalfe IS, Ray B, Dejoie C, Hu W, de Leeuwe C, Dueso C, Garcia-Garcia FR, Mak CM, Papaioannou EI, Thompson CR, Evans JSO *Overcoming chemical equilibrium limitation using a thermodynamical reversible chemical reactor* Nature Chemistry **Accepted 2019**

Miyoshi S, Hong J.-O., Yashiro K., Kaimai A., Nigara Y., Kawamura K., Kawada T. and Mizusaki J., *Lattice creation and annihilation of LaMnO3+d caused by nonstoichiometry change* Solid State Ionics, 154, p 257-263, 2002

Mizusaki J, Tagawa H, Naraya K, Sasamoto T *Non-stoichiometry and thermochemical stability of the perovskite type $la_{1-x}Sr_xMnO_{3-\delta}$* Solid State Ionics 49 p 111-118 1991

Mizusaki J, Yamauchi S, Fueki K, Ishikawa A *Nonstoichiomert of the perviosklioe typoe oxide $La_{1-x}Sr_xCrO_{3-\delta}$* Solid state Ionics, 12 119-124 1984

Mizusaki J, Yonemura Y, Kamata H, Ohyama K, Mori N, Takai H, Tagawa H, Dokiya M, Naraya K, Sasamoto T, Inaba H, Hashimoto T *Electronic conductivity, Seebeck coefficient, defect and electronic structure of nonstoichiometric $La_{1-x}Sr_xMnO_3$* Solid State Ionics, 132(3-4) p 167-180 2000

Mizusaki, J, Yoshihiro M, Yamauchi S, Fueki K., *Nonstoichiometry and defect structure of the perovskite-type oxides $La_{1-x}Sr_xFeO_{3-\delta}$*. Journal of Solid State Chemistry. 58(2): p. 257-266. 1985

Moharana MK, Peela NR, Khandekar S, Kunzru D *Distrabuted $H_2$ production from ethanol in a microfuel processor: Issues and challenges* Renewable and sustainable energy reviews 15(1) p 524-533 2011

Mondal, K, Lorethova H, Hippo E Wiltowski T Lalvani SB. *Reduction of iron oxide in CO atmosphere - reaction controlled kinetics*. Fuel Processing Technology, 86(1): p. 33-47. 2004

Moghtaderi B., "*Review of the Recent Chemial Looping Process Developments for Novel Energy and Fuel Applications*" Energy & Fuels, 2012, **26**, 15-40

Mosleh M, Sogaard M, Hendriksen P V *kinetics and mechanisms of oxygen surface exchange on La0.6Sr0.4FeO3-δ thin films* Journal of The Electrochemical Society 156(4) 2009

Müller C R, Bohn C D, Song Q, Scott S A Dennis J S. ., *The production of separate streams of pure $H_2$ and $CO_2$ from coal via an iron-oxide redox cycle.* Chemical Engineering Journal. 166(3): p. 1052-1060. 2011

Murugan A, *PhD Thesis*, Newcastle University, 2012

Murugan, A. Thursfield and I. S. Metcalfe, *A chemical looping process for $H_2$ production using iron-containing perovskites* Energy Environ. Sci., 4, 4639–4649. 2011

Nagai, T. and W. Ito, *Stabilization of cubic perovskite structure upon trivalent cation substitution in Co-based mixed conductors (BaxSr1-x)(Co0.9Y0.1)O3-δ*. Solid State Ionics. 262(0): p. 650-653. 2014

Nansheng X., Zhao H., Zhou X., Wei W., Lu X., Ding W. and Li F., *Dependence of critical radius of the cubic perovskite ABO3 oxides on the radius of A- and B-site cations* International Journal of $H_2$ Energy35(14), 7295-7301 2010

Noh T, Kim J, Kim Y, Chun HH, J MS, Lee H*, Mn valence state and electrode performance of perovskite-type cathode La0·8Sr0·2Mn1 − x Cu x O3 − δ (x = 0, 0·2) for intermediate-temperature solid oxide fuel cells* Bulletin of Materials Science 36 p 1261-1266 2013

Noorman S, van Sint Annaland M, Kuipers *Packed bed reactor technology for chemical-looping combustion* Industrial & Engineering Chemistry Research, 46 (2007), pp. 4212-4220

Noorman S *Packed Bed reactor technology for Chemical-looping Combustion* Ipskamp Drukkers, Netherlands, 2009

Obayashi H, Kudo T, *Properties of oxygen deficient perovskite-type compounds and their use as alcohol sensors*, Nippon Kagaku Kaishi pp 1568–72. In Japanese 1980

Olsson R and Turkdogan E, *Catalytic effect of iron on decomposition fo CO: II. Effect of additions of $H_2$ $H_2O$, $CO_2$, $SO_2$ and $H_2S$ Metallurgical Transactions*, 1974, 5, 1543-1940

Omae I *Aspects of $CO_2$ utilization* Catalysis today 115(1) p33-52 2006

Otsuka, K., Yamada C, Kaburagi T Takenaka S *$H_2$ storage and production by redox of iron oxide for polymer electrolyte fuel cell vehicles.* International Journal of $H_2$ Energy 28(3): p. 335-342. 2003

Otsuka, K, Kaburagi T, Yamada C, Takenaka S., *Chemical storage of $H_2$ by modified iron oxides*. Journal of Power Sources 122(2): p. 111-121. 2003

Oswald S, Bruchner W *XPS depth profile analysis of non-stoichiometric NiO films* Surface and interface analysis 36 p17-22 2004

Park J and Levenspiel O, *The crackling core model for the multistep reaction of solid particles* Chemical Engineering Science., 1977, **32**, 233-234

Patankar S V *Numerical Heat transfer and Fluid Flow* New York McGraw-Hill p102

Peña J, Lorente E, Romero E, Herguido J, *Kinetic study of the redox process for storing $H_2$: reduction stage* Catalysis Today, , 116, p.439-444 2006

Pineau, A., N. Kanari, and I. Gaballah, *Kinetics of reduction of iron oxides by H2: Part I: Low temperature reduction of hematite*. Thermochimica Acta, 447(1): p. 89-100. 2006.

Philiber C *Renewable Energy for Industry International energy agency* insights series 2017

Pudukudy M, Yaakob Z, Mohammad M, Narayanan B, Sopian K.. *Renewable $H_2$ economy in Asia – Opportunities and challenges: An overview.* Renewable and Sustainable Energy Reviews. 30 (edit), Pages 743–757. (2014)

Raissi, A T. and. Block D.L, *$H_2$: automotive fuel of the future*. Power and Energy Magazine, IEEE,. 2(6): p. 40-45. 2004

Readman JE, Olafsen A, Larring Y, Blom R, *$La_{0.8}Sr_{0.2}Co_{0.2}Fe_{0.8}O_{3-\delta}$ as a potential oxygen carrier in a chemical looping type reactor, an in-situ powder* X-ray diffraction study Journal of Materials Chemistry 15(1931-1937) 2004

Reeber RR *Thermal expansion of some group IV elements and ZnS* physica satus solidi 32(1) pp 321-331 1975

Riess, I., *Mixed ionic–electronic conductors—material properties and applications.* Solid State Ionics 157(1–4): p. 1-17. 2003

Roman J. Press, K. S. V. S., Massoud J. Miri, Alla V. Bailey, Gerald A. *Introduction to $H_2$ Technology*. 307 (John Wiley & Sons, Inc., 2008

Ryden M and Lyngfelt A, *Using steam reforming to produce $H_2$ with $CO_2$ capture by chemical-looping combustion International*. Journal $H_2$ Energy, **31**, 1271–1283 2006

Rydén, M., Lyngfelt A, Mattisson T, Chen D, Holmen A, Bjorgum E. (2008) *Novel oxygen-carrier materials for chemical-looping combustion and chemical-looping reforming; LaxSr1-xFeyCo1-yO3-δ perovskites and mixed-metal oxides of NiO, Fe2O3 and Mn3O4* International Journal of Greenhouse Gas Control, 2(1): p. 21-36.

Rylander P, *Hydrogenation and DeHydrogenation* Ullmann's Encyclopedia of Industrial Chemistry, Wiley-VCH, Weinheim, 2005.

Scheffe J. R., Weibel D. and Steinfeld A., *Lanthanum-Strontium−Manganese Perovskites as Redox Materials for Solar Thermochemical Splitting of H2O and CO2* Energy & Fuels, 27, p 4250-4257, 2013.

Schmidt M and Campbell SJ *Crystal and Magnetic Structures of Sr2Fe2O5 at Elevated temperature* Journal of Solid State Chemistry 156(2) p 292-304 (2001)

Schouten J. P., *Chemical Reaction Engineering: History, Recent Developments, Future Scope*, Book of Abstracts, 20th International Symposium on Chemical Reaction Engineering (ISCRE 20), Kyoto, 7 to 10, pp. 6–7. September 2008

Selan M, Lehrhofer J, Friedrich K, Kordesch K, Simader G *Sponge iron: economic ecological, technical and process-specific aspects* Journal of Power Sources 61(1-2) p 247-253 1996

Simbeck, D.R., *$CO_2$ capture and storage - the essential bridge to the $H_2$ economy*. Energy, 2004. 29(9-10): p. 1633-1641.

Singh K, Nowotny J and Thangadurai V, *Amphoteric oxide semiconductors for energy conversion devices: a tutorial review* Chemical Society Reviews, 2013, 42, p. 1961-1972 2013

Sircar S, Golden T C *Purification fo $H_2$ by pressure swing adsorption* Separation science and technology 35(5) p 667-687 2000

Shannon RD *Revised Effective Ionic Radii and Systematic Studies of Interatomic Distances in Halides and Chalcogenides* Central Research and Development Department, Experimental

Station, E. I. Du Pont de Nemours and Company, Wilmington, Delaware 19898, U.S.A. Published in Acta Crystallographica. A32, Pages 751-767. 1976

Shen L, Gao Z, Wu J, Xiao J *Sulfur behaviour in chemical looping combustion with NiO/$Al_2O_3$ oxygen carrier* Combustion and Flame 157(5) 2010

Shen, Q, Zheng Y, Luo C, Zheng C., *Development and characterization of Ba1−xSrxCo0.8Fe0.2O3−δ perovskite for oxygen production in oxyfuel combustion system*. Chemical Engineering Journal,. 255(0): p. 462-470. 2014

Smith J, Kuczera K, Karplus M *Dynamics of myoglobin: comparison of simulation results with netron scattering spectra* Proceedings of the national academy of science of the United States of America 87(4) 1990

Smyth, D.M. *The effects of dopants on the properties of metal oxides.* Solid State Ionics,. 129(1–4): p. 5-12. 2000

Søgaard, M., P. Vang Hendriksen, and M. Mogensen, *Oxygen nonstoichiometry and transport properties of strontium substituted lanthanum ferrite*. Journal of Solid State Chemistry. 180(4): p. 1489-1503. 2007

Solunke RD, Veser G $H_2$ Production via Chemical Looping Steam Reforming in a Periodically Operated Fixed-Bed Reactor Industrial & Engineering Chemistry Research 49 (21), p11037-11044 2010#

Son SR, Go K S, Kim SD. Thermogravimetric anlaysis of copper oxide fro chemical-looping $H_2$ generation Industrial & Engineering Chemistry research 48(1) 2008

Steinfeld A, Sanders A Palumbo, Design aspects of solar thermochemical engineering- a case study: two-step $H_2O$-splitting cycle using the $Fe_3O_4$/FeO redox system Solar energy 65(1) p 43-53 1999

Stølen, S., E. Bakken, and C.E. Mohn, *Oxygen-deficient perovskites: linking structure, energetics and ion transport.* Physical Chemistry Chemical Physics,. 8(4): p. 429-447. 2006

Sun, Y., Yan N, Li J, Wu H, Luo J, Chuang K *The effect of calcination temperature on the electrochemical properties of La0.3Sr0.7Fe0.7Cr0.3O3−x (LSFC) perovskite oxide anode of solid oxide fuel cells (SOFCs)*. Sustainable Energy Technologies and Assessments 8(0): p. 92-98. 2014

Svoboda K, Slowinski G, Rogut J Baxter D thermodynamic possibilities and constraints for pure $H_2$ production by iron based chemical looping process at lower temperatures Energy Conversion and Management 48(12) p 3063-3073 2007

Svoboda K, Siewiorek A, Baxter D, Rogut J and Pohorely M Thermodynamic possibilities and constraints for pure $H_2$ production by a nickle and cobaly-based chemical looping process at lower temperatures Energy Conversion and Management 49(2) p 221-231 2008

Szekely J, Gas-Solid Reactions, Academic Press, New York, 1976

Takenaka S Kaburagi T, Yamada C Nomura K, Otsuka K *Storage and supply of $H_2$ by means of the redox of the iron oxides modified with Mo and Rh species.* Journal of Catalysis. 228(1): p. 66-74. 2004

Teraoka, Y., Shimokawa H, Kang Ch Y, Kusaba H, Sasaki K., *Fe-based perovskite-type oxides as excellent oxygen-permeable and reduction-tolerant materia*ls. Solid State Ionics, 177(26–32): p. 2245-2248. 2006

Thompson C R *$H_2$ Production via Chemical Looping with $La_{0.7}Sr_{0.3}FeO_{3-\delta}$ and Iron Oxides: A Kinetic and Thermodynamic Study* PhD Thesis 2015

Thursfield A, Murugan A, Franca R and Metcalfe I S. *Chemical looping and oxygen permeable ceramic membranes for $H_2$ production – a review*. Energy Environ. Sci.. 5, 7421–7459. 2012

Traversa E, Matsushima S, Okada G, Sadaoka Y, Sakai Y, WatanabeK *NO2 sensitive LaFeO3 thin films prepared by R.F. sputtering* Sensors and Actuators B, 25 pp. 661-664 1995

Turner J, Sverdrup G, Mann MK, Magness PC, Kroposki B, Ghirardi M, Evans RJ, Blake D *Renewable $H_2$ production* International journal of energy research 32(5) p 379-407

U.S. Department of Energy, *Fuel Cell Handbook*, ed. I. EG&G Technical Services. 2004.

U.S. Energy Information Administration. *The Impact of Increased Use of $H_2$ on Petroleum Consumption and $CO_2$ Emissions*. U.S. Energy Information Administration. August 2008.

Vaclav S *Enriching the Earth: Fritz Haber, Carl Bosch, and the Transformation of World Food Production*. Cambridge, MA: . (2004). MIT Press.

Vaidya PD and Rodrigues AE, "*Insight into steam reforming of methanol to produce $H_2$ fro fuel cells"*, Chemical Engineering Journal 117(1) 39-49 (2006)

Vasala, S., H. Yamauchi, and M. Karppinen, *Synthesis, crystal structure and magnetic properties of a new B-site ordered double perovskite Sr2CuIrO6.* Journal of Solid State Chemistry 220(0): p. 28-31. 2014

Vogt UF , Holtappels P, Sfeir J, Richter J, Duval S, Wiedenmann D, Züttel A, *Influence of A-site variation and B-site substitution on the physical properties of (La,Sr)FeO3 based perovskites* Fuel Cells 9 pp899-906 2009

Wang B, Yan R, Lee DH, Liang D T, Zheng Y, Zhao H, Zheng C *Thermodynamic Investigation of carbon deposition and sulphur evolution in chemical loping combustion with syngas* Energy and Fuels 22(2) 2008

Wang, Y. Liao Q, ZhoL, Waang H., *Oxygen permeability and structure stability of a novel cobalt-free perovskite Gd0.33Ba0.67FeO3−δ.* Journal of Membrane Science, 457: p. 82-87. 2014.

Wang W, Zhang Hb, Lin GD, Xiong ZT *Study of Ag/$La_{0.6}Sr_{0.4}MnO_3$ catalysts for complete oxidation for methanol and ethanol at low concentrations.* Applied Catalysis B: Environmental 24(3-4) p 219-232 2000

Wang K, Reeber RR *Mode Grunesisen parameter and negative thermal expansion of cubic ZrW 2 O 8 and ZrMo 2 O 8* Applied Physics Letters 76.16 pp 2203-2204 2000

Wenzel M., Aditya Dharanipragada N., Galvita V., Poelman H., Marin, L. Rihko-Struckmamn G., Sundmacher K., *CO production from CO2 via reverse $H_2O$-gas shift reaction performed in a chemical looping mode@ Kinetics on modified iron oxide* Journal of CO2 Utilization 17 pp60-68 2017

Xu, N. ,Zhao H, Zhou X, Wei w, Lu X, Ding W., *Dependence of critical radius of the cubic perovskite $ABO_3$ oxides on the radius of A- and B-site cations*. International Journal of $H_2$ Energy. 35(14): p. 7295-7301. 2010

Yaws, Carl L..*Yaws' Handbook of Properties of the Chemical Elements*. Knovel. Table 27. Retrieved from https://app.knovel.com/hotlink/toc/id:kpYHPCE007/yaws-handbook-properties/yaws-handbook-properties (2011).

Yeo Y, *Chemical Engineering Computation* with MATLAB, CRC Press, Boca Raton, 2017

Yoshihara J., Campbell C.,*Methanol Sythesis and Everse $H_2O$-gas shift Kinetics over CU(110) Model Catalysts: Structural Senstivty* Jouranl of Catalysis 161(2), pp776-782 1996

Young RA .(1995) "*The Rietveld method*" (Oxford University Press, Oxford, UK 1995)

Zeng L, He F, Li F, F LS *Coal-direct Chemical looping gasification for $H_2$ Production: reactor Modelling and Process Simulation* Energy fuels 26(6) pp 3690-3690 2012

Zhou L, Enakonda L, Harb M, Saih Y, Aguilar-Tapia A, Ould-Chikh S, Hazemann J, Li J, Wei N, Gary D, Del-Gallo P and Basset J. *Fe catalysts for methane decomposition to produce $H_2$ and carbon nano materials* Applied Catalysis B: Environmental 208 p44-59 2017